The Dissertation Committee for Cedric Michael Hurth Certifies that this is the approved version of the following dissertation:

Scanning Probe Microscopy Studies of Active Enzymes at Solid Surfaces

Committee:

_____

Allen J. Bard, Supervisor

_____

Françoise Argoul

_____

Eric Borguet

_____

Elisabeth Charlaix

_____

Keith J. Stevenson

_____

Laurent Servant

Scanning Probe Microscopy Studies of Active Enzymes at Solid Surfaces

by

Cedric Michael Hurth, M.Sc.

Dissertation

Presented to the Faculty of the Graduate School of

The University of Texas at Austin

in Partial Fulfillment

of the Requirements

for the Degree of

Doctor of Philosophy

The University of Texas at Austin

December 2005

Acknowledgments

Academic acknowledgments

First and foremost, let me sincerely thank Dr. Eric Borguet, Prof. Elisabeth Charlaix, Prof. Laurent Servant and Dr. Keith J. Stevenson for reading my manuscript with the scientific excellence that distinguishes them worldwide. I also thank Dr. Philippe Richetti for sparing me some of the hassle of an administratively complicated doctoral program.

Then, I wish to express my everlasting gratitude to my advisers. I thank Dr. Françoise Argoul for devising the most intricate but, in the end, the most exciting graduate research topics. I could extensively acknowledge Prof. Allen J. Bard for his insatiable appetite, over a half-century, of outstanding science at a level that many can only dream about along with the sincere humility and true work ethic that go with it. But I will merely repeat what the 150 or more electrochemists that have worked in his Laboratory for Electrochemistry have already written. And, last but not least, I'd like to thank Drs. Abdelhamid Maali and Jean-Pierre Aimé for their true passion for science and their ability to transmit their vision of nanosciences.

Funding

Work done at the Department of Chemistry of The University of Texas at Austin was supported by the National Science Foundation (NSF) and the Robert A. Welch Foundation. Work done at Université Bordeaux 1 was supported by grants from the Région Aquitaine and by Actions Concertées Incitatives (ACI) from the French Ministry of Research.

I personally acknowledge regular funding from the French Ministry of Research – Allocation du Ministére de l'Education Nationale, de la Recherche et de la Technologie

(MENRT) and Co-Tutelle Ministérielle as well as additional funding from the Centre National de la Recherche Scientifque (CNRS) and the Department of Chemistry and Biochemistry of the University of Texas at Austin.

Finally, this xchange program would not have been possible without the consent of the presidents of the two concerned universities; Dr. Larry R. Faulkner (The University of Texas at Austin) and Pr. Francis Hardouin (Université Bordeaux 1). They are therefore deeply acknowledged and, through them, let me thank the entire administration of both institutions.

Personal acknowledgments

Unlike regular programs, a joint program involves many persons that have had a significant impact on my work. I will thank them for advice, fruitful discussions and warm encouragements whenever needed in alphabetical order because I do not wish to classify their importance:

- Dr. Julio C. Aguilar, now at Universidad Nacional Autónoma de México, Mexico
- Dr. Mario A. Alpuche Aviles, at the University of Texas at Austin, USA
- Ms. Yoonjung Bae, at the University of Texas at Austin, USA
- Dr. Philippe Barois, Université Bordeaux 1 (CRPP), France
- Ms. Charlotte Bernard, Université Bordeaux 1 (CPMOH), France
- Pr. Vu Thien Binh, Université Claude Bernard, Lyon, France
- Dr. Rodolphe Boisgard, Université Bordeaux 1 (CPMOH), France
- Dr. Mihai Buda, now at the “Politehnica” University, Bucharest, Romania
- U.S. Navy Cdr. Robert Calhoun, at the University of Texas at Austin, USA
- Dr. Maurizio Carano, now at Clemson University, Clemson, SC, USA
- Dr. Jai-Pil Choi now at the University of North Carolina at Chapel Hill, USA
- Pr. Touria Cohen-Bouhacina, Université Bordeaux 1 (CPMOH), France
- Pr. Gérard Couturier, Université Bordeaux 1 (CPMOH), France
- Dr. Alain Dautant, Université Bordeaux 2 (IBGC), France
- Ms. Amanda Davidson, at the University of Texas at Austin, USA
- Dr. Dirk Dietzel, now at Universität Münster, Germany
- Dr. Tanya E. S. Dahms, at the University of Regina, Canada
- Dr. Michel Desmadril, Université Paris XI, France
- Dr. Fabien Dubourg, Université Bordeaux 1 (CPMOH), France
- Dr. Juan Elezgaray, Université Bordeaux 1 (IECB), France

- Dr. Fu-Ren F. Fan, at the University of Texas at Austin, USA
- Dr. Jose L. Fernandez, now at Universidad del Littoral, Santa Fe, Argentina
- Dr. Fernando Fungo, now at Universidad National de Rio Cuarto, Argentina
- Mrs. Christine Gauthier, Université Bordeaux 1 (CRPP), France
- Dr. Peixin He, CH Instruments, Inc., Austin, TX, USA
- Dr. Katherine B. Holt, now at University College London, United Kingdom
- Mr. Cédric Jai, Université Bordeaux 1 (CPMOH), France
- Dr. Sophie Kopp-Marsaudon, Université Bordeaux 1 (CPMOH), France
- Dr. George Kriek, Lanxess USA (Bayer Corporation), Pittsburgh, PA, USA
- Dr. Joseph Leandri, Université Bordeaux 1 (CPMOH), France
- Dr. Samuel Lesko, Veeco Instruments France SA, Dourdan, France
- Dr. Robert J. Lesuer, now at the University of Chicago, USA
- Dr. Chunzeng Li, Veeco Instruments, Inc., Santa Barbara, CA, USA
- Dr. Xiao Li, at the University of Texas at Austin, USA
- Dr. Chong-Yang Liu, at the University of Texas at Austin, USA
- Dr. Jean-Christophe Loudet, Université Bordeaux 1 (CRPP), France
- Dr. Charles R. Luman, now at the Federal Bureau of Investigation, Washington, DC, USA
- Dr. Abdelhamid Maali, Université Bordeaux 1 (CPMOH), France
- Dr. Stephen Maldonado, at the University of Texas at Austin, USA
- Dr. Gilles Marcou, now at Université Louis Pasteur, Strasbourg, France
- Dr. Pascal Martin, now at The University of Tokyo (IIS), Japan
- Dr. Janine Mauzeroll, now at Université du Québec à Montréal, Canada
- Dr. Todd M. McEvoy, now at the Naval Research Laboratory, Washington, DC, USA
- Dr. Masoud A. Mehrgardi, now at Shiraz University, Iran
- Dr. Wujian Miao, now at The University of Southern Mississippi, Hattiesburg, MS, USA
- Dr. Philippe Minard, Université Paris XI, France
- Dr. Noseung Myung, now at Konkuk University, Korea
- Dr. François Nadal, now at the Commissariat à l'Energie Atomique (CESTA), France
- Mrs. Angela S. Nelson, at the University of Texas at Austin, USA
- Dr. Dragan Nikic, at The University of Mississippi, USA
- Mr. Samuel Nikolay, now at Université de Liège, Belgium
- Dr. David Olea, now at Universidad Autonòma de Madrid, Spain
- Dr. Jong Hyeok Park, now at the Korea Advanced Institute of Science & Technology, Korea
- Dr. Gilles Pécastaings, Université Bordeaux 1 (CRPP), France
- Dr. Antonio Pereira, now at Imperial College, London, United Kingdom
- Dr. Donald L. Pile, now at Sandia National Laboratories, Los Alamos, NM, USA
- Dr. Philippe Poulin, Université Bordeaux 1 (CRPP), France
- Mr. Fabian Rios, now at Georgia State University, Atlanta, GA, USA
- Dr. Michael Rohwerder, at the Max Plank Institut für Eisenforschung, Düsseldorf, Germany
- Dr. Hassan Saadaoui, Université Bordeaux 1 (CRPP), France

- Pr. Jean Salardenne, Université Bordeaux 1 (CPMOH), France
- Dr. Yves-Henri Sannejouand, Ecole Normale Supérieure de Lyon, France
- Mr. Matthew Sartin, at the University of Texas at Austin, USA
- Pr. Jean-Michel Savéant, Université Denis Diderot, Paris, France
- Dr. Yangmin Sun, at the University of Texas at Austin, USA
- Dr. Jean-Claude Talbot, Université Bordeaux 2 (IBGC), France
- Dr. Chantal Tassius, Ecole Normale Supérieure de Lyon, France
- Dr. Ran Tel-Vered, at the University of Texas at Austin, USA
- Mr. Charles Thonig, at the University of Texas at Austin, USA
- Pr. Jean-Marie Turlet, Université Bordeaux 1 (CPMOH), France
- Pr. Odile Viratelle, Université Bordeaux 2 (CRPP), France
- Dr. Darren A. Walsh, now at the University of Newcastle, United Kingdom
- Ms. Yuching Weng, now at the National Cheng Kung University, Taiwan
- Mrs. Deane M. Willis, at the University of Texas at Austin, USA
- Dr. Wei Zhan, at the University of Texas at Austin, USA

Extended acknowledgments

Aditionally, I'd like to thank Dr. Eric Borguet, now at Temple University in Philadelphia, PA for providing a tremendous introduction to academic research during an undoubtedly fruitful summer undergrad research experience at the Surface Science Center of the University of Pittsburgh between May and August 2000. Similarly, these pages would never have been written without the patience and dedication of Dr. Ronald Melki who introduced me to the intricacies of protein biochemistry during my master degree research at the Laboratoire d'Enzymologie et de Biochimie Structurales in Gif-sur-Yvette, Essonne, France between September 2000 and July 2001.

Scanning Probe Microscopy Studies of Active Enzymes at Solid Surfaces

Publication No. _____

Cedric Michael Hurth, PhD
The University of Texas at Austin, 2005

Supervisor: Allen J. Bard

This work is a study of active enzymes by several scanning probe microscopies in order to extract mechanical, electrochemical and electrical properties. It is divided into three parts. Atomic Force Microscopy (AFM) studies of yeast 3-phosphoglycerate kinase (PGK) *ex situ* and *in situ* is coupled to UV-visible spectrophotometry to compare the enzyme activity of the immobilized enzyme to that of the free enzyme. Glucose Oxidase and the decomposition of hydrogen peroxide are studied by Scanning Electrochemical Microscopy (SECM) to extract heterogeneous rate constant. Finally, Scanning Electrochemical Potential Microscopy (SECPM) is studied from an instrumentation-based point of view because it could be of use in the future.

Table of Contents

Chapter 1: Introduction

The interest in studying active enzymes down to the single-molecule level is quite obvious. Enzymes are the most accomplished expression of molecular catalysis; they allow an organism to perform within milliseconds reactions that would otherwise take years or more to complete. Enzymes are the building blocks of life as they are the primary actors of a cell's metabolism and, by extension, that of a whole complex organism.

If it is true that most of the enzymes studied here usually evolve within the cytoplasm of living cells free of interactions with a solid surface, studying them at solid interfaces is motivating because it could reveal new features and also constitutes an ultimate challenge of our understanding of fundamental physical and chemical processes. Enrico Fermi (1901-1954) once said: "God made the solid phase and left the surface to the Devil". He underlines there the ultimate intricacy of surface studies. Moreover, if one wishes to study active enzymes at the level of one or a few molecules, the use of a solid surface cannot be avoided since it freezes the system to allow its observation with tools that often work with much higher time constants than those of the system studied, especially those of the free movement of one single molecule in a dispersed solution.

The following chapters present a study of several well-known enzymes with a variety of scanning probe techniques from a mechanical and an electrochemical point of view. Each chapter contains the background elements necessary to the reader; the basics of each technique will however be exposed thereafter for more clarity.

1. Atomic Force Microscopy (AFM): mechanical measurements at the nanometer scale

Unlike the static mode of AFM, commonly named Contact Mode (CM), the dynamic modes of AFM like the Amplitude-Modulation (AM) or the Frequency-Modulation (FM) modes, use a vibrating cantilever described as a damped harmonic oscillator to create a modulation of the force acting on the sample. Therefore, a variety of local mechanical measurements can be made including adhesion properties, elasticity, viscosity, structural properties …

1.1 General work principle of AFM

In an AFM setup (Figure 1.1), a laser beam (λ = 670 nm) from a laser diode source is focused on the silicon cantilever beam on which the pyramid-shaped tip is grown. The spot is slightly elliptical with dimensions of roughly 20 μm (length) x 9 μm (width). The reflected part of the laser beam is collected by a photodetector made with four interconnected diodes that can be named A1, A2, B1 and B2 disposed as shown in Figure 1.1. The cantilever is sometimes coated with a metallic layer to increase the reflectivity of its surface. Two sets of signals are then analyzed by the electronic modules of the AFM: (A1+A2)-(B1+B2) corresponding to the difference between the signal on the two upper diodes and the two bottom diodes or (A1+B1)-(A2+B2) corresponding to the difference between the signal on the two diodes on the left and the two diodes on the right. The latter is essentially used in friction measurements.

The sample is magnetically held on a piezoelectric scanner made with one piezoelectric tube for each direction that allows very fine movements of the sample.

The tip is grown on the cantilever beam which is itself fixed on the cantilever holder and placed in a stainless steel (glass or Plexiglas® in the case of measurements in a liquid environment) element containing a small piezoelectric element embedded at the basis of the cantilever holder that drives the oscillation of the cantilever with a complex transfer function. In the liquid cell, the piezoelectric element is placed farther away from the cantilever holder.

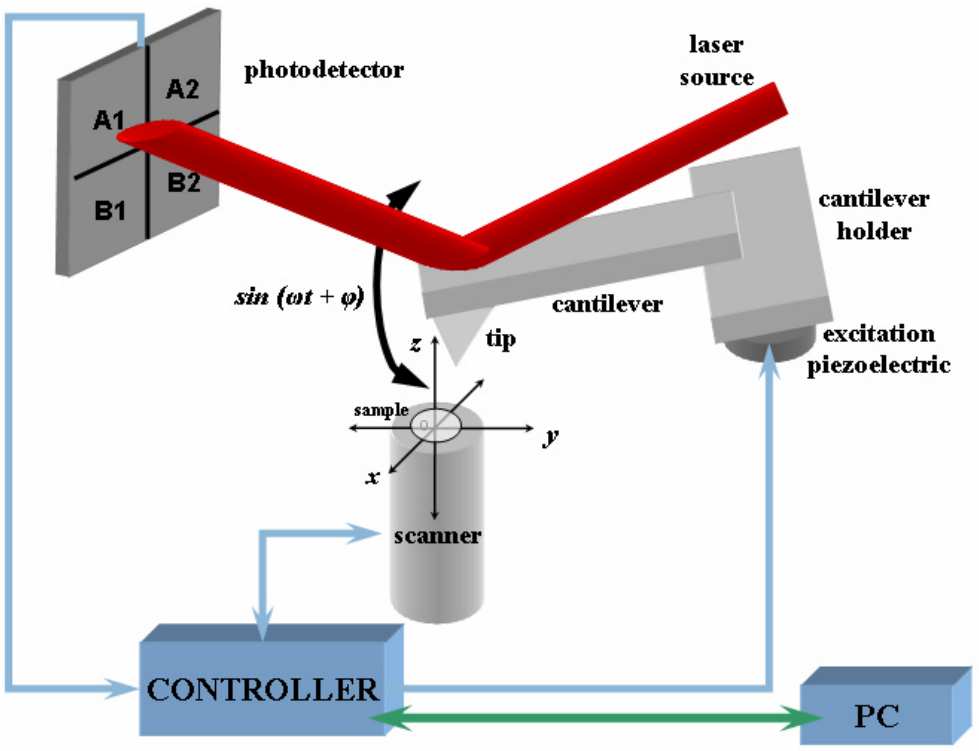

Figure 1.1: Simplified experimental setup of an Atomic Force Microscope (AFM) working in the dynamic mode. The different elements are not on scale for readability.

What makes the interpretation of an AFM experiment often difficult is the nature itself of the measured quantities, i.e. forces or interactions. They can be of very different origin and range[1]:

- Van der Waals forces, i.e. electrodynamic dipole-dipole interactions;

- Capillary and other adhesive forces that are actually a case of Van der Waals forces with a dominant dispersive term. They are of particular importance when experiments are carried out in ambient air and strongly depend on the relative humidity (RH);

- Electrostatic (columbic) interactions between point charges. They are negligible, especially in aqueous solutions, since most tips used are made of Si;

- Specific "chemical" interaction, e.g. biological ligand-receptor recognition. They are of dominant importance when tips are chemically modified with the target of the receptor that is on the surface for instance.

1.2 The harmonic oscillator description

1.2.1 Without probe-surface interaction

When there is no interaction between the sample and the probe, i.e. far away from the surface, the tip/cantilever system is well described by a Damped Linear Harmonic Oscillator (DLHO). Concretely, the tip/cantilever can be treated as a point mass *m* attached to a spring with a spring constant *k* following Hooke's law and a dashpot characterized by a viscosity *h* and driven by an excitation $f(t) = f_0 cos(wt)$ following Newton's law. They are associated either in series (Maxwell model) or in parallel (Voigt-Kelvin model).

One gets the following analytical expressions[2,3,4] after solving the equation of motion obtained from the application of Newton's second law:

- for the oscillation amplitude:

$$A(w) = \frac{f_0}{\sqrt{m^2\left(w_0^2 - w^2\right)^2 + g_0^2 w^2}} \qquad (1.1)$$

- for the phase lag between the supplied excitation signal and the oscillation of the tip/cantilever system:

$$\tan(j) = \frac{g_0}{2m\left(w_0^2 - w^2\right)} \qquad (1.2)$$

In both cases, g_0 is the damping coefficient in the absence of an interaction with the surface and $w_0 = \sqrt{\frac{k}{m}}$ defines the resonance of a free (undamped) oscillator. An important parameter, namely the quality factor *Q* of the oscillation, can be introduced. It characterizes energy losses (from non-conservative interactions) in the tip/cantilever system. Near the resonance, the quality factor can be defined by:

$$Q = \frac{m\left(w_0^2 - w^2\right)}{g_0 w} \approx \frac{m w_0}{g_0} \qquad (2)$$

This allows defining the resonant frequency of the damped harmonic oscillator:

$$w_r = w_0 \sqrt{1 - \frac{1}{4Q^2}} \qquad (3)$$

1.2.2 Interaction with the surface

Upon establishment of a probe-surface interaction, non linear phenomena arise. The immediate consequence is the distortion of the resonance curves of the tip/cantilever oscillator. The resonant frequency is shifted to lower values for an attractive interaction and to higher values for a repulsive interaction[5]. In real experimental situations though, the system will be exposed to both repulsive and attractive forces and dissipation from non-conservative processes will also have marked effects.

1.3 The different modes of dynamic AFM

1.3.1 Amplitude-modulation (AM) or Tapping Mode

1.3.1.1 Information contained in AM-AFM images

In this mode, the cantilever is supplied with a sinusoidal excitation of fixed frequency *?* and fixed amplitude a_{exc}. At each point defining the scan area, the extension or retraction height h of the z piezoelectric tube needed to maintain the oscillation amplitude of the cantilever A equal to a target value A_s (setpoint value) is recorded. Simultaneously, the phase lag of the oscillator j is measured via an auxiliary channel for each point. The image consists of a matrix of data [$h(x, y); j(x, y)$] for each of the scan points. In principle, for high values of Q essentially, the real topography of the sample can be obtained and the phase data gives information about local variations of mechanical properties, i.e. to simplify, the distribution of harder or softer parts of the scanned part of the surface.

The main advantage of this mode is the reduced shear force and therefore soft sample deformation as compared to the static (contact mode). However, if tapping mode is a straightforward operating mode of AFM, it is not always possible to measure conservative and dissipative interactions separately because the phase lag and the oscillation amplitude are not

independent. The relation can be established by comparing the power supplied to the cantilever and the dissipated power averaged over an oscillation cycle (one period *T*). Those two quantities have to be equal at all time because the whole tip-sample-driving force system is conservative. Furthermore, the dissipation term can be separated into two contributions: viscous damping i.e. cantilever energy dissipation to the surrounding media, $< P_{visc} >_T$, and cantilever (tip) energy dissipation to the sample, $< P_{tip} >_T$. This leads to the following expression of the power with all the parameters defined as earlier in the text[6]:

$$< P_{tip} >_T = < P_{supplied} >_T - < P_{visc} >_T = \frac{1}{2}\frac{kA^2 w_0}{Q}\left[\frac{A_0}{A}\sin(j) - 1\right] \qquad (4)$$

Where *A* is the amplitude compared to the amplitude at the resonant frequency w_0 and without tip-sample interaction A_0. Even if A/A_0 is kept constant by the feedback loop, the loop has a response time that leads to minor changes in A/A_0 from the sample topography and therefore the energy dissipated in the tip cannot strictly be linked to phase changes only. In Tapping Mode AFM conservative and dissipative effects cannot be separated in amplitude and phase changes respectively.

1.3.1.2 Regimes of the AM-AFM mode

In AM-AFM approach curves, two typical extreme profiles are usually observed:

- The phase lag j – set to -45° far away from the surface (no interaction) – evolves between -90° and -180°. The attractive regime is dominant. This occurs for small oscillation amplitudes (< 5 nm)[7] because the time during which the tip is closest to the sample, i.e. during which an attractive Van der Waals interaction is sensed, is longer than for large amplitudes for the same frequency. This situation is called “attractive regime”.

- The phase lag j – set to -45° far away from the surface (no interaction) – stays larger than -90° and increases as the surface approaches. The repulsive regime is dominant. This occurs for larger oscillation amplitudes (> 5 nm)[7] and is called “repulsive regime”.

1.3.2 Frequency-modulation (FM) or Non-Contact Mode

In this mode, the cantilever is supplied with a sinusoidal excitation of frequency *?* and amplitude a_{exc}. At each point defining the scan area, the excitation amplitude is adjusted via an automatic gain control electronic loop to maintain the amplitude corresponding to the resonance frequency constant. This adjustment constitutes a measurement of the relative damping at each point materialized by the ratio γ/g_0 where g is the damping coefficient and g_0 is the damping coefficient far away from the surface (no interaction). Simultaneously, the frequency shift from the resonant frequency far away from the surface Dn is recorded. The feedback channel, i.e. the one through which z-piezoelectric adjustments to maintain a setpoint value are controlled, can be set to either γ/g_0 or Dn. Dn increases as the surface gets closer because of the increasing dissipation of the energy of the oscillating tip – reflected in the increase of γ/g_0. The FM-AFM mode is a more physical way to perform dynamic AFM because it measures conservative and dissipative contributions to the tip-sample interaction separately provided the oscillator has reached a quasi steady-state for each measurement (data point).

1.4 Interest of dynamic AFM for the study active enzymes

First, one can notice that the size of most tip apexes used in dynamic AFM experiments is of the same order as that of most globular proteins, i.e. between 5 and 10 nm as obtained by Transmission Electron Microscopy (TEM), Nuclear Magnetic Resonance (NMR) and X-ray diffraction methods[8]. Dynamic AFM appears as an indispensable tool in terms of the resolution needed to image a single protein molecule. AFM also makes it possible to measure forces at the nanometer scale, i.e. at the single-molecule level.

The forces measured with an atomic force microscope can be between either a bare clean tip and an enzyme molecule immobilized or deposited on the surface[9,10] or between a tip that has been previously carefully chemically modified with a molecule or another protein that are known to interact with the studied protein present on the surface[11,12]. The first case usually applies to situations where structural imaging is sought[13,14,15] or when more physical information is sought like in elasticity measurements[16] or when mapping flexible domains inside a protein structure[17] or

even when reversibly unfolding single protein molecules[18]. Tip modification is usually helpful when one wishes to investigate protein-protein interactions in real time[19] or substrate-protein interactions like in the case of the biotin-streptadivin complex where the complete energy landscape can be measured[20].

Most of the examples cited above do not use the dynamic mode; we wish to use the additional features of the dynamic mode of AFM to obtain new structural and mechanical information on the studied enzymes. Indeed, aside from the established advantage of the dynamic mode in terms of reduced lateral shear force, dynamic AFM can also open new fields of study. For instance, with the harmonic oscillator model, dynamic AFM relies on non-linear properties and can therefore amplify processes that were hardly detectable in the static mode.

Moreover, one can expect to study protein dynamics while they perform biological catalytic acts by coupling their possible conformational changes[8] to the oscillation of the cantilever. This raises the essential question of the nature of the probe to use; its material and its dimensions.

Indeed, similarly to the situation of impedance adaptation in electrodynamics where an electrical signal will not propagate between two impedances Z_1 and Z_2 if they are too different[21], if the cantilever and the studied sample have too different spring constants, no dynamic response of the sample can be monitored (Figure 1.2). If one assumes that one phosphoglycerate kinase (PGK) molecule studied in Chapter 3 is a rectangular object of length L = 8 nm, width w = 5 nm and thickness t = 2 nm according to X-ray diffraction data[22] and that the elastic Young modulus of a single PGK molecule, E_{PGK}, is not much different from the experimental values for routinely available polymers like Nylon® (Polyamide-66), i.e. 1.73 GPa[23], the spring constant of an individual PGK molecule oriented as shown in Figure 1.2 can be evaluated by Equation (5)[24]:

$$k_{PGK} = E_{PGK}\Phi \qquad (5)$$

Where Φ is the average section diameter of the cylinder that represents a single PGK molecule.

Equation (5) yields $k_{PGK} \sim 3$ N.m^{-1}. Since most of the commercially available cantilevers have spring constant between 0.1 and 40 N.m^{-1}, measurements by coupling should be possible provided a proper cantilever is chosen. When the cantilever stiffness is too low ($< 10^{-2}$ N/m), additional problems from adhesion of the cantilever to the surface arise. However, the value of

the Young modulus used can be very different from that of a polyelectrolyte polymer since additional stabilization by Van der Waals interactions or hydrogen bonding may occur inside a protein molecule and therefore drastically rigidify the structure. Additionally, proteins that exhibit conformational changes may even be softer than a polymer in order to minimize the energy required to perform the conformation change.

The need to characterize existing cantilevers and determine if more suitable ones need to be built is developed in Chapter 2 and applied to the study of immobilized phosphoglycerate kinase (PGK) in Chapter 3.

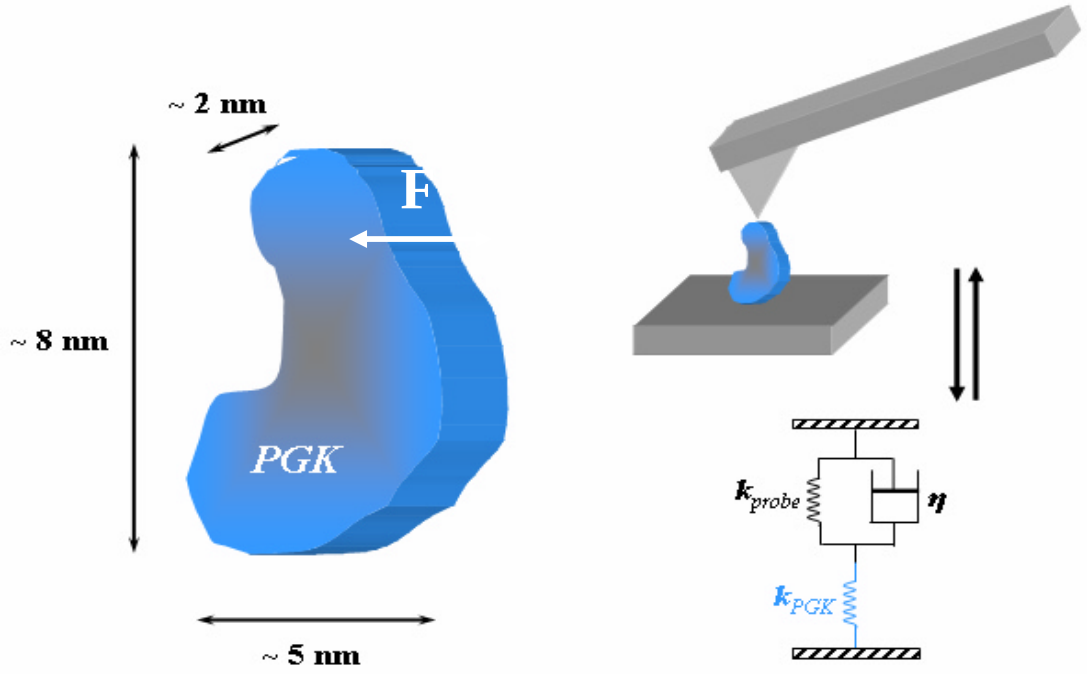

Figure 1.2: Schematic of the adaptive spring constant issue in the expected coupling experiments of the protein dynamics with the oscillating tip. The second dashpot describing the protein molecule interacting with the tip has been omitted for clarity.

Dynamic AFM appears as an innovative tool to study active enzymes. It can yield many new mechanical measurements. However, unless a special tip is used, it provides comparable electrodynamic or electrostatic information only after the measured force profile can be linked to surface potentials. That's why other local probe techniques are used in this dissertation.

2. *Scanning Electrochemical Microscopy (SECM): chemically-specific local measurements*

2.1 SECM framework

Like AFM, SECM uses a probe whose movements are controlled at a very fine level with piezoelectric elements to study surface processes. However, the probes used are often made manually because of their complexity and are therefore much larger, which limits the resolution of SECM as compared to AFM.

The resolution of SECM may be lower than that of AFM but it possesses an undeniable advantage through its chemical sensitivity since the probe is an ultramicroelectrode (UME)[25] that can selectively oxidize or reduce a compound, an ion selective probe[26,27] or even a gas-phase Clark ultramicroelectrode for oxygen sensing[28]. A counter electrode, a reference electrode and a Teflon® cell complete the setup roughly depicted in Figure 1.3.

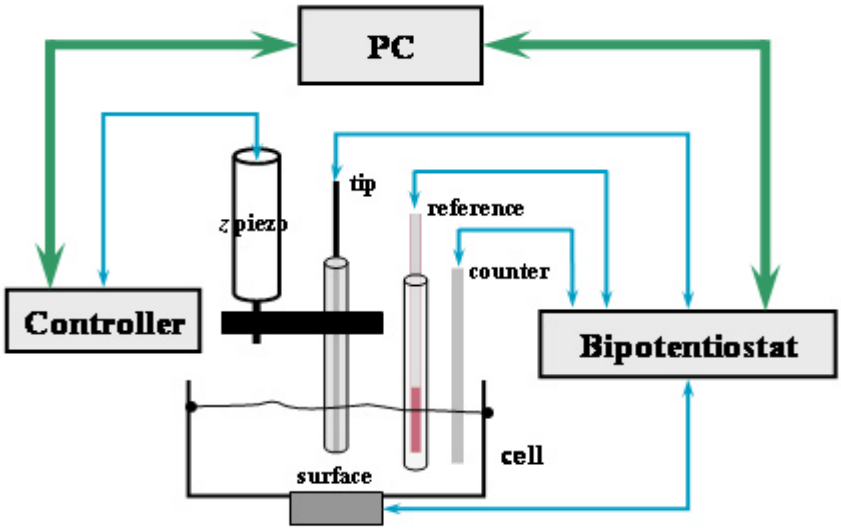

Figure 1.3: Simplified experimental setup of a Scanning Electrochemical Microscope (SECM). In this case, the surface is conductive and can act as a second working electrode. The different elements are not on scale for readability.

The electrode fabrication has been detailed elsewhere[29]. It typically consists in heat-sealing a thin metallic wire (Pt, Au, Ag, Cu…) or even a carbon fiber in borosilicate glass, making electrical contact to a copper wire with an electrically conductive oven-curable silver epoxy resin (H20E, Epoxy Technology, Billerica, MA). Usually, one wishes to get as close as possible to a planar disc geometry by sharpening the borosilicate glass on grit paper and polishing the exposed electrode surface with several alumina solutions of decreasing particle size.

2.2 SECM operation modes

2.2.1 Collection modes

A redox species can be either collected by the tip, poised at the proper potential, as it is generated at the substrate and reaches the tip by mass-transfer (Surface Generation/Tip Collection (SG/TC) mode) or collected by the surface, poised at the adequate potential, as it is generated at the tip and reaches the surface by mass-transfer (Tip Generation/Surface Collection (TG/SC) mode). The latter is often preferred since the SG/TC response contains a more significant transient component because the tip area is much smaller than the surface area, which decreases the collection efficiency, and the redox species has to diffuse through the gap of solution between the surface and the tip, which is an unavoidable lag phase.

The collection modes are the most adapted techniques to study homogeneous kinetics such as chemical decomposition studies since the tip is placed far away from the surface to avoid surface effects. The important parameter is the collection efficiency that is the ratio of the amount of species collected and that generated. It depends on the relative geometries and positions of the tip and the surface. Homogeneous parameters are obtained by comparing experimental results with digital simulations.

In collection modes, the first step is always to place the tip at a certain known distance and then poise either the tip or the surface at the determined potential and measure the variations of the sensed tip or surface currents. Tip positioning is often carried out in the other SECM mode (feedback mode) with a solution redox couple (mediator) different from the one that is generated and/or collected in the collection experiment. This mode is detailed in the next section.

2.2.2 Feedback mode

The feedback mode of SECM is detailed in Chapter 4 (section 1.3). Therefore, only the basic principles will be exposed here. In the feedback mode, the probe is held at the desired potential with respect to the reference electrode approached to the surface with precise piezoelectric elements at a resolution of about 10 nm slowly enough to minimize convection contributions to

the measured tip current. The response obtained depends on the nature of the surface; conductor, insulator or mixed (Interdigitated Arrays (IDA), biochemical sensors …).

In the case of a conductor, the species oxidized (reduced) at the tip will be reduced (oxidized) back at the surface at a certain rate (heterogeneous reaction rate) and the tip current will therefore be modified as it gets closer to the surface where the electrochemical process occurs. In the case of an insulator, hindered hemispherical diffusion of the redox species from the solution bulk to the tip will progressively occur as the tip is approached to the surface since the surface is much larger than the tip. This blocking effect will also be seen in the monitored tip current.

The feedback response is very dependent on the rate of mediator regeneration at the surface and is therefore the best choice if one wishes to study heterogeneous reactions. Consequently, the work presented here (Chapter 4 essentially) will focus exclusively on the feedback mode of SECM.

2.3 Application of SECM to the study of active enzymes

Since 1989, the year SECM has been invented[30], many enzymatic systems have been studied using the feedback mode. These include: glucose oxidase[31], cytochrome c reductase[32], diaphorase[33], horseradish peroxidase[34], nitrate reductase[35] or β-galactosidase[36]. All the knowledge gathered from this proficient research on enzymatic activity by SECM will be used in Chapter 4 where the possible influence of an external DC electric field on the enzymatic activity is investigated. A detailed literature review on the possible expected effects of a DC electric field is included in Chapter 4 (section 1.2). The choice of the feedback mode of SECM is due to the sensitivity of the steady-state regime of reduction (or oxidation) of a dissolved mediator that does not interfere with the studied electroactive enzyme to an external perturbation related to enzymatic activity that regenerates or consumes more of the mediator.

Additionally, the feedback mode of SECM is applied to the study of hydrogen peroxide decomposition by catalase and by platinum nanoparticles in Chapter 4. In this case, emphasis is laid on the feedback loop itself. Indeed, the usual stoichiometry of 1 regenerated mediator molecule for 1 molecule transformed at the tip is not respected for the study of hydrogen peroxide decomposition developed in Chapter 4. The results could be successfully applied to

study new catalytic substrates as well as all the enzymes involving hydrogen peroxide, i.e. not only catalase or horseradish peroxidase but also glucose oxidase.

To complete electrical studies of enzymatic activity, one might also be interested in measuring non-faradaic processes. If SECM is not suitable for these types of studies, other local probe techniques were recently made available. If the original idea was to use them to monitor enzymatic activity, the state of development of these new techniques is such that the first step of developing the instrument had to be carried out first. Chapter 5 studies Scanning Electrochemical Potential Microscopy (SECPM) to investigate the feasibility of high-resolution measurements on biological systems.

3. STM/EC-STM/SECPM: a logical evolution of local electrical measurements?

3.1 Scanning tunneling Microscopy (STM)

Historically, Scanning Tunneling Microscopy (STM) was the first scanning probe technique made available and its inventors were awarded the Nobel Prize in Physics in 1982[37].

3.1.1 Setup

Similarly to all other Scanning Probe Techniques, STM consists of a piezoelectric scanner to position the sample with subnanometer precision, an electrically conductive $Pt_{80}Ir_{20}$ (or W) wire mechanically or electrochemically sharpened at one end and a measuring head. In the STM measuring head, the laser detection used in AFM is replaced by an amplifier stage that measures and amplifies the tunneling current sensed between the PtIr tip and a conductive sample.

3.1.2 Measured quantities

Unlike AFM, STM does mot measure forces but the tunneling current flowing from the tip to the sample or vice and versa depending on the polarity of the tip-sample bias applied. That current is then maintained at a certain value (setpoint current) by the electronic feedback loop;

Piezo adjustments are recorded at each point to create a topography image of the sample studied. The need for a tunneling current immediately limits the use of the technique to conductors (metals or graphite) and semi-conductors (silicon, gallium arsenide…).

From quantum mechanics, the probability of an electron tunneling through a one-dimensional rectangular barrier of thickness Dz and height j (Figure 1.4) is given by[38]:

$$W = \frac{|A_t|^2}{|A_0|^2} \approx \exp(-k\Delta z) \qquad (6)$$

Where A_0 is the amplitude of the electron wave before the barrier and A_t the amplitude of the transmitted wave after the barrier. k is the attenuation constant of the wave in the barrier and is given by $k = \sqrt{2m(j - E)/h^2}$ if m is the electron mass, E its energy and h is the Planck constant.

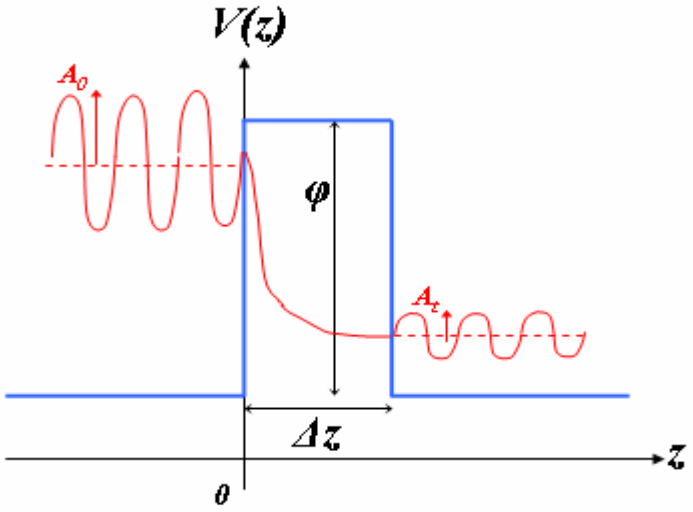

Figure 1.4: Rectangular potential barrier modelling the situation of an electron tunelling through vacuum from the tip to the sample or vice and versa and schematic representation of the electron wave before and after the barrier as well as the exponential attenuation within the barrier.

The tunneling current density (Figure 1.5) for large values of the bias voltage ($E_{bias} > j$), is given by the Fowler-Nordheim formula[39]:

$$J = \frac{e^3 E_{bias}^{\ 2}}{8\pi h j (\Delta z)^2} \exp\left(-\frac{8\pi\sqrt{2m}\, j^{3/2}\Delta z}{3ehE_{bias}}\right) \qquad (7)$$

Where E_{bias} is the applied bias voltage, e is the electron charge, m is the electron mass and h is the Plank constant.

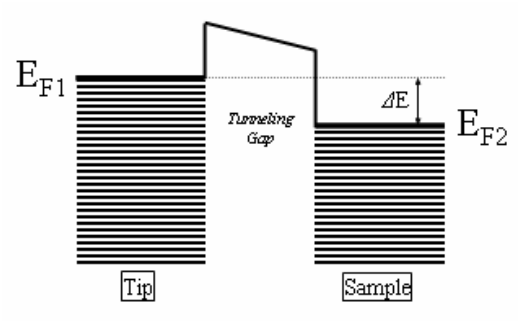

Figure 1.5: Energy level diagram of the tip and the sample under the applied bias E_{bias}.

The exponential dependence of the measured tunneling current on the distance *Dz* (thickness of the potential barrier) allows adjusting the tip-sample distance with a very high accuracy.

3.1.3 From vacuum to liquid media: Electrochemical STM (EC-STM)

In chemistry in particular, it is often of much higher interest to study dissolved or surface-adsorbed molecules *in situ*. In order to use the STM in liquid media, a few modifications had to be implemented. In order to control the tip and surface potentials precisely to apply the tip-sample bias a reference and a counter electrode as well as a bipotentiostat are required. In most cases, the reference and counter electrodes are quasi-reference electrodes (Pt wire) because of the limited available space in the STM setup, a prerequisite to a low noise level. The potentiostat usually has a final current/voltage converter sensitivity of about 1 nA/V. When needed, potentiostats with picoampere sensitivity are available as well. Because a bipotentiostat is involved, this modification of the Scanning Tunneling Microscopy is called Electrochemical STM (EC-STM).

3.2 Scanning Electrochemical Potential Microscopy (SECPM)

This latest modification of the EC-STM setup has been newly introduced and aims at mapping surface potentials without significant perturbation by the probe electrode. The limitation to conductors or semi-conductors disappears since in principal any charged surface could be imaged by this technique. Chapter 5 is an instrumentation-oriented study of the new technique and contains many details on the setup. Basically, the setup modification consists in replacing the

STM current pre-amplifier by a very high input impedance potential difference amplifier. It is shown that SECPM could be an important breakthrough in scanning probe microscopies especially for the study of biological samples such as active enzymes.

References

[1] Atkins P., and de Paula J., *Physical Chemistry*, 7th Ed., Oxford University Press, Oxford, 2002
[2] Garcia R., and Perez R. (2002), *Surf. Sci. Reports*, **47**, 197-301
[3] San Paulo A., and Ricardo G. (2001), *Phys. Rev. B*, **64**, 1934-38
[4] Dürig U. (2000), *Appl. Phys. Lett.*, **76**, 1203-1206
[5] Nony L., Boisgard R., and Aimé J.P. (1999), *J. Chem. Phys.*, **111(4)**, 1615-1627
[6] Cleveland J.P., Anczykowski B., Schmid A.E., and Elings V.B. (1998), *Appl. Phys. Lett.*, **72**, 2613-2615
[7] Nony L., Boisgard R., and Aimé J.P. (2001), *Biomacromolecules*, **2**, 227-235
[8] Branden C.I., and Tooze J., *Introduction to Protein Structure*, 2nd Ed., Garland Publishing, New York, 1999
[9] Engel A., and Müller D.J. (2000), *Nature Struct. Biol.*, **7(9)**, 715-718
[10] Rief M., Gautel M., Oesterhelt F., Fernandez J.M., and Gaub H.E. (1997), *Science*, **276**, 1109-112
[11] Vinckier A., Gervasoni P., Zaugg F., Ziegler U., Lindner P., Groscurth P., Plückthun A., and Semenza G. (1998), *Biophys. J.*, **74**, 3256-3263
[12] Wang T., Arakawa H., and Ikai A. (2001), *Biochem. Biophys. Res. Comm.*, **285**, 9-14
[13] Fotiadis D., Müller D.J., Tsiotis G., Hasler L., Tittmann P., Mini T., Jenö P, Gross H., and Engel A. (1998), *J. Mol. Bio.*, **283**, 83-94
[14] Stamouli A., Kafi S., Klein D.C.G., Oosterkamp T.H., Frenken J.W.M., Cogdell R.J., and Aartsma T.J. (2003), *Biophys. J.*, **84**, 2483-2491
[15] Paige M.F., Rainey J.K., and Goh M.C. (1998), *Biophys. J.*, **74**, 3211-3216
[16] Fisher T.E., Oberhauser A.F., Carrion-Vazquez M., Marszalek P.E., and Fernandez J.M. (1999), *Trends in Biochemical Sciences*, **24**, 379-384
[17] Müller DJ., Fotiadis D., and Engel A. (1998), *FEBS Lett.*, **430**, 105-111
[18] Oesterhelt F., Oesterhelt D., Pfeiffer M., Engel A., Gaub H.E., and Müller D.J. (2000), *Science*, **288**, 143-146
[19] Viani M.B., Pietrasanta L.I., Thompson J.B., Chand A., Gebeshuber I.B., Kindt J.H., Richter M., Hansma H.G, and Hansma P.K. (2000), *Nature Struct. Biol.*, **7(8)**, 644-647
[20] Yuan C., Chen A., Kolb P., and Moy V.T. (2000), *Biochemistry*, **39**, 10219-10223
[21] Jackson J.D., *Classical Electrodynamics*, 3rd Ed., John Wiley & Sons, New York, 1999
[22] Mas M.T., Resplandor Z.E., and Riggs A.D. (1987) , *Biochemistry*, **26(17)**, 5369-5377
[23] Lide D.R., *CRC Handbook of Physics and Chemistry*, 79th Ed., CRC Press, Boca Raton (1999)
[24] Kosevich A.M., Lifshitz E.M., Landau L.D., and Pitaevskii L.P., *Course of Theoretical Physics VII: Theory of Elasticity*, Pergamon Press, London, 1960
[25] Fleischmann M., Pons S., Rolison D.R., and Schmidt P., *Ultramicroelectrodes*, Datatech Systems, Inc. Publications, Morganton, 1987
[26] Amemiya S., and Bard A.J. (2000), *Anal. Chem.*, **72**, 4940-4948
[27] Horrocks B.R., Mirkin M.V., Pierce D.T., Bard A.J., Nagy G., and Toth K. (1993), *Anal. Chem.*, **65**, 1213-1224
[28] Carano M., Holt K.B., and Bard A.J. (2003), *Anal. Chem.*¸ **75**, 5071-5079
[29] Bard A.J., and Mirkin M.V., *Scanning Electrochemical Microscopy*, Marcel Dekker, New York, 2001
[30] Bard A.J., Fan F.R.F, Kwak J., and Lev O. (1989), *Anal. Chem.*, **61(2)**, 132-138
[31] Pierce D.T., Unwin P.R., and Bard A.J. (1992), *Anal. Chem.*, **64(17)**, 1795-1804
[32] Pierce D.T., and Bard A.J. (1993), *Anal. Chem.*, **65(24)**, 3598-3604
[33] Shiku H., Takeda T., Yamada H., Matsue T., and Uchida I. (1995), *Anal. Chem.*, **67(2)**, 312-317
[34] Shiku H., Matsue T., and Uchida I. (1996), *Anal .Chem.*, **68(7)**, 1276-1278
[35] Zaumseil J., Wittstock G., Bahrs S., and Steinrücke P. (2000), *Fresenius J. Anal. Chem.*, **367**, 352-357
[36] Zhao C., Sinha J.K., Wijayawardhana C.A., and Wittstock G. (2004), *J. Electroanal. Chem.*, **561**, 83-91
[37] Binnig G., Rohrer H., Gerber Ch., and Weibel E. (1982), *Phys. Rev. Lett.*¸**49(1)**, 57-61
[38] Cohen-Tannoudji C. Diu B., and Laloe F., *Quantum Mechanics*, Hermann, Paris, 1977
[39] Sarid D., *Scanning Force Microscopy*, Ch. 4, 55-64, Oxford University Press, Oxford, 1991

Chapter 2: Hydrodynamics of an Oscillating Atomic Force Microscopy (AFM) Cantilever

Most results published recently on protein imaging in liquid media have to be taken very carefully, especially when one wishes to draw quantitative mechanical information from these images. For instance, the so-called resonant peak of the cantilever used in the feedback loop for the imaging is actually, in most cases, a peak resulting from the coupling of the cantilever oscillation with the Plexiglas® cell vibration during the electro-acoustic excitation of the small piezoelectric element embedded in the cell. It is not a real resonance peak of the cantilever considered as a linear harmonic oscillator. Therefore, quality factors, *Q*, around 20-40 are often reported whereas thermal noise analysis of such probes in the same media when the cantilever is not excited show quality factors between 1 and 8 typically. This common mistake found in the literature relating to dynamic Atomic Force Microscopy (AFM) experiments in liquid media on biological samples raises an underlying complex hydrodynamic problem. The next sections aim at studying this hydrodynamic problem in detail, as its comprehension is a prerequisite to proper quantitative imaging in liquid media.

1. Presentation of the problem

The different oscillating modes of an AFM microscope provide a series of very sensitive force sensors. Therefore, dynamic AFM is widely used to investigate mechanical properties and structures of soft materials at the nanometer scale. Because of this high force sensitivity, numerous attempts have been made to introduce oscillating modes in liquid with the obvious goal of developing a dynamic AFM for life science. However, unlike in vacuum, the size of the cantilever is of great importance. When the cantilever oscillates in a fluid, hydrodynamic forces can play a significant role. In particular, the hydrodynamic forces in water become large enough – a few nanonewtons typically – to overcome the interaction between the tip apex and the surface.

Consequently, pioneering experimental works investigated the oscillation behaviors of small cantilevers[1,2,3] in order to reduce the amount of liquid moving with them and therefore the drag force. Aside from experimental work, developments of new vibrating cantilevers need an

accurate understanding of their damping characteristic in liquids. Thus, based on previous mathematical analysis[4], systematic approaches of hydrodynamics in the probe vicinity were developed[5,6,7,8,9].

In experiments reported here, the thermal noise was analyzed. Thermal noise examination was preferred over direct acoustic excitation of the cantilever to circumvent the intricate interpretation of the transfer function between the piezoelectric excitation and the Plexiglas cell.

Based on the theoretical expressions derived previously[4,5], experimental results are readily compared. While building a useful basis to analyze the experimental data, available analytical expressions might not be appropriate for higher harmonics[5]. A simplified expression of the hydrodynamic function *G* will be introduced. The advantage of this approach is that the damping coefficient and added mass appear as a simple function of the beam geometrical parameters. The obtained simplified expressions help to interpret the experimental data. From the measurement of the quality factor and resonant frequency shift when moving from air to liquid, the added mass and damping coefficient are extracted as a function of the eigenmode resonant frequency.

2. Experimental methodology

2.1 Formalism

Analytical solutions of the equations governing the oscillation of an AFM cantilever in water will be introduced. The complex geometry of the cantilever and tip system is the main difficulty in the problem. Based on several developments made from 1963 to 1969, a cylindrical cantilever is assumed first – thus neglecting the pyramidal tip. Then, analytical solutions to a rectangular geometry are provided – still neglecting the tip.

2.1.1 Cylindrical cantilever

In all forthcoming situations, the cantilever and tip will always be considered to be located far from the surface (D > 500 µm) where no tip-sample interaction is involved. The first step to

get a complete analytical solution to the problem is to calculate the hydrodynamic force acting on the oscillating cantilever. In 1963, Berker showed that the hydrodynamic force acting on a cylinder moving at a constant velocity and oscillating perpendicularly to its axis admitted an analytical solution[10]. This model gives an expression of the hydrodynamic force but lacks a realistic evaluation of the hydrodynamic damping and is hardly suitable for oscillating systems. Consequently, more complex calculations corresponding to a cylinder moving in block perpendicularly to its axis (Figure 2.1) have been carried out by Rosenhead[11] in 1963 and Tuck[4] in 1969. A summary of these works follows.

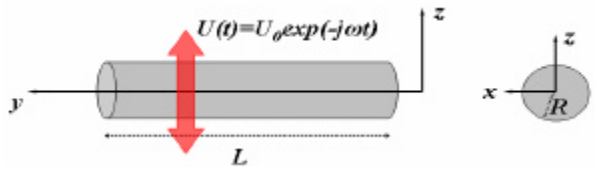

Figure 2.1: Situation of a cylinder of length *L* oscillating freely perpendicularly to its axis considered by Tuck[4] to get analytical expressions for the movement of a cantilever in AFM.

In the cylindrical coordinate system, the velocity ***V(r,q,t)*** has both an angular and a radial component. Its expression is:

$$\begin{cases} V_q(r,q) = -U_0 \exp(-jwt).\sin q \\ V_r(r,q) = U_0 \exp(-jwt).\cos q \end{cases} \qquad (1)$$

The general solution to equation (1) can be rewritten as the sum of two terms:

$$y(r,q) = y_1(r,q) + y_2(r,q)$$
$$\begin{cases} y_1(r,q) = F_1(r).\exp(-jwt).\sin q \\ y_2(r,q) = F_2(r).\exp(-jwt).\cos q \end{cases} \quad \text{with:} \quad \begin{cases} V_r = \dfrac{1}{r}\dfrac{\partial y}{\partial q} \\ V_q = -\dfrac{\partial y}{\partial r} \end{cases} \qquad (2)$$

To obtain analytical solutions to the Navier-Stokes equation[12] one needs to linearize it. The main criterion to linearize the Navier-Stokes equation is to compare the non-linear inertial term $\left| r_{fluid}\left(\vec{v}.\vec{\nabla}\right)\vec{v}\right|$ to the viscous term $\left|h_{fluid}\Delta\vec{v}\right|$ if ρ_{fluid} and η_{fluid} are the fluid density and viscosity respectively. The ratio of these two terms is often referred to as the Reynolds number[12,13]:

$$\mathrm{Re} = \frac{\left| r_{fluid}\left(\vec{v}.\vec{\nabla}\right)\vec{v}\right|}{\left|h_{fluid}\Delta\vec{v}\right|} \approx \frac{r_{fluid} v L}{h_{fluid}} \qquad (3)$$

v and *L* are respectively a typical velocity and dimension of the system in motion. *L* = *R* (radius of the cylinder):

$$\mathrm{Re} \approx \frac{r_{fluid} v R}{h_{fluid}} \quad (4)$$

Under conditions where the Reynolds number is very small, the Navier-Stokes equation becomes:

$$\frac{\partial \vec{v}}{\partial t} + \frac{\nabla \vec{p}}{r_{fluid}} - \frac{h_{fluid}}{r_{fluid}} \Delta \vec{v} = 0 \quad (5)$$

Another important criterion to understand the dynamics of oscillating cantilever is to compare the transient term $\left| r_{fluid} \frac{\partial \vec{v}}{\partial t} \right|$ to the viscous term $\left| h_{fluid} \Delta \vec{v} \right|$. This introduces a parameter b of particular importance when considering oscillating systems:

$$b = \frac{\left| r_{fluid} \frac{\partial \vec{v}}{\partial t} \right|}{\left| h_{fluid} \Delta \vec{v} \right|} \approx \frac{r_{fluid} w R^2}{h_{fluid}} \quad (6)$$

The pressure p can be eliminated from equation (1.5) by introducing the vorticity $\vec{W} = \overrightarrow{rot}\left(\vec{v}\right)$ for an incompressible fluid characterized by $div\left(\vec{v}\right) = 0$. It yields:

$$\frac{\partial \vec{W}}{\partial t} - \frac{h_{fluid}}{r_{fluid}} \Delta \vec{W} = 0 \text{ with the vector } \vec{W} = [0,0,-\Delta y] \quad (7)$$

This means that: $\left(\frac{\partial}{\partial t} - \frac{p}{h_{fluid}} \Delta \right) \Delta y = 0$. Then, If $Y = Y1 + Y2$:

$$\begin{cases} \Delta y_1 = \left[\frac{1}{r} \left(\frac{\partial F_1}{\partial r} + r \frac{\partial^2 F_1}{\partial r^2} \right) - \frac{F_1}{r^2} \right] \exp(-jwt).\sin q = 0 \\ \Delta y_2 - \frac{r_{fluid}}{h_{fluid}} \frac{\partial y_2}{\partial t} = \left(\left[\frac{1}{r} \left(\frac{\partial F_2}{\partial r} + r \frac{\partial^2 F_2}{\partial r^2} \right) - \frac{F_2}{r^2} \right] - \frac{r_{fluid}}{h_{fluid}} (-jw) F_2 \right) \exp(-jwt).\cos q = 0 \end{cases} \quad (8)$$

The calculation of the pressure and the functions $F_1(r)$ and $F_2(r)$ are done with the boundary conditions. The boundary conditions express the fact that liquid molecules stick to the cantilever (rigid boundary approximation):

$$\begin{cases} V_r(r = R, q, t = 0) = U_0 \cos q \\ V_q(r = R, q, t = 0) = -U_0 \sin q \end{cases} \quad (9)$$

These yield an expression of the hydrodynamic force:

$$F_h^{cyl} = jwpr_{fluid}R^2L\Gamma_{cyl}(b)U_0\exp(-jwt) = -pr_{fluid}R^2L\Gamma_{cyl}'(b)\frac{\partial U}{\partial t} - wpr_{fluid}R^2L\Gamma_{cyl}''(b)U \quad (10)$$

Where: $\Gamma_{cyl}(b) = 1 + \frac{4K_1\left(\sqrt{-jb}\right)}{\sqrt{-jb}\,K_0\left(\sqrt{-jb}\right)} = \Gamma_{cyl}'(b) + \Gamma_{cyl}''(b)$ with *K0* and *K1* the two first modified Bessel functions. The hydrodynamic force can be rewritten:

$$F = -m_{added}\frac{\partial U}{\partial t} - g_{diss}U \qquad (11.1)$$

The real part of the force puts an additional mass on the cantilever originating from the mass of fluid that the cantilever displaces while oscillating. One can speak of added hydrodynamic mass. The imaginary part of the force stands for a dissipative term.

$$\begin{cases} m_{added} = pr_{fluid}R^2L\Gamma_{cyl}'(b) \\ g_{diss} = wpr_{fluid}R^2L\Gamma_{cyl}''(b) \end{cases} \qquad (11.2)$$

With the definition of the quality factor *Q*:

$$Q \approx \frac{m_{total}w}{g_{diss}} = \frac{(m_{lever} + m_{added})w}{g_{diss}} = \frac{r_{lever} + r_{fluid}\Gamma_{cyl}'(b)}{r_{fluid}\Gamma_{cyl}''(b)} \qquad (12)$$

Moreover, the resonant frequencies f_0 (or pulsation $?_0$) in the viscous fluid and in vacuum are linked by:

$$\frac{f_0^{fluid}}{f_0^{vacuum}} = \frac{w_0^{fluid}}{w_0^{vacuum}} = \sqrt{\frac{r_{lever}}{r_{lever} + r_{fluid}\Gamma_{cyl}'(b)}} \qquad (13)$$

For larger b parameters: $\Gamma_{cyl}'(b) \to 1$ and:

$$\frac{f_0^{fluid}}{f_0^{vacuum}} = \frac{w_0^{fluid}}{w_0^{vacuum}} \approx \sqrt{\frac{r_{lever}}{r_{lever} + r_{fluid}}} \qquad (14)$$

2.1.2 Rectangular cantilever

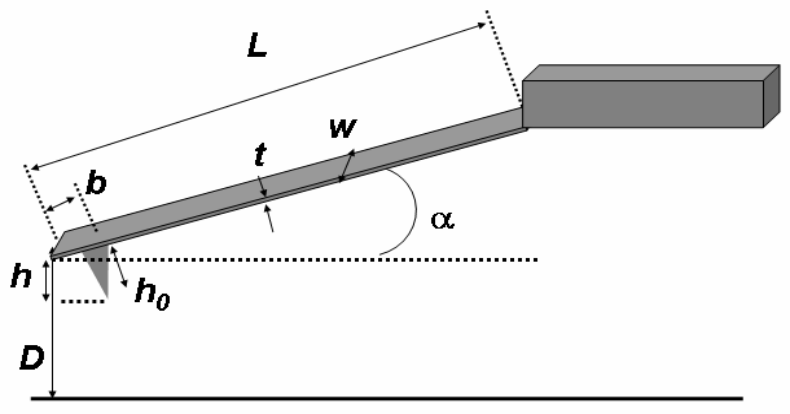

Figure 2.2: Geometrical parameters used to describe rectangular cantilevers (width *W*, length *L*, thickness *t* and tip height h_0)

In 1995, Kanwal gave an analytical expression of the hydrodynamic force acting on an oscillating rectangle[8]. However, it is very difficult to use because of the presence of Matthieu functions. In 1998, Sader suggests an easier way to get the expression of the hydrodynamic force acting on an oscillating rectangular cantilever[5]. Essentially, it consists in approximating the rectangular cantilever with a cylinder of radius $R = W/2$ if W is the width of the rectangle:

$$F_h^{rect} = jw\frac{p}{4}\rho_{fluid}W^2L\Gamma_{rect}(b)U_0\exp(-jwt) \qquad (15)$$

Where W and L are respectively the width and the length of the cantilever.

$$\Gamma_{rect}(b) = \Gamma'_{rect}(b) + j\Gamma''_{rect}(b) = \Gamma_{cyl}(b)\left[\Omega'(b) + j\Omega''(b)\right] \qquad (16)$$

$W(b)$ is a correction function to adapt the expression of G_{cyl} (valid only for a cylinder) to a rectangular geometry. Sader proposed numerical expressions for $W(b)$. G_{rect} depends on the pulsation w through its dependence on the b parameter. The latter needs to be redefined since the geometry – and thus typical dimensions – have changed:

$$b = \frac{\rho_{fluid}wW^2}{4h_{fluid}} \qquad (17)$$

Basically, we consider the oscillating rectangular cantilever to be equivalent to a cylinder with the radius of its section equal to $W/2$. Figure 2.2 defines the parameters used throughout this

chapter. Again, the real part of the force takes the added hydrodynamic mass into account whereas the imaginary part accounts for an additional dissipative term. These quantities are given by:

$$\begin{cases} m_{added} = \frac{p}{4} r_{fluid} W^2 L \Gamma'_{rect}(b) \\ g_{diss} = w \frac{p}{4} r_{fluid} W^2 L \Gamma''_{rect}(b) \end{cases} \quad (18)$$

The corresponding expression of the quality factor Q as well as the relation between the resonant frequency in the fluid and in vacuum can be given:

$$Q \approx \frac{m_{total} w}{g_{diss}} = \frac{(m_{lever} + m_{added}) w}{g_{diss}} = \frac{r_{lever} t + \frac{p}{4} r_{fluid} W \Gamma'_{rect}(b)}{\frac{p}{4} r_{fluid} W \Gamma''_{rect}(b)} \quad (19.1)$$

$$\frac{f_0^{fluid}}{f_0^{vacuum}} = \frac{w_0^{fluid}}{w_0^{vacuum}} = \sqrt{\frac{r_{lever}}{r_{lever} + \frac{p}{4} \frac{W}{t} r_{fluid} \Gamma'_{rect}(b)}} \quad (19.2)$$

W, *L* and *t* are the width, length and thickness of the rectangular cantilever, respectively.

Similarly, Rosenhead and Tuck's calculations show that for larger values of *b* (limit situation): $\Gamma'_{rect}(b) \to 1 + \sqrt{\frac{8}{b}}$. And:

$$\frac{f_0^{fluid}}{f_0^{vacuum}} = \frac{w_0^{fluid}}{w_0^{vacuum}} \approx \sqrt{\frac{1}{1 + \frac{p r_{fluid} W}{4 r_{lever} t} \left(1 + \sqrt{\frac{8}{b}}\right)}} \quad (20)$$

2.1.3 Validity of the approximations made

At first sight, it may seem unnatural that the expressions above do not directly depend on the length of the cantilever *L*. However, it should be noted that many quantities describing the cantilever's response to the acoustic piezoelectric forcing depend on that length:

- The spring constant: $k \propto \frac{Wt}{L^3}$
- The resonant frequency (or pulsation): $w \propto \frac{t}{L^2}$

It also appears that the validity of the model detailed in the previous section and the behavior of AFM cantilevers will depend on relative values of width *W*¸ length *L* and thickness *t*. Commercially available rectangular cantilevers commonly used in Tapping Mode AFM have a nominal width of 35 μm, a length of 125 μm and resonant frequencies around 180 kHz. In water, r = 997 kg.m^{-3} and h = 8.59 10^{-4} kg.m^{-1}.s^{-1} from tabulated values at 25 °C and 1 atm.

First, one needs to check if the Navier-Stokes equation can be linearized i.e., if the Reynolds number is small. For rectangular cantilevers, the typical dimension is *W/2*. The maximum velocity is $v_{\max} = wA_0$ where A_0 is the maximum oscillation amplitude and is usually between 1 and 10 nm. Consequently, the Reynolds number is around: $\mathrm{Re} \approx \frac{r_{fluid} vW}{2h_{fluid}} \approx \frac{r_{fluid} wW}{2h_{fluid}} A_0 \approx 0.23$. This number is smaller than 1 and allows the Navier-Stokes equation to be linearized. The corresponding b parameter is around: $b \approx \frac{r_{fluid} wW^2}{4h_{fluid}} \approx \frac{r_{fluid} w^3 A_0^{\,2}}{4h_{fluid}} \approx 402$. Practically, this number is large enough to validate the approximations made.

Another physical parameter of the problem can be introduced here. d is the length giving the thickness of the thin viscous layer surrounding the cantilever in which the velocity has dropped by a factor of 1/*e*. Its interpretation is similar to that of the diffuse double layer thickness in

electrochemistry or the penetration depth of electromagnetic waves in metallic materials. It is defined by[13]:

$$d = \sqrt{\frac{2h_{fluid}}{r_{fluid} w_0}} \qquad (21.1)$$

The Reynolds number and the b parameter can then be rewritten with d:

$$\begin{cases} \mathrm{Re} \approx \dfrac{\mathrm{A}_0 W}{d^2} \\ b \approx \dfrac{W^2}{2d^2} \end{cases} \qquad (21.2)$$

In particular, the approximation of large b values is entirely governed by the relative values of W and d i.e., it is totally dependent on the geometric parameters of a given cantilever (width W, length L, and thickness t). The quality factor Q and the relation between resonant frequencies in air and in water can also be rewritten with d:

$$Q^{fluid} = \frac{W}{2\sqrt{2}d}\left(1 + \frac{4 r_{lever} t}{p r_{fluid} W}\right) \qquad (22)$$

For simplicity, one wishes to neglect the correction term $\frac{4 r_{lever} t}{p r_{fluid} W}$. This is valid for some cantilevers, but if one considers usual rectangular Tapping Mode cantilevers (L = 125 µm, W = 35 µm and t = 4 µm), $\frac{4 r_{lever} t}{p r_{fluid} W} \approx 2.04$ and is not negligible. But, experiments show that the influence of this corrective term remains small. In the next section, a methodology valid for all cantilevers tested will be introduced.

2.1.4 Accuracy for the situation of dynamic AFM

As known from fundamental equations of fluid mechanics[12,13], when a body of arbitrary shape oscillates in a liquid, inertial and viscous forces acting against the motion scale with the size of the body and a characteristic length that define the thickness of a viscous skin around the

body. There is an additional mass that corresponds to the fluid dragged by the cantilever in motion. The effect of the fluid motion is often negligible in ambient air, but becomes significant when the tip is placed in a denser medium, like water. Equations (19.1) and (19.2) can be rewritten with masses instead of densities:

$$\begin{cases} Q = \dfrac{m^{*}w}{g} = \dfrac{\left(m_{lever} + m_{added}\right)w}{g} \\ \dfrac{f_{water}}{f_{air}} \cong \sqrt{\dfrac{m_{lever}}{m_{lever} + m_{water}}} \end{cases} \qquad (23)$$

Where g is the damping coefficient, in which, also, a liquid mass is involved, and w is the pulsation of the cantilever. The added mass in air has been neglected and f_{air} and f_{water} are the resonant frequencies in air and water, respectively. The cantilever mass is given by $m_{lever} = r_{lever}LWt$ with L, W, and t the geometrical parameters of the beam and r_{lever} the density of the lever material (Figure 2.2).

In AFM, the cantilever is clamped at one end and eigenmodes of high harmonic number can exhibit behavior, which might not be properly described with the assumption of a rigid transverse motion. Therefore, questions rise on the ability of equation (23) to accurately describe the added mass and the damping of the fluid on the cantilever oscillation. In particular, three-dimensional motion of the liquid can significantly modify the hydrodynamic function at high harmonic numbers and it might be of interest to use high harmonic oscillations in liquid if a higher quality factor Q is obtained. Thus, from a fundamental and practical point of view it is of interest to check the validity of those expressions as a function of the vibrating cantilever modes.

When considering cantilevers with a rectangular cross-section, one can directly use the results given in reference 4 or a correction function added to the cylinder G function. Sader gave a complete numerical expression of the corrected G function[5] that can be more readily used with good accuracy. We will use justified simplified expressions of the hydrodynamic function G for values of the parameter b ranging between 1 and 1000 instead of the limit values of the G function used in equations (14) and (20) that, for certain cantilevers tested, represent too rough an approximation to properly describe the situation. Boundary values chosen for b correspond to cantilevers and oscillation frequencies reported here. A comparison between approximated

functions from equation (24) below and the numerical expressions 20, 21a, 21b and 22 from reference 5 is shown in Figure 2.3:

$$\begin{cases} \Gamma' = a_1 + a_2 \dfrac{d}{W} \\ \Gamma'' = b_1 \dfrac{d}{W} + b_2 \left(\dfrac{d}{W} \right)^2 \end{cases} \qquad (24)$$

The parameters for an infinitely thin rectangular beam are $a_1 = 1.0553$, $a_2 = 3.7997$, $b_1 = 3.8018$, and $b_2 = 2.7364$.

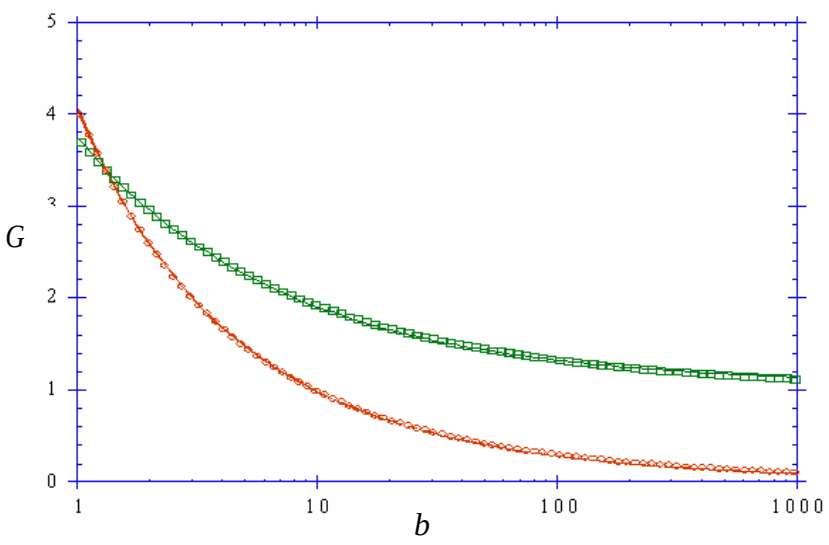

Figure 2.3: Simplification of the hydrodynamic *G* function. The real part (boxes) and the imaginary part (circles) were fitted with Equation (24) (continuous line). The approximated functions obtained are valid for values of the parameter *b* between 1 and 1000. This range of values corresponds to typical numbers for the cantilevers used and for the frequencies considered.

According to equations (18) and (24), when $d << W$ the added mass is proportional to the volume W^2L while the viscous layer of thickness d becomes significant as soon as $d \approx W/4$. In water and for frequencies around 100 kHz, d is a few microns. Therefore, for most of the available cantilevers the damping coefficient is expected to obey a linear dependence in d or, equivalently, square root dependence in pulsation w. As long as the width of the beam is not smaller than d, the linear dependence means that the volume of liquid involved in the damping process is given by the product, WdL. These rather simple predictions should be quite easy to verify experimentally.

2.2 Experimental setup

In order to have experimental situations close to those described by equation (18), we have chosen a beam long enough, i.e. $L \approx 520$ µm, to neglect boundary conditions at both ends when describing the fluid motion surrounding the beam. Figure 2.4 shows a Scanning Electron Microscopy (SEM) micrograph of the beam used in experiments reported.

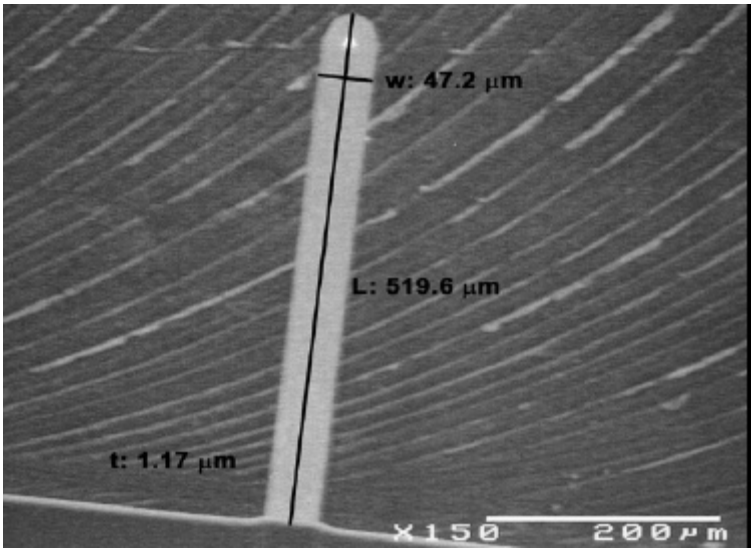

Figure 2.4: Scanning electron microscopy image of the studied cantilever with a rectangular cross-section (Nanosensors, Neuchatel, Switzerland). The measured width, thickness and length are 47.1 µm, 1.17 µm and 519.6 µm, respectively. These values were considered to be relevant for comparison with the hydrodynamic study (see text). The cantilever stiffness of the mode n = 1, deduced from the resonance frequency as a function of the dimension of the cantilever, is k = 0.023 N.m^{-1}

All experiments were carried out with a commercial AFM (NanoScope III – Extended Multimode) but no excitation was supplied to the piezoelectric element embedded in the fluid cell. The photodiode signal is recorded via a homemade electronic box and fed into a SIGNAL RECOVERY Model 7280 lock-in amplifier functioning in noise mode i.e., like a spectrum analyzer. The peaks of the spectral density signal were fitted to the amplitude response function of a simple harmonic oscillator:

$$G(w) = \sum_n \frac{G_n}{\sqrt{\left(1 - \frac{w^2}{w_n^2}\right)^2 + \frac{1}{Q_n^2}\left(\frac{w}{w_n}\right)^2}} \qquad (25)$$

Where G_n is the thermal noise coefficient of the mode n[14]. In the present work, since we are mostly interested with determination of Q_n and w_n, the coefficient G_n is set as an arbitrary fitted constant. Except for the first mode in water, the *1/f* noise correction has an influence on the Q value of about 1 % only and has no noticeable influence on the value of the measured resonance frequencies.

3. Results and discussion

3.1 Results

Several cantilevers differing by their dimensions and thus their spring constant and resonant frequencies were tested. Triangular cantilevers with low spring constants were also analyzed, but expressions deduced from equation (18) are not of great help for this geometry. Equations (18) and (24) are strictly valid only for an infinitely long beam and an infinitely thin rectangular cross section; therefore it is worthwhile to investigate a cantilever that fulfills these conditions (Figure 2.4). Observation up to the eighth resonant mode both in ambient air and in deionized (18 MΩ.cm) filtered Milli-Q^{TM} water (Millipore, Molsheim, France) were recorded (Figure 2.5).

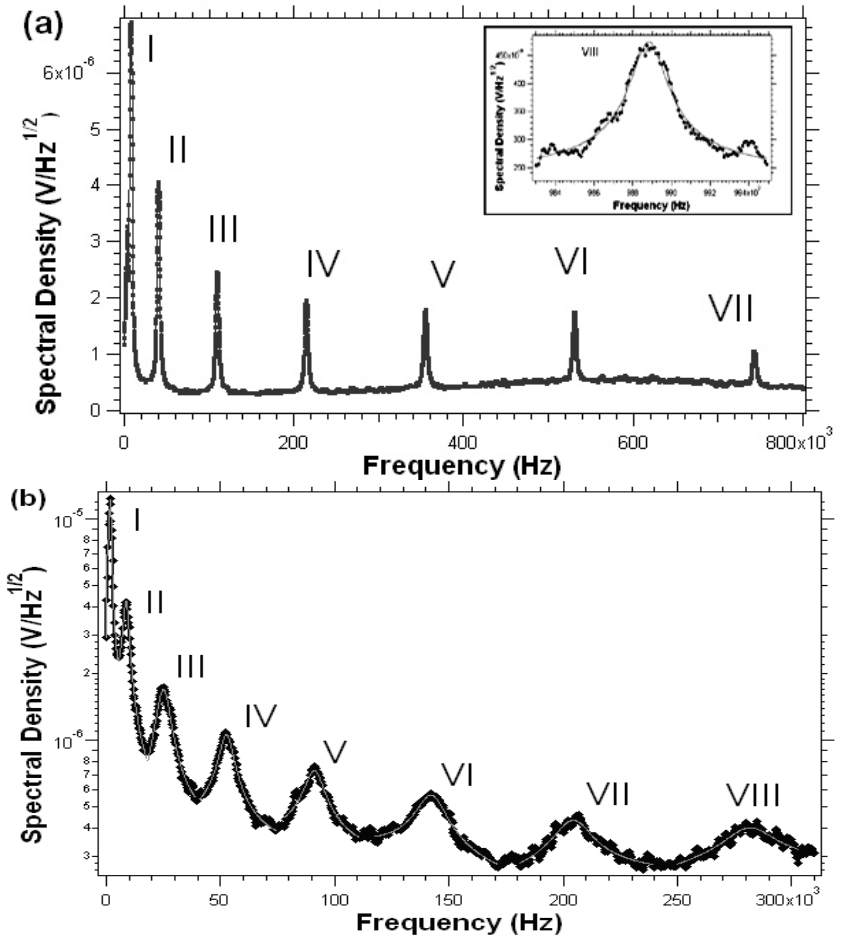

Figure 2.5: Resonant frequency distributions of a long cantilever with a rectangular cross-section in ambient air (a) as well as in pure Milli-Q conductivity water (b). In air, the frequencies (in kHz) from the first to the eighth mode inset) are 6.23 (Q=16), 38.57 (Q=53.4), 108.11 (Q=99.2), 213.05 (Q=154.3), 353.47 (Q=219.8), 529.52 (Q=307.9), 741.33 (Q=424.1) and 988.83 (Q=455.2). In water, they drop to 1.08 (Q=1.5), 8.34 (Q=3.0), 25.16 (Q=5.1), 52.87 (Q=7.5), 91.02 (Q=9.6), 141.65 (Q=11.8), 204.89 (Q=14.8) and 283.83 (Q=21.4).

The values of resonant frequencies and quality factors were extracted from fits of the spectrum density data to equation (25). The measured frequencies were identified with resonant modes of a cantilever by comparing experimental values of the ratio between the frequency of the *n*-th oscillation mode and that of the first mode to theoretical values obtained through the expressions of eigenfrequencies of a rectangular cantilever clamped at one end oscillating in vacuum[9]. The tip mass is only approximately 1% of the cantilever mass and has therefore been neglected. The eigenfrequencies are determined by the ratio of coefficients given by the boundary conditions:

$$w_n = \frac{a_n^2 t}{L^2}\sqrt{\frac{E}{12\,r_{lever}}} \qquad n = 1,2... \quad \text{and} \quad \frac{a_n}{a_1} = \sqrt{\frac{w_n}{w_1}} \qquad (26)$$

Where E is the elastic Young modulus of the lever material.

The results from Figure 2.5 are summarized in Table 1. The comparison between theoretical values of a_n and extracted experimental values from the spectrum shown in Figure 2.5 indicates a good agreement. The residual difference accounts for the effect of the air medium and the mass of the tip (not more than 1% of the total mass) whereas theoretical values are for vacuum conditions and without considering the mass of the tip[14].

Table 1: Table 1 compares theoretical a_n/a_1 values[15] in vacuum to experimental values for a long rectangular cantilever. The theoretical values are those for a beam of rectangular cross-section clamped at one end. The tip mass has been neglected since it only represents around 1% of the beam mass. The ratios can be linked to resonant frequencies for the eight modes via equation (26).

Mode *n*	***1***	***2***	***3***	***4***	***5***	***6***	***7***	***8***
Theoretical α_n/α_1 (vacuum)[15]	1	2.5034	4.1655	5.8640	7.5394	9.2149	10.8903	12.5657
Experimental α_n/α_1 (air)	1	2.4882	4.1890	5.8478	7.5323	9.2191	10.9082	12.5982
Relative error	–	0.61 %	0.56 %	0.28 %	0.09 %	0.05 %	0.17 %	0.26 %

3.2 Discussion

With equations (23) and (24), one can use the experimental quantities, quality factors and resonant frequency shifts to calculate the added mass and damping coefficient for each eigenmode:

$$\begin{cases} m_{added}^{water} = m_{lever}\left(\left(\frac{f_{air}}{f_{water}}\right)^2 - 1\right) \\ g_{air} = \frac{m_{lever} w_{air}}{Q_{air}} \quad \text{and} \quad g_{water} = \frac{\left(m_{lever} + m_{added}^{water}\right) w_{water}}{Q_{water}} \end{cases} \qquad (27)$$

Since the main discrepancy between theoretical predictions and experimental results are observed on the damping coefficient, we shall first discuss the evolution of the damping, then we will examine the results on the added mass.

When $d << W$, equations (18) and (21) predict that the damping coefficient should increase as the square root of the resonant frequency, or equivalently should exhibit a linear dependence with the harmonic number n. As displayed in Figure 2.6 and Figure 2.7, for high values of n, damping coefficients are significantly smaller than expected. In water (Figure 2.7), at a value of n as low as 3, the damping coefficient markedly deviates from the theoretical prediction.

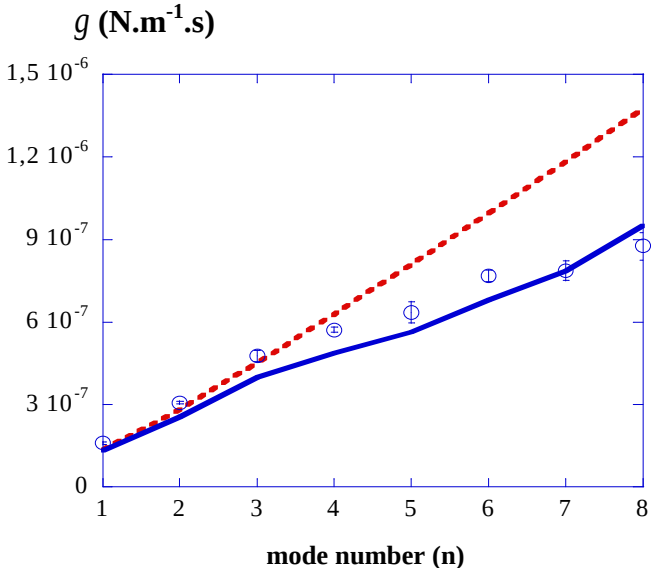

Figure 2.6: Comparison between the experimental determination of the damping coefficient in air as a function of the harmonic order (empty circle) and theoretical prediction using Equations (18) and (23) and the expression given in reference 4 (dashed line) and the numerical solution solving the 3-D Navier-Stokes equation (continuous line).

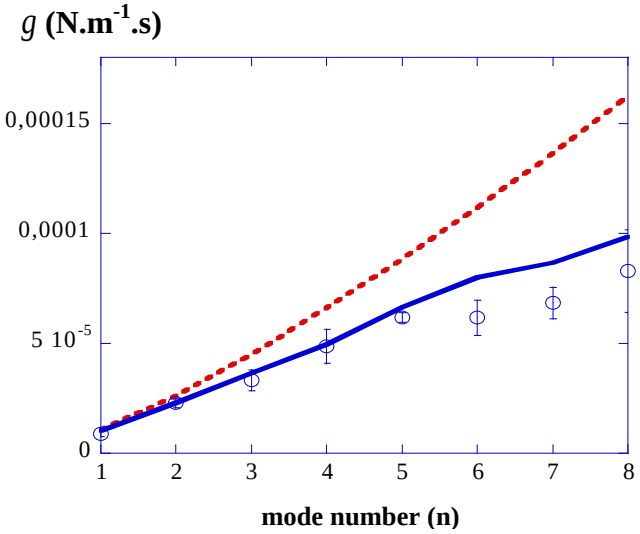

Figure 2.7: comparison between the experimental determination of the damping coefficient in water (empty circle) as a function of the harmonic order and theoretical prediction using the expression given in reference 4 (dashed line) and the numerical solution solving the 3-D Navier-Stokes equation (continuous line).

To understand the origin of the discrepancy between the experimental and theoretical values a first step is to question the basic assumptions of the model. The main assumptions are that the cantilever beam is expected to behave as an infinite long one with an infinitely thin rectangular section and that the motion corresponds to pure transverse oscillations. The cantilever beam chosen for this study, i.e. t = 1.2 µm (thickness) << width W = 47 µm (width) << L = 520 µm (length), meets the geometrical assumptions, or is, at least, close enough. Since for higher modes, the cantilever oscillation includes an additional fluid motion along the beam axis, the assumption of a 2-dimensional motion of rigid transverse oscillation might become questionable. Therefore, one must ask how a change of the velocity field along the beam axis can modify the fluid flow in such a way that the overall viscous damping becomes smaller. Unfortunately, there is no obvious analytical solution to answer this question, but an attempt to numerically solve the three-dimensional Navier-Stokes equation can help to understand the experimental results.

A simulation method (Femlab routine) has been used to take into account the velocity gradient along the beam axis as a function of the mode number *n*. The main results are displayed in Figure 2.6 and Figure 2.7. The overall trends are well reproduced for air and for water with a fairly good agreement for quantitative correspondence between calculated and experimental data.

The numerical results show that smaller values of the damping with respect to the one calculated for rigid transverse oscillations is mostly due to flow of the fluid along the beam axis. A way to qualitatively understand this result will be to consider that the variation of the beam velocity along the beam reduces the pressure field around a section compared to the one corresponding to pure 2-dimensional transverse oscillations with the same *w* value. An exact quantitative correspondence has not been achieved. At this stage, it is not easy to understand the difference, however small, between the numerical results and the experimental data since in water the numerical solutions are mostly higher than the experimental results, while in air it is the opposite.

The comparison between the experimental results of the added mass and the numerical ones calculated from the three-dimensional Navier-Stokes equation are displayed in Figure 2.8. For the added mass, the numerical results give a very good quantitative agreement with the experimental results. However, note that even the 2-dimensional model of a rigid transverse motion is able to provide a rather good tendency on the overall evolution of the added mass as a function of the harmonics order mode.

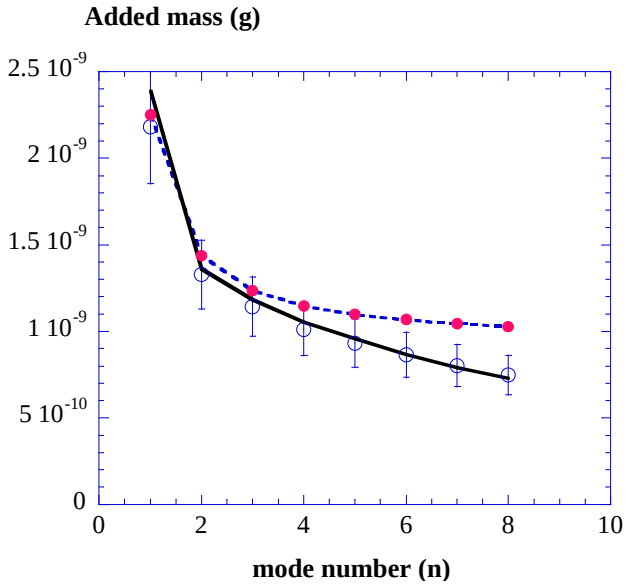

Figure 2.8: Comparison between the experimental determination of the added mass (empty circle) as a function of the harmonic order and theoretical predictions: dotted line from references 4 and 5, filled circle numerical solutions of the 2-D Navier-Stokes equation, continuous line numerical solutions of the 3-D Navier-Stokes equation.

4. Application to the study of biological materials in solution

The sections above describe the complex situation of an AFM cantilever oscillating far away from the surface in a viscous fluid like water. The aim of the thermal noise study developed was to characterize and understand the oscillation of several commercially available cantilevers with the intent to use them to make correct measurements on biological samples in liquid media. Some general elements are of particular importance.

4.1 The hydrodynamic force

The main difficulty to overcome to be able to make precise measurements on biological samples in liquid media is the hydrodynamic force. For typical commercially available cantilevers (width 35 µm, thickness 1 µm and length 125 µm for example), the hydrodynamic force can be as large as several nanonewtons. But, typical forces that characterize biological samples such as proteins are in the order of only 100 pN or less[16,17,18]. Additionally, a too large hydrodynamic force could also laterally displace samples on the surface or even damage them if they are irreversibly inelastically deformed by the tip. The hydrodynamic force needs to be decreased; otherwise it may totally screen out any specific biological force that one expects to measure. $|F_h| = g_{diss} V \approx g_{diss} w A_0 \propto w^2 W^2 L d / W$ from Equations (18) and (24), or:

$$|F_h| \propto w^{3/2} W L \propto t^{3/2} W / L^2 \qquad (28)$$

In equation (28), it is obvious that the cantilever dimensions totally control the value of the hydrodynamic force. Decreasing them could significantly reduce the hydrodynamic force. For instance, decreasing each dimension by one order of magnitude decreases the force by a factor of almost 3. One must also remember that $k \propto Wt / L^3$. When imaging soft biological samples, the spring constant of the probe must remain low. This means cantilevers lengths cannot be decreased as much as widths or thicknesses. This has already been reported in the literature[19]. Moreover, the hydrodynamic force varies linearly with the oscillation amplitude; this means that

using small amplitudes in the range of 0.1 – 1 nm will reduce the contribution of that force and improve imaging conditions provided the signal to noise ratio can be enhanced.

4.2 More difficulties near the surface

All the treatment developed earlier is valid only when the cantilever oscillates far away from the surface; that is where no additional interaction between the extremity of the cantilever and the surface has to be considered. If one wishes to image biological samples in liquid media, even more complex situations will be encountered once the cantilever approaches the surface. Figure 2.9 shows the relative dissipation obtained from fits of the quality factors from noise spectra taken at several distances from the surface for a V-shaped commercial silicon nitride cantilever (nominal spring constant k = 0.38 N.m^{-1}) oscillating at 13.6 kHz in deionized Milli-Q^{TM} conductivity water. g_0 is the dissipation coefficient far away from the surface (D > 200 µm) and g is its value for different distances D measured from the cantilever to the sample surface (freshly cleaved muscovite mica). For this reason, $D = 0$ in Figure 2.9 corresponds to a situation where the cantilever beam is still about 3 µm away from the surface since pyramidal tips at the extremity of the cantilever have a height h_0 of about 3 µm. Ideally, tipless beams should be used in such experiments. Nevertheless, one can notice the large increase in dissipation as the tips gets nearer to the surface that sets the trend when the probe approaches the sample in water.

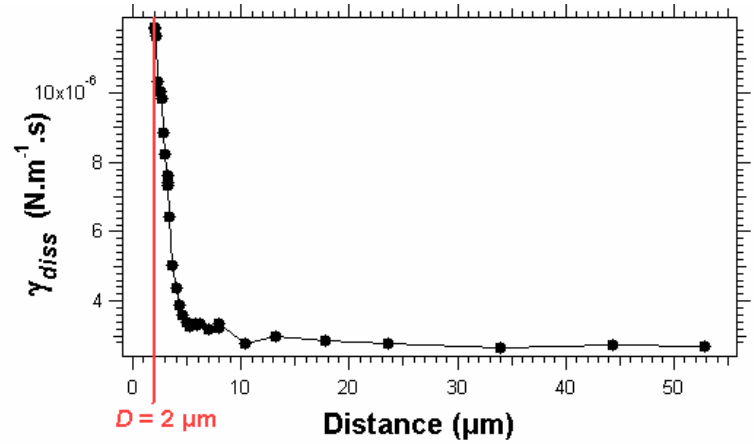

Figure 2.9: Evolution of the relative dissipation of a 100-µm long and 20-µm wide rectangular (Olympus) cantilever oscillating at 30 kHz in deionized Milli-Q conductivity water. The dissipation is obtained from fitted quality factors from noise measurements at several distances *D* from the mica surface. *D* = 0 actually corresponds to a situation where the cantilever beam is still about 2 µm away from the surface (tip height).

The dissipation significantly increases when the tip approaches the surface. This originates in confinement of fluid between the oscillating tip and the surface. Many complex situations can be encountered when water is confined between an oscillating probe and a solid surface. These include slippage of the liquid over the solid surface[20], additional shear force as liquid is expelled from the gap between the tip and the surface. Using cantilevers with high tips (> 15 μm) could drastically reduce the effects of the hydrodynamic force seen in Figure 2.9 since the oscillating beam will therefore be farther away from the surface even in situations close to contact.

4.3 Tip modification to prevent adsorption of material

Another difficulty when imaging biological samples, such as globular soluble proteins that mainly display hydrophilic surfaces[21], is adsorption on the tip during experiments. Tips are essentially made of silicon alloys that are very hydrophilic[22] due to the presence of –OH groups on the surface like isolated, vicinal or geminal silanols as well as siloxanes (Figure 2.10)[23] and are therefore prone to adsorb material coming off the surface.

To prevent such situations, a battery of chemical modifications are available to change the properties of the tip surface without increasing the size of the tip apex and, therefore, the resolution[24,25,26].

We have attempted to deposit Teflon® monolayers to render the tip hydrophobic by vacuum evaporation without much success since the coating is quickly lost as seen in the sudden shift of up to 10 % observed in the resonance frequency between experiments.

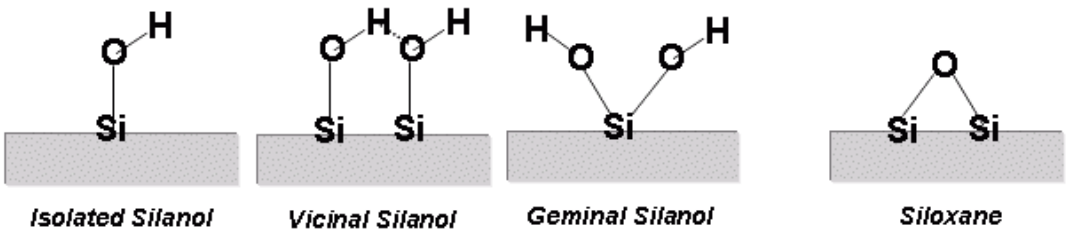

Figure 2.10: Different hydrated groups present at Si surfaces justifying its very hydrophilic nature.

5. Conclusions and future perspectives

5.1 Conclusion on hydrodynamics in liquid AFM

This experimental work was an attempt to measure the influence of the fluid motion on the oscillating behavior of an AFM cantilever. For this purpose, a thermal noise study was conducted in air and in water. Vibration modes up to the eighth were measured.

When the viscous layer has a thickness d small enough compared to the cantilever width W, or equivalently, when the pulsation w becomes large regarding to the scaling frequency u/W^2 where $u = h/r$ is the kinematic viscosity, the experimental results show a marked discrepancy on the damping values with the theoretical ones derived from previous analytical expression. The difference is explained by taking into account the three dimensional motion of the liquid.

These results can be of interest when the cantilever is brought at proximity of the surface and when relatively high frequencies are used.

5.2 Perspectives

The initial motivation to use thermal noise measurements instead of exciting the cantilever with the available commercial setup comes from the difficulty to properly excite the cantilever at its resonance since coupling of the piezoelectric element with the cell (transfer function) convolutes the observed oscillation frequency spectrum of the probe in liquid. This can be solved by rethinking the design of the cell[27].

Once a clean excitation signal is supplied to the probe, the recently available modules to electronically compensate dissipative losses (damping of the oscillator), and therefore increase the quality factor Q of the oscillation, can be used efficiently to overcome dissipation problems when oscillating in liquid media[28,29]. As commercially available cantilevers all have quality factors between 1 and 8, where the approximation of the linear harmonic oscillator is in

jeopardy, such a compensation module could be quite useful. In liquid media, it can enhance *Q* factors from typical values of 1.3 to about 800 before becoming unstable.

When such an oscillation enhancement module (Q-control III) was used directly with the commercial setup (Plexiglass cell) in a liquid environment (deionized water), no increase of the quality factor could be obtained and the system became unstable. On the contrary, with the modified acoustic excitation the same module could be successfully used to image several surfaces such as HOPG or mica in pure water. This is another consequence of the inability of the currently available commercial setup to properly excite the real mechanical resonance of the cantilever determined by the tabulated eigenfrequencies.

References

[1] Walter D.A., Cleveland J.P., Thompson N.H., Hansma P.K., Wendman M.A., Gurley G., and Elings V.B. (1996), *Rev. Sci. Intr.* , **67**, 3583-3590
[2] Schäffer T.E., and Hansma P.K. (1998), *J. Appl. Phys.*, **84(9)**, 4661-4666
[3] Viani M.B., Schäffer T.E., Chand A., Rief M., Gaub H.E., and Hansma P.K. (1999), *J. Appl. Phys.*, **86(4)**, 2258-2262
[4] Tuck E.O. (1969), *J. Eng. Math.*, **3**, 29-44
[5] Sader J.E. (1998), *J. Appl. Phys.*, **84(1)**, 64-76
[6] Kirstein S., Mertesdorf M., and Schönhoff M. (1998), *J. Appl. Phys.*, **84(4)**, 1782-1790
[7] Hosaka K., Itao K., and Kuroda S. (1995), *Sensors and Actuators*, **49**, 87-95
[8] Kanwal R.P. (1955), *Z. Angew. Math. Mech.*, **35**, 17-28
[9] Elmer F.J., and Dreier M. (1997), *J. Appl. Phys.*, **81(12)**, 7709-7714
[10] Berker R., *Encyclopedia of Physics*, VII/2, Flügge, 1963
[11] Rosenhead F., *Laminary boundary layers*, Oxford University Press, Oxford, 1963
[12] Batchelor G.K., *Fluid Dynamics*, Cambridge University Press, Cambridge, 1974
[13] Landau L.D., and Lifshitz E.M., *Course of Theoretical Physics VI : Fluid Mechanics*, Pergamon Press, London, 1960
[14] Butt H.J., and Jaschke M. (1995), *Nanotechnology*, **6**, 1-7
[15] Rabe U., Janser K., and Arnold W. (1996), *Rev. Sci. Instrum.*, **67(9)**, 3281-3293
[16] Oesterhelt F., Oesterhelt D., Pfeiffer M., Engel A., Gaub H.E., and Müller D.J. (2000), *Science*, **288(7)**, 143-146
[17] Fisher T.E., Oberhauser A.F., Carrion-Vazquez M., Marszalek P.E., and Fernandez J.M. (1999), *Trends Biochem. Sciences*, **24**, 379-384
[18] Wang T., Arakawa H., and Ikai A. (2001), *Biophys. Biochem. Res. Comm.*, **285(1)**, 9-14
[19] Viani M.B., Schäffer T.E., Paloczi G.T., Pietrasanta L.I., Smith B.L., Thomson J.B., Richter M., Rief M. Gaub H.E., Plaxco K.W., Cleland A.N., Hansma H.G., and Hansma P.K. (1999), *Rev. Sci. Instr.*, **70(11)**, 4300-4303
[20] Vinogradova O.I. (1995), *Langmuir*, **11(6)**, 2213-2220
[21] Voet D., and Voet J.G., *Biochemistry*, John Wiley & Sons, New York, 1995
[22] O'Reilly J.P., Butts C.P., l'Anson I.A., and Shaw A.M. (2005), *J. Am. Chem. Soc.*, **127**, 1632-1633
[23] Shriver-Lake L., *Silane-modifed surfaces for biomaterial immobilization*, in *Immobilized Biomolecules in Analysis: a Practical Approach*¸Cass T., and Ligler F.S., Oxford University Press, London, 1998
[24] Noy A., Vezenov D.V., and Liber C.M. (1997), *Ann. Rev. Mater. Sci.*, **27**, 381-421
[25] Zsila F., Bikadi Z., Keresztes Z., Deli J., and Simonyi M. (2001), *J. Phys. Chem. B*, **105(39)**, 9413-9421

[26] Tipple C.A., Lavrik N.V., Culha M., Headrick J., Datskos P., and Sepaniak M.J. (2002), *Anal. Chem.*, **74(13)**, 3118-3126
[27] Maali A., Hurth C., Cohen-Bouhacina T., Couturier G., and Aimé J.-P., *Appl. Phys. Lett.*, submitted
[28] Rodriguez T.R., and Garcia R. (2003), *Appl. Phys. Lett.*, **82(26)**, 4821-4823
[29] Humphris A.D.L., Tamayo J., and Miles M.J. (2000), *Langmuir*, **16(21)**, 7891-7894

Chapter 3: Atomic Force Microscopy (AFM) of Immobilized Phophoglycerate Kinase (PGK)

This chapter focuses on immobilized *Saccharomyces cerevisiae* phosphoglycerate kinase activity and structure. First, preliminary Atomic Force Microscopy (AFM) imaging results in liquid (contact mode), ambient air and primary vacuum (dynamic mode) are shown to justify the method used to link the enzyme to the solid surface.

Then, the essential question of the effect of chemical immobilization on the enzymatic activity is approached by measuring the overall heterogeneous rate constant by UV-Visible spectrophotometry. Simultaneously, a model to describe the enzymatic activity of immobilized proteins is discussed.

Finally, the results from Chapter 2 on the hydrodynamic study of oscillating AFM cantilevers are used to image immobilized phosphoglycerate kinase *in situ* by dynamic mode AFM with the proper excitation of the probe that leads to the correct approximation of the harmonic oscillator.

1. Preliminary AFM imaging of phosphoglycerate kinase (PGK) on HOPG

Highly-oriented pyrolitic graphite (HOPG) was chosen as a substrate to deposit yeast phosphoglycerate kinase (PGK) because of its very low roughness over large surface areas (R_q = 0.121 nm over 1 μm^2 or R_q = 0.221 nm over 5 μm^2). The root mean square (RMS) roughness R_q is defined by[1]:

$$R_q = \sqrt{\frac{1}{N}\sum_{i=1}^{N}\left(z_i - \left\langle z_k \right\rangle_{k=1}^{N}\right)^2} \quad (1)$$

Where $\left\langle z_k \right\rangle_{k=1}^{N}$ is the average height calculated over N points. Additionally, HOPG can be easily cleaved to renew the surface almost at will.

1.1 Static (contact) mode AFM in liquid

Initially, efforts were focused on observing phosphoglycerate kinase deposited on HOPG in 20 mM carbonate buffer at pH = 7.5 in the contact mode of Atomic Force Microscopy because of its relative straightforwardness. The tips used were commercially available Si_3N_4 probes of hollow triangular shape and a nominal spring constant k_z = 0.12 $N.m^{-1}$ (Veeco Probes LLC, Santa Barbara, CA). The apex radius is about 20 nm. The tips used were cleaned in a UV-ozone reactor – 184 nm UV lamp generating an ozone flow to the sample – 1 cm away from a UV lamp for 30 minutes prior to use. Such a tip was then placed in the holder embedded in the commercial Plexiglass® cell. The cell was cleaned by ultrasonication (40 kHz) in pure methanol for 20 minutes and then in water.

The samples were prepared by depositing a 100 µL drop of 1 mg/mL PGK solution in 20 mM carbonate buffer at pH = 7.5 on a freshly-cleaved 1 cm^2 HOPG piece (Grade 1, Structure Probe, Inc., West Chester, PA) with a micropipette. The drop was left on the surface for about 5 minutes before inserting the HOPG surface in the cell and sealing the system with a silicone o-ring.

Figure 3.1 shows the image obtained in static mode AFM. The images are flattened line by line with a 2^{nd} order polynomial to correct sample tilt and scan curvature effects. In order to minimize the lateral force exerted by the tip on the sample, the setpoint value, i.e. the deflection of the laser beam on the cantilever as measured by the four-quadrant photodetector that the system maintains constant throughout the scan, is very close to the already low value used to engage the surface.

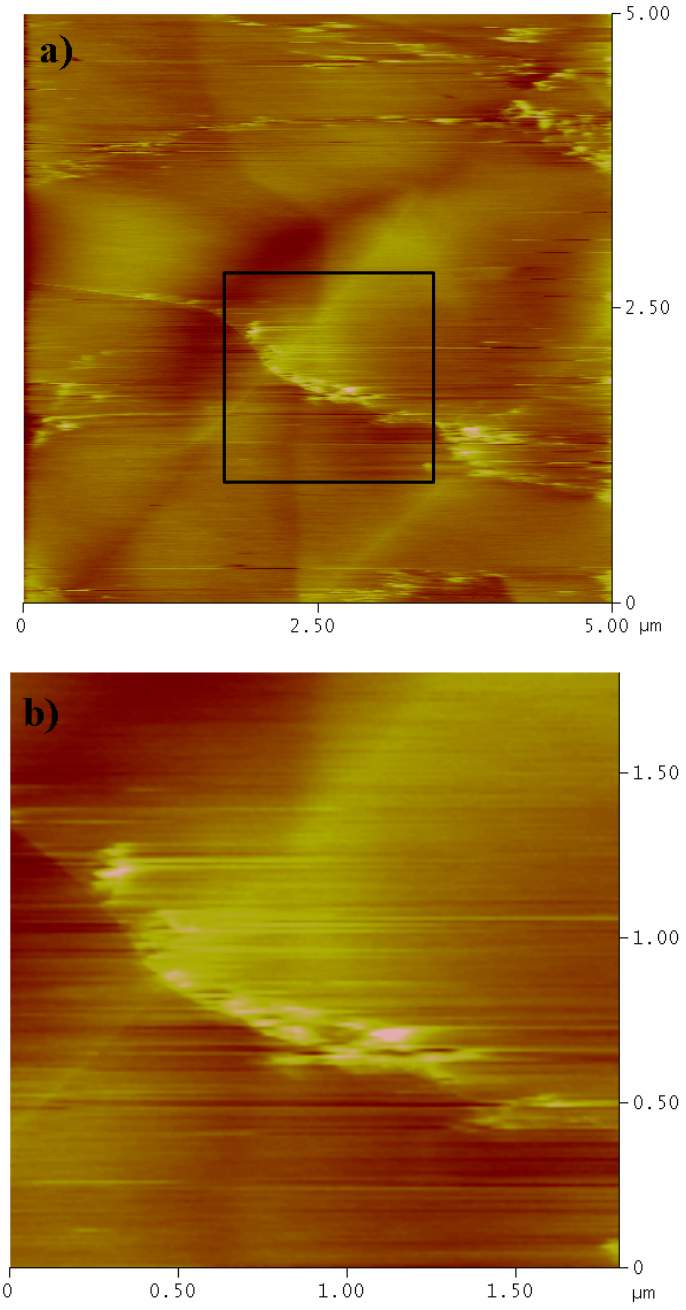

Figure 3.1: Contact mode (static mode) AFM image of PGK on HOPG in 20 mM carbonate buffer at pH = 7.5 (a) and a zoom of the region materialized by the black square (b). The scan rate is 3.0 Hz (30 µM/s) and the z-range is from 0 to 5 nm. The images are flattened by a 2nd order polynomial.

In Figure 3.1 the protein molecules deposited on the surface are essentially gathered along the edges of overlapping graphite planes where numerous dangling carbon bonds[4,5] create a very strong interaction with the deposited molecules that can resist to the lateral force exerted by the scanning tip. No PGK molecule could be seen anywhere else on the

surface. Additionally, the lateral size of the images objects is about 70 x 20 nm, i.e. much larger than the reported dimensions of 2 x 5 x 8 nm from refined X-Ray crystallographic structures[2,3]. This effect can be explained by several points:

- Tip convolution; this can be roughly estimated and de-convoluted with simple geometric arguments (Figure 3.2) since the tip is a slightly asymmetric pyramid with angles at the summit $q_{tip} = q_{tip}^{1} + q_{tip}^{2} = 45° + 35° = 80°$ (from the manufacturer):

$$W_{corrected} = W_{apparent} - H_{apparent} \times \left(\tan\left(J_{tip}^{1}\right) + \tan\left(J_{tip}^{2}\right)\right) \quad (2)$$

  According to Figure 3.1, the measured width $W_{apparent}$ is about 70 nm and the measured height $H_{apparent}$ is around 4 nm. This yields $W_{corrected}$ = 63 nm, which is still larger than the expected dimensions because additional effects can occur;

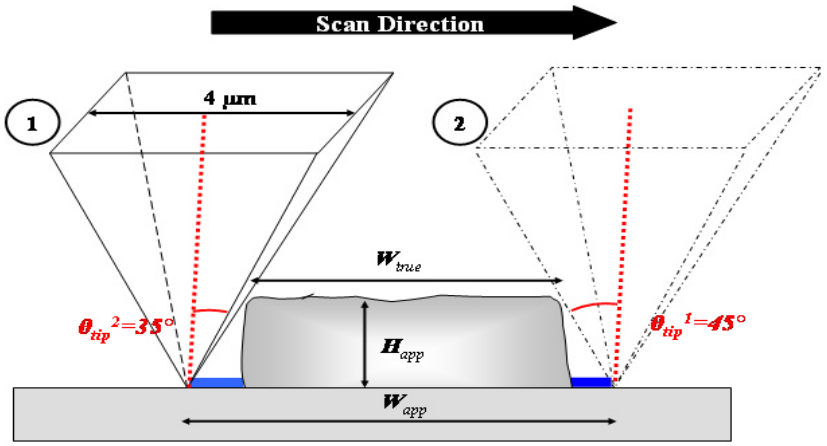

Figure 3.2: Geometric explanation of the simple tip deconvolution method leading to Equation (2). The tip is scanned from position (1) to position (2). Because of its finite dimensions, the areas of the surface marked in blue will also be interpreted as a change in the contact force. The additional distance corresponds approximately to the tangential projections of the apparent heights: $H_{app}\tan(q_{tip}^{1})$ and $H_{app}\tan(q_{tip}^{2})$.

- Deformation of the molecule upon adsorption and/or passage of the tip;
- Aggregation of several molecules induced by the surface that brings molecules much closer to each others.

Actually PGK molecules on the surface could only be observed very occasionally since the lateral force is still way too high and is believed to drag away protein molecules that are not bound by dangling carbon bonds[4,5]. For instance, if one assumes a one-

dimensional elastic force in the *z* direction with the spring constant in that direction, k_z, given by the tip manufacturer:

$$F_{tip \rightarrow sample} = k_{sample} de = k_z dz \qquad (3)$$

Where *de* is the indentation exerted on the sample of stiffness k_{sample} and *dz* is the corresponding metric value of the setpoint maintained by the system, i.e. around 7 nm. In the static mode, the force exerted by the tip to the sample is always equal to that exerted by the sample on the tip if the tip is scanned slowly enough. With $k_z \approx 0.12$ N/m, this corresponds to a force of about 1 nN. Additionally, the lateral force can be evaluated as well since, from simple geometric considerations, the lateral spring constant the $k_{x,y}$ can be obtained from k_z: $k_{x,y} \approx k_z \, L/h$ where $L \sim 100$ µm is the cantilever length and $h \sim 3$ µm is the tip height. In this case, the lateral force is around 33 nN. The forces in the static mode are much too high and perturb the studied system.

A way to minimize the tip sample force is to use the dynamic mode of AFM where the cantilever oscillates above the sample and only touches it intermittently (Tapping Mode, to simplify its description) or never touches it (Non-Contact Mode, to simplify). Because of the difficulties raised in Chapter 2, those techniques were initially performed in ambient air or in primary vacuum.

1.2 Dynamic AFM (Tapping Mode) experiments

Dynamic AFM experiments were initially carried out in two different atmospheres: ambient air (1 atm, 22 °C) and primary vacuum (10^{-3} atm). The goal was to obtain structural information on the protein as it was adsorbed on an HOPG surface.

1.2.1 In ambient air

For this series of experiments the stock protein solution (≈ 5 mg/mL) was diluted 10^6 times with 20 mM phosphate buffer at pH = 7.5. A 4 µL drop was pipetted onto the

freshly-cleaved piece of HOPG and left there for 2 minutes. Then, the entire drop was re-aspirated and the surface was rinsed four times with 5 µL of the same phosphate buffer. The surface was then dried with a stream of filtered dry argon.

The tips used were commercially available Si probes of nominal spring constant k_z = 40 $N.m^{-1}$ (Veeco Probes LLC, Santa Barbara, CA) and an apex radius of about 5-10 nm. They were cleaned in an UV-ozone reactor 1 cm away from the source for 20 minutes. They showed resonant frequencies of about 375 kHz with a quality factor Q = 400–500 far away from the surface (≥ 200 µm) for an oscillation amplitude around 10 nm. The images were obtained in the attractive regime according to approach curves recorded prior to the image acquisition. The movements of the piezoelectric element to amplitude changes (commonly named topography) and the phase of the signal were recorded simultaneously.

Figure 3.3 shows several images of HOPG samples. The images are flattened line by line with a 2^{nd} order polynomial to account for artifacts from sample tilt and scan curvature. To minimize the lateral tip-sample force, the setpoint value, i.e. the RMS of the oscillation amplitude as measured by the four-quadrant photodetector maintained constant by the system for a given excitation signal to the piezoelectric element actuating the probe, is chosen slightly below the oscillation amplitude far away from the surface at the limit of stability of the feedback loop.

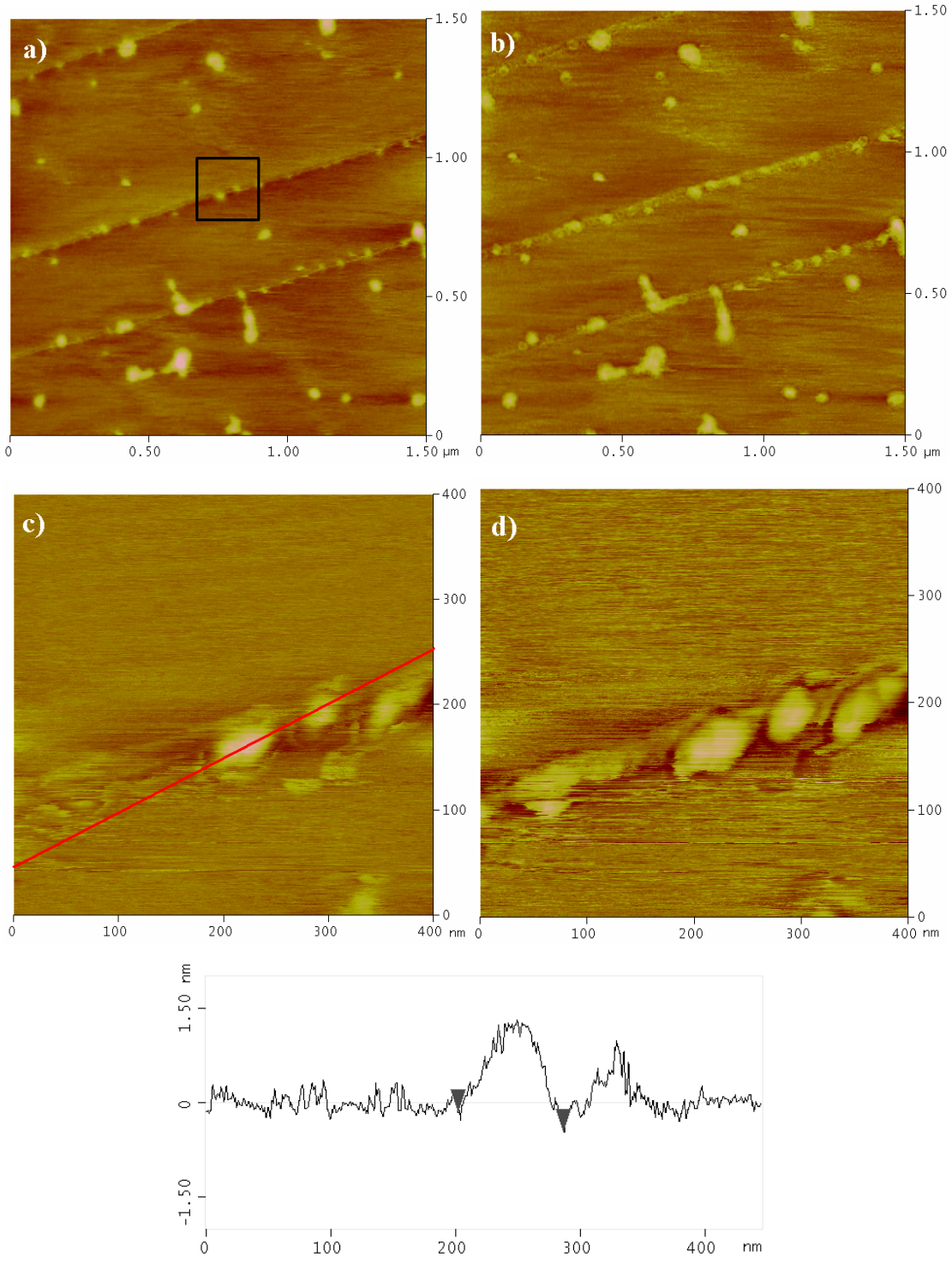

Figure 3.3: Amplitude-modulation (AM) dynamic AFM images of PGK adsorbed on HOPG at a low magnification at 1.8 µm/s: amplitude with z-scale from 0 to 5 nm (a) and phase with z-scale from 0° to 60° (b). Magnification of the squared area at 0.8 µm/s: amplitude with z-scale from 0 to 4 nm (c) and phase with z-scale from 0° to 80° (d). Section along the red line (e). The oscillation amplitude is A_0 = 6 nm

Figure 3.3 shows that, similarly to the experiments in the static mode in liquid (Figure 3.1), the molecules tend to arrange along the graphite edges where dangling carbon bonds provide stronger interaction sites. However, due to the much higher dilution, they are less dense. According to the section analysis in Figure 3.3e, most objects have a lateral size of about 60 nm for a height of about 1.5nm. There is still some tip convolution and possible deformation/aggregation that prevent to see the objects with their reported size.

During one oscillation period T the dissipated energy is equal to:

$$\left\langle E_{diss} \right\rangle_T = \frac{k_Z p A^2}{Q} \qquad (4)$$

A is the oscillation amplitude, k_z is the spring constant and Q is the quality factor of the oscillation.

The dissipated energy can be made much smaller by either decreasing the oscillation amplitude or increasing the quality factor. The latter can be achieved in primary vacuum since when the surrounding air molecules are removed the damping of the oscillation is much less and Q increases (see Chapter 2).

Operating with large quality factors ensures that amplitude changes are really related to topography and that the sample is not perturbed by the tip[6]. Therefore, PGK adsorbed on HOPG was imaged in the dynamic mode of AFM under primary vacuum (10^{-3} torr). Moreover, the strong attractive tip-sample interaction generated by adsorbed water layers will also be drastically decreased in vacuum.

1.2.2 In primary vacuum

The samples were prepared similarly to experiments in ambient air. This time, the experiments were carried out using the frequency-modulation (FM) dynamic mode (commonly named Non-Contact AFM). In this AFM mode, the excitation frequency shift is maintained constant to a certain specified value (setpoint) by a first feedback loop and

the movements of the piezoelectric element are recorded to reconstruct the topography of the sample.

Simultaneously, the system also adjusts the excitation amplitude of the cantilever (drive amplitude) as energy is dissipated in the tip-sample interaction, i.e. energy is lost in non-conservative interactions. The FM mode was chosen because it measures energy dissipation of the oscillating probe much more directly than the AM mode since data acquired in the second channel of the instrument, namely the adjustments in the cantilever excitation signal, is directly proportional to the dissipation and is termed damping.

The PGK-covered HOPG sample was placed in the chamber that was pumped down to about 10^{-3} – 10^{-4} torr. The probes used (Ultrasharp, Veeco Probes LLC) had resonant frequencies around 186 kHz and quality factors $Q_{air} \approx 400$ in air for a nominal spring constant around 40 N.m^{-1} and apex radius of about 5 nm. They were heated to 400 °C for 10 hours to clean the apex. Once a stable vacuum was reached, the quality factor was $Q_{vacuum} \approx 2000$. The images obtained are shown in Figure 3.4.

In the vacuum conditions of Figure 3.4, the tip-sample interaction is governed by Van der Waals forces. The potential in a sphere(1)-sphere(2) geometry is given by[26]:

$$V_{1-2} = -\frac{HR^*}{D}$$

And consequently: $F_{1-2} = -\nabla V_{1-2} = -\partial V_{1-2}/\partial D = -HR^*/D^2$ where R^* is an equivalent common sphere radius defined by $R^* = R_1 R_2/(R_1 + R_2)$. H is the Hamacker constant of the interface between medium 1 (polrizability: r_1) and medium 2 (polarizability: r_2). D is the distance between the two spheres, i.e. the tip-surface distance in the AFM situation.

According to the $V_{1\text{-}2}$ potential, when the tip sample distance is increased in Figure 3.4, the magnitude of the tip-sample interaction decreases. Therefore the contrast should decrease from Figure 3.4a to Figure 3.4c. In the FM-AFM experiment shown in Figure 3.4a and Figure 3.4c, the changes in conservative tip-sample forces observed in the contrast obtained from piezoelectric movements to changing frequency shifts are therefore probably linked to an indentation of the soft sample imaged by the tip that leads to a deformation of the biomolecule induced by the oscillating tip. This hypothesis is

endorsed by the damping images of Figure 3.4b and Figure 3.4d. A large-scale deformation of a single biomolecule or a small aggregate like that imaged in Figure 3.4 is indeed expected to go along with increasing dissipative processes. A careful analysis of the dissipation changes could yield response times of the PGK molecular assembly.

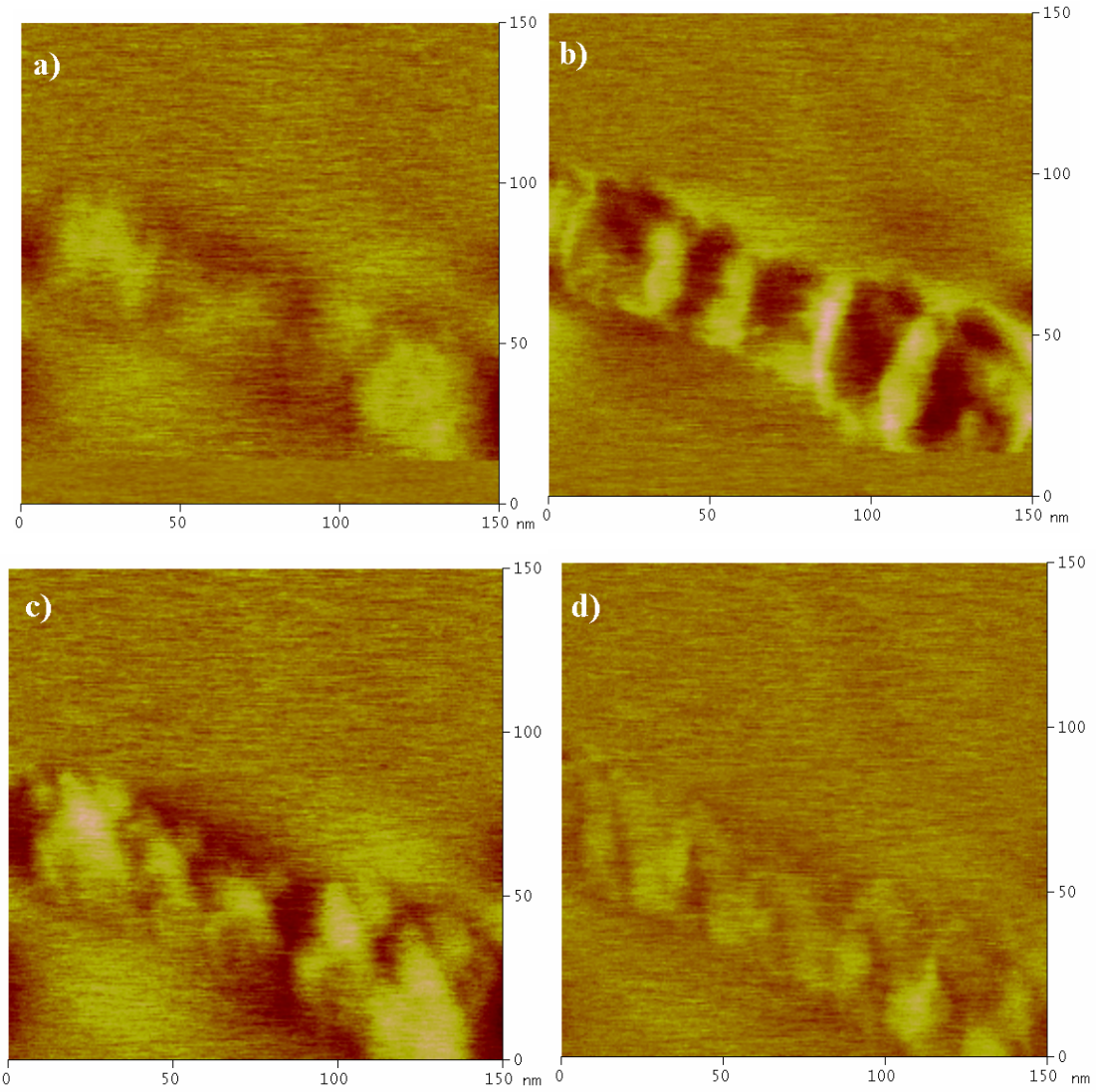

Figure 3.4: Frequency-modulation (FM) dynamic AFM images of PGK adsorbed on HOPG at 30 nm/s: height with z-scale from 0 to 2 nm (a) and damping signal with z-scale from 0 to 0.1 V (b). Same area imaged at a larger tip-surface distance at 30 nm/s: height with z-scale from 0 to 2 nm (c) and the raw damping signal g with z-scale from 0 to 0.1 V (d). The oscillation amplitude in the absence of tip-sample interaction was A_0 = 6 nm.

For the time being, another question needs to be answered. How much enzymatic activity remains upon adsorption or chemical immobilization of initially active biological material on a clean solid surface?

2. Immobilized phosphoglycerate kinase (PGK) activity

The growing interest in biosensors results in an ever increasing demand for information on physico-chemical properties of immobilized enzymes and especially information on their enzymatic activity. To our knowledge no such study exists for phosphoglycerate kinase (PGK), an enzyme involved in the glycolytic path. This work reports the first evidence that recombinant yeast PGK is still significantly active when immobilized on a surface. Two surfaces of interest in surface studies were tested; glass and muscovite mica. The stability over time, as well as stability towards external mechanical aggressions, is then presented.

2.1 Introduction

Phosphoglycerate kinase (PGK) has been extensively studied over the past decades both from structural[7,8] and kinetic[9,2,10] points of view. It is an essential enzyme in glycolysis as it catalyzes the reversible inline transfer of a phosphoryl group from 1,3-bis-phoshoglycerate (1,2-BPG) to Mg-ADP to yield 3-phosphoglycerate (3-PG) and ATP as depicted in Equation (5).

$$\text{1,3-BPG} + \text{Mg-ADP} \Leftrightarrow \text{3-PG} + \text{Mg-ATP} \quad (5)$$

Since 1,3-BPG is unstable in all usual buffers, the direct reaction is quite intricate to study. One way of circumventing this difficulty is to produce 1,3-BPG *in situ* using another enzyme. This can be achieved using glyceraldehyde-3-phosphate dehydrogenase (GAPDH) that uses 3-glyceraldehyde phosphate (GAP) to form 1,3-BPG at a fast rate[11,12,13]. When GAPDH and GAP are in large excess compared to PGK, the measured

activity is indeed that of PGK. The activity test can therefore be termed GAPDH-coupled assay[9,14]. The activity test can be summarized by the set of Equations (6):

$$\mathbf{2}\ \text{GAP} + \text{NAD}^+ + \text{P}_\text{i} \Leftrightarrow \mathbf{2}\ \text{1,3-BPG} + \text{NADH} + \text{H}^+$$
$$\text{1,3-BPG} + \text{Mg-ADP} \Leftrightarrow \text{3-PG} + \text{Mg-ATP} \qquad (6)$$

GAPDH uses nicotinamide adenine dinucleotide (NAD^+/NADH) as a cofactor. The enzymatic activity can consequently be monitored by following the absorbance of produced NADH at 340 nm (ε = 6220 $M^{-1}.cm^{-1}$). Under these conditions, the catalytic speed and the NADH absorbance are related as expressed in Equation (7):

$$v = \frac{d[3PG]}{dt} = 2.\frac{d[NADH]}{dt} = \frac{2}{e^{340}_{NADH}.l}.\frac{dAbs^{340}_{NADH}}{dt} \qquad (7)$$

The factor 2 originates from the 2:1 stoechiometry in Equation (6.1) since NAD^+/NADH is a two-electron couple whereas 1,3-BPG/GAP is a one-electron system.

In this work, we compare direct PGK activities – formation of 3-PG – in bulk and when immobilized on two surfaces routinely used for biosensors i.e., glass and mica. The activities are characterized by the rate of 3-PG formation, as well as by the apparent binding constant of Mg-ADP in the sense of the Michaelis-Menten model[15].

2.2 Materials and methods

2.2.1 Recombinant PGK and other materials

All mentioned chemicals and especially ADP and NAD^+ were purchased from Sigma-Aldrich and used without further purification. GAP was prepared by immersing the beaker containing DL-glyceraldehyde-3-phosphate diethyl acetal barium salt (Sigma-Aldrich) fixed on Dowex® 50x ion-exchange resin (Sigma-Aldrich) in hot water and discarding any precipitated material. Recombinant yeast PGK was obtained and purified according to the procedure described earlier[16]. GAPDH was bought as a suspension in

ammonium sulfate from Roche Applied Science (Meylan, France) and re-dissolved in 1,4-piperazinediethanesulfonic acid (PIPES) buffer after short centrifugation at 4 °C. All aqueous solutions were prepared with 18 MΩ.cm filtered deionized Milli-Q^{TM} water (Millipore, Molsheim, France). All other organic solvents were A.C.S. grade and used without further treatment.

2.2.2 Surfaces preparation

A systematic procedure to chemically immobilize PGK on glass, mica and gold was developed and optimized to give an optimum absorbance signal. On glass, it can be divided into three essential steps. A 1 cm x 3 cm 1-mm-thick microscope glass slide (Fisher Scientific, Pittsburgh, PA, USA) was immersed in freshly prepared Piranha solution (70% H_2SO_4/30% H_2O_2) for 1 minute to remove any organic pollutant from the surface, rinsed with Milli-Q^{TM} water and dried in an oven (150 °C). It was subsequently immersed in 2% (v/v) 3-aminopropyltriethoxysilane (APTES, Aldrich) in pure acetone for 12 hours at room temperature in a desiccator for an efficient silanization. The slide was thoroughly rinsed and ultrasonicated in methanol for 30 seconds to remove physically adsorbed silane molecules before immersion in 4 % (v/v) electron-microscopy-grade glutaraldehyde (Polysciences, Inc., Warrington, PA, USA) in 20 mM phosphate buffer pH = 8.0 for 2 hours at room temperature. The slide was rinsed with 20 mM phosphate buffer pH = 8.0 and finally immersed into a recombinant yeast PGK solution in 20 mM phosphate buffer pH = 7.0 (approximately 0.4 mg/mL) for several hours at 4 °C. Prior to any activity measurement, the slide was thoroughly rinsed with large volumes of 20 mM phosphate buffer pH = 7.0 fractioned in 1 mL sprays per face and per slide, as well as immersed in fresh 20 mM phosphate buffer pH = 7.0 for several hours at 4 °C.

Mica slides **(**Grade V-4 green muscovite mica from Structure Probe, Inc., West Chester, PA, USA) were treated similarly with the exception that cleaving mica with scotch-tape is a more efficient method to obtain clean surfaces before silanization. Then the mica slides were subsequently immersed in the 3-aminopropyltriethoxysilane

(APTES, Aldrich) and in the glutaraldehyde solution. They were thoroughly rinsed with large amounts of phosphate buffer before each measurement.

2.2.3 Enzymatic activity assay

All PGK activity measurements were performed in a commercial computer-controlled UNICAM model UV4 UV/Visible spectrophotometer (Unicam, Cambridge, UK) at room temperature (22 °C) in disposable 3-mL plastic cuvettes that did not absorb any light in the domain of interest.

The reaction mixture containing 1 mM Mg-ADP, 20 mM $MgCl_2$, 500 µM NAD^+ and 500 µM GAP in PIPES buffer pH = 7.5 was first left in the cuvette for 5 minutes to equilibrate in temperature. Typically 3 to 5 minutes after addition of GAPDH, the absorbance reaches equilibrium. For activity measurements in bulk conditions, recombinant yeast PGK was then added at a final concentration of approximately 1 nM and the absorbance signal at 340 nm was recorded for typically 3 to 5 minutes. The initial slope of the obtained line gives the PGK catalytic activity.

When measuring PGK activity from the treated surfaces, the slides were placed against each side of the cuvette in the beam path to avoid problems caused by diffusion processes at the surface or too low signal. The resulting absorbance signal was always below the saturation level of the instrument and within its linear response regime. Systematically, to determine if the observed activity was related to enzyme molecules immobilized on the surfaces rather than adsorbed material, the same measurement was repeated immediately after removing the slides, to check for enzymatic activity of any adsorbed molecules that had re-dissolved into the reaction mixture. Moreover, a systematic drift of the GAPDH saturation plateau signal of about 3 $nmole_{3\text{-}PG}.L^{-1}.s^{-1}$ is observed. This can be explained by the known instability of 1,3-BPG in aqueous solutions; hydrolysis of the newly formed substrate prevents the reaction from reaching its thermodynamic equilibrium completely. This value was subtracted from any measured slope related to PGK activity when slides were added to the mixture.

2.3 Results

2.3.1 Enzymatic activity in bulk condition

Before measuring PGK activity of chemically immobilized molecules, the activity of the stock solution was measured according to the procedure given earlier. This served as a reference for any subsequent measurement using immobilized enzymes. In the Michaelis-Menten kinetics, this rate can be related to the catalytic constant k_{cat} when the initial concentration of enzyme is known (1 nM). The experiment was carried out under conditions where 1,3-BPG is in large excess so that the enzyme was saturated with its second substrate. More specifically, since 1,3-BPG is generated *in situ* by another coupling enzyme, the 1,3-BPG excess condition is met when the coupling enzyme, namely GAPDH, is in large excess since the turnover rate of PGK and GAPDH are similar[11].

Non-linear or linear (Lineweaver-Burk) fits of the data yield an association constant of the Mg-ADP complex to the phosphoglycerate kinase enzyme molecules $K_{m,b}^{Mg\text{-}ADP}$ = 176 ± 17 μM and a maximum catalytic reaction rate V_{max} = 963.1 ± 3.4 $nmole_{3\text{-}PG}.L^{-1}.s^{-1}$, i.e. a catalytic constant k_{cat} = 963.1 s^{-1} since $[PGK]_0$ ~ 1 nM (with M_{PGK} ~ 45 kDa). The results are shown in Figure 3.5. The value of $K_{m,b}^{Mg\text{-}ADP}$ obtained is very close to that reported in the literature[17], whereas k_{cat} is about 20% lower than the value usually reported[18]. The observed difference can be explained by aging of the stock protein solution from conservation at -20 °C. This difference will not be of much importance in the subsequent measurements with the immobilized enzyme since another stock protein solution from the same protein preparation batch will be used to prepare the PGK-covered glass or mica surfaces.

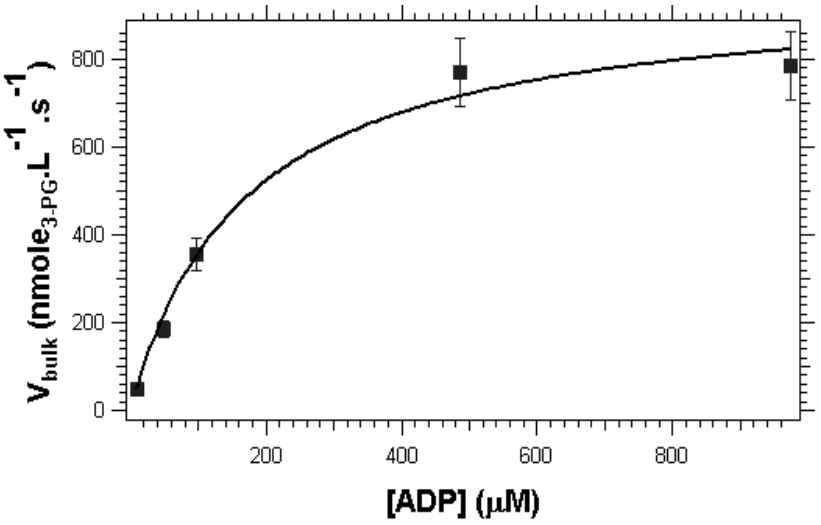

Figure 3.5: Determination of the apparent binding constant of Mg-ADP in bulk conditions, $K_{m,b}^{Mg\text{-}ADP}$, according to the Michaelis-Menten model[27]. The concentrations are corrected for dilution effects when additional volumes of ADP are added as the experiment advances. The solid line represents the fit to the Michaelis-Menten expression of the reaction rate.

2.3.2 Enzymatic activity of immobilized phosphoglycerate kinase

The best results were obtained on glass. Upon addition of the two treated glass slides in the beam path, the absorbance signal increased with a slope much larger than the GAPDH saturation plateau drift suggesting some PGK activity from the surface. The slope remained the same after several rinses with large amounts of 20 mM phosphate buffer pH = 7.0 or pure Milli-Q^{TM} water. The same results could be obtained reproducibly on five different surface preparations. Additionally, whenever the slides were removed from the beam path, the slope of the absorbance signal vs. time immediately dropped back down to that of the steady-state GAPDH signal drift. Moreover, no PGK activity could be measured from the rinsing solutions. This clearly indicates that no enzyme molecule previously bound to the surface was freed in the solution provided the expected signal was above the sensitivity of the detectors. In the case of immobilization on glass, the maximum rate of formation of 3-PG, i.e. twice the slope of the absorbance difference vs. time according to Equation (7), is V_{max} = 58 nmole$_{3\text{-}PG}$.L^{-1}.s^{-1} for 1 mM Mg-ADP (Figure 3.6).

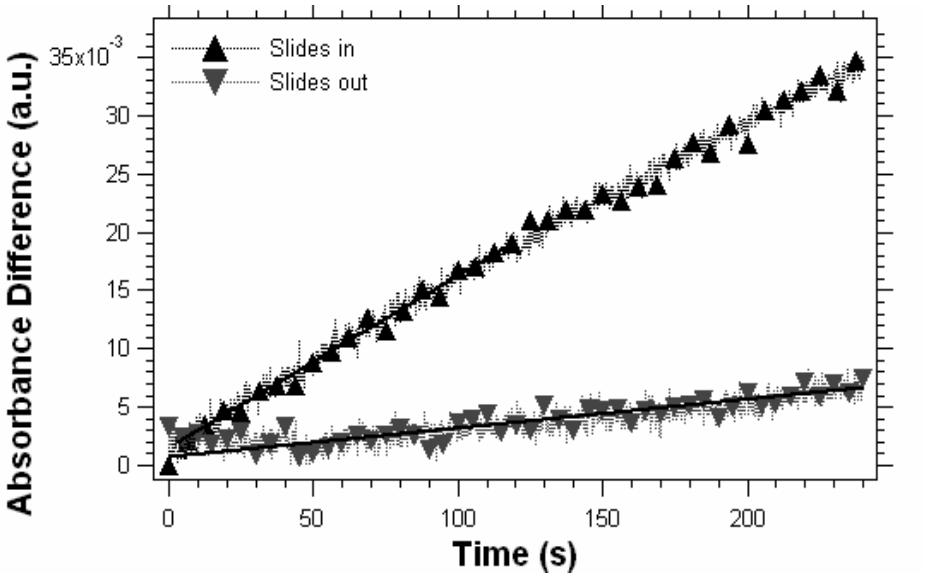

Figure 3.6: Absorbance at 340 nm when two slides are placed against the cuvette faces in the beam path (-▲-) and when they are subsequently removed (-? -). Only the first 100 seconds are taken into account to determine the slope since, after a while, the substrates become rate-limiting. The slope of the lower line is equal to the GAPDH saturation plateau drift due to 1,3-PG instability.

The apparent binding constant of Mg-ADP was also determined for glass-bound PGK within the Michaelis-Menten model. Although the model is not necessarily valid for surface reactions due to possible substrate diffusion limitation effects close to the surface, enzyme orientation upon immobilization or even accessibility of the enzyme molecules to substrates, the data fit suggests it can still be applied to immobilized enzymes in first approximation. The use of the Michaelis-Menten model in the study reported here will be justified in a following section.

From non-linear fits of the data or linear Lineweaver-Burk fits, the apparent binding constant of Mg-ADP was determined as $K_{m,s}^{Mg\text{-}ADP} = 100.3 \pm 3.1$ μM, i.e. slightly lower than the value in bulk conditions, and the maximum catalytic rate was evaluated to $V_{max} = 128.3 \pm 2.6$ $nmole_{3\text{-}PG}.L^{-1}.s^{-1}$ which is almost 8 times smaller the value determined in section 2.3.1 for the free enzyme in similar conditions of Mg-ADP and GAPDH concentrations. Figure 3.7 shows the data obtained from PGK immobilized on glass slides and the non-linear fit curve based on a Michaelis-Menten model that will be justified later on.

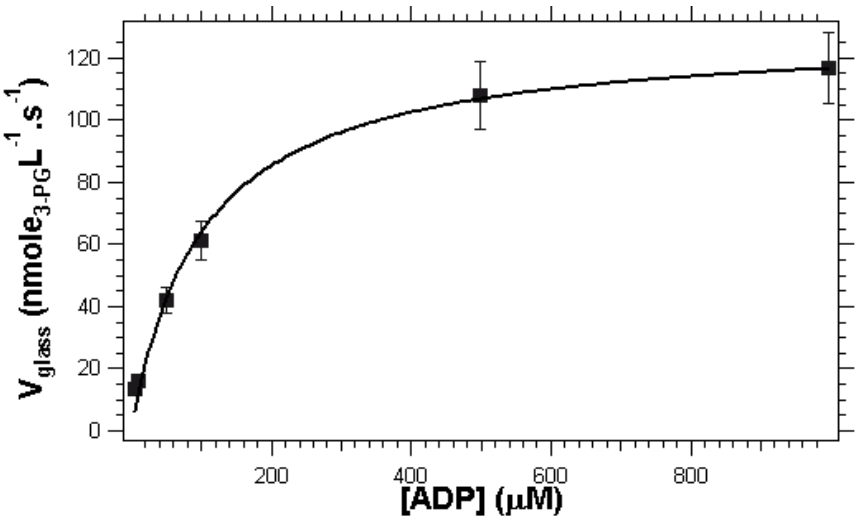

Figure 3.7: Determination of the apparent binding constant of Mg-ADP for PGK immobilized on glass, $K_{m,s}^{Mg\text{-}ADP}$, according to the Michaelis-Menten model[27]. The values of the reaction rate were corrected with the optical path modification occurring when two 1-mm thick glass slides are inserted into the measuring cell. The concentrations are corrected for dilution effects when additional volumes of ADP are added as the experiment advances. The solid line represents the fit to the Michaelis expression of the reaction rate.

Since they were particularly thin, the mica slides could also be placed directly in the beam path. PGK activity from mica slides was then monitored in a similar way. The maximum catalytic rate of 3-PG formation was lower than for glass slides but still superior to the GAPDH saturation plateau drift level indicating that enzyme molecules were still active on the mica surface as well. Typically, the maximum catalytic rate was determined to be V_{max} = 35 $nmole_{3\text{-}PG}.L^{-1}.s^{-1}$ when the mica slides were silanized with APTES. Additionally, V_{max} = 21 $nmole_{3\text{-}PG}.L^{-1}.s^{-1}$ when similar slides were silanized with mercaptopropyltriethoxysilane (MPTS). However, in some cases, the detected activity was still present when the slides were removed from the solution, even after additional rinses with large volumes of 20 mM phosphate buffer pH = 7.0 and Milli-Q^{TM} water and multiple immersions in 20 mM phosphate buffer pH = 7.0 for several hours. Since many proteins tend to easily adsorb onto mica[19,20] or even APTES-treated mica[21,22], it is not possible to strictly discriminate between re-dissolution of adsorbed molecules and instability of the enzyme immobilization strategy to mica. Additionally, unlike glass, the silanization of mica slides is expected to occur more via electrostatic interaction between the silane moieties and the charged mica lattice than via Si-O-Si covalent bonds.

2.3.3 Stability of PGK-covered glass surfaces

The stability over time of freshly prepared glass slides was also investigated. For that purpose, the rate of 3-PG formation was measured, with the procedure described earlier, at three different times after the preparation; immediately after, after 20 minutes in ambient air and after 12 hours in 20 mM phosphate buffer pH = 7.0 at 4 °C. The results suggest that keeping the slides immersed in phosphate buffer at 4 °C is a far better means of storage than leaving them in ambient air (Table 1).

Table 1: Evolution of the rate of 3-PG formation of freshly prepared glass slides, after 20 minutes in ambient air and after 12 hours at 4 °C to probe their stability over time.

Experiment	First use	20 min in air (22 °C)	12 h in buffer (4 °C)
Without the slides	GAPDH drift level	GAPDH drift level	GAPDH drift level
3-PG formation [$nmole_{3\text{-}PG}.L^{-1}.s^{-1}$]	116.2	86.4	80.4
Slides removed	GAPDH drift level	GAPDH drift level	GAPDH drift level

Additionally, the resistance of a newly prepared surface to outer mechanical constraints was also investigated. Immersing the glass slides in 20 mM phosphate buffer pH = 7.0 and ultrasonication at 40 kHz for 8 minutes (Bransonics, Model B1510) was chosen to model external constraints that might be applied on the slides during storage, since long expositions of organic layers on surfaces are believed to irreversibly damage the layers. Almost all PGK activity was lost after ultrasonication (Figure 3.8). Besides, PGK activity could be measured from the ultrasonication solution bath once the slides had been removed. This suggests that the enzyme molecules, together with the silane agent and the cross-linker molecules that bind them to the solid surface were re-dissolved into the buffer upon the action of the ultrasonic waves of high energy or de-activated by denaturation. Therefore the glass slides prepared were believed to have only a limited resistance to mechanical constraints.

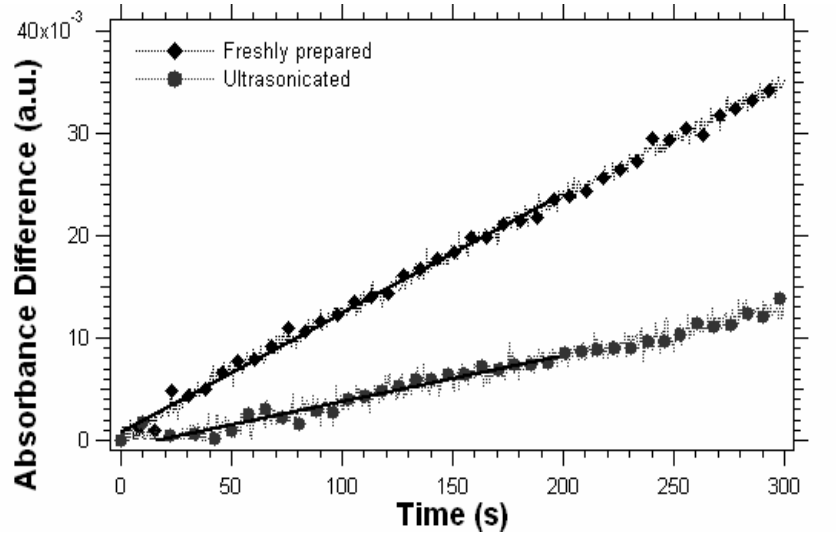

Figure 3.8: Effect of ultrasonication (8 min, 40kHz) on glass slides and PGK activity. The slope falls from 1.17 10^{-4} Abs.s^{-1} for newly prepared slides (-¨-) to 4.48 10^{-5} Abs.s^{-1} for the same slides after ultrasonication (-··-).

2.4 Discussion: validity of the model used

From the measurements above, one can conclude that PGK retains some activity when immobilized on solid supports like glass and mica. The best immobilization yield seems to be obtained on glass. Additionally, storing slides in 20 mM phosphate buffer at neutral pH at 4 °C in an environment exerting low mechanical constraints on the surfaces for no longer than 1 week is recommended to preserve most of the activity.

From a more theoretical point of view, the use of the Michaelis-Menten kinetic model to describe activity measurements for immobilized enzymes has to be justified.

2.4.1 Diffusion equation for a charged substrate in an electrolyte

In the case of yeast PGK activity monitored by UV-Visible spectrophotometry, the substrates, 1,3-biphosphoglycerate as well as Mg-ADP, diffuse from the solution bulk to a charged surface (silanized glass or mica) and possess an overall negative charge. In this case, the substrates can be described by their electrochemical potentials:

$$\begin{cases} \overline{m}_{BPG} = m_{BPG} + z_{BPG} F\Psi = m^0_{BPG} + RT\ln(C_{BPG}) + z_{BPG} F\Psi \\ \overline{m}_{ADP} = m_{ADP} + z_{ADP} F\Psi = m^0_{ADP} + RT\ln(C_{ADP}) + z_{ADP} F\Psi \end{cases} \quad (8)$$

Where *?* is the surface potential, F is the Faraday constant, C_i is the bulk concentration of the species I and z_i is the overall charge of species i.

Additionally, such a charged substrate diffuses to the surface covered with active enzyme molecules under the electrochemical potential gradient under the generalized diffusion law (Nernst-Planck equation)[23,24]:

$$\overrightarrow{J_i} = -\frac{D_i}{RT} C_i \vec{\nabla} \overline{\mu_i} = -\left(D_i \vec{\nabla} C_i + \frac{F}{RT} D_i z_i C_i \vec{\nabla}\Psi \right) \quad (9)$$

D_i is the diffusion coefficient of the species i.

If one considers a substrate s (respectively product p) with a charge z and a diffusion coefficient D_s (respectively D_P) at a concentration $C_s^{¥}$ (respectively $C_P^{¥}$) in the solution far away from the surface and C_s^0 (respectively C_P^0) at the surface (x=0), then:

$$\overrightarrow{J_s} = -\left(D_s \vec{\nabla} C_s + \frac{F}{RT} D_s z C_s \vec{\nabla}\Psi \right) \quad (10)$$

In the case of a one-dimensional flux along the normal to the surface x and with the steady-state approximation:

$$J_S = -M \frac{D_S}{d} \left(C_S(x) - C_s^0 \exp\left(\frac{zF\Psi(0)}{RT} \right) \right) \quad (11)$$

Where d is the Nernst diffusion layer thickness, i.e. the thickness of the stagnant layer at the surface, and is set by the force of the solution stirring. It is of particular importance in Rotating Disk Electrode (RDE) experiments[25] or in any complex hydrodynamic problems such as those treated in Chapter 2. It is assumed from now on that d remains constant throughout the experiment. One can also define the mass-transfer coefficient m that characterizes diffusive processes:

$$m = \frac{D_S}{d} \quad (12)$$

The dimensionless number *M* is called the electrostatic modifier and is defined by[23,24]:

$$M^{-1} = \frac{1}{d}\int_0^d \exp\left(\frac{zF\Psi(x)}{RT}\right)dx \quad (13)$$

With the Gouy-Chapman-Stern model, one can describe the distribution of a charged species in the electrostatic potential $y(x)$. Further details on the model are given in Chapter 5. To simplify the expression, small potentials and a symmetric electrolyte will be considered. This approximation is deemed quite valid in the case of mica from the work of Israelachvili et al. using Surface Force Apparatus (SFA)[26]. They report values of $y_0 = y(0) \tilde{} \ 100\ mV$ in pure conductivity water. In this case:

$$\Psi(x) \approx \Psi_0 \exp(-kx) \quad (14)$$

$y_0 = y(0)$ is actually the potential at the inner Helmholtz plane of closest approach (Stern). If the bulk concentration C_S^0 is expressed in mole/L, k is the reciprocal diffuse layer thickness (or reciprocal Debye length) and is defined by:

$$k = \left(\frac{2000 C_S^{\ 0} z^2 e^2}{e e_0 k_B T}\right)^{1/2} \quad (15)$$

And consequently:

$$M^{-1} = 1 + \frac{2(\exp(a/2)-1)}{kd} \quad (16)$$

The dimensionless parameter a is defined by: $a = \frac{zF\Psi_0}{RT}$.

2.4.2 Michaelis-Menten kinetic model

In the steady-state regime where the concentration of the enzyme-substrate complex is constant and if the concentration of the substrate is larger than that of the enzyme, many enzymatic reactions in solution can be described by the Michaelis-Menten kinetic model[27].

$$S + E \underset{k_{-1}}{\overset{k_1}{\rightleftharpoons}} ES \xrightarrow{k_2} E + P \quad (17)$$

$v = \frac{V_{\max}[S]}{K_M + [S]}$ with $V_{\max} = k_2[E]_{total}$ and $K_M = \frac{k_{-1} + k_2}{k_1}$ is the catalytic rate, i.e. the rate of apparition of the product *P* or of consumption of the substrate *S*.

The same model will be applied to the situation of immobilized enzymes by considering the surface concentrations of the enzyme G_E and of the enzyme-substrate complex G_{ES}. Therefore, the kinetic constants k_1, k_{-1} and k_2 have to be rewritten. Typically, if one roughly assumes a uniform and homogenous enzyme layer of thickness *l*, then: $k_i^S \approx \frac{k_i}{l}$ for *i* equal to *1*, *-1* or *2*.

One can write the following set of equations with notations introduced in section 2.4.1:

$$\begin{cases} \frac{d\Gamma_{ES}}{dt} = k_1^S \Gamma_E C_S^0 - \left(k_{-1}^S + k_2^S\right)\Gamma_{ES} \\ -v = \frac{dC_S^0}{dt} = k_{-1}^S \Gamma_{ES} - k_1^S \Gamma_E C_S^0 - J_S(x=0) \\ v = \frac{dC_P^0}{dt} = k_2^S \Gamma_{ES} + J_P(x=0) \end{cases} \qquad (18)$$

Due to the steady-state hypothesis, the flows of substrate *S* and product *P* do not change with time and are both equal to the catalytic rate *v* and the Michaelis-Menten equation can be adapted.

Finally, by combining Equations (16), (17) and (18) and rearranging the result, one gets:

$$\frac{m}{1 + \frac{2(\exp(a/2) - 1)}{kd}}\left(C_S^\infty - C_S^0 \exp(a)\right) = v = \frac{V_{\max} C_S^0}{K_M + C_S^0} \qquad (19)$$

In fact, because the substrate concentration, C_s^0, at the surface may be very different from the bulk value, $C_s^{¥}$, the reaction rate *v* measured by the method used here, namely UV-visible spectrophotometry can be linked to the bulk values of the substrate

concentration through a Michaelis-Menten law. An efficiency parameter x can be defined[23]:

$$v = x\frac{V_{\max}C_s^{\infty}}{K_M + C_s^{\infty}} = \frac{V_{\max}^{app}C_s^{\infty}}{K_M^{app} + C_s^{\infty}} \quad (20)$$

The efficiency parameter can be calculated as[23]:

$$x = 2\frac{(1+b)}{\left(b + f + \exp(a) + \sqrt{(b + f + \exp(a))^2 - 4bf}\right)} \quad (21)$$

With $b = C_S^{\infty}/K_M$ and $f = V_{\max}/MmK_M$.

Several limit cases can now be considered:

- The surface potential y_0 and the charge of the substrate z have the **same** sign, i.e. there is an electrostatic repulsion of the substrate molecules by the charged surface. Then, $a > 0$ and $\exp(a) > 1$. For surface potential values of -150 mV, i.e. the typical value for mica in pure conductivity water[26], and a substrate like 1,3-biphsophoglycerate at pH = 7.5 for which $z = -2$, $\exp(a) \tilde{} \ 1.4\ 10^5 >> 1$. Equation (21) becomes:

  $$x \approx (1+b)\exp(-a) << 1 \qquad (22.1)$$

  Due to the repulsion of the substrates by the charges on the surface, the reaction is slowed down considerably compared to an equivalent solution of free enzyme.

- The surface potential $?_0$ and the charge of the substrate z have **opposite** signs, i.e. there is an electrostatic attraction of the substrate molecules by the charged surface. Then, $a < 0$ and $\exp(a) < 1$. For surface potential values of +150 mV and a substrate for which $z = -2$, $\exp(a) \tilde{} \ 8.4\ 10^{-6} << 1$ and Equation (21) becomes:

  $$x \approx \frac{2(1+b)}{\left(b + f + \sqrt{(b-f)^2}\right)} \qquad (22.2)$$

  From here, two other limit subcases can occur:

  - $b > f$: Equation (22.2) becomes:

$$x = \frac{(1+b)}{b} \text{ and } v = V_{\max}^{app} = V_{\max} \qquad (22.2.1)$$

One can also use a first-order Taylor development in the expression of K_{Mx}^{app} from reference 23 to obtain:

$$K_M^{app} = K_M \frac{b^2}{(b-f)^2} \exp(a) \quad (22.2.2)$$

In this case, the kinetics are governed by the catalyzed reaction. The situation is reminiscent of Michaelis-Menten bulk kinetics when the enzyme is saturated in substrate *S*, i.e. $C_S^{\infty} >> K_M$. Additionally though, in cases of low resistance to the substrate diffusion, $F \approx 0$ and the observed Michaelis constant K_M^{app} is lower than the corresponding bulk value K_M.

- $b < f$: Equation (22.2) becomes:

$$x = \frac{(1+b)}{f} \text{ and } v = V_{\max} \frac{b}{f} = mMC_S^{\infty} < V_{\max} \quad (22.2.3)$$

Similarly, a first-order Taylor development of K_M^{app} in reference 23 yields:

$$K_M^{app} = K_M \left[b + (f-b)^2 \exp(-a) \right] > K_M \qquad (22.2.4)$$

In this case, the kinetics are controlled by the diffusion of the substrates to the enzyme-covered surface (mass transfer). The reaction is slowed down by mass-transfer processes. The value of the apparent Michaelis constant K_M^{app} is larger than that of the equivalent bulk situation K_M.

2.4.3 Application to yeast PGK

The modification of glass and mica with NH_2-terminated silane molecules certainly results in a quite positive surface charge at pH = 7.5. Additionally, 1,3-BPG as well as ADP contain two phosphate groups that should both be deprotonated at pH = 7.5 leaving two negatively charged substrates. Consequently, the situation of an electrostatic attraction of the substrates is expected (a < 0). Therefore, the condition exp(α) << 1 yields an electrostatic modifier $M \approx 1$ in the expression of F.

1,3-bisphosphoglycerate is a linear molecule of a maximum length (phosphate to phosphate distance) of 6.3 Å. The Stokes-Einstein formula for the Brownian motion of spheres in a medium of viscosity h can be used to obtain an order of magnitude of the diffusion coefficient of 1,3-BPG:

$$D_0 = \frac{k_B T}{6 p h s} \quad (23)$$

Where k_B is the Boltzman constant and s is the radius of the spheres. Equation (23) yields $D_0 \approx 7.2\ 10^{-10}$ m^2/s for an aqueous solution of 1,3-BPG at room temperature (22 °C). Solvatation effects or hydrogen bonding for instance will modify this value. However, in agreement with diffusion coefficients usually obtained for redox species of similar size (Chapters 4 & 5), $D_S \approx 10^{-9}$ $m^2.s^{-1}$ will be used.

The real value of d is difficult to assess and depends on solution stirring. Since no solution stirring was used, one can assume $d \approx 1$ µm. Then, $m \approx 10^{-3}$ $m.s^{-1}$.The reciprocal thickness of the diffuse layer can be obtained from the Gouy-Chapman-Stern model by simplifying the reaction buffer into a 1-1 electrolyte at 100 mM; this yields $k^{-1} \approx 1$ nm. This is another reason to take the electrostatic modifier $M \approx 1$. Consequently, with values of V_{max} and $K_{m,b}^{Mg\text{-}ADP}$ in bulk conditions measured in section 2.3.1, $F \approx 6$ and $b \approx 7$ for Mg-ADP. The values for 1,3-BPG are more difficult to assess since 1,3-BPG is indirectly generated *in situ* by GAPDH from 500 µM GAP. $b > F$, at least for Mg-ADP, and the measurement is not limited by substrate diffusion according to Equation (22.2.1).

The result that $K_{m,s}^{Mg\text{-}ADP} < K_{m,b}^{Mg\text{-}ADP}$ also goes in the same direction since, according to Equation (22.2.2) and with the approximation $\exp(\alpha) << 1$, a lower binding constant is expected in the surface measurement. According to Equation (22.2.2), the surface potential of the APTES-silanized glass surface (helmholtz plane) would be $Y_0 \tilde{}$ +65 mV if z=-2 for a diphosphate molecule at pH = 7.5. Equation (22.2.1) also shows we should measure $v = V_{max}$. The rate measured is much lower; it is difficult to discriminate between possible diffusion-related effects and effects from the surface enzyme coverage (steric effects, active site occlusion...) and possible inactivation following the chemical immobilization procedure – G_E in Equation (18) or, equivalently, $[PGK]_0$ i bulk measurements – since that quantity also determines the measured value of V_{max}.

Nevertheless, the conclusion that no diffusion limitation takes place should be taken carefully since many approximations are made to come to that conclusion and, even within these approximations, b and F are very close suggesting the experiments are actually carried out at the limit of $b \approx \Phi$. Moreover, no measurements are available for the second substrate of higher interest (1,3-BPG).

Another system, namely β-galactosidase, is currently studied with the same strategy since it is a direct measurement of the activity on a single substrate modified to give a signal in the UV/Visible spectral domain, namely o-nitrophenylgalactopyranoside (ONPG). These measurements should allow an easier illustration of the model exposed above.

In studies of the activity of immobilized enzymes another parameter is usually of high importance but very difficult to assess: surface coverage, G_E in Equation (18). To investigate surface coverage, AFM operated *in situ* in the dynamic amplitude-modulation (AM) mode, or Tapping Mode, can be a useful tool. The next section analyses images obtained from the same glass and mica slides than those used to measure the enzymatic activity.

3. In situ AFM imaging of immobilized phosphoglycerate kinase (PGK)

Several parameters including the apparent binding constant of MG-ADP, $K_m^{Mg\text{-}ADP}$, and the maximum catalytic rate of 3-PG formation, V_{max}, could be extracted and compared to bulk values. The collected information allows certain hypotheses on the surface coverage of enzymes to be tested.

The typical dimensions of yeast PGK can be obtained from the refined crystallographic structure obtained by X-ray diffraction[3]. An 8x5x2 nm^3 parallelepiped box can roughly approximate one phosphoglycerate kinase molecule. Since the maximum surface occupied by one molecule of PGK (monolayer) is then 40 nm^2, two 2 cm^2 glass slides can carry up to 2 10^{13} molecules, i.e. an equivalent concentration of about 42 nM with the approximation of a monolayer of enzyme molecules totally covering the surface

of the glass slides immersed in the solution. This yields a catalytic constant, $k_{cat}^{s} = 3.1\ s^{-1}$, which is more than two orders of magnitude smaller than in bulk. Such a drastic decrease is not expected for immobilized enzymes.

Most probably, the coverage and the proportion of still active molecules have been largely overestimated. AFM *in situ* can help determining the average surface coverage which is probably much smaller than that used in the above rough calculation by imaging several areas of a surface prepared similarly to those used to measure the activity of immobilized phosphoglycerate kinase. However, the AFM experiments will not allow discriminating between really active and damaged molecules or even molecules within a layer that are inaccessible to the substrates.

3.1 Experimental details

An enhanced commercial microscope (Extended MultiMode/Nanoscope IIIa, Veeco Instruments, Inc.) was used to image PGK-covered samples similar to those studied in the previous section. The cantilever was vibrated with a lock-in amplifier at a frequency of 32 kHz, slightly lower than the resonant frequency f_0 = 35.4 kHz from the thermal noise analysis. The amplitude and phase were then measured with the same lock-in amplifier in order to increase the signal to noise ratio and therefore allow much smaller oscillation amplitudes to be used. The cantilever holder was modified in order to decrease the convolution between the tip and the cell oscillation in order to properly point the excitation frequency.

Finally, in agreement with conclusions drawn in Chapter 2, thin 100-µm-long Olympus cantilevers with tip heights of about 3 µm were used. They had nominal spring constants around 0.6 N/m. Additionally, to minimize the hydrodynamic drag force, oscillation amplitudes smaller than 1 nm were employed.

Typically, the surface was approached once either in the Amplitude-Modulation (Tapping) mode or in the static (Contact) mode. Then, the Veeco system was bypassed and the lock-in amplifier excitation/detection was used. A force curve was then recorded

to verify the position of the surface and adjust the tip-sample force to the lowest possible value. The images were then recorded at very high speeds (10 μm/s or more) to compensate piezoelectric drifts whereas the feedback loop was shut down by setting the integral and proportional gains to zero.

3.2 Results

3.2.1 PGK on mica

The glass surfaces were prepared according to the procedure given in section 2.2.2 and imaged immediately in a drop (volume of about 100 μL) of freshly prepared 20 mM phosphate buffer at pH = 7.5. The whole system (cantilever and sample) was left to rest for 5 to 10 minutes in order to allow thermal equilibration of the cantilever oscillation.

Figure 3.9 shows a set of images typically obtained at different magnifications: 500 nm (a), 150 nm (c) and 2 μm (d). They reveal both single PGK molecules isolated on the surface and several larger aggregates of up to 6 molecules. The section along the black line in Figure 3.9a, shown in Figure 3.9b (bottom), agrees with that analysis, since it exhibits peaks about 7 nm high as well as smaller ones around 2 nm high.

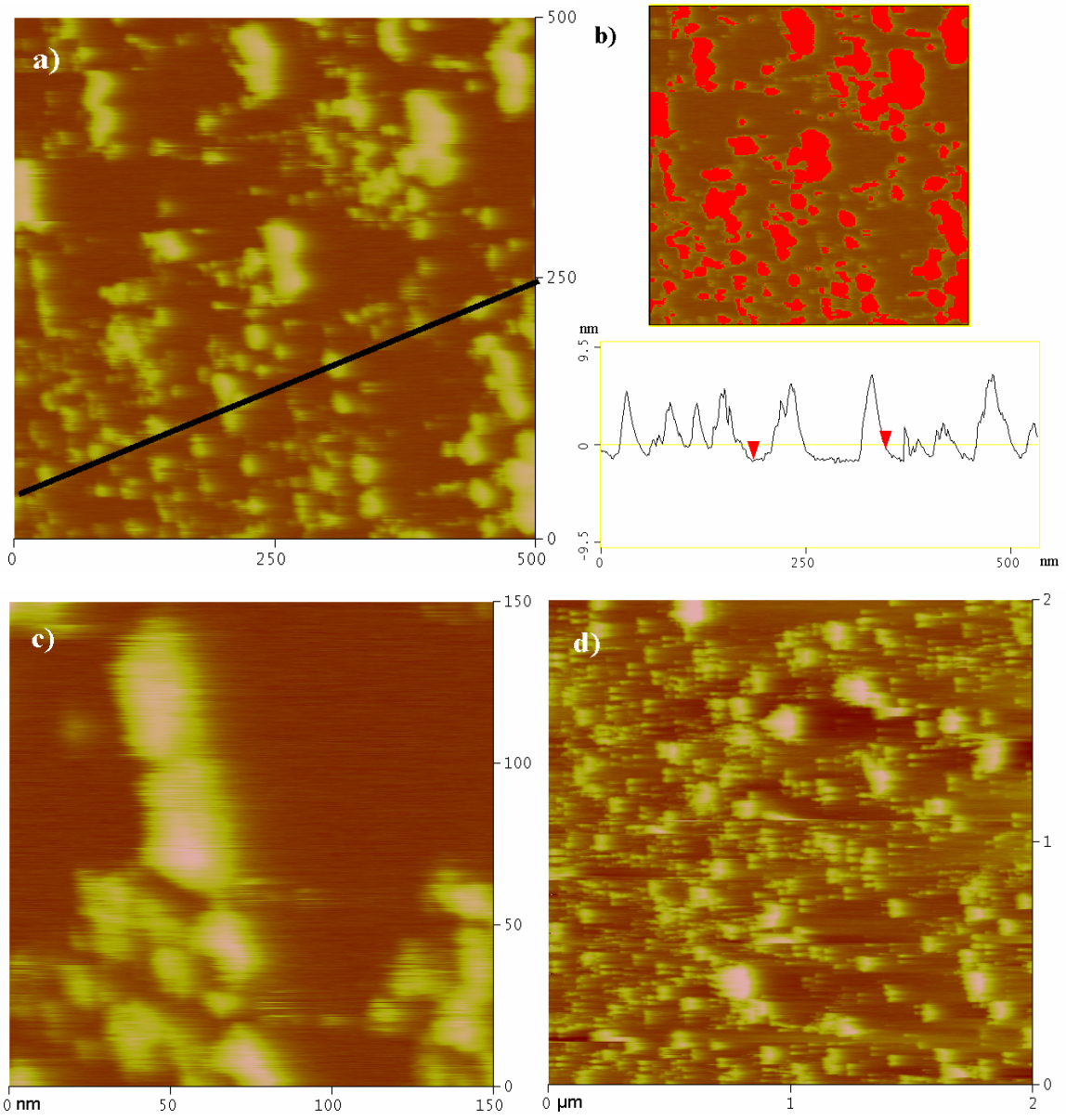

Figure 3.9: Typical AFM images obtained on PGK-covered mica samples at different magnifications: 500 nm – 10 µm/s – z-scale: 0-20 nm (a), 150 nm – 6 µm/s – z-scale: 0-15 nm (c), and 2 µm – 40 µm/s – z-scale: 0-20 nm (d). Image treatments (b): thresholding to determine a surface coverage of about 24% (top) and section along the black line (bottom). The oscillation amplitude was A_0 = 1 nm.

The smallest features in Figure 3.9 appear only reasonably broadened laterally, i.e. not more than twice the expected molecule size, suggesting that only tip convolution occurs and that the hydrodynamic force has been decreased enough by using that appropriate thinner cantilever and oscillation amplitudes smaller than 1 nm to minimize the deformation of molecules upon chemical immobilization on the surface. Consequently, the soft protein molecules are not deformed by the scanning tip. Moreover, images are similar between several consecutives scans suggesting a relative stability of the chemical strategy to immobilize the PGK molecules onto the mica surface. However, some mobility of the proteins by diffusion on the APTES-treated mica surface is always expected but is not observed in the different recorded AFM images. Indeed, after the silane treatment, the density of functional amino groups that will later be used to bind protein molecules via the glutaraldehyde cross-linker is much higher than that of available lysine residues on the surface of one PGK molecule. Consequently, if one particular molecule is anchored to the surface via one particular amine group, it may later on be attached to a different surface amino group through diffusion on the surface which cannot be excluded at room temperature ($T \approx 22$ °C).

AFM imaging in similar conditions of a bare freshly-cleaved mica piece showed a flat surface free of any buffer aggregate proving that the features seen in the images of Figure 3.9 are most likely PGK molecules and not imaging artifacts.

In order to determine the surface coverage, a thresholding of the 500-nm scan is done. Every feature above a user-defined height, the bare APTES-treated mica surface, appears in red (Figure 3.9b – top). A coverage value of about 24% could be determined. Nevertheless, among these molecules, some may still be inactive or inaccessible; especially within the larger aggregates like, for example, the one appearing in the center of Figure 3.9c.

Approach curves obtained on several spots scattered on the PGK-covered mica samples were systematically compared to approach curves recorded with similar parameters (oscillation frequency $f < f_0$, oscillation amplitude far away from the surface

$A_0 \approx 1$ nm and approach speed around 50 nm/s) on a bare freshly-cleaved mica surface in the same buffer solution in order to obtain local mechanical information on the PGK-covered mica samples.

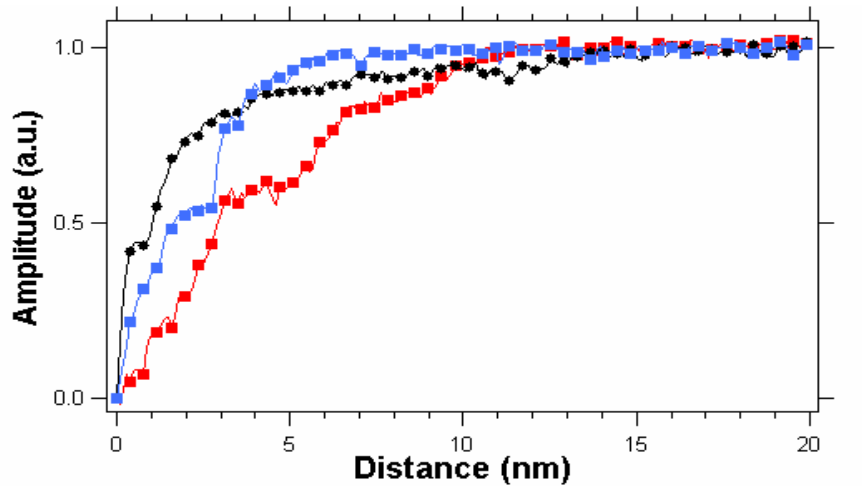

Figure 3.10: Typical approach curves recorded on several spots of the PGK-covered mica surface (squares) and on a freshly-cleaved mica surface (black circles) at about 50 nm/s in 20 mM phosphate buffer at pH = 7.5.

Figure 3.10 shows typical curves obtained on different spots on the surface that illustrate two types of observed decreasing behaviors of the oscillation amplitude as the surface is approached. The slope of the linear part of the amplitude drop in an AM-AFM approach curve is determined by the ratio of the cantilever stiffness k_L modulated by the quality factor Q and the tip indentation to the sample de is given by[28]:

$$p = \frac{1}{1 + \left(\frac{de}{Qk_L} \right)^{2/3}} \qquad (24)$$

Consequently, a slope smaller than unity is obtained when a soft sample (softer than the tip) is deposited on a harder surface (mica, Si/SiO_2 ...). The blue curve drops to zero (contact with the surface) almost as abruptly as in the case of a freshly-cleaved mica surface (black curve) suggesting that this type of spots correspond to areas of almost bare mica without only a few PGK molecules. The red curve however, drops to zero much more slowly than the black reference curve. This suggests that this type of spots corresponds to areas where soft biological material is more densely present (bright areas

in Figure 3.9); most likely a large protein aggregate since the piezoelectric drift does not allow the system to be stable over a whole curve on a single isolated molecule.

Additionally, the blue and red curves seem to display a two-step process with a transition occuring at about 50% of the amplitude drop. This can be attributed to the removal of water molecules between the tip and the surface as it approaches the surface and gradually confines the fluid or even the displacement of one or several enzyme molecules since the molecules still have some mobility at this local scale as explained earlier in this section. In the case of the red curve, where more biological material is supposed to be present on the surface, the slope rupture is more pronounced because more molecules are moving on the surface as the tip approaches.

3.2.2 PGK on glass

The glass surfaces prepared as described in section 2.2.2 were imaged in similar conditions (20 mM phosphate buffer at pH = 7.5) with similar parameters (thin Olympus cantilevers oscillating at amplitudes smaller than 1 nm).

Figure 3.11 shows typical images obtained at different magnifications: 500 nm (a), 100 nm (c), and 2 μm (d). Unlike mica surfaces, the images reveal more frequent and larger protein aggregates. A few isolated PGK molecules can still be seen, but they are much scarcer than in the case of PGK-covered mica surfaces. The section along the black line confirmed the presence of large 6 nm-high aggregates on the surface (Figure 3.11b – bottom).

A thresholding of the 500-nm scan image allowed determining an average coverage value of about 36 %. The coverage seems higher than in the case of mica samples. This can be attributed to a higher density of functional amino groups – later used to bind the PGK molecules via the cross-linking agent – on the APTES-silanized glass surface than on the APTES-treated mica sample because the silane molecules are chemisorbed to the glass surface whereas they are only physisorbed via a large electrostatic interaction on the mica surfaces. Consequently, for the same concentrations of the silane and enzyme

coupling solutions, a larger number of PGK molecules is expected to be immobilized on glass than on mica within a given surface area.

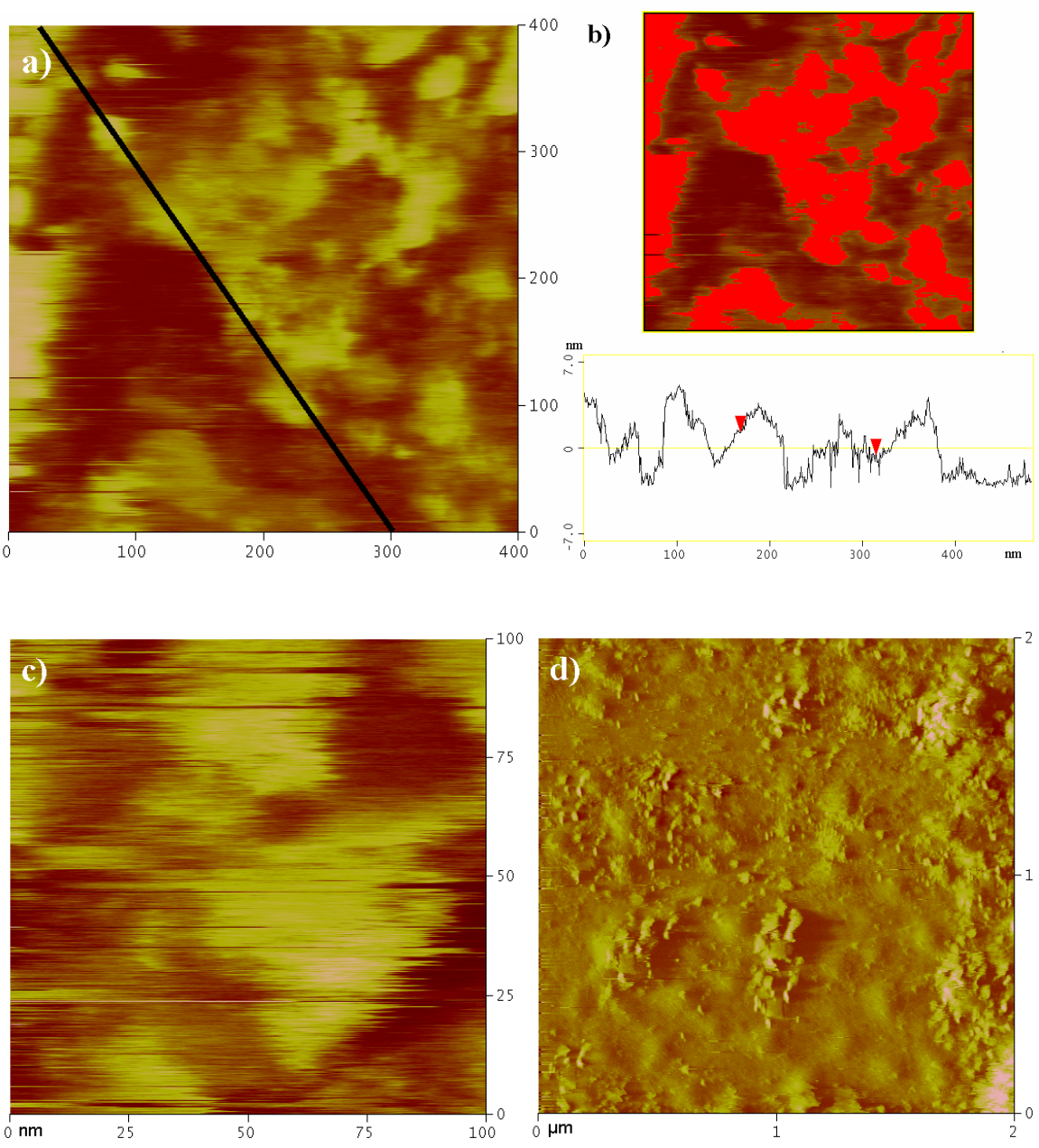

Figure 3.11: Typical AFM images obtained on PGK-covered glass samples at different magnifications: 500 nm – 10 µm/s – z-scale: 0-15 nm (a), 100 nm – 2 µm/s – z-scale: 0-10 nm (c), and 2 µm – 4 µm/s – z-scale: 0-10 nm (d). Image treatments (b): thresholding to determine a surface coverage of about 36% (top) and section along the black line (bottom). The oscillation amplitude was A_0 = 1 nm.

As in the case of mica, the hydrodynamic force has been decreased enough not to deform the imaged molecules during the scan according to the height values obtained in the images. Again, images in 20 mM phosphate buffer at pH = 7.5 of a glass surface freshly cleaned in Piranha solution (70% H_2SO_4/30% H_2O_2) revealed a flat surface (roughness: R_a = 0.075 nm over 0.1 µm^2) without possible buffer aggregates meaning that the features seen in Figure 3.11 are PGK molecules.

As in the case of mica, approach curves were also systematically recorded to qualitatively study mechanical properties at a local scale. The slopes of the amplitude vs. distance curves were not much different from that obtained in the case of a bare glass surface. However, in the case of PGK-covered glass slides, additional local maxima were systematical present in the approach curves recorded on PGK-covered glass surfaces.

The local maxima can be explained by the presence of an additional attractive regime on glass surfaces. Indeed, the images and approach curves are recorded with an oscillation frequency slightly lower than the resonant frequency. Therefore, when the oscillation peak shifts to lower frequencies as the surface draws nearer (attractive field), the cantilever is actually excited with a slightly higher amplitude than in the absence of interaction (far away from the surface) since no feedback is done on the frequency shift in the AM-AFM mode.

The additional attractive interaction can be attributed to a slight adhesion between the silanized parts of the glass surface, not necessarily covered with protein aggregates, to the silicon tip. Indeed, leaving the glass slides in the silane solution for 18 to 24 hours leads to much more than a monolayer of APTES on the glass surface. Consequently, the glass slides can be left with a quite sticky layer below the protein molecules since long silane treatments in quite concentrated solutions are routinely used to improve surface adherence[29]. Since the surface coverage by PGK molecules is much lower than 50 % according to Figure 3.11b, the tip is more likely to sense the silanized areas of the glass surface than the areas covered with enzyme molecules during an approach curve.

In the case of mica, the additional attractive regime is not present because the silane layer is not chemisorbed on the surface but much more weakly bound via electrostatic interactions. Therefore, it is much more difficult to build up a thicker layer of silane

molecules on the mica surface to improve their adhesiveness especially when the mica surfaces are thoroughly rinsed with either non-aqueous solvents (ethanol, acetone...) or aqueous solutions (phosphate buffer at various pH) between each step of the immobilization procedure.

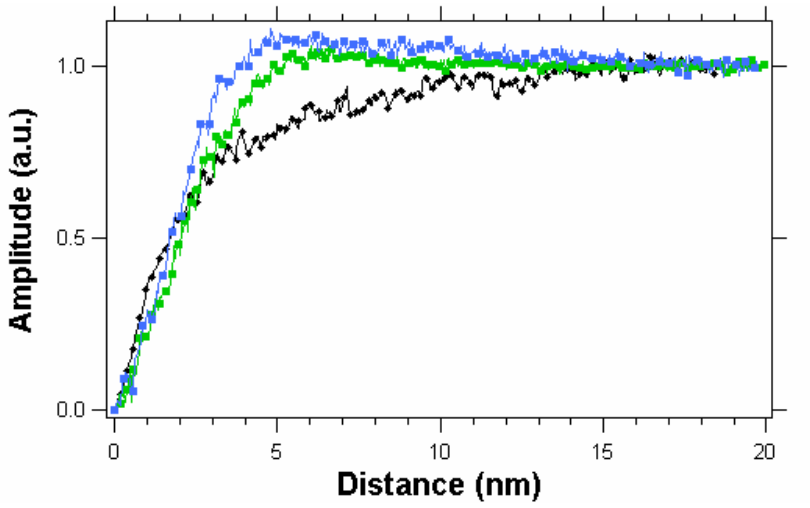

Figure 3.12: Typical approach curves recorded on several spots of the PGK-covered glass surface (squares) and on a freshly-cleaned glass surface (black circles) at about 30 nm/s in 20 mM phosphate buffer at pH = 7.5.

From the AFM experiments on both PGK-covered mica and glass samples, the enzyme surface could be determined at 24% and 36% respectively. But, these two types of surfaces have different mechanical signatures at the local scale. These elements could be important for the conservation of the enzymatic activity upon immobilization as well.

However, in the case of PGK-covered glass slides, for example, if one assumes a surface coverage of 36%, the corresponding k_{cat} constant would be equal to 17 s^{-1}. This value is still much lower than the value obtained for a bulk PGK solution. Such a large difference can be explained by inactivation of a large number of molecules upon immobilization either by denaturation or because their active site is not properly oriented to be accessible to the substrates or even buried inside an aggregate. To obtain a catalytic constant similar to that measured in bulk conditions, only about 2% of the material present on the surface and seen during an AFM scan should remain active after

immobilization. It is difficult to discriminate between active and inactive material with an atomic force microscope because of the lack of biochemical sensitivity of this tool.

4. Conclusions and future perspectives

4.1 Conclusions on surface enzymatic activity

The above sections aimed at answering a few fundamental questions raised when biologically active materials like enzymes are adsorbed or chemically immobilized on solid flat surfaces, namely the mobility of the material on the surface, the remaining activity of the deposited material, the stability of the prepared surfaces over time and their resistance to external aggression, as well as the efficiency of the deposition in terms of surface coverage.

A non-exhaustive answer was provided to each of these questions. First, it was shown that chemical immobilization, i.e. creation of a covalent (on glass) or strong electrostatic (on mica) bond between the enzyme and the solid surface, drastically decreases the lateral mobility on the surface, but certainly does not freeze the molecules on the surface. Therefore, very high resolution (near-atomic) structural studies of enzymes for instance, will not be possible with this method by dynamic AFM.

Then, an estimate of only 2% preserved activity upon chemical immobilization could be given. This means that although most of the activity is lost by denaturation or simply by inaccessibility to the substrates diffusing towards the surface, it suffices to maintain a signal measurable by standard techniques. Nevertheless, the approximation that the measured reaction rate is not limited by diffusion of the substrates should be taken with extreme care since calculations show the experiments are actually carried out at the limit of this hypothesis. This could also change the value of the measured reaction rate and more than 2% active molecules could be present on the surface.

Finally, experiments showed that it is better to store freshly-prepared surfaces in a buffered medium at 4 °C in an environment where only very low mechanical constraints (friction with other samples or presence of abrasive chemicals) are exerted on the surface.

4.2 Future perspectives

In order to measure the enzymatic activity of PGK, a very complicated indirect method has to be used. This makes it very difficult to properly evaluate the contribution of substrate diffusion to the measured reaction rate. Therefore, the use of a simpler mono-substrate system will be favored in the future. β-galactosidase and its modified substrate o-nitrophenylgalactopyranoside (ONPG) is one possibility.

Then, the AFM could be used to study the enzymatic activity locally from a mechanical point of view. Indeed, if a probe optimized to minimize the contribution of the hydrodynamic force (Chapter 2) is placed directly on top of a small aggregate of active molecules, one could expect to detect changes due to the enzymatic activity. For example, the thermal noise in a buffer solution as the tip is poised as close as a few nanometers to the enzyme-covered surface could be compared to that recorded once the substrate is introduced in the solution. Then, information relative to dynamic changes could be extracted.

Similarly, Chapter 2 suggests the expression of the resonant frequency shift as a function of local viscosity; this could be exploited to measure the activity of a small aggregate of enzymes. Local viscosity changes during the catalytic act on a small molecule like ONPG or even 1,3-BPG are most likely below the present sensitivity of the AFM instrument. To enhance the expected effects, such changes could be measured on an enzyme that induces polymerization or de-polymerization of a large substrate such as collagenase.

This section is an application of the elements learned from Chapter 2 in terms of minimizing the hydrodynamic force exerted by the tip oscillation. Now this seems to be under control and could open the way to more qualitative imaging or mechanical studies

of biological materials generally. Modern biochemistry and biophysics need new tools to increase our knowledge and Dynamic AFM could be one of the answers.

References

[1] Bucher J.L., *The Metrology Handbook*, ASQ Quality Press, Milwaukee, 2004
[2] Mas M.T., Resplandor Z.E., and Riggs A.D. (1987) , *Biochemistry*, **26(17)**, 5369-5377
[3] McPhillips T.M., Hsu B.T., Sherman M.A., Mas M.T., and Rees D.C. (1996) , *Biochemistry*, **35(13)**, 5369-5377
[4] Conway N.M.J., Ilie A., Robertson J., Milne W.I., and Tagliaferro A. (1998), *Appl. Phys. Lett.*, **73(17)**, 2456-2458
[5] Hahn J.R., and Kang H. (1999), *Phys. Rev. B*, **60(8)**, 6007-6017
[6] Nony L., Boisgard R., and Aimé J.P. (2001), *Biomacromolécules*, **2**, 827-835
[7] Auerbach G., Huber R., Grättinger M., Zaiss K., Schuring H., Jaenicke R., and Jacob U. (1997), *Structure*, **5**, 1475-1483
[8] Bernstein B.E., Michels P.A.M., and Hol W.G.J. (1997), *Nature*, **375**, 275-278
[9] Betton J.M., Desmadril M., Mitraki A., and Yon J.M. (1985), *Biochemistry*, **24**, 4570-4577
[10] Schmidt P.P., Travers F., and Barman T. (1995), *Biochemistry*, **34**, 824-832
[11] Souza J.M., and Radi R. (1998), *Arch. Biochem. Biophys.*, **360**, 187-194
[12] Boschi-Muller S., and Branlant G. (1999), *Arch. Biochem. Biophys.*, **363**, 259-266
[13] Daubenberger C.A., Pötl-Frank F., Jiang G., Lipp J., Certa U., and Pluschke G. (2000), *Gene*, **246**, 255-264
[14] Bücher T. (1955), *Methods Enzymol.*, **I**, 415-422
[15] Voet D., and Voet J.G., *Biochemistry*, J. Wiley & Sons, New York, 1995
[16] Minard P., Desmadril M., Ballery N., Perahia D., Mouawad L., Hall L., and Yon J.M. (1989), *Eur. J. Biochem.*, **185**, 419-423

[17] Molnar M., and Vas M. (1993), *Biochem. J.*, **295**, 595-599
[18] Collinet B., Hervé M., Pecorari F., Minard P., Elder O., and Desmadril M. (2000), *J. Biol. Chem.*, **275(23)**, 17428-17433
[19] Yang J., Mou J., and Shao Z. (1994), *FEBS Letters*, **338**, 89-92
[20] Fritz M., Radmacher M., Cleveland J.P., Allersma M.W., Stewart R.J., Gieselmann R., Janmey P., Schmidt C.F., and Hansma P.K. (1995), *Langmuir*, **11**, 3529-3535
[21] Bergkvist M., Carlsson J., Karlsson T., and Oscarsson S. (1998), *J. Colloid Interface Sci.*, **206**, 475-481

[22] You H.X, and Lowe C.R. (1996), *J. Colloid Interface Sci.*, **182**, 586-601
[23] Shiraishi F. (1995), *J. Ferm. Bioeng.*, **79(4)**, 373-377
[24] Kato M. (1995), *J. theor. Biol.*, **177**, 299-304
[25] Bard A.J., and Faulkner L.R., *Electrochemical Methods : Fundamentals and Applications*, 2nd Edition, John Wiley & Sons, New York, 2002
[26] Israelachvili J.N., *Intermolecular and Surface Forces*, 2nd Edition, Academic Press, London, 1992
[27] Michaelis L., and Menten M. (1913), *Biochem. Z.*, **49**, 333-369
[28] Dubourg F., Aimé J.P., Couturier G., and Salardenne J. (2003), *Europhys. Lett.*, **62(5)**, 671-676
[29] Plueddemann E.P., *Silane Coupling Agents*, 2nd Edition, Plenum Press, New York, 1991

Chapter 4: Scanning Electrochemical Microscopy (SECM) Studies of Electroactive Enzymes

In the previous chapter, the enzymatic activity of surface-bound proteins was studied. The method used (UV-visible spectrophotometry) allowed to measure heterogeneous rate constants, i.e. reaction rates of reactions occurring between two different phases of condensed matter or, in most cases, near interfaces (solid and liquid phases) as opposed to homogeneous reactions where only one phase is involved and often termed "bulk" reactions (liquid phase)[1]. However, the response was averaged over the whole area probed by the UV-visible spectrophotometer beam, i.e. around 0.5 cm^2 that is of the order of the sample size (≈ 3 cm^2). In this chapter, efforts at measuring heterogeneous rate constants averaged only over a few μm^2, i.e. the size of the probe and therefore on a much smaller scale than the sample size, will be exposed. This method gives much more information on local processes. Such measurements are possible in Scanning Electrochemical Microscopy (SECM) but are limited to redox-active materials that involve electron-transfer reactions between donor and acceptor molecules. A complicated indirect measurement involving the perturbation of the feedback current of a 1-electron mediator[2] by the consumption of the nicotinamide-adenosine-dinucleotide (NAD^+/NADH) co-substrate of glyceraldehyde-3-phosphate dehydrogenase (GAPDH) would allow the use of SECM to study a non-redox system like 3-phosphoglycerate kinase (PGK). Further details on the enzymatic activity test of immobilized PGK are given in Chapter 3. Nevertheless, due to the too large number of uncontrolled intermediate steps, simple redox systems like glucose-oxidase (GOD) and catalase were preferred.

Another aspect of the study presented here, at least in the case of glucose oxidase, is the influence of an external DC electric field on enzymatic activity and the experimental difficulties encountered to properly apply such a field in an electrolyte containing many charged species.

1. Introduction: DC-electric field effect on enzymatic activity

Unlike in molecular biology where the coding DNA sequence is *intrinsically* modified by site-directed mutagenesis to change the sequence of amino-acids of the enzyme, essentially around the active site, to alter the measured catalytic activity[3], the following section lists the different possibilities to *externally* modify the observed enzymatic activity, i.e. the increase in the rate of reaction of a specified chemical reaction that an enzyme produces in a specific assay system[1].

1.1 Parameters controlling the enzymatic activity

There are many different ways to alter enzymatic activity. The most widely known way of altering enzymatic activity is the use of molecules – called inhibitors – decreasing the overall rate constant by either binding irreversibly to the active site (enzyme inactivation), competing with the natural substrate for the active site (competitive inhibition) or binding the protein at a location different from the active site (uncompetitive binding)[4]. This has been the most widely studied because of the immediate implication in therapeutics and medicine treatments.

However, from a more fundamental point of view, if one considers the enzyme as a complex chemical system, much can be done by applying kinetic or thermodynamic perturbations. Indeed, in the stability domain, temperature and pressure can influence the activity. Moreover, near a surface, there can be an additional electric field whether or not there is charge transport. This section lists the possible *external* perturbations of the enzyme considered as a thermodynamic system at equilibrium.

- The rate constant of conversion of *S* to *P* by an active enzyme can be indirectly drastically modified by slowing down – or even preventing – the diffusion of substrates to the enzyme. This can be done, for example, by trapping the enzyme in an electrochemically grown polymer deposited on the electrode such as polypyrrole[5,6]. In this case, the enzymatic activity is often modified as well by the hindered substrate-binding efficiency to the enzyme because of

unfavorable protein orientations or deformation of molecules embedded in the polymer matrix. Moreover, the response obtained is an overall response averaged over the whole film where some molecules may have lost their activity significantly whereas others remain unaffected. The perturbation of the diffusion of substrates to the enzyme can be generalized to any modification of the viscosity of the solvent or even, ultimately, enzymes working in non-aqueous conditions. Indeed, Klibanov et al have reported altered activities as well as improved stability of well-characterized enzymes like α-chymotrypsin, ribonuclease or several esterases in anhydrous organic solvents[7].

- A more common factor influencing the activity of the enzyme is the temperature through an Arrhenius law for the rate constant that controls the reaction rate *k* of the transition state if the simplified thermodynamic pathway of Figure 4.1 is assumed:

$$k = k^0 \exp\left(-\frac{E_a}{RT}\right) \quad (1)$$

Decreasing the temperature immediately leads to an exponential decrease of the rate constant of the conversion reaction of the simple mechanism described by:

$$E + S \underset{k_{-1}}{\overset{k_1}{\Leftrightarrow}} [E..S]^{\#} \xrightarrow{k_2} E + P \qquad (2)$$

E, *S* and *P* respectively denote the enzyme, substrate and reaction product. *[E..S]*$^{\#}$ refers to the enzyme-substrate complex, a hypothetical transition state where the substrate is bound to the enzyme but has not undergone any chemical modification changes yet.

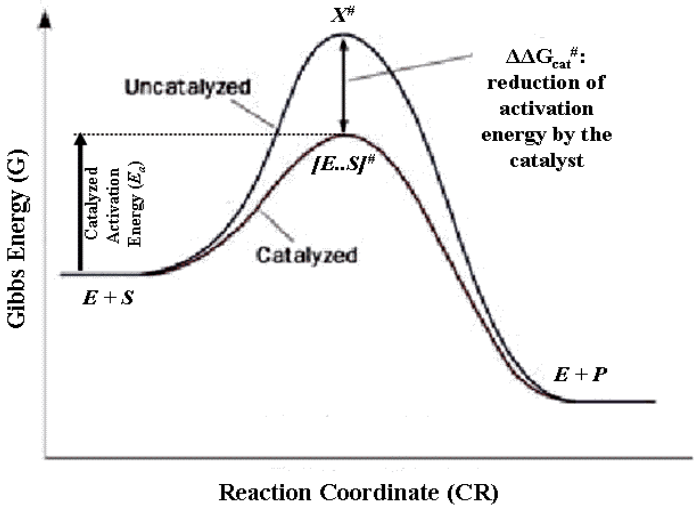

Figure 4.1: Simplified thermodynamic pathway of a general catalytic enzymatic mechanism leading to the conversion of the substrate *S* to the product *P* via an intermediate transition state – marked with *#*. The enzyme proficiency is assessed by the difference in Gibbs energies of the transition states between the uncatalyzed and the catalyzed reactions. It is usually within[8] 10^5 – 10^{10}. In reality, the Gibbs energy profile might be much less smooth suggesting a multitude of local minima corresponding to different transition states where the state corresponding to the highest energy point would only be the less kinetically unstable.

For this simple mechanism and assuming the enzyme-substrate complex does not accumulate in the system (quasi-stationary approximation), the overall reaction rate constant is given by:

$$k = \frac{k_1}{k_2 + k_{-1}} \quad (3)$$

Naively, one could think that increasing the temperature even more would increase the enzyme efficiency according to equation (1). But, enzymes are generally very sensitive to denaturation (structural conformational changes of the active site leading to activity loss) that gets more important as enzymes are made to work at temperatures above that of their intended native environment, i.e. around 37 °C for yeast-based proteins or 28 °C for proteins from *Escherichia coli* or other bacterial organisms[9].

- Similarly, when none of the substrates is a dissolved gas unlike, for instance, in the case of glucose oxidase where O_2 is required to oxidize the enzyme back to its original state in a second step, the total pressure will have an indirect external effect on the rate constant since high pressures are known to lead to protein unfolding[10], a severe case of denaturation, and therefore loss of activity.

- More unusual external factors modifying the enzymatic activity can be extrapolated from Legendre transforms of the internal energy U, a thermodynamic function homogeneous of degree 1 in terms of the extensive variables (entropy S, volume V and concentration of the constituent i $\{n_i\}_i$) suitable for the study of open systems where a chemical reaction occurs[11].

In particular, the presence of an electric field at the solid/liquid interface can be considered. On one hand, the field can have effects on the protein 3D-structure by redistributing intrinsic charges (charges on constitutive amino-acids at a given pH) and therefore alter the geometry of the active site and modify the activity. Additionally, if faradaic charge transfer occurs, disulfide bridges that maintain the 3D-structure or link two structural domains to form the active site can be reduced; yeast phosphoglycerate kinase (PGK), for instance, does not contain any disulfide bridge but only a buried cysteine residue[12].

On the other hand, the electric field can affect the transport of charged species like substrates or co-substrates as well as ions essential to the structure or the activity. These electrodiffusion effects can occur both in non-redox and redox-active enzymes. More specifically, if the surface is negatively charged, the interfacial field will repel negatively-charged substrates and therefore decrease the measured activity. If the surface is positively charged, negatively-charged substrates will be electrostatically attracted by the surface and an overconcentration of substrates will take place at the surface, which should, in turn, increase the measured activity. This situation is expected in non-redox enzymes like phosphoglycerate kinase. If the enzyme is redox-active like glucose oxidase, in addition to electrodiffusive effects, the electric field will influence the intrinsic charge transfer, which is, in this case, the catalytic step itself.

When charge transport occurs, the additional conjugation of extensive and intensive variables to consider for the Legendre transform of the internal energy U is $\sum_i z_i F F_i n_i$, summed over each charged species i of charge number z_i at a concentration n_i in solution and driven by an electric potential F_i related to surfaces charges that is specific to the phase the charge species i is in. The presence of the Faraday constant F is the signature of charge transport. This description is strictly valid only for ions, i.e. point particles of fixed charge – at least when no solvation limitations occur. The next section will discuss more in details in how far a protein solution can behave like an ionic solution especially near a charged surface. In most case, the pressure P is assumed to be

constant throughout the experiments and one can remember the following thermodynamic relations:

$$\begin{cases} U = TS - PV + \sum_i m_i n_i + F \sum_i z_i f_i n_i \\ dU = TdS - PdV + \sum_i m_i dn_i + F \sum_i z_i f_i dn_i \end{cases} \quad (4)$$

The usual nomenclature is used: temperature *T*, entropy *S*, pressure *P*, volume *V* and chemical potential m_i of each species *i*. Equation (4) can be rewritten with the electrochemical potential of each species *i* defined by : $\overline{m_i} = m_i + z_i F f_i$.

When only polarization effects where no charge is transferred at the surface or in bulk are taken into account, the set of variables to consider for the Legendre transform of the internal energy U is $\vec{E}.\vec{p}$ where $\vec{E}$ is the local electric field and $\vec{p}$ is the dipole moment of the system studied. This situation is more complex since, for instance, one has to use scalar products of vectors to account for spatial orientation effects. On the whole, local deformations of the protein molecules driven by the interaction of the external field with local or overall dipole moments (permanent or induced) are expected to influence the enzyme activity. The deformations can be purely structural (backbone or folded domains) or due to displacement of ions essential to the activity like Mg^{2+} in ATP-ases or H^+ of catalytic residues in acid proteases[9]. Then, one can write the thermodynamical identity for the internal energy *U* and its derivative with the usual nomenclature:

$$\begin{cases} U = TS - PV + (fL) + \sum_i m_i n_i + \vec{E}.\vec{p} \\ dU = TdS - PdV + fdL + \sum_i m_i dn_i + \vec{E}.d\vec{p} \end{cases} \quad (5)$$

To complete the tentative list given above, more marginal effects sometimes have to be taken into consideration when studying the thermodynamic open system defined by an enzyme population near a surface. Effects related to surface work are negligible at solid interfaces. Alterations arising from gravitational or magnetic works are only significant in large centrifugal fields or large magnetic fields respectively. Changes induced by mechanical work of the system are exposed from a different point of view in Chapters 2 and 3. The following sections focus on electrical effects.

1.2 External DC electric fields: expected effects on enzymatic activity

Equations (4) and (5) imply the presence of respectively charges or dipoles on studied enzymes if they are likely to be influenced by an external electric field. One also needs to justify the use of equation (4) to describe enzyme solutions whereas it is strictly developed for ion populations. The local charges on the protein backbone and on the side chains of its amino-acid residues combine to give an overall global charge that can differ between groups of proteins and is assessed by the value of the isoelectric point or pI. Their global charge depends on how different the actual pH of the solution is from that isoelectric point[9]. Figure 4.2 shows a statistical pI study of soluble proteins known in 2001. A usual experimental proof of the presence of surface charges in proteins is found in the first step of a 2-dimensional electrophoresis gel which, called isoelectric focusing (IEF)[13], and consists of separating proteins on a viscous polymeric gel arranged to create a pH gradient.

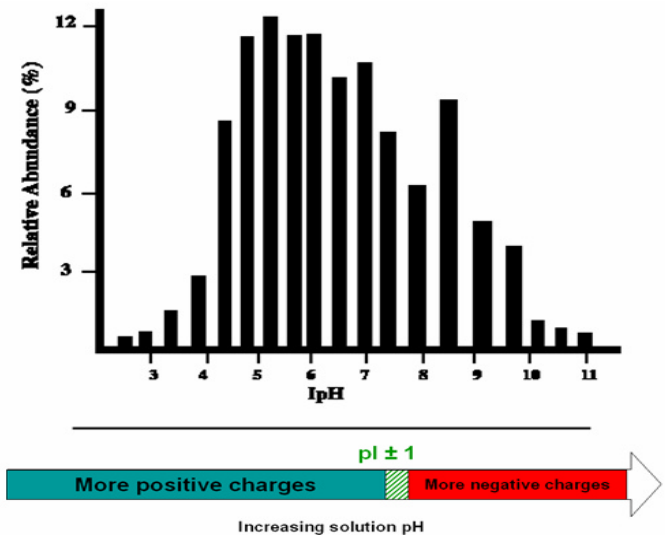

Figure 4.2: Distribution of pI (ipH) values (histogram courtesy of the Natural Toxins Research Center (Texas A&M University)). About 85% of known proteins have a pI value in the range of 4.5 to 8.5. The arrow indicates the nature of the overall charge according to the value of the solution pH as compared to the pI.

According to Figure 4.2, a protein solution can, at vary first approximation, be seen as a colloidal solution made of particles whose charge will depend on the solution pH and the ionic environment. Extremely, at a given pH and ionic strength, a protein solution can be treated as a salt solution with drastic limitations similar to behavioral differences with the models raised by

solvation and organization of ions. A single monomeric protein molecule has an average volume of about 65 nm^3 i.e. around 50,000 times larger than an ion; therefore limitations of the use of ionic models to describe protein solutions appear at a much larger scale, especially in surface processes where steric effects are of particular importance. Nevertheless, the approximation of uniform fixed charged particles can be used to crudely solve certain questions otherwise complex statistical treatment by Monte-Carlo or molecular dynamics simulations will be needed.

If one has to describe the protein population as a colloidal solution, the generalized Poisson-Boltzman equation in a dielectric medium[14] has to be solved:

$$\nabla(e\nabla f) - \frac{e.\sinh(f)}{l^2} = -\frac{4p}{k_B T} r_{fix} \qquad (6)$$

Where l is the Debye length, e the dielectric constant of the medium, r_{ix} the fixed charges and F the electric potential expressed in k_BT/e units. In most cases, f, l and e have spatial dependences. The calculation to get an expression for $\varepsilon(\mathbf{r})$ constitutes an intricate question still under investigation[15].

The presence of a non-uniform charge distribution within the 3-dimensional protein structure itself – exploited in equation (5) – creates local permanent and induced dipoles[16] that can extend from a few residues to a large folded domain. This situation leads to complex structural properties such as charge stabilization by residues from α-helixes[17] or stabilization of bound anions by backbone dipoles[18]. Therefore, separating the different effects transcribed by Equation (4) on one hand and Equation (5) on the other hand is experimentally difficult to achieve and often depends on the nature of the biological system studied.

The following short literature review summarizes various examples of observed effects of DC-electric fields on enzymatic activity where the contributions of polarization and charge transport could be more or less clearly separated.

1.2.1 Effects of DC electric fields with negligible current flow

An external DC electric field can affect the vibrational spectrum (infrared (IR) domain) of proteins such as the carbonyl and nitrosyl stretches in heme-bound and heme-free myoglobin

(coordination of carbon monoxide and nitric oxide by the iron atom of the heme) by the Vibrational Stark Effect (VSE)[19,20]. VSE spectroscopy can then be used to study the changes in the local internal electric field in the heme-binding pocket of bacterial myoglobin upon mutation of residues near the binding site, namely Val68 and His64[21]. The electric fields involved here are typically of 1000 kV/cm and the electrodes of the FTIR/VSE spectrometer are made of nickel-coated Teflon spacers separated by 30 cm. In order to maximize the signal to noise ratio, the electric field was applied parallel to the IR beam[17-19].

Wild type and D85N mutants Bacteriorhodopsin dry films have been exposed to dc electric field and revealed significant changes in the UV-Visible spectrum when the dc field was applied[22,23]. A retinal chromophore is bound to the protein via a Schiff base linkage to residue Lys216 and can absorb a photon to trigger a photocycle which allows the pumping of a proton through the membrane in which the protein is inserted[24]. The Schiff base can be protonated or unprotonated – the protonated form of the protein is blue. Wild type proteins and D85N mutants have different pKa values of the Schiff base since the immediate environment of Lys216 is modified and have been assessed to 11.3[25], and 8.9[20,26] respectively. When the dc field is on, the mutant films exhibit a decrease of the absorbance at 600 nm and an increase of the absorbance at 400 nm if the blank is made when the field is off[21]. This is the usual evidence for the transition between the protonated and the unprotonated form of the protein[23].

The most convincing explanation is a shift of the pKa of the Schiff base induced by the electric field. It can be attributed to electrostatic electron depletion of the acidic proton bond. At the *effective* pH of the films (the value of the pH of the suspension that exhibits the same protonated-Schiff-base fraction as that of the dry film), i.e. pH^{*} = 8.6, the fraction of deprotonated molecules is thus increased when the DC field is on. The effect is inversed when the polarity of the field is inversed because the molecules are highly oriented in the films. The originality of these experiments is the setup since the films were spin-coated with polyvinyl alcohol onto glass slides covered with indium tin oxide (ITO), dried out, covered with a 12-µm-thick Mylar layer and sealed with another ITO-covered piece of glass. Therefore, all effects of the electric field on the solution ions are strongly minimized. The magnitude of the dc field was around 700 kV/cm and was applied in pulses of typically 20 s and 10 s rise and fall times respectively.

In the above examples, experiments are carried out with only traces of water. The systems used are dried solid-state devices that usually contain only a few molecules of water. This case corresponds to the ideal limit where only non-faradaic processes take place, i.e. no electron is transferred to and from the system. Experimental accounts of similar effects in solution are not available to this date. Conceptually, since dipole moments are involved in those situations according to equation (5), AC electric fields of appropriate frequency and intensity might be more efficient to access such properties.

When a similar system is studied in solution, faradaic processes often largely dominate. The following section relates DC field effects on enzymatic systems under faradaic control.

1.2.2 Effects of DC electric fields – electrochemistry

Electrochemistry experiments can also reveal interesting features of proteins. In such experiments, two different situations should be distinguished: effects mainly or solely related to faradaic processes and those where no significant faradaic reaction occurs.

The first situation has been more extensively investigated and includes stimulation and/or inhibition of adsorbed enzyme activity[27,28,29] as well as characterization of several electrochemically-induced forms of cytochrome c_3 from *Desulfovibrio vulgaris* adsorbed on a mercury electrode[30]. This study is original and unusually rigorous because of the method used to detect and characterize adsorbed cytochrome c_3. It is generally admitted that ultrapurified monoclonal antibodies ensure highly specific detection when used in radioimmunoassays or Enzyme-Linked Immunosorbent Assays (ELISA). Besides, the binding properties of the two antibodies investigated in solution phase cytochrome c_3 preparations revealed that one of them (4H8) had a sequential epitope since it similarly bound to heat-denatured and native wild type cytochrome c_3 whereas the other (2A2) had a conformational isomer since it bound only to denatured cytochrome c_3. Consequently, it could be shown that the three electrochemically-generated forms of cytochrome c_3 on the electrode were denatured states.

The ability to control the enzymatic activity by an external easily adjustable parameter is often the ultimate goal. This has been achieved, for instance, by voltammetry on the extrinsic domain of the membrane protein Succinate Deshydrogenase (SDH) adsorbed on a pyrolytic graphite electrode. At a given pH, the enzyme can be tuned to function either in the direction of succinate oxidation or fumarate reduction by scanning the potential of the graphite electrode. The physiological signification is somewhat difficult to extract since the study above does not concern the whole membrane-bound complex; the intrinsic domain not present in the study reported above might have a slight influence on the protein activity, e.g. additional electrochemistry from the electroactive "anchor" peptides.

An earlier study of urease adsorbed at a thermistor mercury electrode (tme) also shows a strong dependence of the enzymatic activity on the applied surface potential[29]. The enzymatic activity was monitored by measuring the temperature change induced by urea conversion by the enzyme:

$$(NH_2)_2CO + 3\,H_2O \rightleftharpoons 2\,NH_4^+ + HCO_3^- + OH^- \qquad D_r\mathbf{H} < \mathbf{0}$$

After immersion of the enzyme-covered thermistor mercury electrode in the urea solution, the system was left to reach a steady-state temperature. Then the potential was slowly stepped to -0.58 V vs. SCE (saturated calomel electrode); reduction occurred that made the temperature decrease denoting loss of activity. If the potential was subsequently slowly stepped to -0.40 V vs. SCE the temperature slowly jumped back to 78% of its original value suggesting partial restoration of the activity (Figure 4.3).

Activity changes were attributed to different conformational states during reduction and oxidation related to redox cycles of a disulfide bridge oriented towards the mercury surface. More recent high resolution crystal structure of urease from bacterial (prokaryotic) organisms such as *Klebsiella aerogenes*[31,32], *Bacillus pasteurii*[33] and *Helicobacter pilori*[34] did not report any structurally relevant disulfide bond. All three refined data sets reveal between 3 and 6 exposed cysteines at the protein surface, which accounts for the strong interaction with mercury. The distances between the cysteines range from 11 to 75 angstroms (average: 25 Å) and the residues are all regrouped within a same chain. Upon chemisorption to the mercury surface, a disulfide bridge could be formed then reduced, which leads to large-scale deformations and thus activity loss, and finally re-oxidized to partly restore the initial activity.

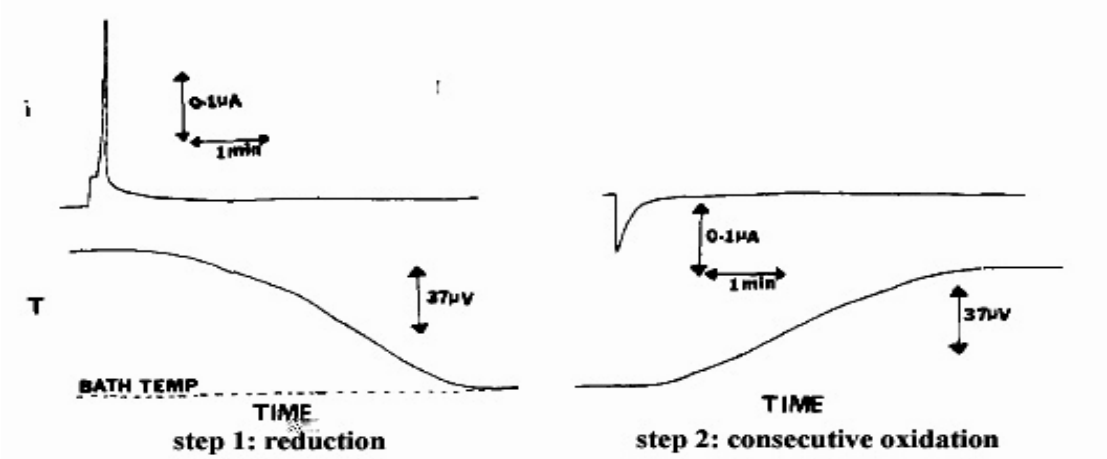

Figure 4.3: electrochemical control of the activity of urease adsorbed on mercury[29].

Almost all of the examples cited above underline the importance of disulfide bridges in electrochemical experiments. Consequently, it is useful to sum up here what several decades of investigations have reported about cysteine electrochemistry. Many proteins that have external surfaces cysteines are likely to adsorb on mercury or gold. In this case, it is possible to run a cyclic voltammogram and see the absorption reduction and oxidation waves most probably related to disulfide bridges electrochemistry. One can remember the value of the cathodic peak potential, E^p_c: -0.58 V *vs.* SCE (-0.33 V *vs.* NHE) for urease on mercury. Another study reported -0.28 V *vs.* SCE for the half-wave adsorption potential of certain subclasses of human IgG immunoglobulins – the following diffusion wave half-wave potential was -0.48 V *vs.* SCE[35].

1.3 Interest of SECM to study electric-field dependence of enzymatic activity

Direct electrochemistry on immobilized or surface-adsorbed redox enzymes that contain a redox active co-substrate linked to their 3-dimensional structure like flavin adenosine dinucleotide (FAD) in glucose oxidase is not possible[36] since the electroactive FAD domain of glucose oxidase is buried > 13 Å into the 3-dimensional structure[37]. Early experiments carried out by cyclic voltammetry in a 1 mg/mL solution of glucose oxidase from *Apsergilus niger* (Sigma-Aldrich, Saint-Louis, MO) in 20 mM phosphate buffer at pH = 5.7 with 0.1 M K_2SO_4 in the

absence and even in the presence of 8 M urea to force the release of the FAD moiety as the protein gets denatured did not show the expected reduction peaks of FAD.

For the following reasons, the only ways to make electrochemical measurements on such a system are to use mediators in solution that will react with the redox enzyme by perturbating its usual redox cycle[38], chemically linking another electroactive domain like ferrocene-derivatives to the enzyme without modifying its structure[39] or wiring the active site with an electroactive molecule grafted to a polymer matrix deposited on the electrode[40]. One of these methods will have to be chosen if one wishes to measure the activity of glucose oxidase immobilized on a surface.

In the feedback mode of SECM, a micrometric probe electrode (ultramicroelectrode (UME)) – consisting of a 25-µm diameter pure metallic disk inlaid in borosilicate glass (diameter ≈ 125 µm) for insulation purposes – is approached to a surface by piezoelectric elements with a vertical resolution of about 0.01 µm[41]. The probe is held at a potential at which a reversible redox couple called mediator, e.g. ferrocenemethanol, at a concentration of about 1 mM is oxidized (or reduced) in the steady-state regime of the hemispherical diffusion. As the surface draws nearer, several situations can occur depending on the nature of the approached surface and the potential applied to the probe electrode (tip). The tip current is measured as a function of the distance traveled by the piezoelectric elements until the surface is sensed. If the surface is a conductor, e.g. gold or highly-oriented pyrolytic graphite (HOPG), and held at a potential for which the mediator oxidized (reduced) at the tip can be reduced (oxidized) back, the current measured at the tip, i_T, will increase from its value far away from the surface, i_T^{∞}, when the distance reaches the value of approximately *2a* where *a* is the radius of the probe electrode disk. This is observed because when the tip gets close enough of the surface the mediator oxidized at the tip gets partly reduced back at the surface, which goes against the steady-state regime of mediator oxidation and increases the current measured at the tip. This situation is called *positive feedback* (Figure 4.4a).

Similarly, when an insulating surface, e.g. a glass slide or a nylon disk, is approached in the feedback mode of SECM, the current measured at the tip, i_T, will increase from its value far away from the surface, i_T^{∞}, when the distance reaches the value of approximately *2a*. This is explained by hemispherical diffusion modifications in the vicinity of the surface. Indeed, because of the insulating glass sheath around the probe electrode disk, hemispherical diffusion of mediator from

the solution bulk to the electrode is hindered by the presence of the surface (blocking effect), which decreases the current measured at the tip. This situation is called *negative feedback* (Figure 4.4b). In any case, the current measured far away from the surface, i.e. 10 to 15 times the diameter of the disk electrode *a*, where the mediator is oxidized (or reduced) in the steady-state regime of hemispherical diffusion is given by[41]:

$$i_T^{\infty} = 4nFDaC^* \qquad (7)$$

n is the number of electrons transferred. *F* is the Faraday constant. *D* is the diffusion coefficient of the mediator. *a* is the disk radius and C^* is the bulk concentration of the mediator.

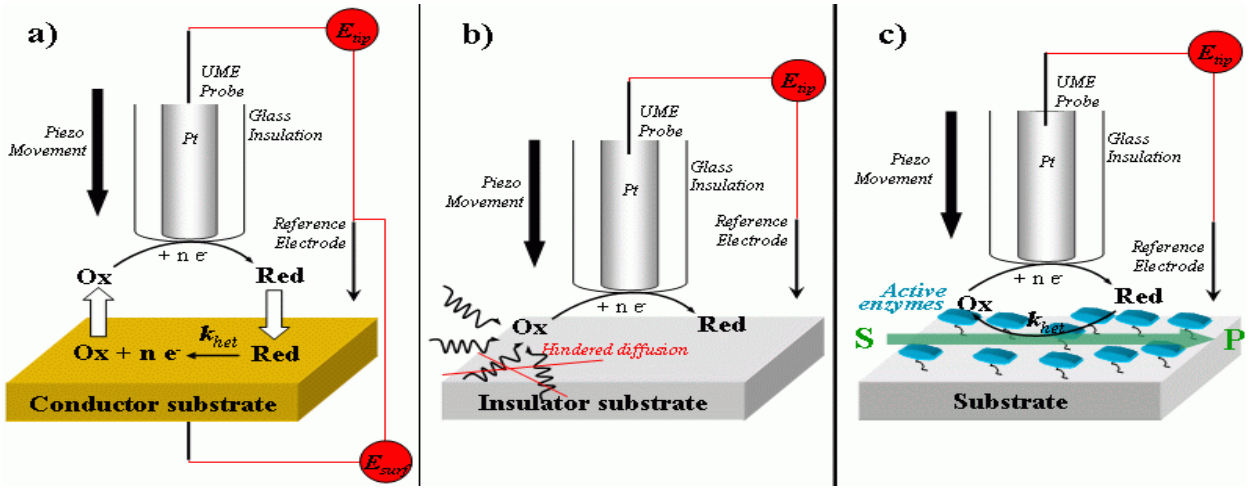

Figure 4.4: different situations encountered in the feedback mode of SECM: positive feedback on a conductor (a), negative feedback on an insulator (b) and the mixed situation of an active redox enzyme immobilized or adsorbed on an insulator-like substrate (c). More details are given in the text.

In the mixed situation where a redox active enzyme like glucose oxidase is either adsorbed or chemically immobilized on an insulator substrate for instance (Figure 4.4c), a mixed approach curve is observed as the surface is approached in the feedback mode of SECM in the presence of a mediator and when the substrates of the enzyme are added. Hindered diffusion predicts that negative feedback is observed when the surface is approached. This is indeed the case when no enzyme substrate is added to the electrolyte solution. However, as soon as the enzyme substrate is added, the observed curve shows an increase of the tip current from the bulk value, $i_T^{¥}$, followed by the usual decrease expected for an insulating surface. This can be explained by the activity of the enzyme taking place at the surface when the tip gets close enough[42]. In the case of glucose oxidase, for example, the catalytic cycle can be simplified into:

k_1

$$GOD^{oxidized} + \beta\text{-D-glucose} \underset{k_{-1}}{\rightleftharpoons} [GOD^{reduced}\ldots\text{D-glucose}]^{\#} \quad (8.1)$$

$$[GOD^{reduced}\ldots\text{D-glucose}]^{\#} \xrightarrow{k_2} GOD^{reduced} + \text{D-gluconolactone} \quad (8.2)$$

$$GOD^{reduced} + O_2 \xrightarrow{k_3} GOD^{oxidized} + H_2O_2 \quad (8.3)$$

In the presence of a 1-electron reversible mediator like ferrocenemethanol ($[FcMeOH]^+$/FcMeOH) and in anaerobic conditions where dissolved O_2 is removed from the solution, equation (8.3) is replaced by:

$$GOD^{reduced} + 2\,[FcMeOH]^+ \xrightarrow{k_4} GOD^{oxidized} + 2\,FcMeOH + 2\,H^+ \quad (8.4)$$

Consequently, the catalytic activity of glucose oxidase can regenerate part of the mediator molecules oxidized by the tip and increase the measured tip current from the bulk value, i_T¥. However, when the tip gets even closer to the surface, hindered diffusion will prevail and the usual negative feedback curve will be observed. In order to be able to observe positive feedback from the enzyme, the maximum catalytic rate k_{cat} must be of the order of the mediator diffusion velocity to the electrode.

As exposed above, the SECM feedback method allows the measurement of local heterogeneous rate constants over only a few molecules. The probed area is only determined by the size of the probe used. A 25-μm diameter platinum disk was chosen as a compromise between a small probed area and a detectable signal. The 25-μm-diameter platinum disk tip is prepared by heat-sealing a platinum wire into a borosilicate glass capillary, closed at one end with a butane/O_2 flame, under slight vacuum with a resistively heated nickel coil following standard procedures previously described[41]. The tip is then successively polished with 1 μm, 0.3 μm and 0.05 μm alumina and sharpened with grit paper until the RG, i.e. the ratio of the radius of the surrounding glass to the radius of the metallic disk electrode, reaches a value between 3 and 5. Such tips are then tested in a 1 mM ferrocenemethanol and 0.1 M KCl solution until the typical sigmoidal-shaped steady-state voltammogram is obtained. If needed, the electrode is re-polished with alumina until the hysteresis between forward and reverse scans in the voltammograms disappears. The tip is ultrasonicated in pure low conductivity (high resistivity) water before use in SECM to remove any alumina particle still adsorbed on the electrode surface.

The interest of the glucose oxidase system in SECM to investigate DC electric field effects on enzymatic activity comes from the already abundant literature available on that topic[42,43,44].

2. Strategy used with the glucose oxidase system

Glucose oxidase from *Aspergilus niger* (EC 1.1.3.4) is a dimeric protein with a molecular weight of 150,000 kDa that contains two tightly bound FAD cofactors[45] (one per monomer) and can be obtained as a stable lyophilized powder from Sigma-Aldrich. It was used as received and the activity in bulk conditions was occasionally checked by UV-visible spectrophotometry with *o*-dianisidine (Sigma), D-glucose (Aldrich) and horseradish peroxidase (Sigma) according to the usual method[46].

2.1 Preliminary result

Glucose oxidase was deposited on a glass slide (Firsher Scientific, Pittsburgh, PA) cleaned in 70/30 piranha[50] solution heated to 80 °C from a 5 mg/mL solution in 20 mM phosphate buffer at pH = 7. The slide was left to dry in ambient air until a thick film of proteins was clearly visible. Only α-D-glucose is available (Aldrich) but the enzyme has a strong selectivity for ß-D-glucose[45]. β-D-glucose can be prepared by dissolving α-D-glucose in water and allowing the mutarotation of glucose to reach its equilibrium for at least 4 hours. This yields a solution containing 63.6% β-D-glucose at 25 °C[47]. Then, the slide was approached in the SECM setup with a 25-μm diameter platinum tip in 20 mM phosphate buffer at pH = 5.8 with 0.1 M NaCl, 1 mM ferrocenemethanol and 50 mM D-glucose.

The first approach curve showed almost pure positive feedback because of the large coverage of such a dried enzyme film. But, upon the subsequent approach curve at 1 μm/s, the signal returned to a negative feedback profile expected on a clean glass surface. The film was no longer visible on the glass slide.

This shows that a stable chemical immobilization procedure is needed to allow longer investigations.

2.2 Immobilization chemistry

Glucose oxidase was initially immobilized on glass slides and nylon-66 disks (Durethan® A-30, Bayer Corporation, Pittsburgh, PA) because high yields were needed to study the SECM response. Since one wishes to study the dependence of the enzymatic activity on an external DC-electric field, the protein has to be chemically bound to a metallic conductor. Thin film gold (100 nm) deposited by vacuum evaporation on glass slides with a thin chromium pre-layer (5-7 nm) to improve gold adherence was chosen because of the available detailed results on alkanethiolate self-assembled monolayers (SAM) chemistry on gold or, to a lesser extent platinum and mercury[48].

2.2.1 Immobilization on glass slides

The immobilization procedure on glass consists of essentially three steps and actually rests on the functionalization of the glass surface by silane molecules, i.e. silanization[49].

2.2.1.1 Silanization

3-aminopropyltriethoxysilane (Aldrich) was used to functionalize the glass surface with amine $-NH_2$ functions. When properly cleaned and treated by immersion in 70/30 piranha[50] solution at 80 °C glass surface displays a large number of hydroxylated silicon groups that are able to react with the Si moiety of the silane molecule by a hydrolization reaction[51]. In this case, it is easy to understand the reaction has to be carried out in anhydrous solutions.

1 cm x 2 cm glass slides were cleaned with piranha solution for 15 minutes, rinsed with deionized Milli-Q™ water (18 MΩ.cm) and dried in a 120 °C oven for 1 hour prior to use. They were then immersed in an argon-degassed 2% (v/v) 3-aminopropyltriethoxy silane in ACS grade acetone for 12 to 24 hours at room temperature inside a desiccator filled with $CaCl_2$ to reduce the humidity. They were then thoroughly rinsed with ACS grade acetone and deionized water.

Glass slides silanized according to this procedure were characterized by contact angle measurements with a 10 µL deionized water drop. The contact angle after the silanization step was $q_1 = 53 \pm 1°$ whereas the contact angle was not measurable immediately after treatment with the piranha solution, i.e. $q_0 < 5°$. This value is consistent with the literature[52].

2.2.1.2 Cross-linking

The glass slide now has available amine groups that can react with glutaraldehyde, a molecule possessing two aldehyde groups on each end. The glutaraldehyde solution is prepared from an 8% electron microscopy grade aqueous solution stored in ampoules under argon and diluted to 4% (v/v) with 20 mM phosphate buffer at pH = 7.3. The slides are immersed in the solution for 2 hours at room temperature in a $CaCl_2$ desiccator. They were then rinsed with 100 mM carbonate buffer at pH = 10. This higher pH was chosen to prevent hydrolysis of the newly formed amide bonds between the surface and the linker molecule.

Contact angle measurements performed on such glass slides gave an angle $q_2 = 35 \pm 1° < q_1$. This value is lower than that for silanized glass slides since glutaraldehyde is a hydrophilic molecule. The value suggests that the coverage by glutaraldehyde is only partial otherwise a lower value would have been measured. Moreover, such glass slides turned purple after treatment with a drop of Schiff's reagent or fuchsin sulfite (Sigma) whereas silanized glass slides remain colorless. This suggests the presence of free aldehyde functions on the glass surface.

2.2.1.3 Enzyme coupling

In this final step, the glass slides were immersed in a 5 mg/mL solution of glucose oxidase in 20 mM phosphate buffer at pH = 7.9 for 16-20 hours at room temperature in the $CaCl_2$ desiccator. This step allows the coupling of the enzyme with the surface by creation of an amide bond between the free aldehyde moiety of the glutaraldehyde layer and amine groups from lysine residues of the protein surface. An examination of the 3-dimensional X-ray structure of glucose oxidase from *Aspergilus niger* shows 27 accessible residues on the surface of the protein. This means that this immobilization procedure does not allow selecting a preferred orientation for the

enzyme on the surface. The slides were finally rinsed with 20 mM phosphate buffer at pH = 5.7 and stored in the same buffer for no more than 2 hours before SECM experiments.

2.2.2 Immobilization on nylon disks

Immobilization on nylon was performed through a modified Morris O-alkylation procedure[53]. It consists of three steps.

Nylon is a polyamide molecule; the amide bond cannot react if it is not activated. Moreover, the samples received are probably covered with protective layers that need to be dissolved. This is achieved by ultrasonication (40 kHz) for 15 minutes in several organic solvents – methanol, acetone and dichloromethane successively – and deionized Milli-Q^{TM} water. The activation is done by immersion in a 0.1 M solution of triethyloxonium tetrafluoroborate (TOTFB) in dichloromethane for 5 minutes at room temperature. The disks are then rinsed with methanol and immersed in a 1 M solution of 1,4-diaminobutane in 100 mM carbonate buffer at pH = 9.8 for 16 hours at room temperature in a sealed glass beaker. The surface of the nylon disk is now functionalized with –NH2 amino group. The following steps are identical to the procedure to immobilize glucose oxidase on glass slides.

2.2.3 Immobilization on thin gold films

The immobilization on gold is different form that on glass and nylon. It contains three steps[54] and the electrode functionalization has to be carried out with alkanethiolates instead of organosilanes[48].

2.2.3.1 Formation of the self-assembled monolayer (SAM)

The thin gold films are cleaned by immersion in 70/30 piranha solution at 80 °C for 15 minutes and thorough rinsing with deionized Milli-Q^{TM} water. They are then immersed in a 1 mM 16-mercaptohexadecanoic acid solution in absolute ethanol for 12 to 24 hours at room temperature in a sealed compartment. In principle, the SAM is formed after a few minutes but leaving the samples in the solution for much longer results in better structured layers since an equilibrium with the thiol solution is ultimately established[48]. The surfaces are then thoroughly

rinsed with absolute ethanol and 20 mM phosphate buffer at pH = 5.7. The efficiency of the SAM formation can be checked by cyclic voltammetry in a 1 mM ferrocenemethanol solution with 0.1 M KCl since such a long chain (16 carbon atoms) will definitely prevent electron transfer from a dissolved electron-donor to the gold surface if the coverage is high enough (passivation of the gold electrode). Such a voltammogram is shown in Figure 4.5.

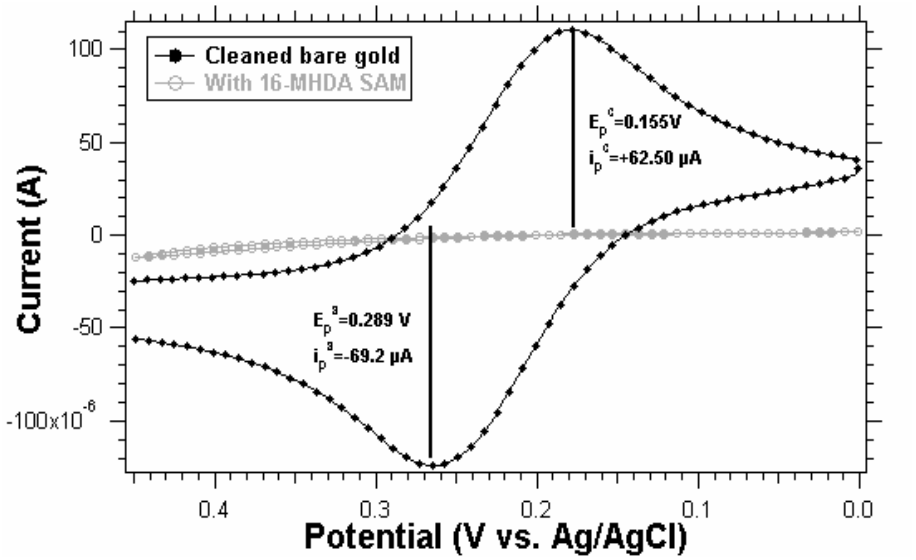

Figure 4.5: Passivation of the gold electrode to electron transfer: voltammograms in 1 mM ferrocenemethanol and 0.1 M KCl of a bare cleaned thin film gold electrode (?) and the same electrode after 24 hours immersion in 1 mM 16-mercaptohexadecanoic acid (16-MHDA) (?). The geometric electrode area is 0.6 cm^2.

2.2.3.2 SAM activation and enzyme coupling

The thiol used is terminated by a –COOH acid function that we further wish to condense to an $–NH_2$ amine group from a surface lysine residue of the enzyme. This reaction is thermodynamically impossible since the pH diagrams of an amine and a carboxylic acid are disjoint. Consequently, the acid group needs to be activated with chemical groups that enhance the electrophilic character of the C atom of the acid function. This can be done with N-(3-dimethylpropyl)-N'-ethylcarbodiimide (EDC)[55] and N-hydrosuccinimide (NHS)[56].

For this purpose, the gold surfaces are immersed in a 75 mM EDC and 25 mM NHS solution in 20 mM phosphate buffer at pH = 7.3. Higher pH values would be preferable to preserve the basic character of amine groups, but EDC and NHS are unstable at pH values greater than 7.5 for 2 hours at room temperature in a sealed compartment.

The surfaces are not rinsed and immediately placed in a 5 mg/mL solution of glucose oxidase in 20 mM phosphate buffer at pH = 7.9 for 12 to 24 hours at room temperature in a sealed

compartment. They are then rinsed with 20 mM phosphate buffer at pH = 7.0 and stored in the same buffer for no more than 2 hours prior to use in the SECM.

2.3 Feedback responses obtained

2.3.1 Comparison between immobilization strategies

Figure 4.6 shows the comparison of feedback responses obtained by approaching samples prepared by the different procedures described above in the SECM feedback mode using ferrocenemethanol as a mediator (1 mM) in the presence of 0.1 M KCl and 50 mM glucose. In the case of gold, a voltammogram in the same solution (without glucose) was always recorded prior to any SECM approach curve to make sure the gold electrode was properly passivated for electron transfer by the self-assembled monolayer.

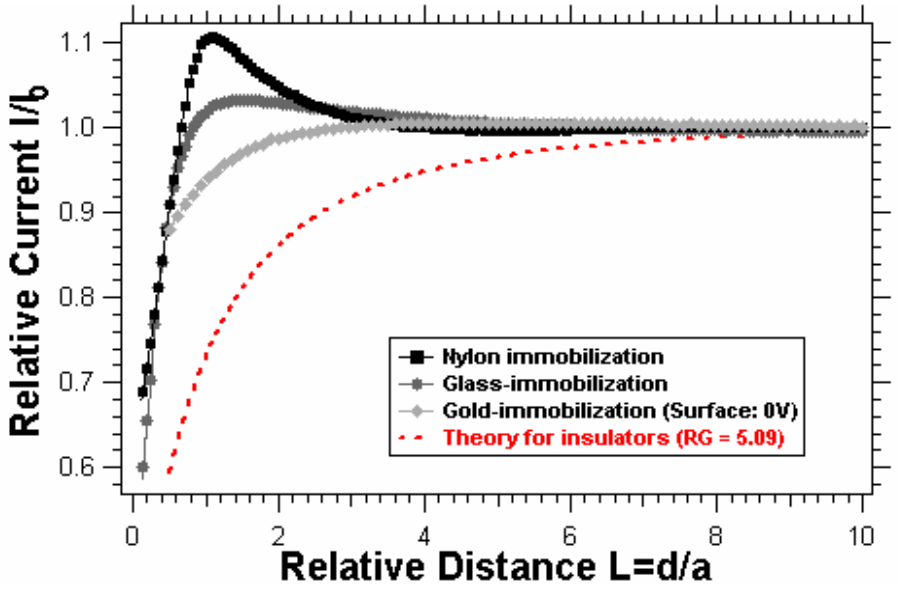

Figure 4.6: comparison of feedback responses obtained from glucose oxidase immobilized on nylon disks (¦), glass slides (?) and on a thin gold film (?). The electrolyte is 1 mM ferrocenemethanol with 0.1 M KCl and 50 mM D-glucose in 20 mM phosphate buffer at pH = 5.9. The tip is held at 0.4 V vs. Ag/AgCl. The gold surface is held at 0 V vs. Ag/AgCl. The dashed line is the theoretical curve on an insulator (Tip RG = 5.09).

For each immobilization strategies, the recorded approach curve corresponding to the change in the reaction rate of ferrocenemethanol oxidation deviates from the negative feedback response obtained on a bare insulator. This suggests that some ferrocenemethanol molecules are

regenerated (reduced back) at the surface where a heterogeneous process occurs It is characterized by a catalytic rate *k* in $cm.s^{-1}$. As the distance between the microelectrode (tip) and the surface reaches twice the radius of the exposed Pt electrode, the current increases because the surface reduction of ferrocenemethanol starts to overcome its steady-state oxidation at the tip state regime at the tip and the diffusion process from the tip to the surface.

The procedure on nylon disks seems to have the highest immobilization yield. Simulations by a two-dimensional finite difference method in cylindrical coordinates of SECM feedback approach curves are available and empirical analytical expressions depending on the tip glass to platinum radius ratio can be obtained[41]. They were used to fit the curves presented in Figure 4.6. The results are summarized in Table 1.

Table 1: fitted heterogeneous rate constants of glucose oxidase chemically immobilized on several surfaces

Surface	$i_T^{¥}$ (nA)	Fitted *ka/D*	*k* ($cm.s^{-1}$)
Nylon	2.529	1.70 ± 0.05	$5.54\ 10^{-3}$
Glass	2.921	0.387 ± 0.002	$1.26\ 10^{-3}$
Gold	3.924	0.136 ± 0.002	$0.44\ 10^{-3}$

The diffusion coefficient of ferrocenemethanol in 20 mM phosphate buffer at pH = 8.2 at a planar gold electrode (A = 0.56 cm^2) has been determined[57]: $D = 4.08\ 10^{-6} \pm 0.02\ cm^2.s^{-1}$. The tip radius, *a*, is 12.5 µm. We can therefore extract the heterogeneous rate constant of immobilized glucose oxidase. These values agree well with other reported values of the heterogeneous rate constant of immobilized glucose oxidase[42].

However, the comparison with reported bulk values of glucose oxidase activity[58] is difficult since the heterogeneous value measured by SECM depends on the enzyme coverage inside the area probed by the tip as well as on what fraction of the enzymes present in that area are really active (fully folded, active site easily accessible,...).

2.3.1 pH dependence of GOD activity

In order to relate the observed activity with reported values in bulk conditions, the pH dependence of the measured immobilized activity was studies. Immobilization on nylon disks

was chosen since it corresponds to the highest immobilization yield. The electrolyte was an argon-degassed solution of ferrocenemethanol with 0.1 M KCl with different buffers as summarized in Table 2:

Table 2: Composition of the different electrolytes to study the pH dependence of the activity of glucose oxidase immobilized on nylon disks

Measured pH	Buffer composition	C^* (ferrocenemethanol)
3.92	100 mM acetate	1.255 mM
5.97	20 mM phosphate	1.255 mM
7.24	20 mM phosphate	1.912 mM
9.78	100mM carbonate	1.226 mM

D-glucose is added to a final concentration of 50 mM. The tip is held at 0.4 V vs. Ag/AgCl (sat. KCl) where the steady-state regime of ferrocenemethanol oxidation under hemispherical diffusion occurs and the surface is approached at 2 μm/s. The cell is flushed and rinsed with the buffer that will be used next between each experiment. The resulting SECM approach curves are shown in Figure 4.7. The curves are compared to the available theoretical expression of the feedback current from an insulator with a 25-μm diameter platinum tip with a RG ratio of 5.09[59]. The tip used had an RG of approximately 5 under the optical microscope.

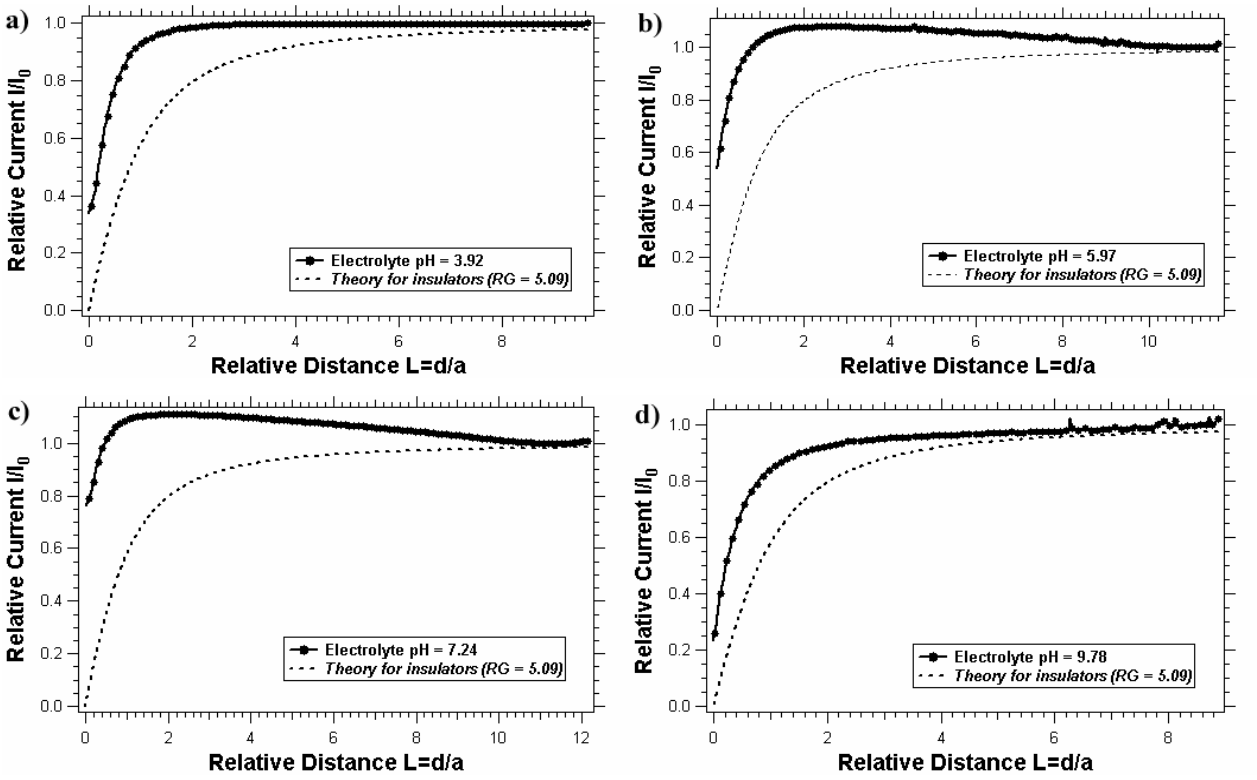

Figure 4.7: Evolution of SECM feedback curves at pH = 3.92 (a), 5.97 (b), 7.24 (c) and 9.78 (d). A maximum of the measured activity occurs around pH = 7.

An activity peak appears around pH = 7. This value can be compared to the bulk value of glucose oxidase activity in aerobic conditions[60]. The authors decompose the mechanism in four steps and individually measure each constant either directly by spectrophotometric assay or indirectly by the use of inhibitors:

$$E_{ox} + S \underset{k_{-1}}{\overset{k_1}{\rightleftharpoons}} [E_{ox}..S]^{\#} \xrightarrow{k_2} E_{red} + P \qquad (9.1)$$

$$E_{red} + O_2 \xrightarrow{k_4} [E_{ox}..P2]^{\#} \xrightarrow{k_5} E_{ox} + H_2O_2 \qquad (9.2)$$

To compare to our case, the constant k_5 is of particular interest. Its value also displays a peak around pH = 6.0 as can be seen in Figure 4.8.

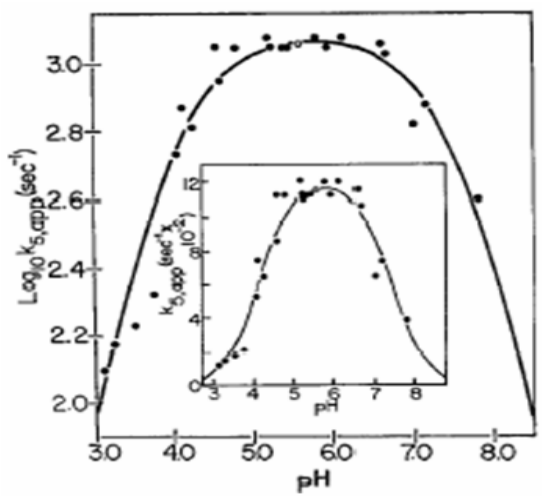

Figure 4.8: The pH dependence pf k_5. Data are from spectrophotometric turnover measurements with D-glucose (?). The lines were calculated with k_5 = 1200 s^{-1}. The temperature was 25 °C; the ionic strength is 250 mM. The insert shows the non-semilog data plot. Adapted from reference 60.

The difference between the values of the pH at the maxima for immobilized and free GOD is equal to about one pH unit. The difference can arise from the proximity of the surface that has a non-zero surface charge since some amino groups might still be free. Moreover, it should be noted that the experiment on immobilized GOD, unlike the bulk measurement, is performed under anaerobic conditions where the enzyme is forced to use the mediator in the second step. However, the presence of a maximum as well as the difference of only one pH unit shows that the measurement of immobilized activities by SECM is a valid technique since the feedback curves obtained on surface bound glucose oxidase reproduce the evolution of the activity with pH in bulk conditions.

2.4 Electric field dependence

2.4.1Expected effects

Before experimentally investigating electric field effects, a quick look at the 3D structure of the glucose oxidase type used shows that two types of effects can be expected; non-faradaic effects like those from changes in the local environment (pH) and faradaic (charge transfer) reactions involving structural disulfide bridges.

Figure 4.9: Position of the disulfide bridge (yellow) and the free thiol (orange) of Glucose Oxidase from *Aspergillus niger*. Figure generated by RasMol (Molinaro et al, UC Berkeley) from the original refined atom coordinates file (Brookhaven Protein Data Bank accession number 1CF3[61]).

Glucose Oxidase from *Aspergillus niger* has a structurally crucial disulfide bridge as well and a free internal cysteine that might have an essential catalytic role[61] as depicted in Figure 4.9. One could monitor the changes in the SECM feedback responses when the potential of the surface on which the enzyme is immobilized is stepped to the values reported earlier to reduce cysteine bridges, i.e. observe the effect of a wide-range conformational change followed by a large decrease in the activity.

Figure 4.10 shows the results of an experiment that validates the above assertion. Glucose oxidase from *Aspergilus niger* was immobilized on glass according to the procedure exposed in section 2.2.1. The surface was approached in the SECM feedback mode in a 1 mM ferrocenemethanol solution with 0.1 M KCl without and with 50 mM glucose. The experiment gave the usual observed profile. Then the glass slide was immersed in a 1.5 M β-mercapthoethanol solution in 20 mM phosphate buffer at pH = 5.7 for 20 minutes and thoroughly rinsed with the same buffer. Then the SECM approach curve was repeated under the same conditions. This time, the profile was purely that of negative feedback. This shows that reducing the disulfide bridge is lethal for the glucose oxidase activity. One wishes now to reproduce that experiment by applying a potential on the surface as the enzyme is immobilized on gold.

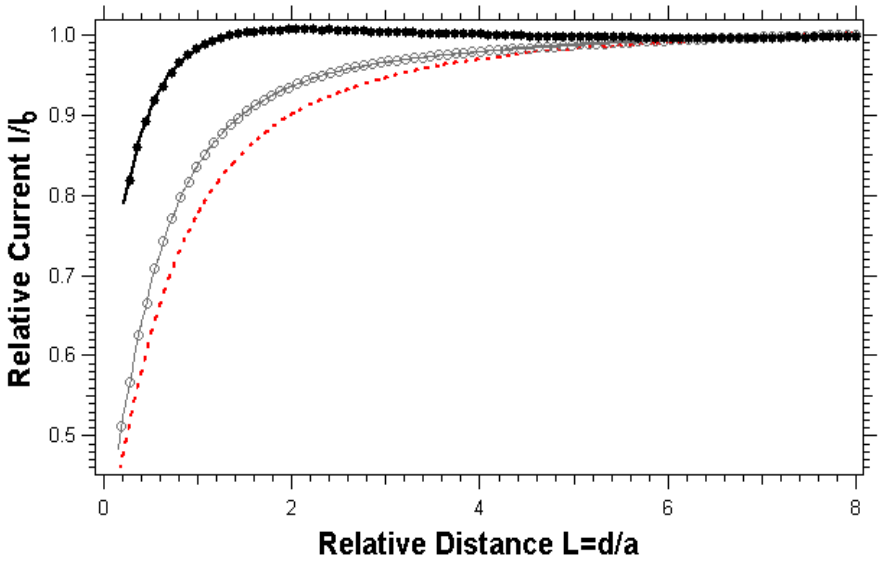

Figure 4.10: SECM approach curve on glass-immobilized glucose oxidase in the presence of 50 mM glucose (?) in a phosphate buffer at pH = 5.9 and after immersing the slide in 1.5 M b–mercapthoethanol for 20 minutes (?). The tip was held at 0.4 V vs. Ag/AgCl. The dashed curve is the expected response on an insulator for a tip with an RG of 5.09. Glucose activity is lost after reduction of the structurally essential disulfide bridge.

2.4.2 Results

Surface potentials from -0.8 V to + 0.8 V vs. Ag/AgCl (sat. KCl) were tested with 0.1 V increments. Priority was given to potentials close to the reported -0.58 V vs. SCE cathodic peak potential for disulfide bridges reduction (section 1.2.2). Several values of pH ranging from 3.9 to 9.8 were also tested. Systematically, the curve was approached at 2 µm/s with a 25-µm diameter Pt tip sharpened to a RG ratio around 5 in an electrolyte containing 1 mM ferrocenemethanol and 0.1 M KCl in the specific buffer. The first approach curve was recorded. Then, D-glucose was added to a final concentration of 50 mM.

Figure 4.11 and Figure 4.12 show a typical response for several values of the surface potential tested at two different pH values of the buffer solution. Apart from the effects of the changes in pH discussed in more details in sections 2.3.1 and 3.1 to 3.2, no significant measurable difference could be observed in the approach curves. When overlaid, no distinction can be made between experiments where only the gold surface potential was varied. The tip is held at 0.4 V vs. Ag/AgCl in each case to ensure a steady-state regime of ferrocenemethanol oxidation.

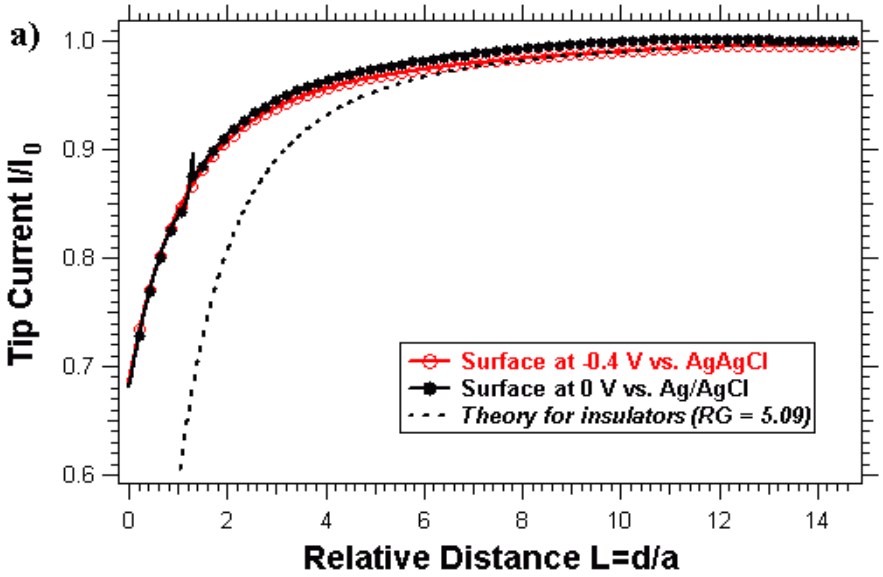

Figure 4.11: Typical observed dependences on applied surface potential of gold-immobilized GOD activity. The potential is stepped from 0 V (full circles), to -0.4 V (empty circles). The theoretical expected approach curve in the case of negative feedback on an insulator for an RG ratio of 5.09[59] is shown as guide to the eyes (dashed line). Experiments are carried out in 20 mM phosphate buffer at pH = 7.2. The tip is held at 0.4 V vs. Ag/AgCl (sat. KCl).

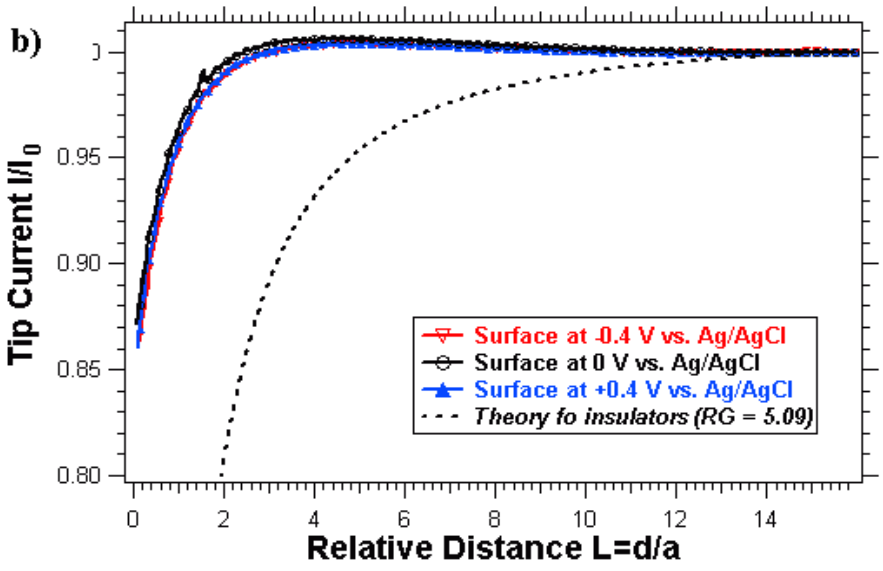

Figure 4.12: typical observed dependences on applied surface potential of gold-immobilized GOD activity. The potential is stepped from 0 V (empty circles), to -0.4 V (empty triangles) and to +0.4 V vs. Ag/AgCl (full triangles). The theoretical expected approach curve in the case of negative feedback on an insulator for an RG ratio of 5.09[59] is shown as guide to the eyes (dashed line). Experiments are carried out in 100 mM carbonate buffer at pH = 9.8. The tip is held at 0.4 V vs. Ag/AgCl (sat. KCl).

The attempts made to investigate the effects of an externally applied DC electric field at the gold surface did not show any modulation of the Glucose Oxidase activity by the surface potential. Only effects due to a change of the pH of the buffer solution could be seen; they are due to the pH dependence of the overall glucose oxidation reaction catalyzed by Glucose Oxidase as well as to protonation/deprotonation equilibriums of the Self-Assembled Monolayer (SAM) used to bind the enzyme to the solid surface as explained in the next sections.

3. Limitations of the strategy used for glucose oxidase on gold

The non-dependence of the activity on the interfacial DC electric field needs to be explained. The next sections focus on the self-assembled layer that might be the cause of the results shown in Figure 4.12. Charge effects originating from the SAM layer are investigated by SECM approach curves as well as by impedance spectroscopy under different electrolyte conditions.

The system chosen to investigate interfacial electric field effects on enzymatic activity is extremely complex since there is a layer of variably charged flexible molecules chemisorbed on top of the electrode surface. The properties of the SAM layer could screen out the effects of an external electric field the enzymatic activity of immobilized glucose oxidase. Moreover, this screening depends on the electrolyte composition (ionic strength, pH...)

3.1 pH effect on feedback from SAM-treated gold

Similarly to the experiment reported in section 2.3.2, the pH dependence of SECM feedback approach curves was investigated. A thin film of gold (100 nm) deposited on glass in a vacuum evaporator with a pre-layer of chromium (7 nm) was first cleaned by immersion in 70/30 piranha solution at 80 °C for 15 minutes, rinsed with absolute ethanol and water, dried with pure argon and immersed in 2 mM ethanolic solution of 16-mercaptohexadecanoic acid for 24 hours at room temperature in a sealed dry glass environment. The slides were thoroughly rinsed by absolute ethanol and placed in the Teflon® cell of the SECM setup.

The 25-µm Pt tip with an RG ratio of about 5 was held at 0.4 V vs. Ag/AgCl throughout the approach curve. A voltammogram in a 1 mM ferrocenemethanol solution with 0.1 M KCl in the considered buffer was systematically recorded prior to SECM experiments to ensure efficient passivation to electron-transfer. The surface was held at 0 V vs. Ag/AgCl in the experiments presented, but no noticeable difference can be seen if the surface is held at -0.4 V or +0.4 V vs. Ag/AgCl. The results shown in Figure 4.11 are qualitatively interpreted in Figure 4.14.

A transition between negative feedback in acid solutions and positive feedback in alkaline conditions is clearly observed indicating changing properties of the SAM layer on the gold electrode. This can be explained by different protonation states of the acidic –COOH moiety of the alkanethiolate layer used; the pKa is around 6 for a free carboxylic acid in solution. Additionally, the pKa of a surface-bound ω-carboxyalkanethiol has been reported to be shifted to lower values due to stabilization of the unprotonated form by hydrogen bonding[62].

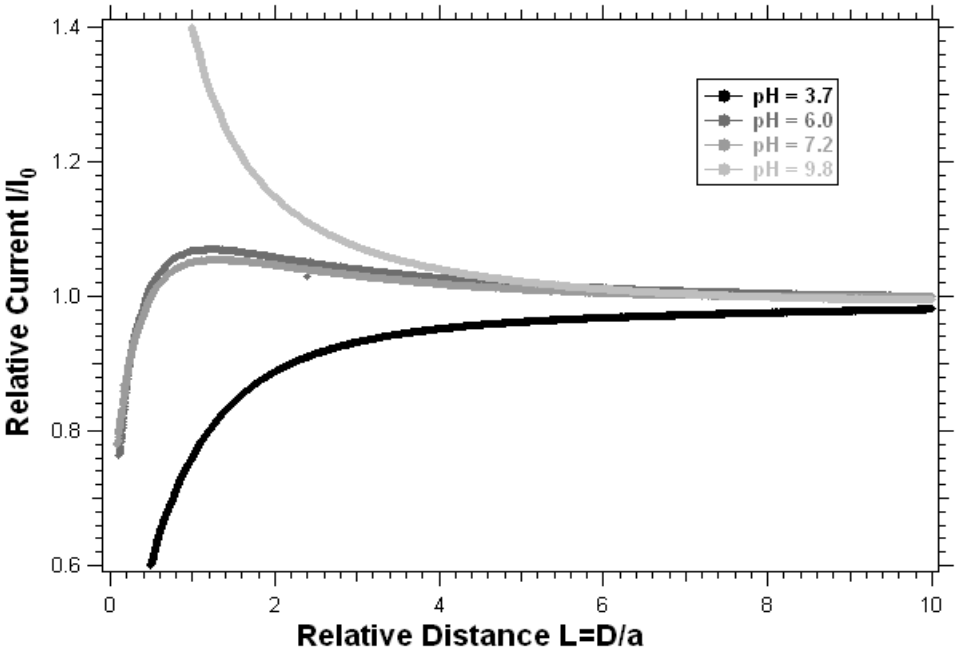

Figure 4.13: Effect of the change in pH on the SECM feedback repsonse recorded during an approach curve at about 1 µm/s as the surface is held at 0 V vs. Ag/AgCl. The result is the same f the surface is held at -0.4 V or +0.4 V vs. Ag/AgCl.

At low pH values (acid conditions), all –COOH groups present on the functionalized gold surface are protonated. There is no overall surface charge, the SAM layer is perfectly stacked by Van der Waals forces between the 15-carbon atoms long chain[48]. As the pH increases, a fraction

of the –COOH groups shifts to a negatively charged carboxylate state –COO^-. Electrostatic repulsion between neighboring carboxylate groups occurs and rearranges the SAM. The SAM layer is no longer rigidly held together by Van der Waals forces and large pinholes randomly located on the surface start to appear. Oxidized ferrocenemethanol molecules generated by the tip can now diffuse to the gold electrode though these holes and get reduced back to ferrocenemethanol creating a mixed situation of positive and negative feedback. Ultimately, in alkaline solutions, almost all the surface groups are deprotonated so that the holes in the SAM structure created by electrostatic repulsion between neighboring groups grow bigger. The passivation to electron transfer is lost; the positive feedback situation observed when approaching a bare gold electrode is met. Figure 4.14 summarizes the proposed explanation. This hypothesis has been proposed earlier[63,64] and will be investigated more precisely by impedance spectroscopy and cyclic voltammetry in the next section.

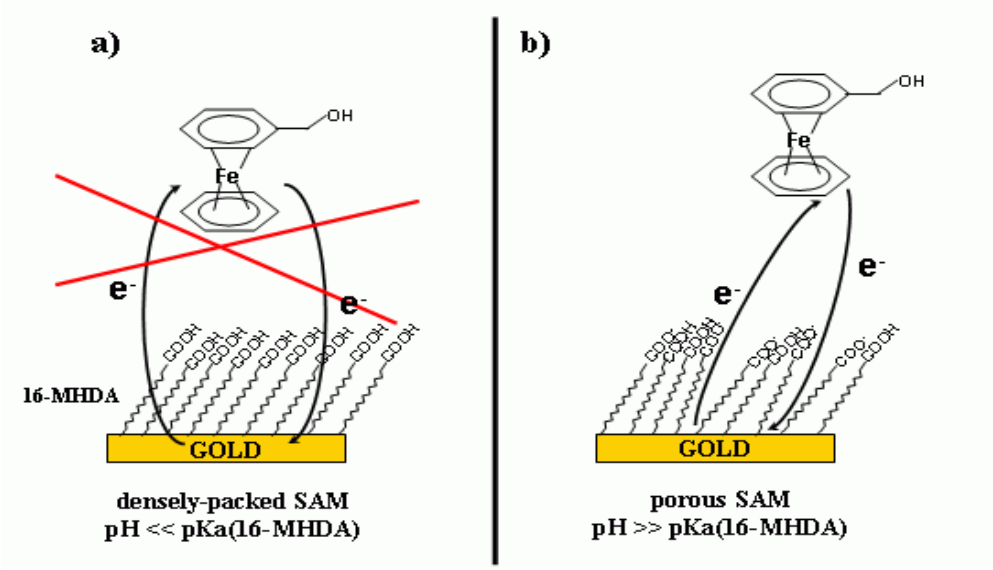

Figure 4.14: Schematic explanation of the observed transition of the feedback response between acid (a) and alkaline (b) conditions of the 16-mercaptohexadecanoic acid (16-MHDA) SAM on gold.

3.2 Impedance spectroscopy study of SAM-treated gold

Under a small sinusoidal excitation, an electrochemical cell can be described by the Randles equivalent circuit (Figure 4.15) with simple circuit elements in parallel since the current response is the sum of faradaic and double layer charging contributions[65]. The double layer capacitance

can be represented by a pure linear capacitance C_d (see Chapter 5 for details) but faradaic processes must be considered as a general impedance, Z_f, as their response may depend on frequency. The solution resistance R_W, or more likely the uncompensated resistance R_u between the working and reference electrodes, cannot be avoided.

The faradaic impedance can be decomposed in different ways. Two simple models are:

- A series of a pure resistance, R_s, and a pseudo-capacitance, C_s.
- A pure resistance to charge-transfer R_{ct} and another impedance term Z_W called the Warburg impedance and accounting for resistance to mass transfer.

The objective of impedance spectroscopy measurements is to determine the frequency dependence of R_s and C_s and relate it to real chemical or physical processes. For instance, the presence of a SAM on a metallic electrode can be treated by adding an additional capacitance C_{SAM} in series with the double layer capacitance and an additional resistance R_{SAM} in parallel[66]. Intuitively, in the case of an ionizable alkanethiol like 16-mercaptohexadecanoic acid, the capacitance will have a strong dependence on pH.

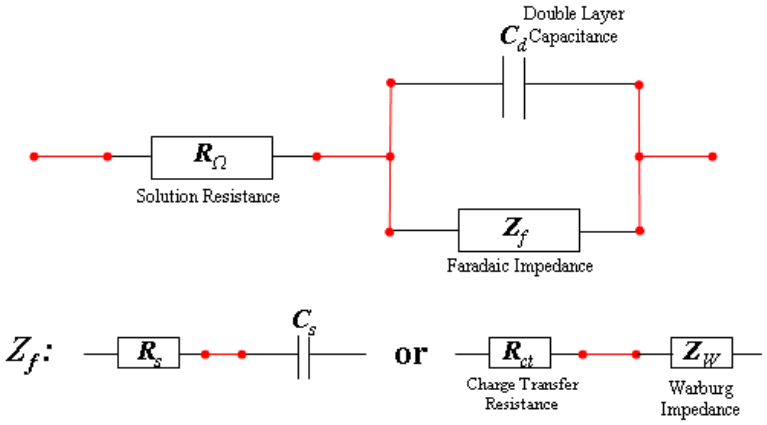

Figure 4.15: Equivalent Randles circuit representation of an electrochemical cell. The complicated faradaic impedance has two prevailing representations.

In our case though, only semi-quantitative information will be drawn since the equipment used for impedance measurements (CH Instruments 600A, Austin, TX) showed significant discrepancies with the expected calculated response for a simple real component parallel RC circuit.

3.2.1 pH effect

Similarly to section 3.1, the effect of pH change on a thin gold film evaporated on glass (100 nm, 7 nm Cr) treated with 16-mercaptohexadecanoic acid to form a self-assembled monolayer (SAM) was studied. Nevertheless, to ensure the SAM layer could sustain the high frequency signals (up to 100 kHz) of impedance measurements, the preparation of the SAM was slightly modified according to common procedures[67]. A first step was added where the gold surface – cleaned with 70/30 piranha at 80 °C – was immersed in a 1 mM thiol solution in absolute ethanol with 0.1 M $LiClO_4$ as the gold surface is maintained at a surface potential of -500 mV vs. Ag/AgCl (0.1 M $LiClO_4$ in ethanol) for the first hour and then left in the solution at open-circuit for an additional 12 hours at room temperature. This additional step is believed to yield more ordered thiol structures since applying a cathodic potential negative to the point of zero charge (pzc) slows down the initial adsorption phase allowing larger and more ordered domains to develop[67]. The gold surfaces are then taken out and rinsed with large amounts of ethanol and deionized Milli-Q^{TM} water before use in impedance measurements.

Table 3 summarizes the different electrolyte compositions (pH, ionic strength, supporting electrolyte) used for impedance measurements.

Table 3: Electrolyte composition and measured pH value for the different conditions used during the impedance measurements.

Measured pH	Buffer composition	*C** (ferrocenemethanol)	Supporting electrolyte
3.55	100 mM acetate	1.12 mM	0.1 M KCl
4.35	100 mM acetate	1.12 mM	0.1 M KCl
5.80	100 mM acetate	1.12 mM	0.1 M KCl
6.50	20 mM phosphate	1.12 mM	0.1 M KCl
6.99	20 mM phosphate	1.12 mM	0.1 M KCl
7.49	20 mM phosphate	1.12 mM	0.1 M KCl
8.04	20 mM phosphate	1.12 mM	0.1 M KCl
8.91	100 mM acetate	1.12 mM	0.1 M KCl
9.85	100 mM acetate	1.12 mM	0.1 M KCl
10.69	100 mM acetate	1.12 mM	0.1 M KCl

The excitation signal is a sine wave of amplitude 0.01 V RMS oscillating around the surface potential of 0.2 V vs. Ag/AgCl (sat. KCl), i.e. the half wave potential of ferrocenemethanol oxidation under similar conditions. Figure 4.16 shows the Nyquist diagrams obtained over the frequency range from 0.01 Hz to 100 kHz for different pH values.

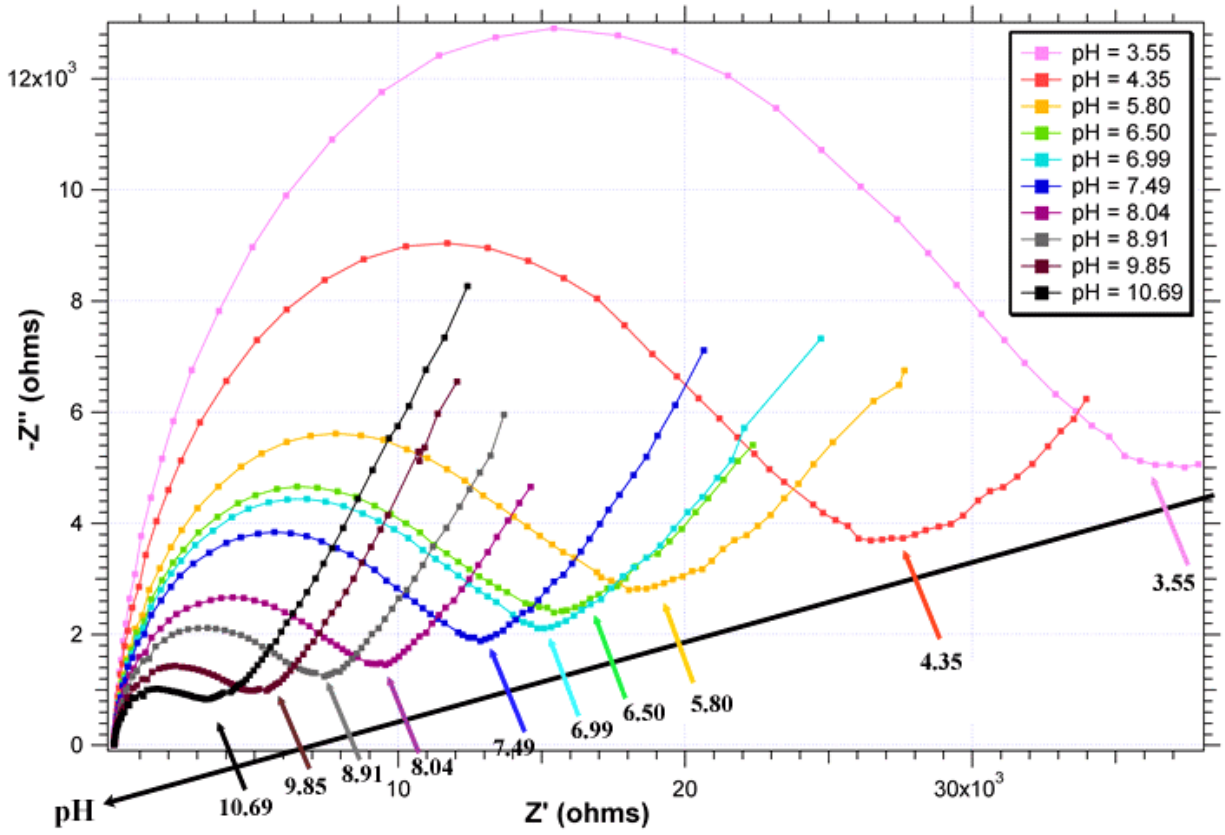

Figure 4.16: Nyquist diagrams of a SAM-treated gold thin film at different pH values. The arrow indicates the pH scale. The curve obtained for a bare cleaned gold thin film was similar to that obtained for pH = 10.69 but displayed the linear behavior except close the (0;0) point of the Nyquist diagram (frequency around 1 MHz) where a small semi-circle appeared. More details are given in the text.

The Nyquist diagram of a bare cleaned thin film gold surface taken under the same conditions showed the linear 45° behavior both in acid and basic media except at very high frequencies (~ 1 MHz) where a characteristic semi-circle appeared. Again, a clear transition is clearly visible in Figure 4.16; the impedance of the SAM-treated system slowly evolves towards that of the bare piece of gold as the pH is increased and the electrolyte gets more alkaline. The linear 45° behavior is dominant at high pH whereas the semi-circular behavior is dominant at low pH values in the frequency domain explored.

Since the precision of the instrument does not really allow it and since fitting a system with as many parameters as a model with associated simple electric components requires can lead to misinterpretations, only deviations from the expression of the Randles model for a bare electrode will be analyzed.

- In the Randles model, for a system in which the Warburg impedance is negligible, the semi-circle is centered on R_W (solution resistance) and its diameter is equal to R_{ct} (charge-transfer resistance). Therefore the semi-circle can be linked to kinetic control and electron transfer[65].

- In the Randles model, the linear 45° behavior is linked to mass-transfer control, i.e., for instance, diffusion of reactants to the electrode[65].

In the case of SAM-treated gold, one can easily conceive that the charge transfer resistance not only contains the resistance to heterogeneous electron transfer but also the resistance to tunneling through the monolayer. As the pH increases the diameter of the semi-circle part decreases because R_{ct} gets smaller. Since the same phenomenon is not observed on a bare gold electrode, the decrease in R_{ct} is due to a decrease in the resistance to tunneling through the SAM because more functional –COOH groups of the SAM get deprotonated. One can notice the asymmetry of the semi-circle; this suggests that the response at high frequency is different from that at lower frequencies. The Warburg impedance can therefore not be neglected. Simultaneously, the linear part prevails as the pH increases suggesting mass-transfer control at higher pH whereas the system is controlled by kinetics at low pH values. This shows that more ferrocenemethanol can diffuse to the electrode and get oxidized in alkaline conditions and reinforces the assertion made earlier.

The results obtained by impedance measurements are consistent with SECM feedback approach curves and the hypothesis sketched in Figure 4.14. Cyclic voltammetry was also performed to attempt to extract information on the pinholes created by progressive deprotonation of the surface groups (average size, density).

3.2.2 Investigating the SAM porosity changes by cyclic voltammetry

In parallel with the impedance measurements, cyclic voltammograms were taken at a rate of 100 mV/s for each pH prior to the impedance scan. Some resulting voltammograms, ranging from pH = 3.55 to pH = 10.69, are shown in Figure 4.17a. The first forward and reverse scans taken in a 1 mM ferrocenemethanol solution with 0.1 M KCl in the corresponding buffer are shown. If one roughly assumes, no faradaic process occurs at any pH value, the current difference between the first data point of the first forward scan and the last data point of the consecutive reverse scan can be interpreted as the current charging the double layer modified by the presence of the SAM. These values are shown in Figure 4.17b as a function of pH.

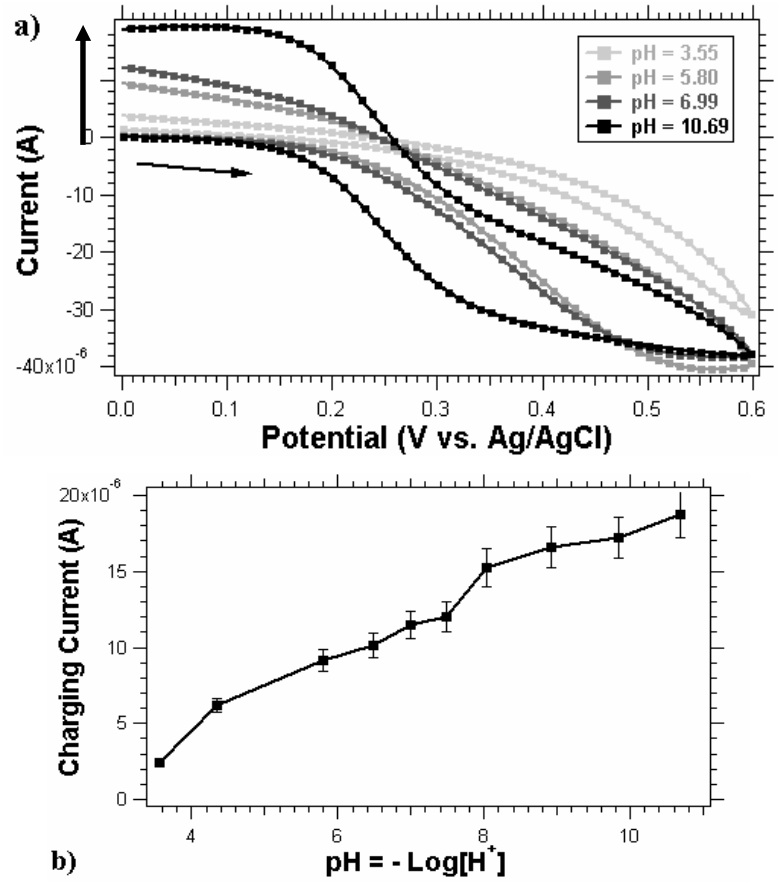

Figure 4.17: (a) 1st forward and reverse scans (100 mV/s) of the SAM-treated gold surface in 1 mM ferrocenemethanol with 0.1 M KCl in buffers ranging from pH = 3.55 to pH = 10.69. The arrow indicates the initial polarity. (b) The charging current (arrow) seems to increase with pH.

When the pH increases, the fraction of deprotonated COOH surface groups increases and a negative charge progressively builds-up at the SAM/electrolyte interface. That charge has to be compensated by an excess of positive charges (holes) at the electrode/SAM interface since the presence of the ionizable SAM adds an extra capacitance to the Helmholtz capacitance of the electric double layer on a bare gold surface (see Chapter 5). These considerations explain the evolution of the charging current (hysteresis between first forward and reverse scans).

More information on the changing porosity of the SAM layer with pH can be drawn by considering the diffusion occurring at microscopic active sites of a partially blocked electrode[68]. Savéant et al consider the limiting situation of the partially blocked electrode (coverage $q \approx 1$) described by an array of disc-type active sites regularly spaced by a distance of $2R_0$ larger than the disc diameter $2R_a$. They simplify the problem by considering only two possible values for the apparent standard rate constant k_S^{ap}:

- $k_S^{ap} = k_{S,0}^{ap} \neq 0$ at the active sites
- $k_S^{ap} = 0$ where the electrode is covered by the passivation layer

For high coverage values ($q \rightarrow 1$), the average distance between active sites becomes small compared to the diffusion layer thickness: $2R_0 << \left(\frac{DRT}{Fv}\right)^{1/2}$ where v is the sweep rate, D is the diffusion coefficient of the redox species and F is the Faraday constant. Under these conditions, if C^* is the bulk concentration of the redox species and S the total surface of the covered electrode, the voltammograms tend to have the shape of a polarogram with a plateau height equal to:

$$i_{\lim} = \frac{FSC^*D}{2R_0(1-q)} \qquad (10)$$

Simultaneously, if a is the electron transfer coefficient, the half-wave potential is given by:

$$E_{1/2} = E^0 + \frac{RT}{aF}\ln\left(k_{S,0}^{ap}\frac{2R_0(1-q)^2}{D}\right) \qquad (11)$$

In the case of a SAM-treated gold electrode, the coverage q is assumed to be close to unity and stay the same as the pH varies. Moreover, although the main effect of the pH increase and therefore the increased repulsion between ionized surface groups will be on the size of the active sites R_a, we will assume it transposes to a proportional effect on the separation between active sites R_0. In order to eliminate the fractional coverage q from Equations (10) and (11), ratios between plateaus and differences between half-wave potentials of consecutive voltammograms corresponding to a different pH value will be considered. Table 4 summarizes the results obtained.

Table 4: Relevant parameters for the study of the SAM-treated gold electrode as a function of pH. The data show a clear increase of the distance separating two active sites R_0 with pH.

*** the measure of the half-wave potential and plateau current are difficult for low pH values as the shape of the voltammogram strongly deviates from the expected sigmoid shape. Generally, half-wave potential shifts are deemed more reliable.**

pH	$E_{1/2}$ **(mV vs. SSCE)**	i_{lim} ***(μA)***	$i_{lim}^{(n)} / i_{lim}^{pH=3.55} = R_0^{pH=3.55} / R_0^{(n)}$	$E_{1/2}^{(n)} - E_{1/2}^{pH=3.55} = RT/aF \ln\left(R_0^{(n)} / R_0^{pH=3.55}\right)$
3.55	472*	-31.2*	N/A	N/A
4.35	408	-43.4	1.39	-64 mV
5.80	367	-40.5	1.30	-105 mV
6.50	340	-38.4	1.23	-132 mV
6.99	331	-38.2	1.22	-141 mV
7.49	330	-38.8	1.24	-142 mV
8.04	321	-41.6	1.33	-151 mV
8.91	299	-37.2	1.19	-173 mV
9.85	280	-36.7	1.17	-192 mV
10.69	262	-38.2	1.22	-210 mV

With the hypotheses made, the data from Table 4 clearly show an increase of the average distance separating two microscopic active sites R_0 from the value at low pH as the pH increases toward more alkaline values. This clearly validates the assumption; local electrostatic repulsion between neighbor groups occurs when surface groups get deprotonated as the pH increases.

3.3 Problem of the SAM layer thickness

Finally, another limitation of the method used to study the electric field dependence of glucose oxidase activity may appear when considering the thickness of the SAM on top of the gold electrode. The calculated length of several ω-carboxyalkanethiol like 3-mercaptopropionic acid (3-MPA), 11-mercaptoundecanoic acid (11-MUDA) and 16-mercaptohexadecanoic acid (16-MHDA) presented in Figure 4.18 evaluates the thickness of a SAM of these compounds on a gold surface.

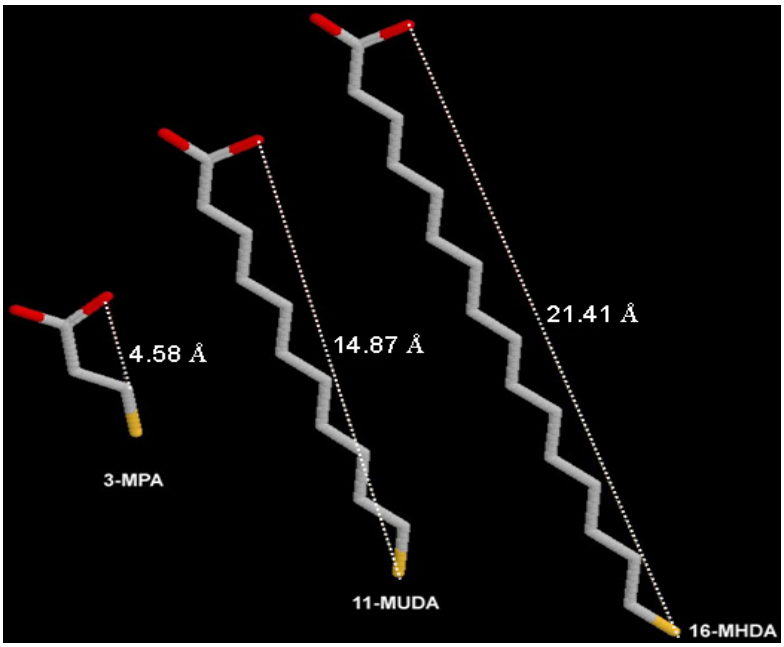

Figure 4.18: Calculated length of several commonly used ω-carboxyalkanethiol molecules. From left to right: 3-mercaptopropionic acid (3-MPA), 11-mercaptundecanoic acid (11-MUDA) and 16-mercaptohexadecanoic acid (16-MHDA). The calculation was performed with a built-in routine of the Rasmol Molecular Renderer viewer (Molinaro et al, University of California at Berkeley).

Studies in the case of alkanethiols, showed that in the packed SAM structure the thiol molecules are tilted by about 30° with respect to the surface normal[69]. Table 5 summarizes the expected maximum thickness of a SAM made from these three compounds by assuming no mechanical stress occurs than could decrease the thickness during the formation of the layer.

Table 5: Maximum SAM thickness for 3 common ω-carboxyalkanethiols corrected with the reported 30° tilt in the SAM configuration on gold[69].

Molecule	Max. thiol length	Max. SAM thickness
3-MPA	4.58 Å	**0.4 nm**
11-MUDA	14.87 Å	**1.3 nm**
16-MHDA	21.41 Å	**1.9 nm**

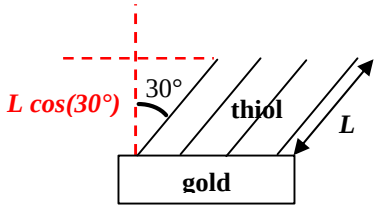

The calculated SAM thicknesses have to be compared to the electrical double layer thickness in a I-I electrolyte like KCl to assess the range of a DC electrical field on the electrode surface. According to the Gouy-Chapman model (see Chapter 5 for details), the Debye length at which the surface potential has dropped by about 63% is equal to 0.96 nm in 0.1 M KCl and to 3 nm in 0.01 M KCl. Consequently, since electric field dependence experiments were carried out in 0.1 M KCl with 16-MHDA, glucose oxidase was located too far away to be sensitive to the DC field. A possible improvement of the system would be to use shorter ω-carboxyalkanethiols, but these molecules make much more porous SAM according to own attempts, which is incompatible with the required electrode passivation for electron-transfer.

Given all the investigations carried out above, it appears the strategy used to study the DC field effect dependence of glucose oxidase activity does not permit to properly study the field dependence. It was originally chosen because it is a straightforward and efficient way to immobilize soluble proteins that has enjoyed a long-time success.

Another option to monitor glucose oxidase activity by SECM is to measure the production of hydrogen peroxide in aerobic conditions during the second step of the mechanism (Equations (8.3) and (9.2)) locally by approaching the tip to the surface and measuring the tip current in a variant of the surface generation/tip collection (SG-TC) mode of SECM[41]. The measurement of hydrogen peroxide reduction is a very difficult experiment and requires an adequate electrode. The next sections are devoted to the study of hydrogen peroxide decomposition as a preliminary work to the direct measurement of hydrogen peroxide from glucose oxidase activity.

4. SECM study of heterogeneous hydrogen peroxide decomposition

A scanning electrochemical microscopy (SECM) approach for the analysis of heterogeneous catalytic-reactions at solid-liquid interfaces is described and applied. In this configuration, the reactant generated at a tip undergoes a reaction, e.g. a disproportionation, at the planar electrode. The theoretical background for this study, performed by digital simulations using a finite difference method, considers a chemical reaction at the surface with general stoichiometry. In this case the fraction of regenerated mediator (ν_S) may differ with respect to a surface reaction that is the reverse of the tip reaction, resulting in an asymmetric mediator loop. Simulated tip current transients and approach curves at different values of the kinetic rate constant for reactions where $\nu_S < 1$ were used to analyze this new SECM situation. This approach was used to study the catalytic decomposition of hydrogen peroxide ($HO_2^- \rightarrow 1/2O_2 + OH^-$), where $\nu_S = 0.5$, on supported catalysts.

4.1 Position of the problem

Heterogeneous catalytic reactions at the liquid solid interface are important in chemistry, e.g. in synthesis and electrode reactions. One important case is the heterogeneous decomposition of hydrogen peroxide into O_2 and OH^- (Equation (12)) that occurs at high rate on noble metals such as platinum and its alloys[70-72], on oxides,[73-76] immobilized complexes[77,78] and enzymes such as catalase[79-82]. There is also interest in H_2O_2 removal from final products and wastes[79-83] and in fundamental studies of the reaction mechanism in electrode reactions, like oxygen electro-reduction[84].

$$2\ H_2O_2 \rightarrow O_2 + 2\ H_2O \qquad (12.1)$$

or

$$HO_2^- \rightarrow 1/2\ O_2 + HO^- \quad \text{(strongly alkaline media)} \qquad (12.2)$$

In studying the kinetics of hydrogen peroxide decomposition catalyzed by solids, the catalyst is often dispersed into a solution containing hydrogen peroxide. The concentration of peroxide or the volume of evolved oxygen is monitored in time[71-83,85]. Thus, the heterogeneous rate constant

($cm.s^{-1}$) can be calculated from a pseudo-homogeneous rate constant (s^{-1}) estimated from the dependency of peroxide concentration on time[86]. The method is time consuming and may require significant amounts of material to reach the desired detection limits. Scanning electrochemical microscopy (SECM) is a good alternative method because of its simple and efficient way of studying many types of surfaces[41]. The usefulness of this technique to study of electrode reaction kinetics is well known. Catalyzed heterogeneous processes have been extensively analyzed by SECM, mainly enzyme-assisted reactions[87] and corrosion processes[88]. Chemical reactions catalyzed by metals, such us the reduction of proton by methylviologen on platinum, have been analyzed by SECM, allowing the direct measurement of the heterogeneous rate constant[89]. Moreover, gas evolution is not necessary since quantification is performed through electrochemical signals, significantly more sensitive than the currently used analytical methods.

The study of catalytic decomposition reactions by SECM is different from earlier studies, and the theoretical formulation for this type of problem has not yet been reported. Figure 4.19a shows the main difference with the usual system with an electrode reaction at the substrate. In this case the mediator *Ox* is electro-reduced at the tip under mass-transport control generating *Red*, which diffuses toward the planar electrode. The electrode surface catalyzes the decomposition of *Red* to *Ox*, which diffuses back to the tip, thus closing the feedback loop. However, because the substrate and tip reactions are different, they may have dissimilar *Ox* stoichiometric coefficients. As a consequence, the flux of *Ox* that is regenerated at the substrate will decrease by a factor ν_S with respect to the reverse reaction. Questions that need to be addressed include how the asymmetry in the mediator regeneration affects the transient tip current response and how an approach curve is modified by the value of ν_S. A theoretical treatment of this system based on a numerical simulation that addresses these issues has been reported[90]. An SECM-based kinetic study of hydrogen peroxide decomposition ($\nu_S = 0.5$) in alkaline solution on well-known metal and enzyme immobilized catalysts is performed and quantitavely analyzed with the available digital simulations.

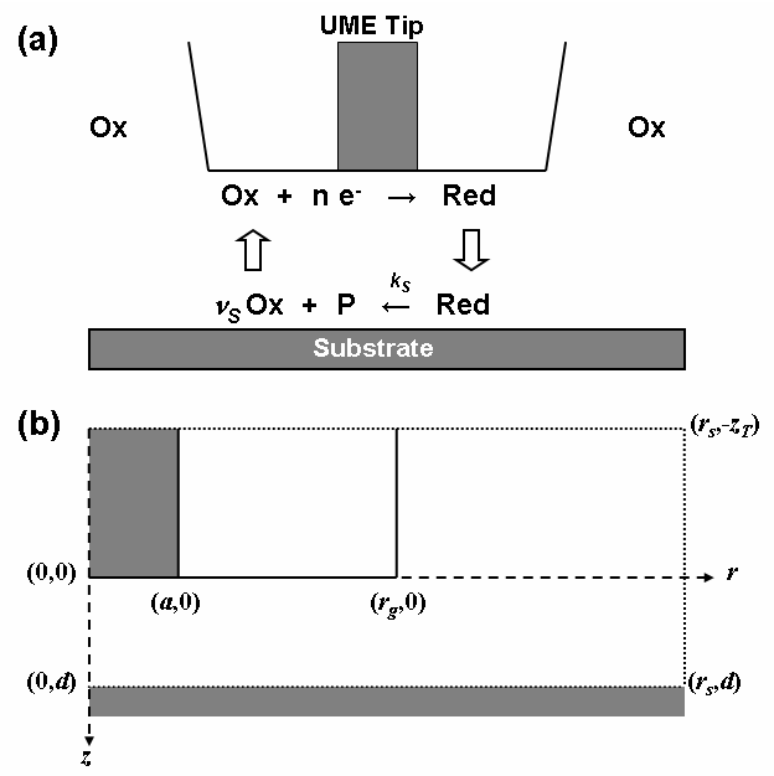

Figure 4.19: (a) Schematic of the SECM feedback mode operating with a generic asymmetric mediator loop. (b) Cylindrical coordinate system for digital simulations[90].

4.2 Experimental details

4.2.1 Chemicals and materials

The 25-µm diameter gold wire was from Goodfellow (Devon, PA). Bovine liver catalase (EC 1.11.1.6) powder from Sigma-Aldrich (Saint-Louis, MO) was used without further purification. Triethyloxonium tetrafluoroborate (TOTFB), 1,4-diaminobutane (DAB), dichloromethane and methanol from Sigma-Aldrich were used as received. Glutaraldehyde was obtained in nitrogen-filled ampoules of 8% (v/v) aqueous solutions at electron microscopy grade from Polysciences, Inc. (Warrington, PA). The nylon samples used (Durethan A30) were 1-cm-diameter 3-mm-thick disks (Bayer Corp., Pittsburgh, PA). Prior to each sample preparation, the shaped disks were cleaned by ultrasonication in methanol for 30 min followed by 30 min ultrasonication in water. 3-mercapto-propyltrimethoxysilane (MPTS) was from Sigma-Aldrich (Saint-Louis, MO). Sodium

borohydride ($NaBH_4$) and hexachloroplatinic acid (H_2PtCl_6) were used as received from Alfa Aesar (Ward Hill, MA).

All glassware was cleaned in 70/30 HNO_3/H_2SO_4 before use. Milli-Q^{TM} purity water was used to make all aqueous solutions mentioned.

4.2.2 SECM probes

Gold-mercury amalgam 25-µm-diameter ultramicroelectrode (UME) disks were used as SECM tips. They were prepared following the procedure described by Mandler et al[89]. A 25-µm-diameter gold disk tip is prepared by heat-sealing a gold wire into a borosilicate glass capillary following the standard procedure previously described[41]. The tip is then polished and sharpened. Then, mercury is electrodeposited on the Au disk from a 0.1 M $HgNO_3$ (Alfa Aesar) solution at -0.2 V vs. Hg/Hg_2SO_4 for 3 min. This procedure generates an Hg hemisphere deposited on the Au disk. A rough and soft Au-Hg amalgam is spontaneously formed onto the electrode in less than 5 min. To make a smooth disk of this material, the tip is softly polished over a polishing cloth containing a diluted dispersion of alumina 0.05 µm in water, rinsed thoroughly with water and cleaned by ultrasonication for 30 s.

4.2.3 SECM substrates

4.2.3.1 Catalase immobilized on nylon disks

A modified Morris O-alkylation[53] can be used to immobilize the protein on the nylon surface through external free amine groups similarly to the method described in section 2.2.2.

4.2.3.2 Platinum particles immobilized on glass

Platinum nanoparticles were synthesized and immobilized on 1-mm thick plain glass microscope slides (Fisher Scientific, Pittsburgh, PA) via silanization with a thiol-terminated molecule. A 10 mM $NaBH_4$ solution was added drop by drop to a 2.6 mM H_2PtCl_6 solution under stirring, reducing the Pt salt to nanometer-sized Pt particles in suspension[91]. $NaBH_4$ was added until the solution showed a persistent yellow-grey color. Completion of this process was checked by UV-visible spectroscopy. The glass supports were prepared as follows. New glass microscope

slides were cleaned in a (30/70) H_2O_2/H_2SO_4 solution heated to 80°C for 20 min, rinsed with water and dried at 100°C. They were then immersed in a 1 % (v/v) MPTS solution in methanol for 20 h at room temperature in a calcium chloride desiccator. After intense rinsing with methanol, they were placed in the fresh platinum colloidal suspension for 3 h at room temperature. Finally, they were rinsed with water and used immediately.

4.2.4 Measurements

The electrochemical studies were performed in 0.2 M phosphate solutions of different pH values in the range $6 \leq pH \leq 12$ at room temperature with a three-electrode cell, using a Au-Hg tip as SECM probe, a Pt wire as counter electrode and Hg/Hg_2SO_4 as reference electrode (Radiometer Analytical, France). The substrate was tightened at the bottom of the Teflon cell via a FETFE (Fluoro Elastomer Fluoro Ethylene) o-ring. SECM measurements were carried out using a CHI 900 microscope (CH Instruments, Austin, TX). Examination of Pt-immobilized glass surfaces was performed by atomic force microscopy (AFM) in the tapping mode with a Veeco Dimension 3100 microscope and a Nanoscope IV controller (Veeco Instruments, Inc., Santa Barbara, CA) in air at room temperature. Standard commercial silicon etched probes (Nanosensors Point Probe Plus NCH, Switzerland) with a nominal spring constant of 21 – 78 Nm^{-1} were used. They typically had a resonant frequency around 265 kHz with a quality factor of about 450. To obtain a pure attractive regime and reduce the effect of the damping of the oscillation near the surface, a frequency smaller than the resonant frequency for which the phase delay was equal to $-\pi/4$ was used and the free oscillation amplitude for that frequency was adjusted to values typically slightly smaller than 10 nm until the phase signal was characteristic of an intermittent contact situation in a purely attractive field[92]. This also allowed excluding initial tip pollution before imaging the surface.

4.3 Results and discussion

The decomposition (disproportionation) of hydrogen peroxide catalyzed by solid surfaces is a case where $\nu_S = 0.5$. It can be studied by this SECM approach by electrogenerating H_2O_2, or HO_2^-

in alkaline conditions, from dissolved O_2 at a tip where the 2e reduction takes place and monitoring the feedback of O_2 from the substrate, according to the scheme in Figure 4.20.

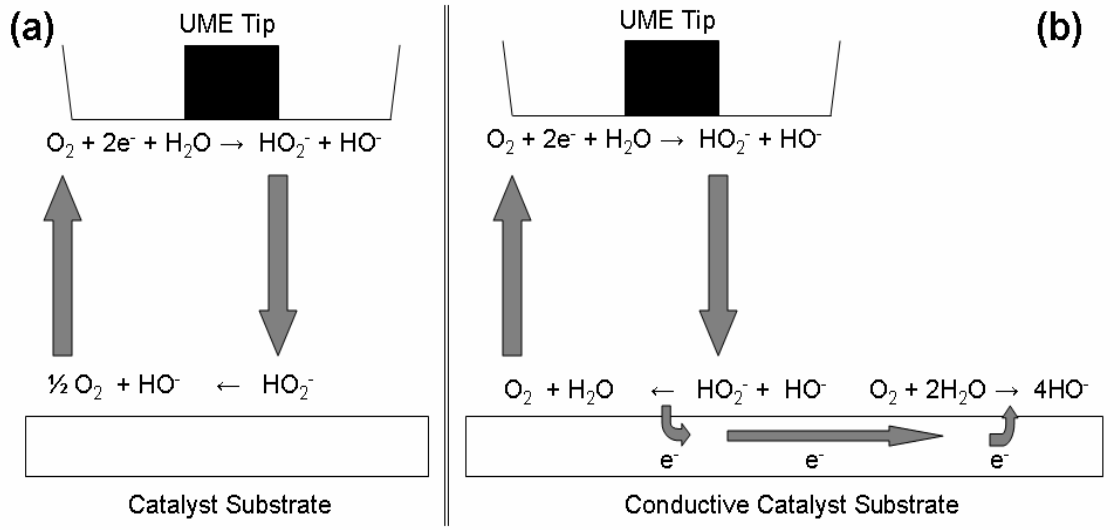

Figure 4.20: (a) Schematic of the tip-substrate O_2/HO_2^- feedback process to study the hydrogen peroxide decomposition reaction by SECM. (b) Schematic of the effect of the lateral reaction involving electron transfer (O_2 electro-reduction) on the tip-substrate O_2/HO_2^- feedback process.

4.3.1 Tip preparation and characterization

Mercury is a good electrode material to carry out exclusively the two-electron 2e reduction of O_2 to HO_2^- under diffusion control at the tip, since it produces two very well-separated current plateaus for two-electron 2e and four-electron 4e reductions of O_2[93]. While hemispheric Hg tips have been used as SECM probes[93,94], their application in this study is not convenient, since the feedback sensitivity would be significantly lower than with a disk[95]. Moreover, the theoretical background used here was developed for a disk electrode. While solid electrode tips such as gold and carbon can be efficient generators of HO_2^- from O_2,[96,97] at low pH (< 8) the 4e pathway becomes significant before the 2e pathway reaches the limiting current. A solid material that possesses the electrochemical properties of mercury is the amalgam Au-Hg, which has already been used as SECM disk probe[89].

As described in the experimental section, its preparation by electrodeposition of Hg on a Au tip is straightforward. Cyclic voltammograms with a Au-Hg tip in air-saturated 0.2 M phosphate solutions at different pH values (12, 7.1 and 5) are shown in Figure 4.21. In alkaline solution one

can clearly identify two waves with half-wave potentials of -0.9 V and -1.7 V for the overall 2e and 4e reduction of O_2, respectively, before hydrogen evolution occurs. As the solution pH decreases, the hydrogen evolution reaction overlaps the 4e O_2 reduction, but the 2e process is still well defined. At the anodic limit of ≈ -0.5 V mercury oxidizes to HgO in alkaline solutions. These voltammograms indicate that the 2e reduction of oxygen is diffusion-controlled at a 25-µm diameter Hg-Au disk tip at -1.25 V vs. Hg/Hg_2SO_4 with a limiting current $i_T^{¥}$ = 4.0 ± 0.1 nA. This value agrees with the UME current 3.95 nA that is calculated from the equation for the UME disk limiting current ($i_{T,}^{¥} = 4nFDac$)[98] assuming an oxygen diffusion coefficient D = $1.5x10^{-5}$ $cm^2.s^{-1}$ and a solubility c = 0.27 mM at 0.21 atm in phosphate solutions[99].

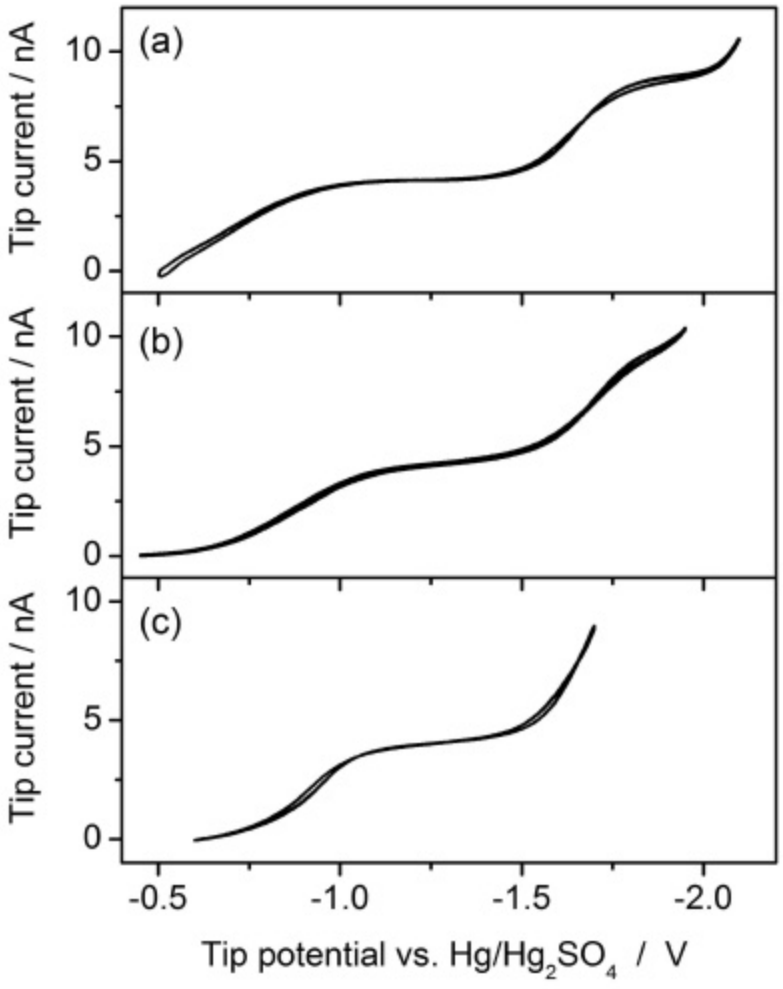

Figure 4.21: Cyclic voltammogram of a Au-Hg amalgam tip (25-µm diameter) in air-saturated 0.2 M phosphate solution at pH = 12.0 (a), 7.1 (b) and 5.0 (c). Scan rate: 0.1 V s^{-1}.

4.3.2 Hydrogen peroxide decomposition on immobilized catalase

Bovine liver catalase specifically catalyzes the conversion of hydrogen peroxide to oxygen and water. It is a homotetrameric hemoprotein[100] of a subunit (MW = 60,000 to 65,000) with 27 lysine residues. 21 of them are located on the external protein surface and are therefore accessible for surface chemistry[101]. This enzyme immobilized on different surfaces such as polymer and oxide pellets, is used for elimination of hydrogen peroxide from industrial fluids such as textile effluents and food products[79-83]. Thus, the described SECM approach was applied as a demonstration to study this type of material. Some approach curves obtained on nylon-immobilized catalase in 0.2 M phosphate solutions at different pH values using a 25-µm Au-Hg tip with RG ≈ 5 are presented in Figure 4.22 (symbols). These curves were measured at a scan rate of 1 µm.s^{-1}, which is sufficiently slow to ensure that steady state conditions are reached for each point. At each pH, the approach curves were measured on three different spots on the substrate surface separated by ≈ 400 µm. Then, the cell was thoroughly rinsed with the new solution and re-filled. After 10 min, a new set of three approach curves were taken. The correlations of these approach curves using the available simulations[90] (solid lines) are shown in Figure 4.22 on top of the respective experimental points. Even when O_2 feedback is small, the approach curves clearly differ from the curve obtained on an inert surface and it is possible to extract precise values of the rate constant.

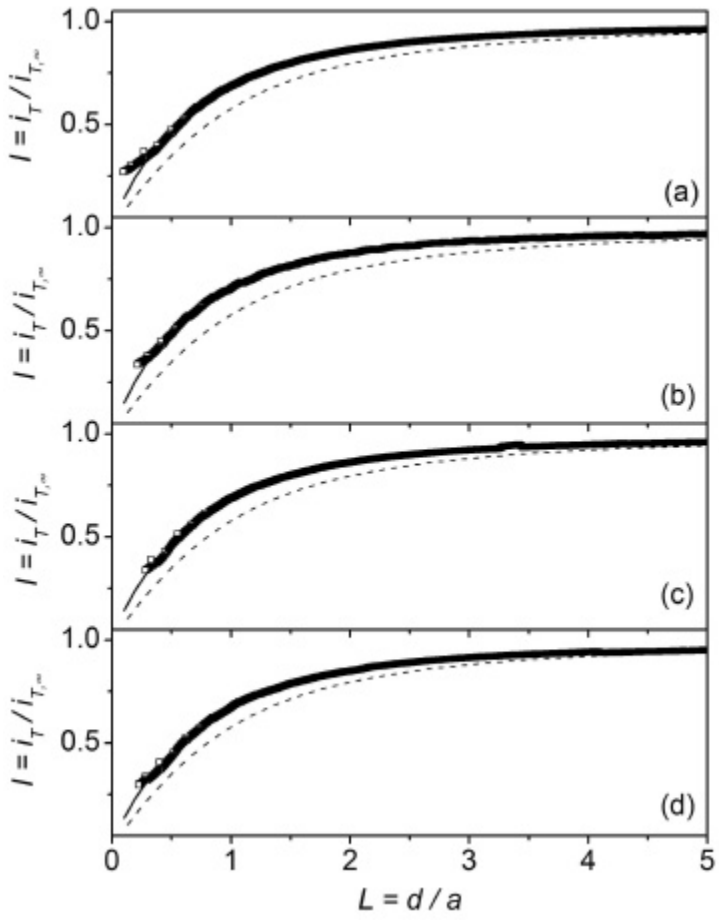

Figure 4.22: Experimental approach curves (□) measured on immobilized catalase-nylon substrate using the O_2/H_2O_2 mediator feedback to a Au-Hg amalgam tip (25-µm diameter, *RG* @ 5) in air-saturated 0.2 M phosphate solutions of pH = 5.5 (a), 7.1 (b), 9.1 (c), 10.3 (d). Scan rate: 1 µm s^{-1}. Solid lines are the theoretical *I* vs. *L* dependencies[90]. The theoretical negative feedback approach curve for a tip with RG = 5 (dash line)[59] is included as a reference.

Figure 4.23 shows the dependence of the rate constant ($cm.s^{-1}$) determined on immobilized catalase on the pH. Each point is the mean value of three measurements. To convert the dimensionless rate constant (k) measured from the approach curves into the k_S value, values of D = 1.5 10^{-5} cm^2 s^{-1} [99] and a = 12.5 10^{-4} cm were used. The highest activity is observed at around pH = 7, in agreement with results obtained on catalase immobilized on alumina pellets and chitosan beads[79-82] The catalyst became deactivated after testing at pH > 12, probably because the amide bonds to the nylon surface were irreversibly hydrolyzed at that pH value. A comparison of the values obtained in this work with results reported for immobilized catalase[80] is not directly possible due to the lack of information to convert the reported apparent pseudo-homogeneous rate constants (k', in s^{-1}) into k_S. If nylon-immobilized catalase (10 µm radius pellets, specific area =

2.6 cm^2mg^{-1}) operates in a discontinuous reactor similar to that used by Tarhan et al. (60 mg in 20 mL of solution)[80], it would have a pseudo-homogeneous rate constant $k' = 2.3\ 10^{-2}\ s^{-1}$ at pH=7 derived from the value of k_S measured by our technique. This value agrees very well with those reported for immobilized catalase on other materials such as alumina ($k' = 1.6\ 10^{-2}\ s^{-1}$) and polymer pellets ($k' = 7.8\ 10^{-3}\ s^{-1}$)[80]. On the other hand, the calculated k_S values, between $1\ 10^{-3}$ and $3\ 10^{-3}$ $cm.s^{-1}$, are similar to those found on other immobilized enzymes for other reactions, such as glucose oxidase for the oxidation of glucose[43].

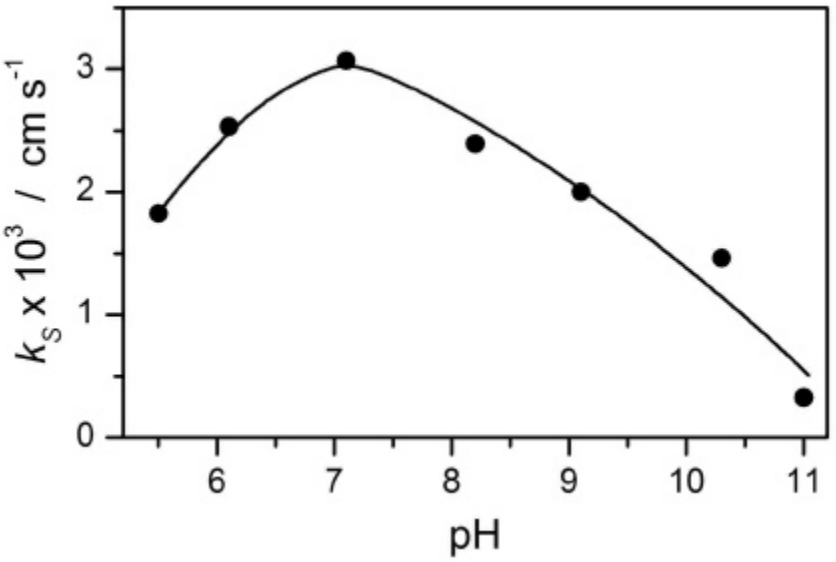

Figure 4.23: Dependence of the hydrogen peroxide decomposition heterogeneous rate constant (k_S) on the pH, measured by SECM on immobilized catalase-nylon substrate in air-saturated 0.2 M phosphate solutions.

4.3.3 Hydrogen peroxide decomposition on immobilized Pt nanoparticles

Pt is a very efficient material for decomposing hydrogen peroxide, and studies of its activity (mechanism, pH dependency, effects of alloying) have been reported since the middle of the past century[70]. In this work, Pt nanoparticles were immobilized on silanized glass surfaces from dilute colloidal solutions prepared by reduction of H_2PtCl_6 with $NaBH_4$. UV-visible spectroscopy was used to check for the completion of platinum reduction. $PtCl_6^{2-}$ shows a strong absorption peak at 260 nm which disappears once the reduction with an excess of $NaBH_4$ is complete[102]. A remaining broad absorption signal was observed after completion of the reaction, characteristic of light scattering by colloidal solutions[103].

The conductivity of this surface was analyzed by performing SECM approach curves using the oxidation of ferrocenemethanol. On conductive surfaces, the reduction of tip-generated ferrocenium is driven at the substrate at open circuit potential due to a lateral electron transfer process[104]. Thus, a positive approach curve is expected on a conductive surface. However, pure negative feedback was observed in approach curves obtained on the Pt-immobilized samples under such conditions, which reveals a surface with essentially no contact between the small conductive particles.

AFM scans of the immobilized material (Figure 4.24) show a surface roughened by particle immobilization. The particles have an average apparent lateral diameter of 40 to 50 nm. However, lateral sizes can generally not be trusted in AFM experiments due to tip convolution. The apparent height of the particles is about 4 to 5 nm, but this value is uncertain because the height reference (glass surface) is not clear in the scan due to limitations from the tip's own size. We therefore estimate an average particle slightly larger than 5 nm.

The AFM scan also shows several types of aggregates made of 2 to 5 particles on the surface. Aggregation is caused by the absence of capping agent during the synthesis step. Nevertheless, the platinum particles covering the glass surface are clearly not totally interconnected. For instance, in the surface cross-section in Figure 4.24, the central 200-nm wide structure delimitated by the black symbols is separated from the neighboring aggregates by 15-nm wide gaps. Several wider gaps also appear in the probed area. Therefore, the surface is essentially insulating over the micrometer range, explaining the SECM results previously described.

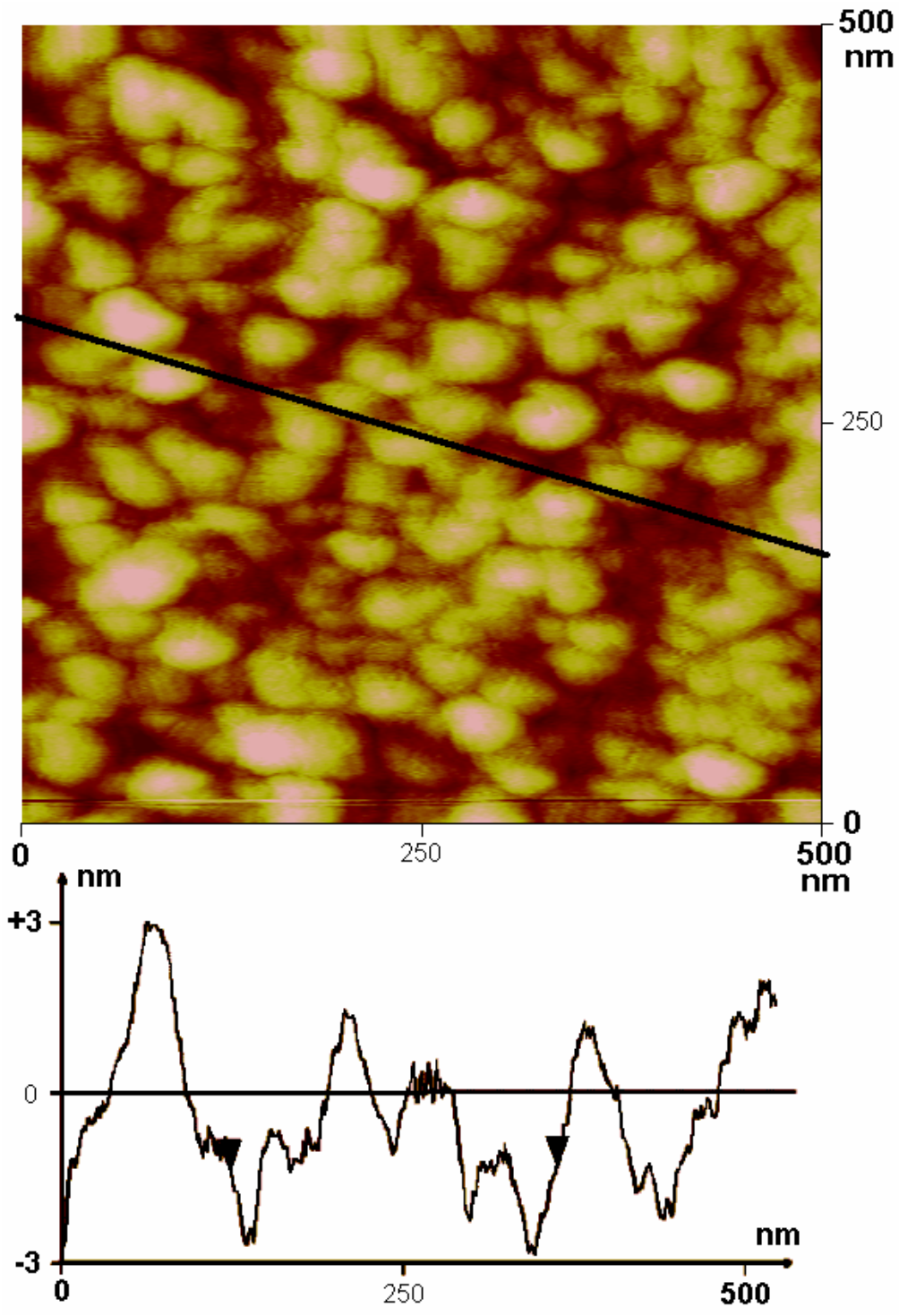

Figure 4.24: Top image: Tapping Mode AFM image of Pt nanoparticles chemically immobilized on glass. The image is flattened to the second order to remove tilt and scan curvature artifacts. Height scale: 0 – 6 nm. Bottom graph: cross section along the black line in the AFM image.

The activity of these surfaces for hydrogen peroxide decomposition at different pH was examined by the described SECM approach. The approach curves measured on these surfaces at different pH values showed significant activity for this reaction, as shown in Figure 4.25 (symbols). They were correlated with available simulations[90] to calculate the heterogeneous rate constants. The activity of immobilized Pt particles shows a maximum at pH ≈ 12 (k_S = 5 10^{-3} cm s^{-1}), as shown in Figure 4.26, similarly to other noble metals[71]. The value of k_S at near-neutral pH is 10^{-4} cm s^{-1}, close to 1.6 10^{-4} cm s^{-1} determined on Pt black[71].

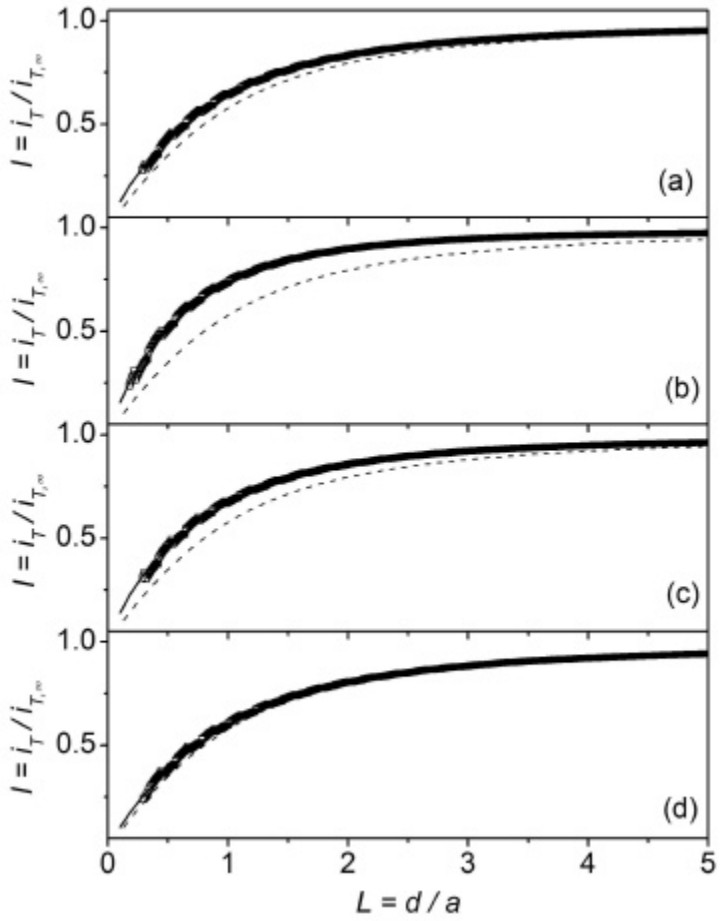

Figure 4.25: Experimental approach curves (□) measured on immobilized Pt nanoparticles-glass using the O_2/HO_2^- mediator feedback at an Au-Hg amalgam tip (25-μm diameter, *RG* » 5) in air-saturated 0.2 M phosphate solutions of pH = 12.8 (a), 11.9 (b), 11.3 (c), 9.56 (d). Scan rate: 1 μm s^{-1}. Solid lines are the theoretical *I* vs. *L* dependencies[90]. The theoretical negative feedback approach curve for a tip with *RG* = 5 (dash line)[59] is included as a reference.

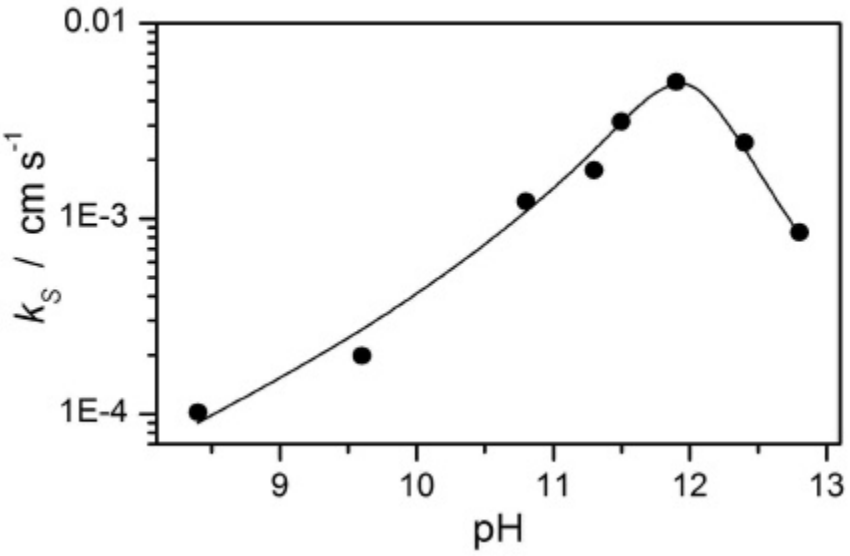

Figure 4.26: Dependence of the hydrogen peroxide decomposition heterogeneous rate constant (k_S) on the pH, measured by SECM on chemically immobilized Pt particles (5-10 nm diameter) over glass, in air-saturated 0.2 M phosphate solutions.

4.3.4 The problem of lateral electron transfer on conductive surfaces

There is a limitation when this SECM approach is applied to study hydrogen peroxide decomposition on conductive surfaces that are active for oxygen electro-reduction, for example a Pt sheet. The open circuit potential of Pt and other electrode surfaces such as Au and carbon in air saturated phosphate solution is a mixed potential at about -0.5 V vs. Hg/Hg_2SO_4 (depending on the material and the solution pH). This potential is governed by the interaction between dissolved oxygen and the electrode surface[84]. When a small fraction of electrode area (underneath the tip) is exposed to hydrogen peroxide, a corrosion process occurs which is schematically presented in Figure 4.20b. Hydrogen peroxide is electro-oxidized to oxygen at this electrode potential while dissolved oxygen is electro-reduced to water on the rest of the electrode surface. The corrosion current of this process is so small that large area electrodes are able to sustain the process even when they are poor catalysts for oxygen electro-reduction. Thus, the feedback of oxygen observed at the tip is in fact generated in the electro-oxidation of hydrogen peroxide at that potential, which is a process with $\nu_S = 1$. Thus, the approach curves measured on large conductive electrodes, for example those shown in Figure 4.27 for a substrate with radius $a_s = 0.5$ mm, do not represent the decomposition reaction but rather the electro-oxidation reaction.

However, as the electrode area becomes smaller and comparable to the tip-affected area, this process is less significant as shown in Figure 4.27 and is negligible, as expected when the substrate is about the size of the tip[105]. For this last condition, however, a new theoretical treatment considering the effect of substrate size would be necessary to correlate the experimental approach curves for hydrogen peroxide decomposition measured on small substrates ($a_s \approx a$). If the catalyst is deposited on an insulator surface, (e.g. glass or nylon) as described here, the problem of substrate size does not arise.

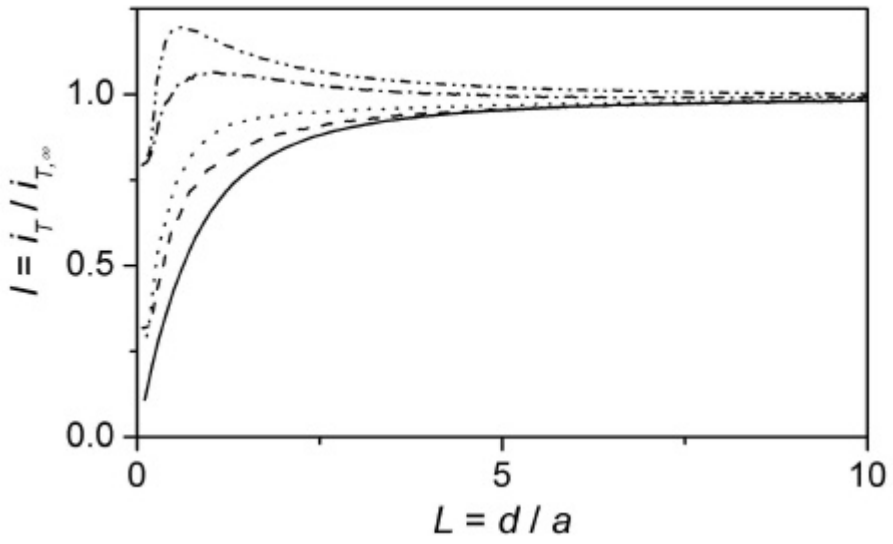

Figure 4.27: Experimental approach curves obtained on smooth Pt disks with different radii (a_S) at open circuit potential, using the O_2/HO_2^- mediator feedback to a Au-Hg amalgam tip (25-µm diameter, *RG* » 5) in air-saturated 0.2 M phosphate solutions of pH = 12.0. a_S = 12.5 µm (dash), 25 µm (dot), 62.5 µm (dash-dot), 0.5 mm (dash-dot-dot). Scan rate: 1 µm.s^{-1}. Solid line: negative feedback approach curve.

We have demonstrated the use of SECM operating with an asymmetric feedback loop to study heterogeneous chemical reactions in liquid solutions. Results from digital simulations verified that even when there is an asymmetry between the reactions at the tip (electrode reaction) and at the substrate (chemical reaction) a steady state feedback process is reached. The feedback-affected tip current is strongly dependent on the stoichiometry of the substrate reaction relative to the tip reaction. The dependence of steady-state tip current vs. tip-substrate distance can be used to determine the rate constant of the chemical reaction, similarly to the classical procedure for SECM kinetic studies of electron-transfer processes. The use of this approach was demonstrated

in the study of hydrogen peroxide decomposition on different types of well-known catalysts including enzymatic and metallic materials. Catalase–modified nylon surfaces show significant activity ($k_S \approx 10^{-3}$ to $3\ 10^{-3}$ cm s^{-1}) in the pH range $5 < pH < 10$, well covered by the detection limits of this technique, with a maximum at pH = 7.05. Pt particles (5-10 nm average diameter) immobilized on silanized glass, present optimum activity for this reaction at pH = 11.9 with an apparent rate constant ($k_S \approx 5\ 10^{-3}$ cm s^{-1}). This material retains its good activity in the pH range $10 < pH < 13$. Conductive surfaces can be studied by this technique only if the size of the analyzed substrate is decreased to the dimensions of the tip probe. Otherwise, the electro-oxidation of hydrogen peroxide driven at the substrate open circuit potential would interfere on the measurements.

5. Conclusions and future perspectives

5.1 Conclusions on SECM studies of enzyme activity

If a straightforward immobilization strategy to chemically link a soluble electroactive enzyme to a solid substrate could be developed and allowed to obtain results on how enzymes perform once they have been immobilized as compared to their native work conditions in solution, it failed to give information on the ultimate goal of the work exposed that was to determine how external DC-electric fields could modify the activity of an immobilized enzyme.

Indeed, the intrinsic nature of the layer of chemical compounds that functionalizes the surface, i.e. its size and especially its variable charge, could prevent proper measurements because it cannot be considered stable during the time-course of an experiment where a DC-field is applied.

Moreover, it is obvious that the density of available chemical groups on the surface is much higher than the density of available reactive groups on the enzyme surface. This may result in a mobility of the enzymes on the surface even though they have been chemically immobilized. This is also a disadvantage when studying the effect of an external DC-field since the latter may even

increase that mobility since the enzymes could migrate in the electrostatic force field created and therefore lead to wrong interpretations of the measurements.

5.2 Future perspectives

A first path to investigate in more detail is the one made available by the study of heterogeneous hydrogen peroxide decomposition. Since glucose oxidase produces hydrogen peroxide when working in its natural aerobic conditions, it should be possible to approach the surface close enough and measure the H_2O_2 produced by the immobilized enzyme. The detection of peroxide in aqueous solution is always complicated but elements provided by the SECM study of catalase – in particular, the advantage of an amalgamated Au-Hg tip – could simplify the experiment. With these modifications, the same strategy can be used when studying the effect of an external DC electric field.

In the longer term, external AC-fields are believed to have more impact on the enzymatic activity and their influence on immobilized activity needs to be investigated. For instance stochastic resonance processes, where the conformational change of an enzyme performing the catalytic act is simplified by a double-well potential, could be observed. It has been theoretically shown that the double-well potential gets deformed by a periodic driving that could be an oscillating AFM cantilever[106] or an external periodic electric field[107].

References

[1] McNaught A.D., and Wilkinson A., *IUPAC Compendium of Chemical Technology*, 2nd Edition, Blackwell Science, Cambridge, 1997
[2] Wienkamp R., and Steckhan E. (1982), *Angew. Chem. Intl. Ed.*, **21(10)**, 782-783
[3] Weaver R.F., *Molecular Biology*, McGraw-Hill, New York, 1999
[4] Purich D., Enzyme Kinetics and Mechanism Part A: Initial Rate and Inhibitor Methods in *Methods in Enzymology*, **63**, Academic Press, Orlando, 1979
[5] Kajiya Y., Sugai H., Iwakura C., and Yoneyama H. (1991), *Anal. Chem.*, **63(1)**, 49-54
[6] Yon-Hin B.F.Y., Smolander M., Crompton T., and Lowe C.R. (1993), *Anal. Chem.*, **65(15)**, 2067-2071
[7] Klibanov A.M. (2001), *Nature*, **409**, 241-246
[8] Radzicka A., and Wolfenden R.A. (1995), *Science*, **267**, 90-93
[9] Voet D., and Voet J.G., *Biochemistry*, John Wiley & Sons, New York, 1995
[10] Ravindra R., and Winter R. (2003), *ChemPhysChem*, **4(4)**, 359-365
[11] Black W.Z., and Hartley J.G., *Thermodynamics*, 3rd Edition, Harper Collins, New York, 1996
[12] Auerback G., Huber R., Grättinger M., Zaiss K., Jaenicke R., and Jacob U. (1997), *Structure*, **5**, 1475-1483
[13] Dossi G., Celentano F., Gianazza E., and Righetti P.G. (1983), *J. Biochem. Biophys. Methods*, **7**, 123-142
[14] Honig B., and Nicholls A. (1995), *Science*, **268**, 1144-1149
[15] Simonson T. (2001), *Curr. Opinion Struct. Biol.*, **11**, 243-252
[16] Van Belle D., Couplet I., Prevost M., and Wodak S.J. (1987), *J. Mol. Bio.*, **198**, 721-735
[17] Aqvist J., Luecke H., Quiocho F.A., and Warshel A. (1991), *Proc. Natl. Acad. Sci.*, **88**, 2026-2031
[18] Gunner M.R., Saleh M.A., Cross E., Ud-Doula A., and Wise M. (2000), *Biophys. J.*, **78**, 1126-1144
[19] Park E.S., Andrews S.S., Hu. R.B., and Boxer S.G. (1999), *J. Phys. Chem. B*, **103**, 9813-9817
[20] Park E.S., and Boxer S.B. (2002), *J. Phys. Chem. B*, **106**, 5800-5806
[21] Park E.S., Thomas M.R., and Boxer S.G. (2000), *J. Am. Chem. Soc.*, **122**, 12297-12303
[22] Kolodner P., Lukashev E.P., Ching Y., and Rousseau D.L. (1996), *Proc. Natl. Acad. Sci.*, **93**, 11618-11621
[23] Kolodner P., Lukashev E.P., and Ching Y. (2000), *Bioelectrochemistry*, **51**, 67-73
[24] Lanyi J. K. (1993), *Biochim. Biophys. Acta*, **1183,** 241–261
[25] Rousso I., Friedman N., Sheves M., and Ottolenghi M. (1995), *Biochemistry*, **34,** 12059–12065
[26] Tittor J., Schweiger U., Oesterhelt D., and Bamberg E. (1994), *Biophys. J.*, **67**, 1682-1690
[27] Horrocks B.R., and Mirkin M.V. (1998), *J. Chem. Soc. Faraday Trans.*, **94**, 1115-1118
[28] Hirst J., Sucheta A., Ackrell A.C., and Armstrong F.A. (1996), *J. Am. Chem. Soc.*, **118**, 5031-5038
[29] Santhanam K.S.V., Jespersen N., and Bard A.J. (1977), *J. Am. Chem. Soc.*, **99**, 274-276
[30] Egodage K.L., de Silva B.S., and Wilson G.S. (1997), *J. Am. Chem. Soc.*, **119**, 5295-5301
[31] Pearson M.A., Michel L.O., Hausinger R.P., and Karplus P.A. (1997), *Biochemistry*, **36**, 8164-8172
[32] Jabri E., and Karplus P.A. (1996), *Biochemistry*, **35**, 10616-10626
[33] Benini S., Rypniewski W.R., Wilson K.S., Miletti S., Ciurli S., and Mangani S. (1999), *Structure*, **7**, 205-216
[34] Ha N.C., Oh S.T., Sung J.Y., Cha K.A., Lee M.H., and Oh B.H. (2001), *Nature Struct. Biol.*, **8**, 505-509
[35] Rivat C., Fontaine M., Ropartz C., and Caullet C. (1973), *Eur. J. Immunol.*, **3**, 537-442
[36] Cass A.E., Davis G., Francis G.D., Hill H.A., Aston W.J., Higgins I.J., Plotkin E.V., Scott L.D.L., and Turner A.P.F. (1984), *Anal. Chem.*, **56(4)**, 667-671
[37] Hecht H.J., Kalisz H.M., Hendle J., Schmid R.D., and Schonburg D.J. (1993), *J. Mol. Bio*, **229**, 153-163
[38] Bourdillon C., Demaille C., Moiroux J., and Savéant J.M. (1993), *J. Am. Chem. Soc.*, **115(1)**, 2-10
[39] Badia A., Carlini R., Fernandez A., Battaglini F., Mikkelsen S.R., and English A.M. (1993), *J. Am. Chem. Soc.*, **115(16)**, 7053-7060
[40] Heller A. (1990), *Acc. Chem. Res.*, **23**, 128-138
[41] Bard A.J., and Mirkin M.V., *Scanning Electrochemical Microscopy*, Marcel Dekker, New York, 2001
[42] Pierce D.T., Unwin P.R., and Bard A.J. (1992), *Anal. Chem.*, **64(17)**, 1795-1804
[43] Pierce D.T., Unwin P.R., and Bard A.J. (1993), *Anal. Chem.*, **65(24)**, 3598-3604
[44] Wittstock G., and Schuhmann W. (1997), *Anal. Chem.*, **69(24)**, 5059-5066
[45] Frederick K.R., Tung J., Emerick R.S., Masiarz F.R., Chamberlain S.H., Vasavada A., Rosenberg S., Chakraborty S., Schopter L.M., and Massey V. (1990), *J. Biol. Chem.*, **7(5)**, 3793-3802
[46] Kelley R.L., and Reddy C.A. (1986), *J. Bacteriol.*, **166**, 269-274

[47] Sundberg R.J., and Carey F.A., *Advanced Organic Chemistry – Part B: Reaction and Synthesis*, 4th Edition, Plenum Press, New York, 2001
[48] Ulman A. (1996), *Chem. Rev.*, **96(4)**, 1533-1554
[49] Tzanov T., Costa S.A., Gübitz G.M., and Cavaco-Paulo A. (2002), *J. Biotechnol.*, **93**, 87-94
[50] 70% concentrated sulfuric acid and 30% hydrogen peroxide
[51] Shriver-Lake L.C. in *Immobilized Biomolecules in Analysis: a Practical Approach*, Cass T., and Ligler F.S., Eds., Ch. 1, Oxford Univeristy Press, Oxford, 1999
[52] Jonas U., del Campo A., Krüger C., Glasser G., and Boos D. (2002), *Proc. Nat. Acad. Sci.*, **99(8)**, 5034-5039
[53] Thompson R.O., Mandoke C.S., and Womack J.P. (1985), *Anal. Letters*, **18(B1)**, 93-107
[54] Collinson M., Bowden E.F ., and Tarlov M.J. (1992), *Langmuir*, **8(5)**, 1247-1250
[55] Tedder J.M., Nechvatal A., and Murray A.W., *Basic organic chemistry*, John Wiley & Sons, London, Ch. 6, 1972
[56] Sehgal D., and Vijay I.K. (1994), *Anal. Biochem.*, **218**, 87-91
[57] Hurth C., and Bard A.J., unpublished
[58] Weibel M.K., and Bright H.J. (1971), *J. Biol. Chem.*, **246(9)**,
[59] Amphlett J.L., and Denuault G. (1998), *J. Phys. Chem B*, **102(49)**, 9946-9951
[60] Bright H.J., and Appleby M. (1969), *J. Biol. Chem.*, **244(18)**, 3625-3634
[61] Wohlfahrt G., Witt S., Hendle J., Schomburg D., Kalisz H.M., and Hecht H.J. (1999), *Acta Crystallogr. D*, **55**, 969-977
[62] Aoki K., and Kakiuchi T. (1999), *J. Electroanal. Chem.*, **478**, 101-107
[63] Molinero V., and Calvo E.J. (1998), *J. Electroanal. Chem.*, **445(1-2)**, 17-25
[64] Komura T., Yamaguchi T., Shimatani H., and Okushio R. (2004), *Electrochimica Acta*, **49(4)**, 597-606
[65] Macdonald J.R., and Kenan W.R., *Impedance Spectroscopy: Emphasizing Solid Materials and Systems*, John Wiley & Sons, New York, 1987
[66] Janek R.P., Fawcett W.R., and Ulman A. (1997), *J. Phys. Chem. B*, **101(42)**, 8550-8558
[67] Rohwerder M., de Weldige K., and Stratmann M. (1998), *J. Solid State Electrochem.*, **2**, 88-93
[68] Amatore C., Savéant J.M., and Tessier D. (1983), *J. Electroanal. Chem.*, **147**, 39-51
[69] Liedberg B., and Cooper J.M. in *Immobilized Biomolecules in Analysis: a Practical Approach*, Cass T., and Ligler F.S., Eds., Ch. 4, Oxford Univeristy Press, Oxford, 1999
[70] Zubovich I.A. (1955), *Zhur. Fiz. Khim*, **29**, 917-924
[71] McKee D.W. (1969), *J. Catalysis*, **14**, 355-362
[72] Pirault-Roy L., Kappenstein C., Guerin M., Eloirdi R., and Pillet N. (2003), *J. Propulsion Power*, **18**, 1235-1243
[73] Ariafard A., Aghabozorg H.R., and Salehirad F. (2003), *Catalysis Commun.*, **4**, 561-573
[74] Falcón H., Carbonio R.E., and Fierro J.L.G. (2001), *J. Catalysis*, **203**, 264-173
[75] Lysova A.A., Kuz'min A.O., and Parmon V.N. (2003), *Kinetics Catalysis*, **44**, 86-97
[76] Vago E.R., and Calvo E.J. (1995), *J. Electroanal. Chem.*, **388**, 161-172
[77] Labadi I., Szilagyi I., Jakab N.I., Hernadi K., and Palinko I. (2003), *Mat. Science*, **21**, 235-241
[78] Tarasevich M.R., and Zakharkin G.I. (1977), *Reaction Kinetics Catalysis Letters*, **6**, 77-81
[79] Çetinus S.A., and Öztop H.N. (2003), *Enzyme Microbial Technol,*. **32**, 889-896
[80] (a) Tarhan L. (1991), *Appl. Biochem. Biotechnol,*. **31**, 109-116 (b) Tarhan L., and Uslan H. (1990), *Process Biochem.*, **14**, 140-144
[81] Costa S.A., Tzanov T., Para A., Gudelj M., Gübitz G.M., and Cavaca-Paulo A. (2001), *Enzyme Microbial Technol.* **28**, 815-825
[82] Costa S.A., Tzanov T., Carneiro F., Gübitz, G.M., and Cavaca-Paulo A. (2002), *Biotechnol. Letters*, **24**, 173-183
[83] Akertek E.,and Tarhan L. (1995), *Appl. Biochem. Biotechnol,*. **50**, 291-298
[84] Adzic R. in *Electrocatalysis*, Lipkowski J., and Ross P. N., Eds., Ch. 5, Wiley-VCH, New York, 1998
[85] Mueller S., Rieder H.D., and Stremmel W. (1997), *Anal. Biochem.* **245**, 55-61
[86] Vetter T.A., and Philip Colombo D. Jr. (2003), *J. Chem. Ed.*, **80**, 788-796
[87] Wittstock G. (2001), *Fresenius J. Anal. Chem.*, **370**, 303-315
[88] Serebrennikova I., Lee,S., and White H.S. (2002), *Faraday Discuss.*, **121**, 199-212
[89] Selzer Y., Turyan I., and Mandler, D. (1999), *J. Phys. Chem. B*, **103**, 1509-1517
[90] Fernandez J.L., Hurth C., and Bard A.J. (2005), *J. Phys. Chem. B*, **109(19)**, 9532-9539
[91] Sarathy K.V., Raina G., Yadav R.T., Kulkarni G.U., and Rao C.N.R. (1997), *J. Phys. Chem. B*, **101,** 9876-9880
[92] Nony L., Boisgard R., and Aimé J.-P. (1999), *J. Chem. Phys.*, **111**, 1615-1627
[93] Ciani I., Burt D.P., Daniele S, and Unwin P.R. (2004), *J. Phys. Chem. B*, **108**, 3801-3809
[94] Mauzeroll J., Hueske E.A., and Bard A.J. (2003), *Anal. Chem.*, **75**, 3880-3889

[95] Selzer Y., and Mandler D. (2000), *Anal. Chem.*, **72**, 2383-2395
[96] Damjanovic A., Genshaw M.A., and Bockris J.O'M. (1967), *J. Electroanal. Chem.*, **15**, 173-188
[97] Taylor R.J., and Humffray A.A. (1975), *J. Electroanal. Chem.*, **64**,85-97
[98] Wightman R.M., and Wipf D.O. in *Electroanalytical Chemistry*, Bard A.J., Ed., Vol. 15, Marcel Dekker, New York, 1989
[99] Lawson D.R., Whiteley L.D., Martin C.R., Szentirmay M.N., and Song J.I. (1988), *J. Electrochem. Soc.*, **135**, 2247-2256
[100] McPherson A., and Rich A. (1973), *Arch. Biochem. Biophys.*, **157**, 23-31
[101] Protein Data Bank code 4BLC. Ko T.P., Jay D., Malkin A., and McPherson A. (1999), *Acta Crystallographica D*, **55**, 1383-1395
[102] Liu Z., Ling X.Y., Lee J.Y., Su X., and Gan L.M. (2003), *J. Mater. Chem.*, **13**, 3049-3055
[103] Furlong D.N., Launikonis A., and Sasse W.H.F. (1984), *J. Chem. Soc. Faraday Trans. I*, **80**, 571-591
[104] Macpherson J.V., Slevin C.J., and Unwin P.R. (1996), *J. Chem. Soc. Faraday Trans.*, **92**, 3799-3809
[105] Bard A.J., Mirkin M.V., Unwin P.R., and Wipf D.O. (1992), *J. Phys. Chem.*, **96(6)**, 1861-1875
[106] Boisgard R., Aimé J.P., and Couturier G. (2002), *Appl. Surf. Sci.*, **188**, 363-371
[107] Gammaitoni L., Hänggi P., Jung P., and Marchesoni F. (1998), *Rev. Mod. Phys.*, **70(1)**, 223-287

Chapter 5: Scanning Electrochemical Potential Microscopy

Since the invention of the Scanning Tunneling Microscope (STM) in 1982[1], most results have been obtained by focusing on the evolution of the tip current as it senses a surface, either bare[2], modified with organic molecules[3] or even biological species[4], than on the change of its potential. The major contribution in electrochemical Scanning Probe Microscopies, namely Scanning Electrochemical Microscopy (SECM)[5], itself focuses much more on current than on potential evolution. However, if one is able to monitor potential changes due to ion distribution in the electrical double layer (EDL) that builds up at liquid-solid interface, virtually any type of charged surface could be imaged. Moreover, once sufficient resolution is attained, charged macromolecules deposited or chemically immobilized on neutral surfaces could also be studied. Once this is achieved, the need to have a tunneling current to image surfaces in Electrochemical Scanning Tunneling Microscopy (EC-STM) that limits the use of the instrument to conductors or semi-conductor with thin oxide layers disappears. It is to be noted though that SECM is able to image and probe both conducting and insulating surfaces[6].

However, other limitations of SECM appear where STM-based techniques seem more appropriate, namely resolution and noise levels. In SECM the resolution is given by the size of the ultramicroelectrode (UME) used and electrodes of less than 100 nm apparent radiuses are hard to make reproducibly whereas standard straightforward techniques are available to make STM probes suitable for atomic resolution imaging. The noise level of the instruments is determined by the typical size of the elements used for positioning, measuring, and amplifying signals. In SECM, those elements are quite larger than those used in STM-based techniques and therefore tend to make very fine resolutions harder to achieve.

Recently, a new technique has been introduced: Scanning Electrochemical Potential Microscopy (SECPM)[7]. It was designed to measure potential profiles in the EDL without significant perturbation by the probe. Early unpublished results report images of Highly-Oriented Pyrolitic Graphite (HOPG) in aqueous solutions with ionic strengths ranging from

10 mM to 1 M as well as in deionized conductivity water (18 MΩ.cm) and other polar solvents such as 1-decanol and glycerol[8].

In the long-term, this instrument seems ideal to map the potential of the surface of biological material, e.g. proteins, deposited or chemically linked to a non-conductive surface of very low roughness like mica, glass or silicon and possibly even changes in that map during biological activity of systems slow enough compared to the low time resolution of most scanning probe microscopies (> 1 s). The requirement of a low surface roughness stems from the need to be able to easily distinguish the samples from the possible corrugation of the surface on which they rest in case of a single-molecule experiment. Before that can be achieved, one has to manage to approach the tip within the double layer of a charged insulating flat surface (mica, silicon/silica or glass to a lower extent) without crashing and verify the measured potential profile fits the Gouy-Chapman-Model for example. A prerequisite for that is of course to be able to fully understand how the system behaves in case of metallic surfaces and build reproducible probe electrodes that fit the needs of SECPM.

We will use the electric double layer description provided by Gouy, Chapman (1913) and Stern (1924) to measure potential profiles on several surfaces of different types, namely: conductors (polycrystalline thin gold films, HOPG, silver foil), semiconductors (Si(100) wafer with native and anodically grown SiO_2 oxide) and insulators (green muscovite mica). The general purpose of the work reported here is to map potential profiles at electrode and insulator surfaces with that newly available commercial setup.

1. Description of the double layer[9,10]

The most complete classical model of the electrical double layer has been developed by Gouy, Chapman and Stern in the early twentieth century and is the continuation of the pioneering work of H. L. F. von Helmholtz around 1853. For clarity, we will briefly re-expose the main points of this model in the following paragraphs.

Helmholtz modelized the electrode-electrolyte interface as a parallel plate capacitor considering the electrode (metal) surface as one plate and the solution as the other plate holding the counter-charge. This yields a constant differential capacitance C_H determined by the distance between the two virtual plates d and the dielectric constant $e > 1$ modulating the permittivity of free space e_0 accounting for the closest proximity of the electrode surface on the solution side:

$$C_H = \frac{ee_0}{d} \qquad (1)$$

This only partially describes the close proximity of the interface; one has to account for mobile charge carriers (ions or other charged molecules) that may diffuse to and away from the electrode surface in a less spatially extended region called the diffuse double layer.

1.1 The Gouy-Chapman theory

Each ion species is treated as a population of charged point particles following a temperature-controlled Boltzmann distribution occupying different energy states determined by the particular action of the electric field originating in the spatial dependence of the potential F measured with respect to its bulk value on the species i. Therefore, the energy of such an ion is the energy needed to bring it from outside the double layer to its actual position near the electrode surface. The concentration n_i of the species i (absolute charge z_i) in an infinitely small layer near the electrode with respect to its bulk concentration n_i^0 is:

$$\frac{n_i}{n_i^0} = \exp\left(-\frac{z_i e f}{k_B T}\right) \qquad (2)$$

e is the electron charge, T is the absolute temperature and k_B is the Boltzmann constant. The total charge per volume in a planar geometry where symmetry considerations allow a one-dimensional approach depending only on the distance x from the electrode:

$$r(x) = \sum_{species,i} n_i^0 z_i e \exp\left(-\frac{z_i e f}{k_B T}\right) \qquad (3)$$

The one-dimensional Poisson Equation relates this total charge to the potential:

$$r(x) = -ee_0 \frac{d^2 f}{dx^2} \qquad (4)$$

$F(x=¥)$ = 0 since the potential is referred to the bulk and $dF/dx(x=¥)$ = 0 since the bulk extends over a large region and there is no change of potential within the bulk region. (4) can be rewritten as:

$$\left(\frac{df}{dx}\right)^2 = \frac{2k_B T}{ee_0} \sum_{species,i} n_i^0 \left[\exp\left(-\frac{z_i e f}{k_B T}\right) - 1\right] \qquad (5)$$

This assumes the dielectric constant of the solvent to be independent of distance and ion concentration. The validity of these assumptions will be discussed later. For a symmetrical electrolyte where each ion species has an absolute charge magnitude *z*, (5) can be simplified and further integration between the electrode surface ($x=0$) where the potential is F_0 and an arbitrary location *x* yields:

$$\frac{\tanh\left(zef/4k_B T\right)}{\tanh\left(zef_0/4k_B T\right)} = \exp\left(-kx\right) \qquad (6)$$

Where $k = \left(\frac{2n^0 z^2 e^2}{ee_0 k_B T}\right)^{1/2} = \left(3.29 \times 10^7\right) z C^{*1/2}$ is the reciprocal of the characteristic diffuse layer thickness or Debye-Huckel length k^{-1} in cm^{-1} if C^* is the bulk concentration in $mol.L^{-1}$.

Once the potential F is determined from (6), several useful quantities such as the electrode surface charge density and the charge density in the solution phase *s* at the interface, the concentration profile of each ion species or the differential capacitance C_d can be obtained from the thermodynamics formalism.

1.2 Stern's improvement

Ions cannot be considered as point charges since they have a finite size determined by their electronic structure, their nucleus as well as their solvation state. Therefore they can only approach the electrode as close as their ionic radius added to a more or less compact layer of solvent molecules. The distance of minimum approach x_2 defines the outer Helmholtz plane (OHP); F_2 is the potential in the OHP.

There is no charge between the electrode surface (x_0, F_0) and the OHP (x_2, F_2). Thus, according to the Poisson Equation (4), the potential drops linearly from F_0 to F_2. With the same definition for k, Equation (6) can be rewritten as:

$$\frac{\tanh(zef/4k_BT)}{\tanh(zef_2/4k_BT)} = \exp(-k(x-x_2)) \quad (7)$$

Ion concentration profiles, surface charge density s_M and differential capacitance C_d can again be obtained from the thermodynamics formalism. In the case of the capacitance:

$$C_d = \left(\frac{\partial s_M}{\partial E}\right) = -ee_0 \frac{\partial}{\partial E}\left(\frac{df}{dx}\right)_{x=x_2} \quad (8)$$

After rearrangement, one obtains:

$$\frac{1}{C_d} = \frac{x_2}{ee_0} + \frac{1}{ee_0 k \cosh(zef_2/2k_BT)} = \frac{1}{C_H} + \frac{1}{C_D} \quad (9)$$

Two contributions to the double layer capacitance clearly appear: C_H and C_D. C_H does not depend on the potential and is the contribution of the Helmholtz compact layer whereas C_D is clearly a contribution form the diffuse layer. For dilute electrolytes i.e. small values of k, C_D is the dominant part in C_d as long as F_0, and therefore F_2, remains small (near the point of zero charge). But, for more concentrated electrolytes and higher values of surface potential, the diffuse part gets negligible, charge is located closer to the electrode surface and the interface approaches the Helmholtz model.

1.3 Other modifications of the Gouy-Chapman-Stern model

As mentioned earlier, an assumption of the Gouy-Chapman theory that has been the subject of many studies[11,12] is the non-dependence of the dielectric constant on the spatial coordinate in the simplification of the Poisson Equation (Equation (4)) and in the following integration to determine the potential profile. From a less mathematical point of view, this relates to the saturation of the dielectric for higher electric field strengths. Electric fields

reach such high values only very close to the electrode surface and should therefore only affect measurements in the compact layer.

Other attempts have been made to treat the electrolyte as a set of N particles of finite size (hard spheres) in a fixed volume v interacting mainly with the charged planar electrode or mainly subject to forces from neighboring particles[13]. For large dilutions, this model confirms the predictions of the Gouy-Chapman model but for high electrolyte concentration, short range ion-ion interactions create local lattices of alternating positive and negative charges. The potential in the diffuse layer in the latter case is smaller and decreases more rapidly than predicted by the Gouy-Chapman theory.

These modifications mainly concern concentrated electrolytes and deal with modifications of the Gouy-Chapman theory introduced by changes in the electrolyte. Another source of discrepancy of the measurement with the ideal Gouy-Chapman-Stern case of Equation (7) is adsorption at the solid electrode surface. What is meant by specific adsorption is strong interaction of the simple inorganic ions from the electrolyte with the charged electrode surface at distances closer than the OHP. According to Anson[14], they can be separated into two classes; IA ions whose adsorption occurs by solvation-breaking through electrostatic interactions with the electrode and IB ions where electrons from the adsorbing ions are donated empty surface orbitals of the metal. Neutral molecules (Class II in ref. 14) adsorb mostly when there is very low net charge on the electrode and their adsorption involves exchange with adsorbed water molecules as water dipoles are weakest for slight negative charges on the electrode. Adsorption of other charged complexing metal ions are induced by relative complexation with coordinating ions and adsorption of these coordinating ions to the electrode (Class III and IV in ref. 14) or by metal-metal bonding with the electrode (Class V in 14).

1.4 Specific electrolyte adsorption

Specific adsorption of ions occurs very close to the electrode at distances x_1 smaller than the OHP ($x = x_2$). The centers of specifically adsorbed ions are located in the Inner Helmholtz Plane (IHP) ($x=x_1$). The point of zero charge (pzc) is the potential in the metallic

electrode for which the surface charge density on the metal s_M is zero in the absence of specific adsorption. Specific adsorption displaces the pzc proportionally to the logarithm of electrolyte concentration (Esin-Markov effect). The historically important experimental advances in explaining specific adsorption have been made by comparing relative surface excess of cation and anion in a 0.1 M aqueous KF solution[15] and 0.1 M aqueous KBr solution[16] on a mercury drop electrode. The relative surface excess of K^+ for example is related to the surface tension g by Equation (10):

$$\Gamma_{K^+(H_2O)} = -\frac{1}{RT}\left(\frac{\partial g}{\partial \ln a_{KF}}\right)_{E_-,m_M} = -\frac{1}{RT}\left(\frac{\partial g}{\partial \ln a_{KBr}}\right)_{E_-,m_M} \quad (10)$$

For one value of the potential E_-, the relative surface excess can be calculated when measuring the surface tension g for different electrolyte activities. This is only achievable at the mercury drop electrode. Different behaviors for the two salts when considering the slopes of $-FG_{(H_2O)}$ as a function of s_M at potentials positive of the pzc are obtained:

$$\begin{cases} s_M = -s_S(KBr) = -\left[FG_{K^+(H_2O)} - FG_{Br^-(H_2O)}\right] \\ s_M = -s_S(KF) = -\left[FG_{K^+(H_2O)} - FG_{F^-(H_2O)}\right] \end{cases} \quad (11)$$

At potentials negative of the pzc, where $s_M < 0$, the slope of $F G_{K+(H2O)}$ vs. s_M is not greater than unity in magnitude for both electrolytes and the slope of $-FG_{F-(H2O)}$ and the slope of $-FG_{Br-(H2O)}$ are close to zero. This suggests that one equivalent of positive charge in solution compensates one equivalent of negative charge from the metal at the electrode surface. But, at potentials positive of the pzc, where $s_M > 0$, the slope of $FG_{K+(H2O)}$ vs. s_M for KF is zero and $FG_{K+(H2O)}$ is negative suggesting that there are more K^+ ions in the solution bulk than at solution-electrode interface. The slope of $-FG_{F-(H2O)}$ vs. s_M is close to 1 in magnitude. Again, one equivalent of negative charge from the solution compensates one equivalent of positive charge on the surface. On the contrary, in the case of KBr, the slope of $FG_{K+(H2O)}$ vs. s_M approaches unity in magnitude and the slope of $-FG_{K+(H2O)}$ vs. s_M is greater than unity in magnitude. This suggests that more than one equivalent of negative charge in solution compensates for one equivalent of positive charge form the metal at the electrode surface. There is specific adsorption of bromide at the electrode that is compensated by an excess of positive charge from the solution to the electrode surface whereas pure

electrostatics considerations predict that it should be repelled from a positively charged surface.

For these reasons, we systematically used dilute KF (10^{-5} M) in the experiments made in SECPM to make sure that the diffuse layer extends as far as possible from the electrode surface (κ^{-1} = 96 nm in a 10^{-5} M I-I electrolyte according to the expression of k in (7)) and that both the cation and the anion followed mainly the diffusive model. In other words, we used conditions where the compact layer (between inner and outer Helmholtz planes) was negligible when compared to the diffusive layer.

2 Elements of Scanning Electrochemical Potential Microscopy (SECPM)

The microscope consists of a potentiostat to control the potential of a surface (exposed area: 0.125 cm^2 through a FETFE™ o-ring[17]) inserted in a three-electrode Teflon cell (electrolyte volume: 80-150 µL) and a measuring head that amplifies the measured voltage difference between the potential-controlled working electrode (surface) and an open-circuit tip (probe) with four selectable gain values (1, 10, 50, 100) and very low input bias current (3 fA at 25°C typically). The Teflon® cell is magnetically held on a piezoelectric tube (maximum scan ranges: 110 µm (lateral) and 5 µm (vertical)) via a 2-mm thick stainless-steel bottom cap that contacts the surface working electrode on its bottom part and is tightened to the Teflon® part via four stainless-steel screws.

The measurement head was modified to amplify the difference between the reference electrode and the tip at open-circuit instead of between the working electrode (surface) and the tip by implementing an external switch connected to the system with aluminium-shielded wires to reduce noise pick-up. The amplified difference value is then inverted by the software for display and feedback loop input. Figure 5.1 shows a simplified block diagram of the SECPM setup.

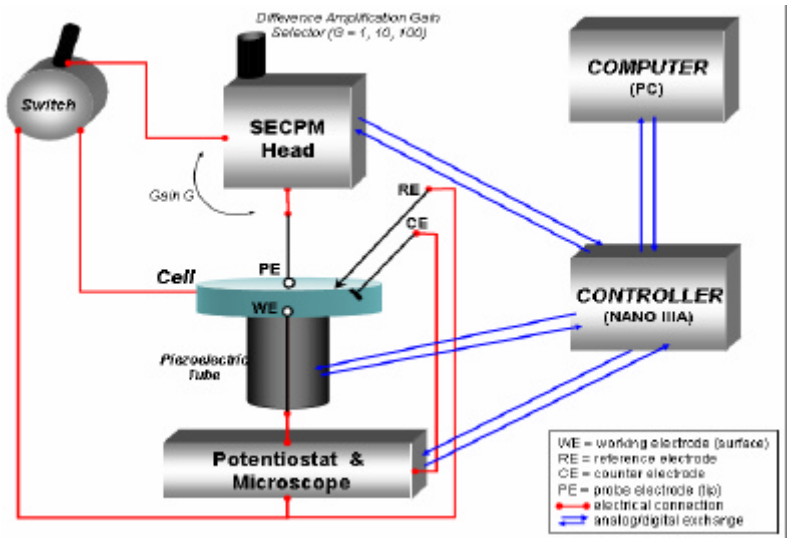

Figure 5.1: simplified block diagram of Scanning Electrochemical Potential Microscopy (SECPM). The system uses a Multimode™ microscope base bypassed for functions other than piezo actuation and feedback control. The central piece is a Teflon® electrochemical cell.

The potentiostat can also work as a bipotentiostat if the system works in STM mode (software switch) and contains several high-pas active filters with a 100 Hz cutoff frequency to filter out some line noise essentially. The current to voltage converter used has a nominal maximum sensitivity of 1 nA/V and can be manually switched to 100 µA/V if needed. A particularity of the system is that the working electrode potential is applied through the magnetic scanner top that holds the conductive bottom cap of the electrochemical cell; an insulated wire is drawn through the piezoelectric tube to connect the scanner top to the potentiostat block. The microscope part (Extended Multimode) is comprised essentially of a voltmeter with an LCD display that permanently measures the working electrode (surface) potential (with respect to ground) or its open-circuit potential and a stepper motor working in coordination with the piezoelectric tube to approach or retract the tip form the surface.

2.1 Reference electrode

What guides the choice of the reference electrode is the limited space available between the measuring head and the electrochemical cell. Attempts to build a small silver/silver chloride (saturated KCl) reference with or without a reservoir filled with the electrolyte

studied proved unfruitful. The main problem was a too high resistance drop across the extremity of the capillary in contact with the electrolyte as leakage prevention was achieved either by filling the capillary with glass wool or by partially sealing it in a natural gas/oxygen flame. We finally opted for an Ag/AgCl quasi-reference electrode (QRE) made by bulk electrolysis of 1 M HCl with a 250-µm-diameter Ag wire (Goodfellow Corp., 99.99 %, annealed) anode and a Pt wire cathode (Goodfellow Corp., 99.99 %, annealed, 0.5-mm diameter). Under these conditions, the QRE electrode equilibrates with the added electrolyte by releasing about 8.10^{-6} M chloride ions.

2.2 Probe electrode (Tip)

In scanning probe microscopies, the lateral resolution and the contrast in imaging are determined by the size of the probe used relatively to the size of the sample to image. In Force Probe Microscopy, the well-developed techniques to shape silicon (Focused Ion Beam or Electron Beam Lithography coupled to chemical etching…) can produce probes with very small apex curvature radius and controlled aspect ratios. More recently, new tips made of multi-walled carbon nanotubes attached at the end of a standard silicon probe have allowed higher resolutions in Atomic Force Microscopy[18] but the exact mechanical properties of probes modified with a single-walled nanotube have only recently been quantitatively studied[19].

Probes for electrochemical SPMs need to be conductive. Vacuum deposition of metals on sharp Si probes usually increases the apex radius because it is difficult to control the flow of evaporated or sputtered metal atoms with nanometer precision and layered electrodes often have gaps where electrolyte can leak into and make such an electrode unstable for a reproducible use in electrochemical environment. Therefore, electrochemical probes need to be made from the conductor itself when high resolutions are sought. For in situ applications, electrochemical etching is often preferred to mechanical techniques because it provides more control on the shape of the apex by using a several parameters to tune the local etching rate[20].

The following sections will describe the procedure to prepare SECPM electrodes with very small (10-20 nm) exposed apexes. It will then focus on tip considerations and the difficulty to obtain a tip at the potential of zero charge (pzc) when it sits far away from the surface (bulk potential) due to adsorption and faradaic perturbations from, for example, dissolved oxygen and protons. Another unknown of such tips is the exact geometry of the exposed area, i.e. the validity of the hemispherical approximation usually made to obtain quantitative information and whether or not the metallic part is recessed inside the insulative coating used. Some elements in an effort to solve these issues will be provided as well. Finally, another fundamental question of the response time of double layers to changes induced by the environment has, to our knowledge, never been treated. Some elements to address that specific problem will also be provided later although more solid simulations are needed.

2.2.1 Etching of $Pt_{80}Ir_{20}$ tips for use in SECPM

Our etching setup consists of two electrodes: a 22-gauge stainless steel syringe wrapped in Teflon tape that holds a 250-micron diameter $Pt_{0.8}Ir_{0.2}$ (Goodfellow Corp., 99.99%, as drawn) mechanically cut to a rod-shape at one end and a large (~ 5 cm^2) amorphous carbon piece placed 3 cm away from the wire. The $Pt_{0.8}Ir_{0.2}$ wire was cleaned by immersion in concentrated nitric acid, rinsing in deionized water and heating to a red glow in a natural gas/air flame. Electrical contact is made to an AC Variac generator and a 60 Hz sine voltage of 30-35 V RMS amplitude is applied. The rod-shaped end of the PtIr wire is immersed downward about 2 mm deep in a glass beaker containing 15 mL of the 60% (w/v) calcium chloride, 4% (v/v) concentrated hydrochloric acid and 36 % (v/v) deionized water etching solution.

A first step is achieved when sparks inside the solution start to appear meaning that large glowing pieces of platinum are removed and taken away from the newly formed electrode by complexation with the excess chloride ions from the etching solution. At this point, a large density of bubbles is observed at the tip corresponding to the formation of H_2 from protons and Cl_2 from the chlorine ions in the etching solution. The bubble flow under the pressure gradient along the immersed part will progressively sharpen the wire by frustrating the

removal of material where the bubble density is larger i.e. the most deeply immersed part. At the other end of the wire, i.e. at the air/solution interface, capillarity and surface tension considerations also lead to a higher density of bubbles which also considerably slows down the etching rate. Consequently, there is an intermediate region along the immersed tip where the etching rate is higher than at the extremities. Platinum is essentially removed there creating thus a structurally weakened narrower region that will later drop off and form a sharp end.

A second step is reached when the sparks stop. This corresponds to the drop-off of a large piece of platinum and a much sharper wire at the immersed end. The density of bubbles suddenly decreases because of a now much smaller immersed area. The AC voltage is decreased down to 0 V RMS and the wire is then slid out of the solution with a micrometer screw. The etched wire is rinsed with de-ionized water and, occasionally, a second etching step in the same setup with new solution is carried out between 3 V and 5 V (RMS) to smooth and blunt the surface, as judged by visualization under an optical microscope. Glycerol can be added to increase the viscosity of the solution and decrease the overall density of bubbles generated and thus prepare tips with a smoother surface[21]. Since a saturated $CaCl_2$ solution is already quite viscous, no such chemical was added in our case. The etching setup used is grossly depicted in Figure 5.2.

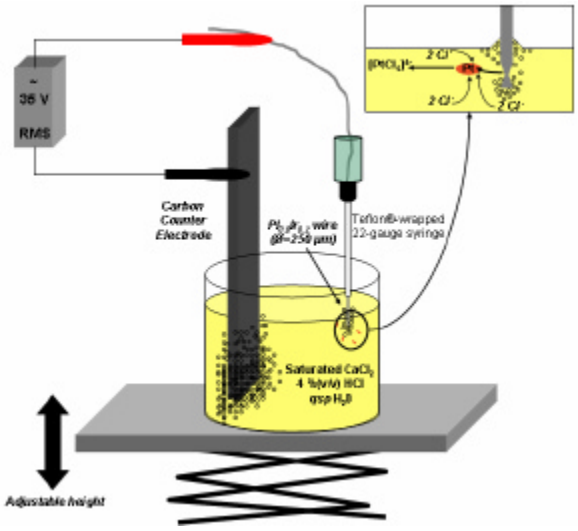

Figure 5.2: Scheme of the etching setup. A sine wave (35 V RMS) is applied between the PtIr wire and a large carbon counter electrode in an acidified (pH » 1) saturated $CaCl_2$ solution until the density of bubbles around the PtIr wire suddenly decreases and sparks of large glowing pieces of platinum disappear. This corresponds to the drop-off of the immersed part of the wire and the creation of a sharp tapered tip.

Tips selected to continue the treatment usually exhibited a sharp conical end tapered over about 500 μm in optical microscopy and were mechanically cut on the other end to a final length of 15 mm.

2.2.2 Insulation of SECPM tips

Such tips were insulated with low-density polyethylene (LDPE, used as glue in commercial hot-melt glue guns) which was preferred to apiezon wax because of a better bonding with the metal surface and therefore a better resistance to mechanical strain. Glue is melted to fill a slit cut in a copper plate heated to about 170 °C and the etched wire is dipped several times in the hot glue until a thick coating covers 2-3 mm of the etched end of the piece of wire. The totally coated tip is then aligned with the normal plane of the hot copper piece under an optical microscope. It is attached to a micrometric stage and approached to the hot copper piece now held at 80 °C – 100 °C to slow down the melting process so that it can be visually monitored. When the sharper etched part starts protruding from the surrounding thicker layer of glue showing a small 2 to 5-μm long sharp bump at the air-glue interface once the wire has been aligned with the focal plane, the stage is quickly withdrawn to stop the melting process.

Tips obtained were checked for leakage with a CH Instruments 900b electrochemical controller by cyclic voltammetry in a 1 M sulfuric acid solution by sweeping the potential between -0.7 and 1 V at 1.7 V/s after 2-3 seconds quiet time in the hydrogen underpotential deposition region according to standard procedure used to study surface states of platinum electrodes[22,23]. A digital second order Bessel low-pass filter with a cutoff frequency of 1.5 Hz was used. Potentials were measured with respect to the saturated mercury sulfate electrode (SME) and the three electrode cell (Pt counter) was placed inside a grounded Faraday cage. Tips would be selected for the remainder of the procedure only if they exhibited a mainly capacitive voltammogram as shown in Figure 5.3.

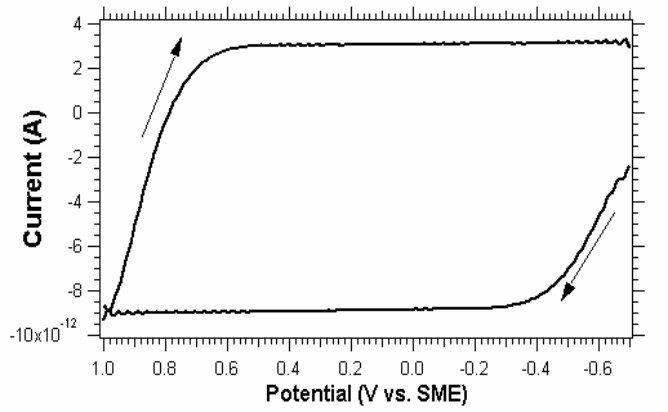

Figure 5.3: typical voltammogram of an etched PtIr wire insulated with a thinned layer of polyethylene. Arrows indicate the scan polarity. The data are smoothed by a Fourier transform with a cutoff frequency of 56 Hz to remove an additional modulation of the signal from a coupling with line noise. More details are given in the text.

The insulated wires prepared by this procedure are mainly capacitive. But, there is some leakage through defects in the coating layer since the current reaches -9 pA on the first sweep and only reaches +3 pA on the second sweep. Currents reached after the first sweeps were always around -10 pA. Such tips possess a negligible faradaic contribution. The situation can be described by a simple electric circuit given in Figure 5.3. The coating will be interpreted as a capacitor C_{PE} in parallel with a resistor R_{PE} to account for leakage. Also, since the reference electrode is placed as close as possible to the tested electrode, $R_u << R_{sol}$ where R_u is the uncompensated resistance and R_{sol} is the solution resistance (about 175 Ω from limiting equivalent ionic conductances[24] of H^+ and SO_4^{2-} since the distance between the working and counter electrodes is about 1.5 cm in the cell used).

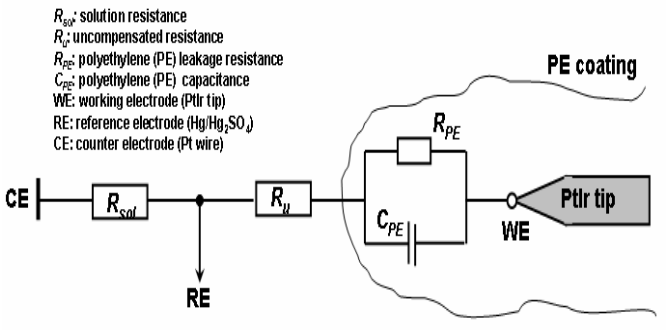

Figure 5.4: electronic representation of etched PtIr wires insulated with polyethylene-based glue (PE) as they are tested for leakage in a 1M H_2SO_4 solution in a 3-electrode teflon cell. RE is the reference elctode: saturated potassium sulfate/mercury/mercury sulfate electrode (SME).

In a classical 3-electrode cell, during a cyclic voltammogram, the voltage is applied between the WE and the RE (SME) and ramped according to $E_{initial} + vt$, where $E_{initial}$, from -0.62 V to -0.7 V vs. SME typically, is the initial (quiet time) potential and v = 1.7 V.s^{-1} is the scan rate. The current i flows between the WE and the CE. A quick calculation yields:

$$i = \left[\frac{E_{initial}}{R_u + R_{PE}} + \frac{vt}{R_u} - \frac{vt}{R_u + R_{PE}} \right] \left(1 - \exp\left(-\frac{t}{t} \right) \right) + \frac{vt}{R_u + R_{PE}} \quad (12)$$

Where $t = \frac{R_u R_{PE}}{R_u + R_{PE}} C_{PE}$ is the time constant of the system.

A glance at Figure 5.3 shows that Equation (12) can be simplified into two regimes:

- $t << t$: the initial slope in the voltammogram where the capacitance gets charged

$$i \approx i_{init} = \left[\frac{E_{initial}}{t\left(R_u + R_{PE}\right)} + \frac{v}{R_u} \right] t \quad (13.1)$$

- $t >> t$: the capacitor is charged and only leakage can modify the current

$$i \approx i_{\lim} = \left(\frac{E_{initial}}{R_u + R_{PE}} + \frac{vtR_{PE}}{R_u\left(R_u + R_{PE}\right)} \right) + \frac{v}{R_u + R_{PE}} t$$

From the voltammogram in Figure 5.3, the plateau reached by the current at -9 pA is very weakly time-dependent since the leakage is low. Therefore, one can use:

$$i \approx i_{\lim} \approx \frac{E_{initial}}{R_u + R_{PE}} + \frac{vtR_{PE}}{R_u\left(R_u + R_{PE}\right)} = \frac{E_{initial}}{R_u + R_{PE}} + \frac{vR_{PE}^{\,2}}{\left(R_u + R_{PE}\right)^2} C_{PE} \quad (13.2)$$

Equation (13.1) can be exploited with a linear fit of the initial current increase and the limit current value in Figure 5.3. It yields:

$$\begin{cases} \frac{di_{init}}{dt} = \frac{E_{initial}}{t\,(R_u + R_{PE})} + \frac{v}{R_u} \approx -4.510^{-11}\ A/s \\ \left|i_{\lim}\right| = \frac{E_{initial}}{(R_u + R_{PE})} + v\frac{R_{PE}^{\,2}}{(R_u + R_{PE})^2} C_{PE} \approx 8.8510^{-12}\ A \end{cases}$$

One can make the approximation $R_{sol} << R_{PE}$ since the solution is quite concentrated and is therefore of very low resistance (1 M H_2SO_4). Moreover, even if it appears rather leaky here, LDPE is a very good insulating material (resistivity r = 1.6 10^{13} Ω.cm[64]). Consequently, one can write $R_u << R_{PE}$. And:

$$\begin{cases} \dfrac{di_{init}}{dt} = \dfrac{E_{initial}}{R_u R_{PE} C_{PE}} + \dfrac{v}{R_u} \approx -4.5\,10^{-11}\ A/s \\ \left|i_{\lim}\right| \approx v C_{PE} \approx 8.85\,10^{-12}\ A \end{cases} \Rightarrow \begin{cases} \dfrac{di_{init}}{dt} = \dfrac{1}{R_u}\left(\dfrac{E_{initial}}{R_{PE} C_{PE}} + v\right) \approx -4.5\,10^{-11}\ A/s \\ C_{PE} \approx 5.2\ pF \end{cases}$$

Also $\dfrac{di_{init}}{dt}$ is very small and negative not because R_u is small obviously but because v and $\dfrac{E_{initial}}{R_{PE} C_{PE}}$ compensate each other due to the negative value of $E_{initial}$. Therefore, one can write: $v \approx \dfrac{-E_{initial}}{R_{PE} C_{PE}}$. And, finally: $\begin{cases} R_{PE} \approx 79\ G\Omega \\ C_{PE} \approx 5.2\ pF \end{cases}$.

We can exploit these values to draw structural information on the polymer (LDPE) coating. First, if one assumes the area of LDPE between the PtIr tip surface and the electrolyte can be approximated by two planes of area A separated by a distance d, then the capacitance is defined by[29]:

$$C_{PE} = \frac{e_0 e_{PE} A}{d} \quad (14)$$

Since the immersed part of the PtIr tip is much larger than the exposed apex, one can assume that the immersed part is roughly a disk of diameter d = 250 µm (diameter of the PtIr wire used), thus neglecting the area of the sharp tapered etched PtIr tip. And the area A simplifies into: $A = pd^2/4$. And: $d = \dfrac{e_0 e_{PE} p d^2}{4 C_{PE}} \approx 192\ nm$. This suggests the average coating thickness around the sharper part of the insulated PtIr tip after local melting of the LDPE coating under an optical microscope is typically 200 nm. This value will be discussed later.

Additionally, information can be obtained from the calculated value of the coating leakage resistance R_{PE} assuming a uniform planar layer around the tip apex. The tabulated

value of LDPE resistivity is 1.6 10^{13} Ω.cm. The calculated value for R_{PE} according to the model from Figure 5.4 would correspond to a coating thickness of about 50 µm. This is not in agreement with the value of C_{PE}, which suggests the coating resistance measured here is much lower than the real value because of the nature of the leakage. There might indeed be some electrolyte entering the microspores of the coating and accounting for the leakage observed between the forward scan and the consecutive backward scan in Figure 5.3. The presence of electrolyte will undoubtedly decrease the resistance of the coating from its tabulated value rendering the coating less efficient.

Now that insulated tips have been characterized, the procedure needs to focus on exposing the smallest and cleanest platinum part possible. Tips made by the regular procedure used worldwide that consists in heating the LDPE glue layer until a point were current flows in a solution containing a dilute redox species like ferrocenemethanol or ferri/ferrocyanide produced poorly reproducible tips that are not suitable for studies of the double layer potential distribution because the exposed platinum area was in the micron range according to Scanning Electron Microscope (SEM) micrographs coupled to EDS (Energy Dispersive Spectroscopy) measurements. In EDS, incident electrons are focused on the SEM sample and emitted X-ray photons are collected. The collected X-ray spectrum is characteristic of the atomic orbital structure, and therefore the nature of the material, that emits them. In our case EDS allowed to distinguish between LDPE-coated areas (rich in carbon) and exposed platinum areas.

2.2.3. Tip apex exposure

Such capacitive tips were then placed in the EC-STM setup in a 10^{-5} M KF electrolyte solution. A 0.13 cm² Pt-foil surface (127.5-µm thick, 99.99%, Sigma-Aldrich), a AgCl-coated Ag wire and a Pt wire were used respectively as working, quasi-reference (QRE) and counter electrodes. The Pt foil was cleaned by ultrasonication in methanol, then deionized water and immersion in a 30 % hydrogen peroxide solution acidified to pH=4 with sulfuric acid for 30 minutes and rinsed with deionized water. The Pt foil was used as a surface in the setup (working electrode) and was held at a potential around -200 mV vs. QRE where only a low steady-state negative (reduction) current between -100 and -200 nA was measured after

up to 10 minutes[25]. Only a small potential-dependent current of 10 to 50 pA determined to be background noise from the STM preamplifier was flowing at the tip far away from the surface. The surface was then approached by a combined sequence of 1 motor step and a piezoelectric ramp from half a motor step retracted position at an apparent rate of 500 nm/s while the tip was held at +600 mV vs. QRE. The tip current to be reached by the feedback loop is set to 150 pA, with high values of the proportional and integral gains, typically 5, to ensure a fast retraction of the z-piezoelectric tube once the surface is sensed by the system. When the coated tip is in close proximity of the surface, electrons tunneling from the surface to the tip are believed to blow a hole the size of the apex of the sharp metal piece wrapped in the polymer coating, once this dielectric medium is saturated with electrons, and expose only a small metallic area similarly to reported filed-emission methods for glass-insulated PtIr tips[26] but with smaller biases (800 mV instead of 15 V). The feedback loop then maintains the chosen current setpoint for a few seconds before the tip is moved by the motor 20 microns away from the surface. The tip current monitored vs. time of the process is shown in Figure 5.5. Attempts at tunneling electrons from the tip to the surface, which would be closer intuitively to a field emission process in vacuum, resulted in much higher tunneling currents (nA regime) as the chosen setpoint suggesting a much larger exposed area. The current measured was essentially dictated by faradaic processes from dissolved oxygen or protons of the electrolyte. We will later discuss the real nature of the process and the geometry of the opening in more details.

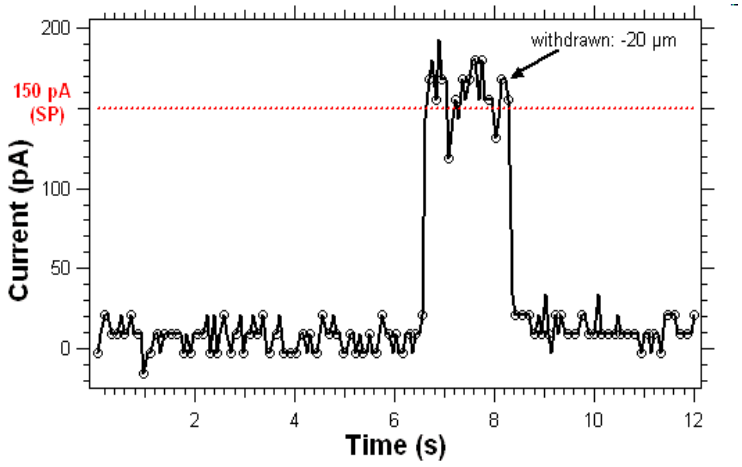

Figure 5.5: Current vs time profile for the tip apex procedure in 10 µM KF in the EC-STM setup. A tip bias is of +800 mV is applied as the insulated tip is forced to approach a Pt foil at -200 mV vs. Ag/AgCl QRE with a setpoint tunneling current of 150 pA (dotted line). The arrow indicates the point where the now open tip is taken 20 µm away from the surface by the stepper motor.

Figure 5.5 shows a typical Current vs. Time curve during the tip apex exposure sequence in 10 µM KF in the EC-STM setup. A tip bias of +800 mV is maintained as the insulated tip is approached at an apparent speed of 500 nm/s of a Pt foil surface held at -200 mV vs. Ag/AgCl QRE. From 0 to 6 s, the current, far away from the surface, is 10 ± 10 pA. This has been determined to be background noise from the STM pre-amplifier as its dependence on the applied tip potential is not consistent with an electrochemical leakage current. Around t = 6.5 s, the current jumps to the setpoint value of 150 pA corresponding to a tunneling process from the surface to the tip. The PtIr tip apex is now exposed as the surface has been sensed and a localized field emission process that has locally removed the insulating polymer-coating has occurred. This point is discussed in more details in the next paragraph. Around t = 8.5 s, the tip is manually withdrawn by invoking a stepper motor movement to place the tip 20 µm away from the surface via the user interface. The tunneling process is aborted and the tip current almost instantly returns to its initial background value without being perturbed, within the sensitivity used here[27], by faradaic processes suggesting a small exposed area.

The localized field-emission process mentioned earlier needs more attention as to its conditions. As the tip approaches the surface, it will ultimately jump into contact with the Pt foil surface after solvent molecules (water) are expelled from the tunneling gap between the tip apex and the surface. Schindler et al[28] have described the tunneling process of gold tips on a Au(111) surface in 20 mM $HClO_4$ over the whole tunneling gap up to the contact point. They report a tunneling barrier modulated by the progressive build-up of water layers on the Au surface (lower barrier originating from tunneling via H atoms form the water molecules) as the tip is retracted from the contact situation whereas the first 0.15 nm away from the surface is defined by a higher vacuum-like tunneling.

The situation described here to open SECPM tips in KF is slightly more complicated by the presence of the polymer coating (dielectric constant e = 2.35 at 1 MHz for LDPE[31]). The polymer layer can also be mechanically compressed after contact with the surface (tensile modulus G = 5-25 MPa for LDPE[31]), but eventually a vacuum-like tunneling situation will be met once the water has been expelled from the gap. Pt foil is made by compacting thin sheets of Pt(100) at a high pressure; therefore, it possesses a roughness of a few nanometers over

0.25 μm^2 as determined by Amplitude-Modulated Dynamic AFM (Tapping Mode) in ambient air.

When, upon contact, water is expelled from the gap, a situation close to a filed emission in vacuum is reached between corrugations of the Pt foil formed by surface roughness as sketched in Figure 5.6.

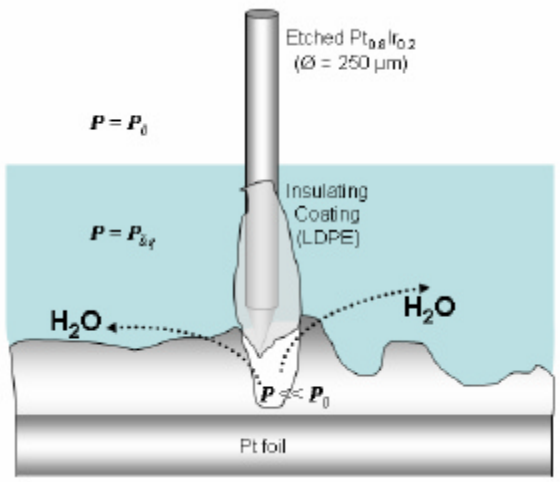

Figure 5.6: Schematic situation of the experiment when contact is made between the insulated etched PtIr wire and the Pt foil surface. Solvent molecules are expelled from the tunneling gap and a vacuum-like field emission situation is approximated because of surface roughness (» 30 nm/μm^2). Further compression of the polymer coating can occur. Dimensions are exaggerated for clarity.

In the solution bulk, one must consider a dielectric body (PE, $e_2 \approx 2.3$) surrounded by a dielectric media (water, $e_1 = 80$). This is equivalent to considering a dielectric body of permeability $e = e_2/e_1 \approx 0.025$ surrounded by vacuum.[29] Once the situation of Figure 5.6 is reached, one must then consider a body of equivalent permeability $e' \approx 2.3$ instead. The equivalent permeability is now 100 times larger, which makes the dielectric induction **D** also a 100 times larger for the same electric field **E** according to Equation (15)[29]:

$$\begin{cases} \overrightarrow{D_{D=\infty}} = e\vec{E} \\ \overrightarrow{D_{contact}} = e'\vec{E} \end{cases} \quad (15)$$

The PE coating is now much more sensitive to electric breakdown since internal electric forces that can collapse the dielectric structure are much larger in the contact situation. Breakdown in a low-density polymer like polyethylene is believed to occur via intrinsic breakdown – where the rate of unstable electrons tunneling from the valence band to the conduction band under an applied field is enough to break the charge distribution in the

dielectric– and related avalanche breakdown – where a single electron emitted from the cathode triggers a succession of electrons by collision ionization to destabilize the electronic structure of the dielectric[30]. Two processes can be distinguished for avalanche breakdown: field-emission breakdown to generate the first electron from, in the case discussed here, the etched PtIr wire and collision avalanche breakdown that will generate enough conduction electrons to disrupt the dielectric media, i.e. the polyethylene coating here. The critical field needed to disrupt the dielectric is given by the experimentally-determined dielectric strength: 27 $kV.mm^{-1}$ for LDPE and 22 $kV.mm^{-1}$ for HDPE[31]. If one assumes the glue used here is a mix of high and low density polymers, an average value of 25 $kV.mm^{-1}$ can be used. The tip bias applied in the EC-STM experiment is usually +800 mV, the dielectric strength is therefore reached only for a thickness of an assumed planar polymer layer of 0.8/25000 = 32 nm. However, the real value of the critical electric field needed to disrupt the dielectric material is probably much lower due to leakage of electrolyte through the defects in the polymer layer as shown in Figure 5.3. But, it will still be approximately an order of magnitude smaller than the coating thickness extracted from the quantitative analysis of Figure 5.3 presented in section 2.2.2, namely 200 nm. This is in favor of a mechanical contact with the Pt foil surface followed by a 10-fold contraction of the polyethylene coating to produce the exposure of the PtIr apex. In a later section, SEM and EC-STM characterizations will provide strong evidence reinforcing this assumption.

Along with an electrochemical characterization in several electrolytes, several other experiments are carried out to obtain solid information as to the surface size and state (roughness, cleanliness, stability…) of $Pt_{0.8}Ir_{0.2}$ tips intended for SECPM.

2.2.4 Electrochemical studies of PtIr SECPM electrodes

The tip voltammogram in a 1 M sulfuric acid solution is again taken at this point to evaluate the electrode area. A typical CV is shown in Figure 5.7. It is obtained by a similar method than in Figure 5.3. The potential is first swept in the positive direction and then back at 1.7 V/s with a second-order Bessel low pass filter of cutoff frequency 15 Hz after 10

seconds of quiet time at -0.62 V. The data is smoothed by a Fourier Transform with a cutoff frequency of 56 Hz to remove a residual line noise.

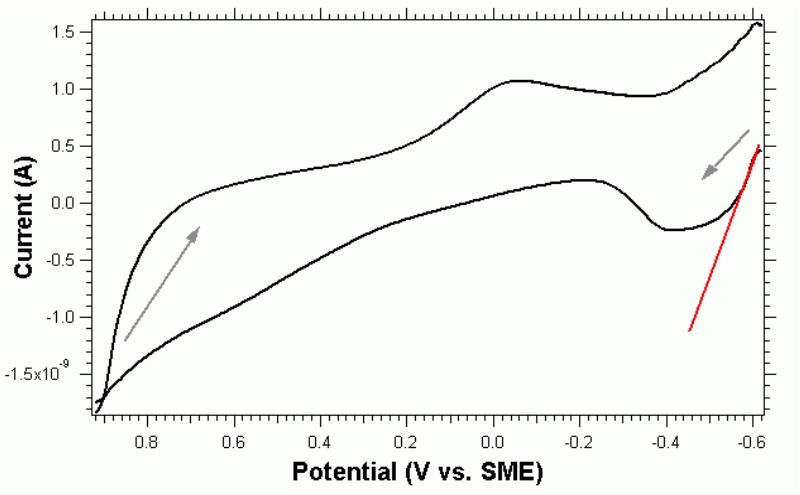

Figure 5.7: typical voltammogram of an insulated capacitive tip in 1 M H_2SO4 after the opening sequence in potassium fluoride. The signature is that of platinum. Arrows indicate the direction of the scans from the 10 s quiet time at -0.62 V. More details are given in the text.

The voltammogram obtained shows the usual features at a platinum electrode in sulfuric acid: first the hydrogen adsorption/desorption region between -0.6 V and -0.3 V, a very short double layer region, the Pt surface oxide formation from -0.1 to 0.75 V and their dissolution centered at 0 V on the scan back. The onset of bulk water oxidation is at 0.75 V.

The shortened double layer region is due to a poor degassing efficiency intended to mimic the difficulty of fitting an efficient degassing setup in the commercial SECPM that is tested here. Therefore, the first wave in the oxide formation region is already present at -0.1 V since dissolved oxygen adsorbs on the platinum surface to further form oxides. The broad hydrogen adsorption/desorption peak is mainly irreversible and does not display a particular structure suggesting a very rough Pt surface without any particular crystallographic orientation. One can use the broad oxidation peak current of desorption of under-potential deposited hydrogen (UPD H) at -0.42 V to qualitatively and comparatively evaluate the overall dimension of the exposed platinum electrode. The current difference between that peak and the current in the double layer region at -0.22 V is -442 pA and was always between -150 and -700 pA for the electrodes that were kept for further steps.

The peak of UPD H electrodesorption from platinum surfaces usually appears broader than adsorption peaks usually observed and structured into a series of finer peaks. For

example on Pt(111), the UPD H desorption area consists of a broad peak structured into up to three finer peaks corresponding to desorption from three types of H absorption sites on the Pt(111) surface at different potentials because these sites have different binding energies for UPD H[32]. In the case of PtIr tips studied here, the peak is just broadened without any particular superimposed structure. This denotes a polycrystalline surface most likely roughened by the violent etching process that has to be used to etch such a thick platinum wire in a reasonable amount of time.

In case of an adsorbed oxidized form that undergoes an irreversible reduction, the current is given by[9]:

$$i = FAk_f\Gamma^* \exp\left(\frac{k_f}{afv}\right) \quad (16)$$

Where $k_f = k_f^1 \exp(afvt) = k^0 \exp\left(-af\left(E_i - E_0^{'}\right)\right)\exp(afvt)$ is the heterogeneous rate constant of the irreversible reduction, H–Pt + e^- + H^+ → H_2 + Pt, if k^0 is the standard rate constant. a is the electron transfer coefficient. G^* is the amount of UPD H adsorbed at $t = 0$ per surface unit. v is the scan rate of the voltammogram, f is the reduced Faraday constant $f = F/RT$ and A is the electrode area of particular interest here.

In the case of the very sluggish kinetics, typically $k^0 < 1000$ s^{-1} and $a \ll 1$, that has been reported for UPD H reduction[33] and is translated into the shape of the peak for UPD H electrodeposition in Figure 5.7 and the current pseudo-plateau for E = – 0 .42 V vs. SME, this situation can be treated with the approximation: $af \ll vt$ for all values of t. In this case:

$$i \approx FA\Gamma^* k_f^i (1 - afvt)\exp\left(\frac{k_f^i(1-afvt)}{afv}\right) \approx FA\Gamma^* k_f^i \exp\left(\frac{k_f^i}{afv}\right)\exp\left(-k_f^i t\right) \qquad (17)$$

The initial slope, when $t \approx 0$, is: $-FA\Gamma^*\left(k_f^i\right)^2 \exp\left(\frac{k_f^i}{afv}\right) \approx -1.07\,10^{-8}$ A.s^{-1} (fit) and the current at the pseudo-plateau is: $-FA\Gamma^* k_f^i \exp\left(\frac{k_f^i}{afv}\right) = i(E = -0.42\text{ V}) \approx -442$ pA if the background double layer current (at E = -0.22 V) is subtracted. Provided one assumes a = 0.5 and $E_0^{'} = E_0$ = 0 V vs. NHE = -0.64 V vs. SME for the sake of argumentation, it yields:

$$\begin{cases} k_f^i \approx 24.2\,\mathrm{s}^{-1} \Rightarrow k^0 \approx 35.7\,\mathrm{s}^{-1} \\ A\Gamma^* \approx 9.11\ 10^{-17}\ \mathrm{mol} \end{cases}$$

The kinetics is relatively sluggish which validates the approximations made. With this model, one cannot separate the electrode area *A*, and the initial saturated surface concentration of UPD H G^*. Roughly, if H^+ from the 1 M H_2SO_4 totally recovers the Pt surface and if the surface is totally saturated within 10 s quiet time at -0.62 V, $G^* \approx 0.5$ mol.cm^{-2} at the very best. In this case, if $A = 2pr^2$ for an approximated hemisphere, the apparent radius of the exposed metallic part would be about 6 nm.

On the way back, the oxide peak is quite broad and extends into the hydrogen region. This suggests that the oxide formed in the first scan is not completely removed and alters the surface of the electrode preventing re-adsorption of hydrogen. This was true even for the first voltammogram taken for a freshly opened platinum electrode.

The previous elements along with the information from the UPD H desorption peak suggest that the procedure to make tips leaves a rough polycrystalline platinum surface covered with oxides. The surface of the platinum electrode can be cleaned by repeatedly cycling the electrode between hydrogen reduction and water oxidation. When this treatment is applied, we found that bubbles formed tend to increase the current range of the voltammogram recorded in sulfuric acid by up to an order of magnitude because less tightly bond polyethylene coating is irreversibly removed exposing more platinum. This goes against the requirement of very small electrodes to study double layers.

Exploitation of voltammograms in sulfuric acid to extract the geometric area is difficult because only surface processes are involved. For example, it is difficult to know the surface concentration at saturation of adsorbed molecular hydrogen since it depends on the number of sites available on polycrystalline platinum, the different types of these sites and the possible interaction between sites of different types (complex adsorption isotherms).

Concentrated (0.1 M) solutions of ferri/ferrocyanide were used to evaluate the apparent radius of the exposed electrode assuming a hemispherical geometry. Ferri/ferrocyanide was preferred to a couple like ferrocenemethanol because potassium salts of ferri/ferrocyanide salts, for instance, have a higher solubility in water, which amplifies the measured currents where the electrode area is expected to be very small. However, ferrocyanide reversibly adsorbs and desorbs onto platinum electrodes as a polymeric hexacyanoferrate complex with

mixed Fe(II) and Fe(III) content from aqueous KCl solutions, inhibiting electron transfer without totally preventing it[34]. Supporting electrolyte was omitted from the concentrated solutions used since the contribution of migration to the steady state current is expected to still be reasonably small in concentrated solutions with a small electrode.

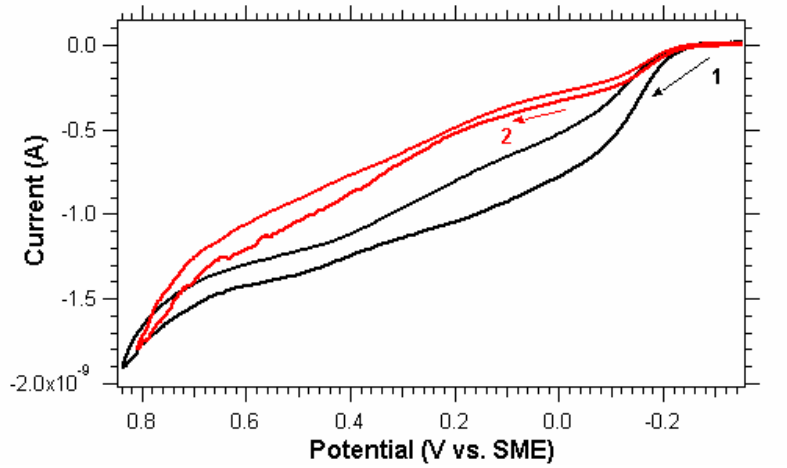

Figure 5.8: cyclic voltammograms in 0.1 M K_4FeCN_6 at 50 mV/s of a polymer-coated PtIr electrode opened in the EC-STM setup. The arrows indicate the polarity of the first scan. 1 indicates the first scan taken and 2 indicates a subsequent scan.

A resulting voltammograms is shown in Figure 5.8. It was taken at 50 mV/s in an argon-degassed solution of 0.1 M K_4FeCN_6 in deionized water[35] between -0.35 V and +0.84 V measured with respect to the saturated mercury sulfate electrode (SME). A negative oxidation current is observed. No wave in the more negative potential was observed. The steady-state wave is distorted from the expected sigmoidal shape because of adsorption/desorption/decomposition cycles on the platinum electrode. This prevents the diffusion-controlled steady-state regime from being reached. The modification of the surface state is also visible in the hysteresis of the voltammogram as a charging current builds up that cannot be due to the double layer at this slow scan rate. However, the onset of water oxidation around 0.6 V can be used to evaluate the diffusion-limited current; it is equal to -1.4 nA at 0.6 V. Another subsequent voltammogram shows more distortion from the sigmoidal shape and a slightly lower current at 0.6 V. Moreover, investigations on similarly small electrodes in 20.2 mM K_3FeCN_6 with 0.2 M KCl show an evolution of the reduction current to $FeCN_6^{4-}$ in cyclic voltammograms from an initial quasi steady-state to a similarly

distorted wave that stabilizes after a 25% current loss form the initial voltammogram[36]. We estimate our steady-state current to be 25% greater than 1.4 nA. That is roughly 1.8 nA.

The diffusion coefficient for a 4.0 mM $FeCN_6^{4-}$ solution with 0.1 M KCl is 6.5 10^{-6} cm^2/s.[37] The steady-state diffusion-limited current at a hemispherical microelectrode is:

$$i_D = gnFDC^* r_{app} \quad (18)$$

D is the diffusion coefficient of the redox species exchanging *n* electrons with the electrode at a bulk concentration of C^*. r_{app} is the apparent radius i.e., the radius an electrode of a known geometry, given by the factor *g* (2π for an hemisphere, 4 for an inlaid disk for instance), with the same steady-state current would have. *F* is the Faraday constant (96485 $C.mol^{-1}$). In the case studied here, r_{app} is approximately equal to 5 nm if a hemispherical geometry is assumed and 8 nm assuming an inlaid disk. There is a large imprecision on this value due to the conditions in which the cyclic voltammogram was taken (choice of redox couple, concentration…). Also more complex geometries can show sigmoidal shapes and can be interpreted with the available expression obtained for known simple diffusion conditions[38]. In particular, electrodes described here have a quite soft polymer coating that could prevent access to the electrolyte to parts of the electrode.

At this point, only qualitative elements describing the electrodes prepared following the procedure exposed earlier can be drawn. The tips are made of a rough polycrystalline surface composed mainly of platinum. They exhibit apparent radii in the range of 10 nm.

2.2.5. Non-electrochemical characterization of SECPM tips

2.2.5.1 Electron Microscopy

A commercial Scanning Electrochemical Microscope (LEO 1530) was used to image the apex of tips opened as described in section 2.2.3. The microscope consists of a Shottky-emitter-enhanced Field Emission Gun, a beam booster and a Gemini column using a setup of electromagnetic lenses that avoid beam crossovers along the column to reduce beam broadening (resolution loss) especially with low-energy electron beams (low overall acceleration voltages). An in-lens detector (conventional Everhart-Thornley) collects secondary electrons re-emitted upon inelastic interaction with the sample and is located in the

column close to the final lens at the gun aperture. It was preferred to the backscattered electron detector because of the large tilt angle that would result in low collection efficiency. Backscattered electrons undergo elastic collisions with the sample surface without modifying it. Since, we are concerned with not modifying the imaged tip in situ, it is wiser to detect secondary electrons to be sensitive to any modification of the sample by the incoming beam. Secondary electrons have low energies and are therefore confined near the surface and are primarily emitted within a thin volume in the interfacial region, which makes their detection very sensitive to the surface state (local roughness). Acceleration voltages of electrons focused on the sample as low as 1 kV (EHT)[39] and working distance (WD) of 3 to 5 mm had to be used to prevent local deterioration of the polyethylene coating upon interaction with the electron beam. In situ reorganization and/or removal of the polyethylene glue coating were observed when large areas where scanned with electrons accelerated to 6 kV 10 mm away form the gun sample. Tips were checked by a cyclic voltammogram in sulfuric acid according to the procedure described in section 2.2.2.4 after SEM experiments; they had a similar current level in 1 M sulfuric acid than before the SEM experiments when a 1 kV EHT was used.

Tips were glued flat on the aluminium stage with sticky carbon tape. They were imaged with the stage tilted by an angle of 15° with respect to the incoming electron beam so that the incident electron beam hits the flat part of the surface with an angle of 15°.

Figure 5.9 shows scanning electron micrographs (slow scan without frame averaging) of a tip prepared by the procedure exposed earlier. Figure 5.9a is taken at a low magnification; it illustrates the general shape of the tip as it appeared under the optical microscope before opening the apex in the EC-STM. The 5-μm long protrusion obtained by locally melting the coating around the sharper platinum wire is not altered by mechanical strain during the opening sequence in the EC-STM at this resolution. The end of the sharp feature appears bright because of a localized field emission of secondary electrons from a slow accumulation of incident electrons compared to the beam scan rate (charging) in a sharp feature of the insulating polymer coating. Figure 5.9b is a zoom on the sharp feature from Figure 5.9a. The protrusion of the coating mentioned earlier is flattened over 2 μm, which suggests some mechanical contact with the Pt foil during the opening sequence in the EC-STM setup. Three spots in the central area of the scan appear brighter; the largest one is over 400 nm wide and

is surrounded by 2 smaller 100-nm wide features. This could represent thin pieces of polymer coating, again charged by the incident electron beam, out of the plane defined by the flatter 2 µm wide area and covering part of the platinum electrode. The electrode could be recessed or embedded as a much smaller inlaid disk inside these features since voltammetry measurements suggest a smaller electrode. At this point, more work would be needed to find optimal imaging parameters to reduce the charging effect of the polymer coating. Attempts at imaging the tip apex with 90° stage tilt, and therefore aligning the beam perpendicularly with the sample surface to minimize focusing artifacts since the polymer coating surface seems to be quite rough according to Figure 5.9b, were unsuccessful at reducing charging effects. Moreover, if the electrode is really around 10-20 nm, the maximum resolution of this SEM will be attained.

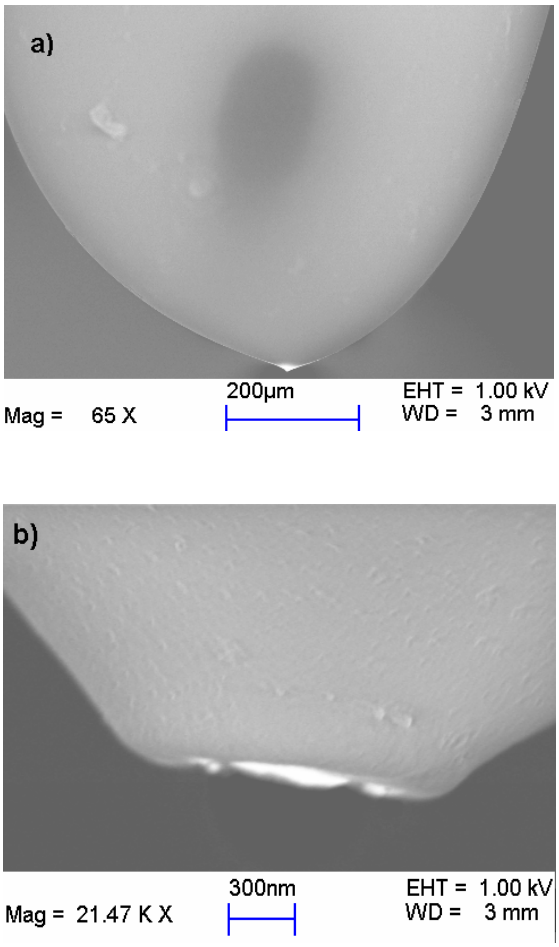

Figure 5.9: Scanning electron micrographs of a PtIr tip prepared by the procedure described earlier in the text. The images are taken at a slow scan rate without frame averaging and display details at low (a) and high (b) magnification. The platinum part appears to be slightly recessed in the glowing central area of insulating polymer coating.

2.2.5.2 Electrochemical Scanning Tunneling Microscopy (EC-STM)

To determine if the platinum electrode was recessed within the polymer coating, a tip prepared as described earlier was used to image the Pt foil in 10^{-5} M KF immediately after the opening sequence around the same spot where the tip was initially approached to expose the apex. This was done using 0° and 90° scan angles and when scanning positively or negatively along the slow scan axis at the same tip velocity (1 µm/s) and for the same scan size (500 x 500 nm, 512 x 512 points). The images were obtained by scanning the tip over the Pt foil immediately after the current jump from the background value when the tip is totally closed to the setpoint tunneling value of 150 pA as depicted in Figure 5.5 at a speed of 1 µm/s. The surface is held at -196 mV vs. Ag/AgCl QRE where the resulting current is about –100 nA and the tip is maintained at +200 mV vs. Ag/AgCl QRE, which yields a tip bias of +400 mV. The images have an RMS roughness R_q = 1.114 nm over 0.25 µm^2. The roughness measured in EC-STM is quite consistent with measurements obtained in contact-mode AFM on similar Pt surfaces (R_q around 2 nm over 0.5 µm^2)[40]. The resulting EC-STM scans of the Pt foil surface with a freshly prepared SECPM tip are shown in Figure 5.10.

The EC-STM scans are flattened by a second order polynomial (line by line) to remove artifacts from sample tilt (first-order) and tip curvature effects during the scan (second-order). Scans at 0° show a pronounced discrepancy between down and up scans suggesting a strong asymmetry in the slow scan axis direction (*x* in Figure 5.10). When scanning at 90°, down and up scans are less different because the asymmetry is much less in the fast scan axis direction (*y* in Figure 5.10). Although the scan speed is quite fast, some effect of piezo drift appears in Figure 5.10 between downward and consecutive upward scans for instance.

A tunneling current of 150 pA with a bias of 400 mV corresponds to a tunneling gap resistance of 2.6 GΩ. The solution resistivity of a 10 µM KF solution based on tabulated limiting equivalent ionic conductances is 0.78 MΩ.cm. This suggests a tunneling distance of about 3 µm. Since a correct contrast (20 nm) and stable imaging conditions with a tunneling current value at the lower limit of the instrument capabilities is obtained quite far away from the surface, the tip cannot be much recessed into the polymer coating surrounding the platinum area.

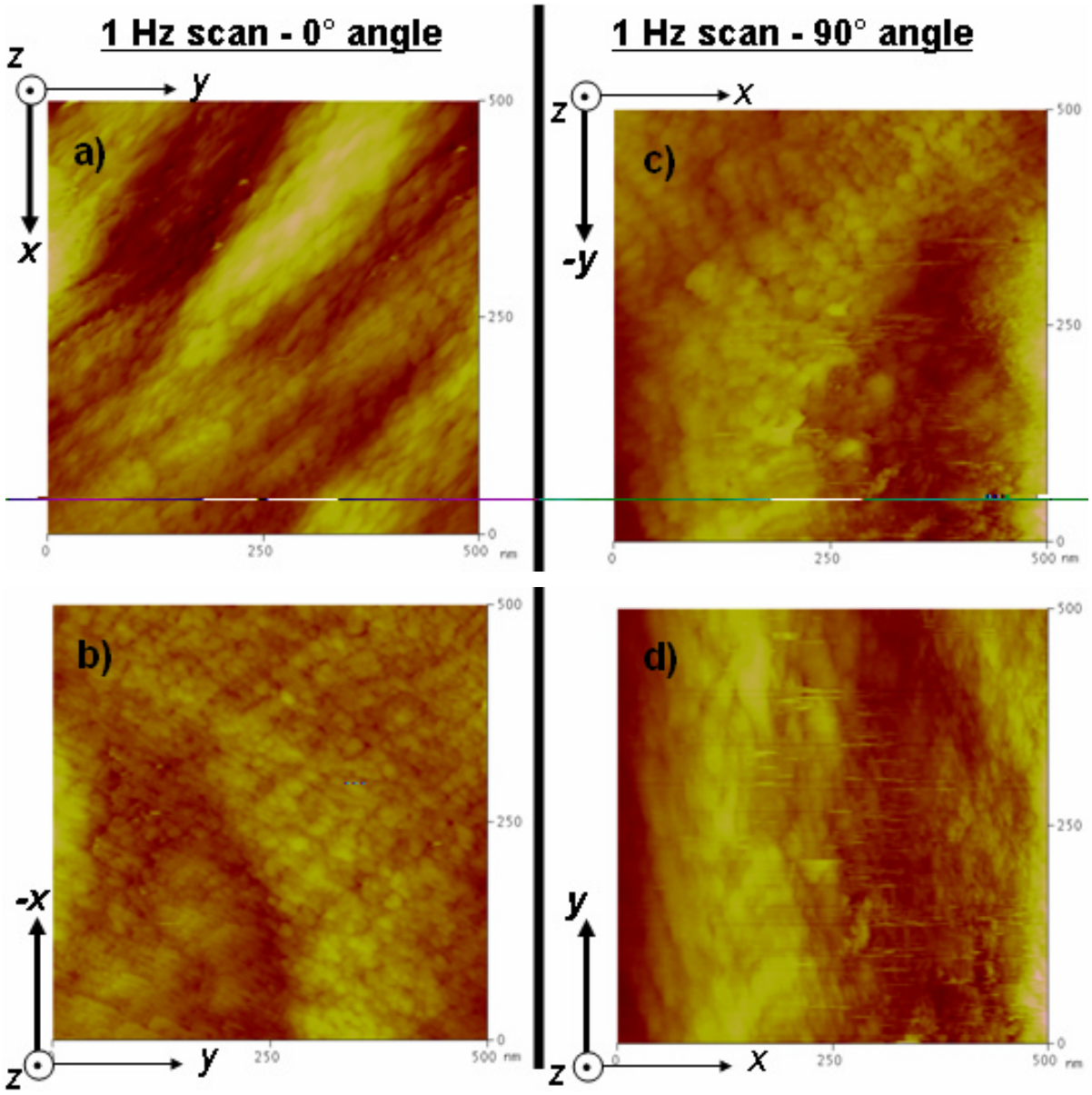

Figure 5.10: EC-STM images of the Pt foil obtained in 10 µM KF with a polymer coated PtIr tip immediately after the opening sequence with the procedure exposed in the text. The tip is first scanned downward at an angle of 0° (a) and upward (b), then downward at and angle of 0° (c) and upward (d). The tip velocity is 1 µm/s. The height data range is 0 – 20 nm. The images are flattened by a second-order polynomial to remove artifacts from sample tilt and tip scanning curvature. They show a large asymmetry in one direction (*x*) and a slightly lower asymmetry in the other direction (*y*).

From the dielectric breakdown considerations, the multidirectional EC-STM scans and SEM micrographs, the tip apex exposure can be fully characterized. There is a mechanical contact that creates a vacuum-like field emission situation due to surface roughness after

compression of the insulating polymer layer schematically represented in Figure 5.6. The presence of a large flat area at the end of the tip in SEM confirms mechanical contact with the Pt foil over a µm-scale. But, due to surface roughness, pressure upon compression of the coating is only exerted on the sides of the sharp platinum tip. Consequently, when the layer relaxes after breaking the contact once the tip starts tunneling, the process leaves a mostly non-recessed metallic area that allows proper imaging in EC-STM. EC-STM scans also suggest a slightly asymmetric tip shape.

Additionally, electrochemical studies in sulfuric acid and ferri/ferrocyanide suggest a rough polycrystalline platinum surface, apparently hemispherical with a radius around 10 nm.

3. Measurements of double layers on several surfaces

In this section, we wish to use $Pt_{0.8}Ir_{0.2}$ tips prepared as described in section 2.2, with a very small exposed platinum electrode to probe electrical double layers in a dilute I-I electrolyte (potassium fluoride, 10 µmol/L) when they are approached to surfaces like gold, platinum (metals), HOPG (conductor), Si/SiO_2 (semi-conductors) or mica (charged inorganic insulator).

3.1 Early experiments with larger exposed areas

The tips used for early SECPM experiments reported in this section were made with a slightly different procedure as the one described in details above. A mechanically cut sharp $Pt_{0.8}Ir_{0.2}$ wire (250-µm diameter, Veeco Probes, LLC) was insulated with either polyethylene hot-melt glue or Apiezon wax heated to about 130 °C on a copper plate until a similar voltammogram than the one shown in Figure 5.3 was obtained. Then the sharper end of the insulated tip was manually approached to 0.5 mm of the cleaned copper plate held at 90 °C for 15 seconds. This was repeated until a linear sweep voltammetry (LSV) experiment taken at 10-20 mV/s in an argon-saturated 1 mM ferrocenemethanol aqueous solution containing 100 mM KCl from 0 to 0.6 V vs. a KCl-saturated Ag/AgCl electrode (SSCE) showed quasi

steady-state diffusion-limited current between 80 pA and 1 nA typically (apparent radii of 50-80 nm in a hemispherical geometry).

All approach curves – or potential-separation plots (P-S plots) in the Nanoscope software provided by the manufacturer – were obtained in argon-saturated KF solutions of various concentrations ranging from 1 µM to 1 mM. Ar was preferred to N_2 because its solubility is twice higher than that of N_2 and equal to that of O_2 in water at 25 °C. Degassing is therefore slightly more efficient with Ar than with N_2. Solutions were carefully degassed with efficient argon bubbling for 15-20 minutes before use. Potential profiles were measured either with respect to the surface (WE) or with respect to the Ag/AgCl QRE described earlier unless otherwise mentioned.

3.1.1 Potential profiles on gold

In this section, we will discuss potential profiles obtained by approaching a piece of polycrystalline gold at different KF concentrations and with different values of the applied surface potential (E). Prior the SECPM experiments, the bulk gold surface was polished with a 0.05 µm alumina suspension in water, thoroughly rinsed with deionized water, ultrasonicated (υ = 40 kHz) in water, methanol and again water for 10 minutes in each cycles. Finally, it was immersed in an 80 °C 70/30 Piranha solution[41] for 15 minutes and thoroughly rinsed with deionized water.

3.1.1.1 Electrolyte concentration dependence

Figure 5.11 shows the potential profiles obtained in 1 µM, 100 µM and 1 mM argon-saturated KF as the gold surface was held at +300 mV vs. Ag QRE. The measured potential difference F (or Ptip in the Nanoscope software) is defined as the difference between the surface (WE) potential and the Tip potential. The first is treated with the Gouy-Chapman-Stern model detailed in section 1. In order to measure potential distributions in the double layer, the tip must induce a negligible perturbation to the ions distribution within the diffuse layer as it is approached to and retracted from the surface. In other words, the situation is simplified by assuming there is no interaction between the tip and surface double layer. In

this case, the interfacial potential of two weakly interacting EDLs is simply the linear superimposition of the potentials of the two EDLs (Linear Superposition Approximation (LSA)[42]). With the LSA, the tip and the surface build-up their own EDL when they are far away from each other but, as the tip approaches the surface and its EDL does not interact strongly with the surface EDL, the EDLs start to overlap and the probe follows the potential changes in the surface diffuse layer. Such a required weak interaction can be attained by rendering the probe surface negligible compared to the surface area. Hence the need to efficiently insulate PtIr tips used in SECPM. More explicitly, under the LSA, the measured potential F is given by $\Phi = E_{surf} - E_{tip} \approx (f_0 - E_{tip}^{\infty}) - E_{surf}^{GC}$ since E_{tip} does not vary much from its value far away from the surface measured versus the applied surface potential F_0 ($\approx F_2$), $F_0 - E_{tip}^{¥}$ ($\approx F_2 - E_{tip}^{¥}$), as it probes the surface potential that is described with the Gouy-Chapman-Stern (GCS) theory E_{surf}^{GCS}. Consequently:

$$\Phi = E_{surf}^{GC} - E_{tip} \approx \left(f_0 - E_{tip}^{\infty}\right)\left(1 - \frac{1}{f_2}\frac{4k_BT}{ze}\,Arcth\left(th\left(\frac{zef_2}{4k_BT}\right)\exp\left(-k\left(x - x_2\right)\right)\right)\right) \qquad (19)$$

F_2 is the surface potential in the OHP located at $x = x_2$. Since the potential drops linearly over a small distance between x_2 and $x = 0$, F_2 is not very different from the applied potential F_0. k is the inverse Debye length and is linked to the electrolyte concentration by: $k = 3.29\times10^{-7} C^{*1/2}$ for a I-I aqueous electrolyte.

The data from Figure 5.11 were fitted according to Equation (19) to extract values of the bulk KF concentration C^* and the tip potential far away from the surface $E_{tip}^{¥}$. The curves are normalized to the fitted value of $F_0 - E_{tip}^{¥}$ for clarity. The parameters obtained summarized and compared to nominal or measured values in table 1. In the fitting procedure, $E_{tip}^{¥}$ is first kept equal to its value from the measured value of the tip potential with respect to the surface potential at a distance $D \approx 500$ µm ($F_0 - E_{tip}^{¥}$) whereas the other parameters are free. Then, in a second step, $E_{tip}^{¥}$ is left free and is adjusted by the fitting routine to further converge the fit, i.e. until the residual error reaches a stable minimum value.

Table 1: fitted KF bulk concentrations C^* and tip potential vs. SSCE far away from the electrode E_{tip}[8] for several nominal concentrations tested. The solution was degassed with argon prior to the SECPM measurements. The corresponding data are shown in Figure 5.11. The PtIr tip used has been insulated with hot-melt polyethylene glue. The gold surface is held at +300 mV vs. Ag QRE.

Applied F_0	Nominal C^*	Fitted C^*	Fitted $E_{tip}^{¥}$	Measured E_{tip} at D » 500 µm
+300 mV	1 µM	2.19 µM	+247.9 mV	+250.2 mV
+300 mV	100 µM	105.4 µM	+103.6 mV	+110.3 mV
+300 mV	1 mM	2.94 mM	+228.8 mV	+231.3 mV

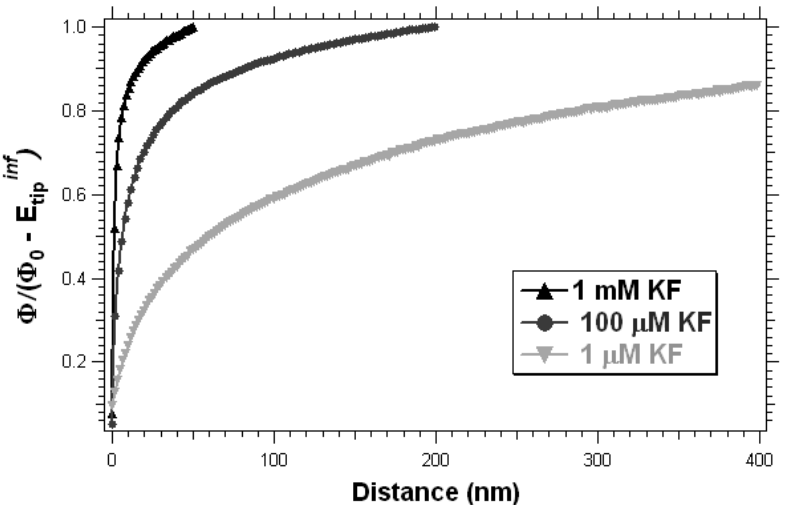

Figure 5.11: Series of approach curves on polycrystalline gold held at +300 mV vs. Ag QRE for different bulk concentrations of KF. The solutions were degassed with argon prior to use in SECPM. The tip potential is measured with respect to the surface. Values fitted with a Gouy-Chapman-Stern model are summarized in table 1. The curves are normalized to the fitted $F_0 - E_{tip}^{¥}$ for clarity.

From the results summarized in table 1, the studied KF solution scales properly with the concentration. However, there is a residual systematic error on the fitted value than cannot be explained by dilution imprecision only. In can be noted that, for C^* = 1 µM, errors may also arise from other dissolved species since, for instance, dissolved atmospheric CO_2, solvated as HCO_3^- and CO_3^{2-}, add up to about 1 µM as well. Furthermore, the tip potential far away from the surface $E_{tip}^{¥}$ does not come back to its initial value after each approach/retract cycle. This indicates tip instability. The value stays close to +200 mV vs. Ag QRE but wanders around between two consecutives cycles. This is because the platinum that constitutes the tip is very

sensitive to dissolved oxygen even after careful degassing with argon. Indeed, before the first scan, as soon as the tip is placed in the degassed KF solution, it jumps to a value of about +150 to +200 mV vs. Ag QRE far away from the surface. This corresponds to an open circuit potential dictated by dissolved oxygen reduction. This point will be discussed in more details in a next section.

3.1.1.2 Surface potential dependence

Similarly, the dependence of the measured potential difference between the tip and the polycrystalline gold surface on the applied surface potential was fitted according to the Gouy-Chapman-Stern theory exposed in section 1. The results are shown in Figure 5.12. Again, the KF solution, at a fixed concentration of 10 µM this time, was carefully degassed with argon before use. Potentials (Tip and surface) are measured with respect to an Ag/AgCl QRE placed about 2 mm away from the planar disk-shaped surface. Figure 5.12 shows a series of approach curves taken in 10 µM KF at 50 nm/s for a gold surface held at -200, +200, +400 or +400 mV vs. Ag/AgCl QRE. For clarity, the curves are first subtracted with the fitted value of $E_{tip}^{¥}$ and then normalized to F_2 ($\approx F_0$). In this series of experiments, the tip potential F (Ptip in the Nanoscope software) as well as the surface potential E are now measured with respect to the reference electrode. Moreover, as soon as the tip enters the surface double layer, it is assumed to follow the surface potential profile without perturbation. This modifies Equation (19) with the tip-sample system still following the LSA:

$$\Phi \approx E_{tip} - E_{RE} = \frac{4k_BT}{ze} Arcth\left(th\left(\frac{zef_2}{4k_BT} \right) \exp\left(-k\left(x - x_2\right)\right) \right) + E_{tip}^{\infty} - E_{RE} \quad (20)$$

Again, the potential F_2 in the OHP is not very different from the applied surface potential Φ_0. $E_{tip}^{¥}$ is still defined as the tip potential far away from the electrode, but measured versus the reference electrode this time, though.

According to Equation (6), the length of the diffuse layer k^{-1} = 96 nm for a 10 µM I-I electrolyte regardless of the value of the applied surface potential. Table 2 compares the

values fitted with Equation (20) for different surface potentials. In the fitting procedure, $E_{tip}^{¥}$ is first kept equal to the measured value of E_{tip} at 500 µm and then left free.

Table 2: surface-potential dependence of the potential profiles obtained in argon-degassed 10 µM KF. The expected Debye length is 96 nm. The table summarizes fitted values of the Debye length k^{-1} and $E_{tip}^{¥}$ for the data shown in Figure 5.12. The PtIr tip used has been insulated with Apiezon wax.

Applied F_0	Fitted k^{-1}	Fitted $E_{tip}^{¥}$	Measured E_{tip} at D » 500 µm
-200 mV	145.7 nm	-72.6 mV	-85.9 mV
+200 mV	265.1 nm	+170.5 mV	+177.3 mV
+400 mV	72.9 nm	+336.5 mV	+350.1 mV
+600 mV	30.9 nm	+372.6 mV	+380.2 mV

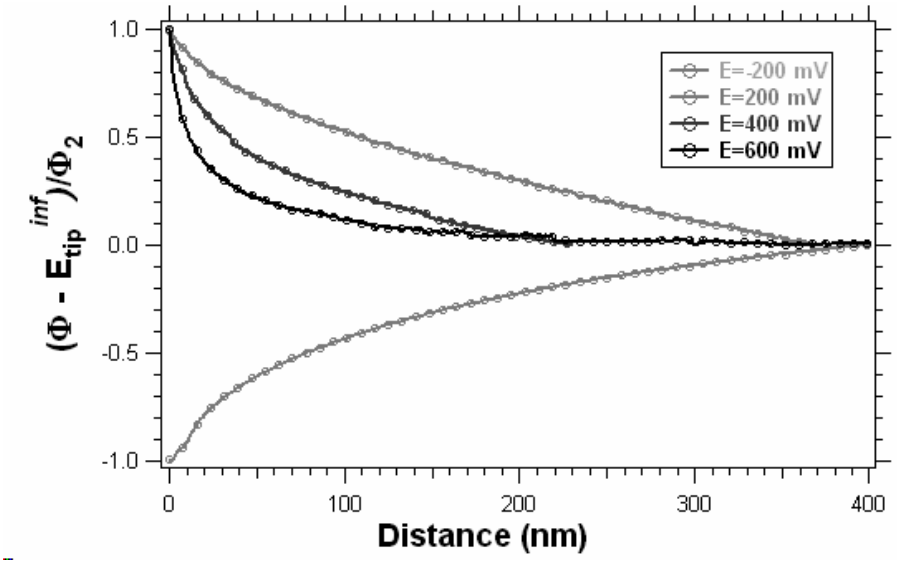

Figure 5.12: Series of approach curves on polycrystalline gold held at -200, +200, +400 and +600 mV vs. Ag/AgCl QRE for a bulk concentration of 10 µM KF. The solution was degassed with argon prior to use in SECPM. The tip potential is measured with respect to the reference electrode. Values fitted with a Gouy-Chapman-Stern model are summarized in table 2. The curves are subtracted with the fitted value of $E_{tip}^{¥}$ and normalized with F_2 (»F_0) for clarity.

The data in Figure 5.12 show a strong dependence of k^{-1} and especially $E_{tip}^{¥}$ on the applied surface potential F_0 whereas the Gouy-Chapman-Stern theory strictly shows the diffuse layer length is independent of the applied electrode potential. This suggests that

processes measured here are not only of non-faradaic nature. A particularly striking fact is the increase in k^{-1} with surface potential. This denotes a non-faradaic interaction of the tip with the sample within the time course of an approach/retract cycle. This hypothesis is confirmed by the dependence of $E_{tip}^{¥}$ (open-circuit potential of the tip far away from the surface) that follows the same trend than k^{-1}. Since this value will be set by faradaic processes from traces of dissolved oxygen or proton reduction or even water oxidation by the Pt surface. The dependence of the Debye length could be due to a faradaic process at the PtIr tip (O_2 or H^+ reduction) as hindered diffusion by the Au surface is more enhanced as the tip gets closer to the surface i.e., a situation close to the feedback mode in SECM[6].

To this date, the only report in the literature of potential profiles where the potential is measured directly in a scanning probe setup is due to Park et al in 2004[43]. However, results on EDL potential measurements were published earlier with Surface Force Apparatus (SFA)[44] where to mica planes are approached with piezoelectric elements to sense an "hydrodynamic force" or Atomic Force Microscopy (AFM)[45] where a charged silica sphere is chemically attached to a commercial silicon nitride cantilever. In each of these reports, the potential measurement is indirect since an electrostatic force is measured and an extrapolation has to be made to obtain potential values. In the results reported here, the measurement is direct since potentials are sensed and recorded in real-time. Park et al studied a Au(111) surface in a 1 mM with gold tips using a homemade instrument similar to the commercial Veeco instrument used here but probably less sensitive. He reports a similar potential-dependent experiment with a major difference. No matter what potential applied to the Au(111) surface is, a difference of 0.12 V always remains between the tip and applied surface potentials even upon contact with the Au surface. In SECPM, the only limitation is the setpoint potential value, i.e. the potential value for which the feedback loop is turned on by the system to maintain the piezoelectric tube within a certain distance of the surface and prevent tip crashing. In all experiments reported here, the setpoint value was chosen so that the tip potential is always 5-10 mV lower than the applied potential surface at the end of the approach cycle. For this reason, in Figure 5.11 for example, the tip potential vs. the surface never reaches zero but gets very close to it. Park et al explain the 0.12 V difference upon contact by the difference in the open-circuit potential values between the surface (WE) and the probe. It might also be linked to the insulating coating (nail varnish[46]) around a slightly

recessed gold tip or even local deformation of the gold sample[47]. The different nature of the tip used in SECPM could explain that our system can sense the surface potential within as close as 5 mV.

3.1.2 Potential profiles on HOPG

According to Equation (6), the Debye length k^{-1} also depends on the dielectric constant of the medium and therefore, on the nature of the solvent. A freshly cleaved Highly-Oriented Pyrolitic Graphite (HOPG) sample was approached at 100 nm/s in SECPM with a PtIr tip insulated with hot-melt polyethylene glue and exposed by heat in deionized water and methanol with dielectric constants at 20 °C of 78.54 and 32.63 respectively[64]. All KF solutions were carefully degassed with pure argon prior to use in SECPM. Table 3 summarizes expected and fitted results for such approach curves. Tip potentials were measured against the surface (working electrode) and cell potentials are given with respect to an Ag QRE.

Table 3: summarized fitted values compared to expected values for SECPM approach curves in methanol and in water. The HOPG surface is held at +100 mV vs. Ag QRE. Tip potentials are measured with respect to the HOPG surface. Curves where fitted with Equation (19).

Applied F_0	**Solvent**	**Expected** C^*	**Fitted** C^*	**Fitted** E_{tip} ¥
+100 mV	Water	100 µM	24.5 µM	-44.4 mV
+100 mV	Water	1 mM	28.2 µM	-21.5 mV
+100 mV	Methanol	100 µM	1.3 µM	-48.8 mV
+100 mV	Methanol	1 mM	3.8 µM	-27.9 mV

Table 3 shows a large discrepancy between fitted values and expected values of the electrolyte concentration even in water. Large errors when fitting approach curves on HOPG with a Gouy-Chapman-Stern model were systematically encountered. This could be due to ion structuration into poly-ions at the hydrophobic HOPG surface. Furthermore, elastic deformation of HOPG samples by an STM tip[48] or an AFM probe[49] is known. More likely, small pieces of graphite can adhere to the tip or the surrounding insulating polyethylene glue

upon slight contact with the HOPG surface and have sometimes been observed in the optical microscope. Such events can drastically modify the measured potential profile.

3.1.3 Potential profiles on Si/SiO_2

A Si/SiO_2 system was approached in the EC-STM mode and in the SECPM mode with polyethylene-glue-coated PtIr SECPM tips with a large exposed metallic apex in 10 µM KF. Approaching a mixed system of a semi-conductor (Si) and its insulating oxide layer (SiO_2) is a first step toward imaging insulators by measuring diffuse layer potential profiles in SECPM.

A 1 cm^2 piece of native-oxide boron-doped Si(100) was used in the SECPM experiments. It was cleaned with standard procedures used to clean Si[50]. Briefly, the procedure consists in three steps: ultrasonication in acetone and methanol for basic degreasing purposes, immersion in 80 °C H_2O2:NH_4OH:H_2O (1:1:5) for 15 minutes that leaves a very hydrophilic clean oxide-covered surface and immersion in 49 %(v) fluorhydric acid (HF) for 5 minutes to etch the oxide layer away and leave a hydrophobic H-terminated Si(100) surface. Samples used were thoroughly rinsed with deionized 18 MΩ.cm Milli-Q water between each step. The Si(100) sample was placed in the SECPM setup immediately after HF-treatment to prevent rapid re-growth of native oxide in ambient atmosphere. The time elapsed between the end of the HF-treatment and the first SECPM approach curve was never more than 3 minutes and the KF solution was carefully degassed prior to use in the SECPM.

The approach sequence was performed in essentially two steps. First, the H-terminated Si(100) surface is approached in the EC-STM since tunneling from H-terminated Si can be readily observed by STM in vacuum[51]. This step was done by holding the surface potential (WE) at -800 mV vs. Ag/AgCl QRE in order to prevent *in situ* growth of silicon oxide in the KF solution. Once the surface was found and a tunneling current of 120 pA could be maintained, the tip was retracted 20 µm away from the surface by the stepper motor, the surface was stepped at a potential of +300 mV vs. Ag/AgCl QRE for 5 minutes to grow an oxide layer on top of the H-terminated silicon surface in order to render the surface insulating. Then, the surface was stepped back to –350 mV vs. Ag/AgCl were the surface

current (residual -24.41 nA for a 0.13 cm^2 surface) was the lowest assuring a minimization of faradaic processes at the Si/SiO_2 electrode and approached in the SECPM mode.

A resulting typical approach curve as the surface was held at -350 mV vs. Ag/AgCl is shown in Figure 5.13. The approach speed is 40 nm/s. The most intriguing feature is the profile between 0 and 100 nm. Although the surface is held at -350 mV and that a setpoint of 200 mV is used, the potential profile only reaches -48 mV vs. Ag/AgCl at d = 100 nm and almost linearly drops to -58 mV within the last 100 nm. This could partially be explained by the presence of the insulating oxide thickness although the thickness is expected to be a few nanometers instead of 100 nm suggested by the potential profile in Figure 5.13.

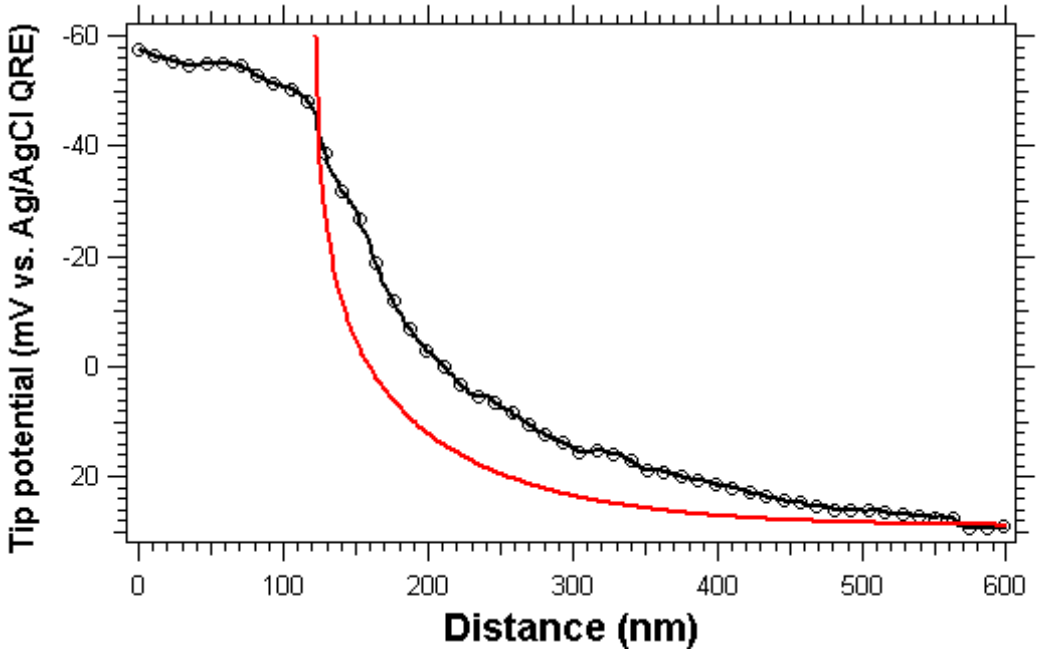

Figure 5.13: potential profile obtained while approaching a Si/SiO_2 surface held at -350 mV vs. Ag/AgCl QRE at 40 nm/s in 10 µM KF carefully degassed with argon. The first part is not too far off from the potential profile predicted by the Gouy-Chapman-Stern model (solid curve). But in a second part, the potential almost linearly drop from -48 mV to -58 mV without ever reaching a value near the -350 mV applied to the Si surface.

The resistivity of SiO_2 grown on Si is typically about 10^{15} Ω.cm[52]. A 1 nm-thick oxide layer grown in the KF solution would have a resistance of about 0.1 GΩ. A potential drop of 290 mV as suggested by the potential profile would require a current of 2.9 nA to flow between the tip and the sample. This value is much too high for an open-circuit potential even if faradaic processes are occurring. Along with the distance of 100 nm over which the

phenomenon occurs according to Figure 5.13, another, more important, contribution must be responsible for the large difference in reported surface potentials. Multilayered adsorption of dissolved organic impurities from the KF solution onto the SiO_2 surface or charge effects arising from hydroxyl groups protonation/deprotonation equilibrium in a non-buffered solution could account for the much larger scale of the resistive drop effect seen in Figure 5.13. Similar effects were observed for more negative values of the applied potential. For instance, if the surface is held at -800 mV vs. Ag/AgCl QRE, the potential profile would show a similar feature over the last 100 nm as well but the potential reached at the extrapolated zero distance would be -450 mV for a setpoint of 600 mV.

3.1.4 Potential profiles on mica

Attempts at engaging a freshly cleaved high grade green muscovite mica surface in the SECPM mode in degassed 10 µM KF were made. Mica has been extensively studied in the late 1970's and through the 1980's by Israelachvili essentially[53]. It was chosen for SECPM studies because it has a high surface charge density (1 charge per 7 nm^2 area[54]). Muscovite mica can be obtained in thin smooth sheets with a lattice of average chemical composition $K_2Al_4Si_6Al_2O_{20}(OH,F)_4$. Upon cleavage in dry air, mica is covered with 2 10^{14} K^+ ions per cm^2 that neutralize the aluminosilicate lattice[55] and about 1 % of them desorb from the surface when mica is immersed in pure conductivity water giving rise to a surface potential of about -150 mV as determined by surface force apparatus (SFA) where two crossed cylindrical sheets of mica placed on top of piezoelectric actuator are approached in a liquid electrolyte and forces can be measured using multiple beam interference fringes[56]. K^+ ions from the mica surface are exchanged with other cations from the solution in which it is immersed like H^+, Cs^+, Ba^{2+} or even Ca^{2+} and Na^+ cations[57]. In the case of K^+ and Na^+, additional so-called repulsive "hydration forces" have been measured by SFA and were attributed to ion-exchange processes at the mica surface that does not occur with H^+ or metallic ions that remain on the surface[58]. Consequently, the surface potential of the mica surface gradually increases from -150 mV in conductivity water or very dilute (< 5 µM) electrolyte to about -50 mV in 10^{-2} M I-I electrolyte like KCl with a slight plateau between 10^{-3} M and 10^{-4} M[58].

Many attempts were made in 10 µM KCl, 10 µM KOH or even Milli-Q water (18 MO.cm) where the expected surface potential would be between -80 mV and -150 mV to engage the SECPM system on the surface. In all cases, only a slight slow drop of about 2-4 mV was observed in the tip potential profile in the coarse approach ("sew tip" mode) before tip crash had obviously occurred. This result can be explained not only by the tip apex size that was too large for a the small surface charge density on mica as compared to metallic electrodes, but also by a lack of sensitivity of the electronics that constitute the measuring head of the SECPM. Indeed, imaging of mica in a humid atmosphere for the purpose of depositing Ag patterns with a commercial EC-STM required the use of a picoamp head stage comprised of a very sensitive operational amplifier as well as a booster (amplification) and noise-filtering stage that could operate with currents as low as a few picoamperes with reasonable noise levels[59].

In all potential profiles shown above, a good share of the discrepancy between the expected values from the Gouy-Chapman-Stern model and the fitted ones can be attributed to remaining dissolved oxygen. It is indeed very difficult to keep O_2 out of a small volume of electrolyte and, since the tips used contain up to 80% Pt, even the slightest trace of oxygen will drastically alter the open circuit potential of the tip. Sensitivity to dissolved oxygen has to be tremendously decreased before one can pretend to measure non-faradaic potential profiles. The next section will expose tip modifications into that direction.

3.2 The problem of dissolved oxygen

In all experiments described above, the KF solution was initially degassed with argon. But, since the volume of the electrolyte used in the cell is very small (80-100 µL), it is difficult to maintain an anaerobic atmosphere even when argon is flown through the aluminium Faraday cage that covers the cell, the piezoelectric tube and the measuring head. A better solution would be to immerse the whole cell including all the electrodes as well as the insulated extremity of the tip in a closed cell filled with the electrolyte and with an inert gas such as Argon bubbling through the cell. In this case though, the piezoelectric elements and the measuring head will have to be kept atop the cell to avoid damaging them.[60]

Platinum is also very sensitive to dissolved oxygen because of its unusual reactivity for O_2 reduction since it can occur via the "parallel" pathway in acid and alkaline solutions[61], i.e. it can reduce weakly-adsorbed oxygen O_2 to hydrogen peroxide (H_2O_2 or HO_2^-) via a 2-electron pathway, reduce O_2 oxygen to water (or OH^- in alkaline) in a direct 4-electron pathway without any hydrogen peroxide intermediate and supposing strongly-adsorbed molecular oxygen O, as well as through a series of mixed pathway involving more intermediates in different adsorbed states. The direct 4-electron pathway is supposed to be predominant. The multiplicity of surface states for adsorption in polycrystalline Pt[62] – especially as rough as the tips made here according to the desorption peak of UPD H in Fig. 3 – make it of difficult use when even traces of dissolved oxygen can shield non-faradaic measurements.

We therefore proposed to electroplate the platinum exposed area with mercury from a mercury (I) nitrate solution since interfering oxygen reduction on mercury can be removed more efficiently by degassing with N_2.[63] From Lingane's experiments in 50 mM KCl, two distinct steady-state diffusion-limited waves can be observed at the hanging mercury drop electrode. The first is a reduction to hydrogen peroxide, via a 2-electron pathway from weakly-adsorbed O_2 only.[61] Then, H_2O_2 is reduced to water via another two-electron step. Mercury is a liquid with very high surface tension at room temperature; the smoothness of the mercury surface may explain the absence of adsorption sites of high binding energies, and therefore the existence of only the 2-electron energy pathway by Adzic[61] and removal of O_2 reduction waves by simply saturating the solution with N_2 reported by Lingane[63]. In the latter case, N2 is both bubbled through the solution and blown into the volume above the solution. This will saturate the solution in N_2 but not totally remove O_2 since its solubility is higher in water at 25 °C[64]. Yet, oxygen electroreduction is no longer detected.

Another advantage of mercury is that it displays the highest overvoltage for hydrogen reduction among many metallic cathodes[65], which provides a large cathodic region where only double layer charging occurs in the absence of any redox couple in solution. This allows selective redox measurements in this cathodic region in acidic solutions without interference from hydrogen evolution[66]. However, due to easy formation of mercury oxides ($E^0_{HgO/Hg}$ = 0.098 V vs. NHE), mercury electrodes are not usable in regions positive of the saturated potassium sulfate mercury/mercury sulfate electrode (SME, +0.64 V vs. NHE).

3.3 Mercury electrodeposition on SECPM tips

Unlike gold, platinum is only dissolved to around 0.1 % atomically in mercury[67] and generation of stable single spherical nuclei of electrodeposited mercury has been described on Pt and carbon microelectrodes[68]. However, total coverage of the platinum surface is needed for SECPM electrodes and coalescence of these single nuclei into a continuous film or non-porous droplet is sought. Mercury was electrodeposited on tips prepared as described in section 2.2 from a 10 µM $HgNO_3$ ($Hg_2(NO_3)_2$, $2H_2O$, Alfa Aesar, 98 %), 0.1 M KNO_3 and 0.5 %(v) HNO_3 according to the procedure and with the formalism of Wightman et al[69].

Under diffusion control, at large overpotentials, the radius of a hemisphere of mercury on an assumed flat platinum surface is[70]:

$$r = \left(\frac{2MC^{*}Dt}{r} \right)^{1/2} \quad (21)$$

M = 200.59 g.mol^{-1} is the atomic weight of mercury, D = 9.6 10^{-8} m^2.s^{-1} is the diffusion coefficient in an aqueous environment of the mercurous ion Hg(I)[68], r = 13546 g.m^{-3} is the density of mercury and C^{*} is the bulk concentration of $HgNO_3$ in mol.m^{-3}.

The steady-state current is then given by Equation (22) for a hemisphere:

$$i_D = 2pFDC^{*}r \quad (22)$$

The lag time t of appearance of the $t^{1/2}$ dependence of the current contains information on the nuclei formation process and will be commented briefly later on.

Typically, a voltammogram is taken at 50 mV.s^{-1} in the argon-degassed deposition solution prior to initiating the mercury growth (Figure 5.14a) to determine the initial and final potentials with respect to the SME electrode to use in the chronoamperometry deposition experiment (Figure 5.14b) to prevent stripping the mercury off the platinum SECPM tip after the deposition. The efficiency of the deposition, i.e. the extent of coverage of the platinum by mercury, is checked by running a voltammogram in 1 M sulfuric acid at

50 $mV.s^{-1}$ from a potential negative of the stripping potential of Hg from Pt to more negative potentials until the hydrogen reduction wave appears and back (Figure 5.14c).

In Figure 5.14a, the voltammogram of an SECPM tip in 10µM $HgNO_3$ shows three essential features. The onset of Hg^+ reduction to Hg on Pt (underpotential deposition of Hg) is at -0.2 V vs. SME. The wave is deformed from the sigmoid shape obtained for diffusion-limited processes at an UME because of the cathodic deposition of Hg (pre-concentration). The onset of H^+ reduction is observed at -0.65 V vs. SME on the negative polarization scan, but the current is higher on the scan back (positive polarization) indicating a drastic change of the surface state. Hg anodically strips from the Pt surface at -0.33 V vs. SME (peak center, current saturation due to a too small sensitivity (10^{-9} A/V) chosen to solely amplify the process of interest, namely Hg deposition).

Then, the current falls back close to its initial double layer value; the charging current is very low indicating a small double layer capacitance C_d suggesting a clean and small exposed Pt surface. From the information given by this voltammogram, deposition of Hg is made by a potential-step chronoamperometry experiment from -0.4 V to -0.6 V vs. SME during 350 s (Figure 5.14b).

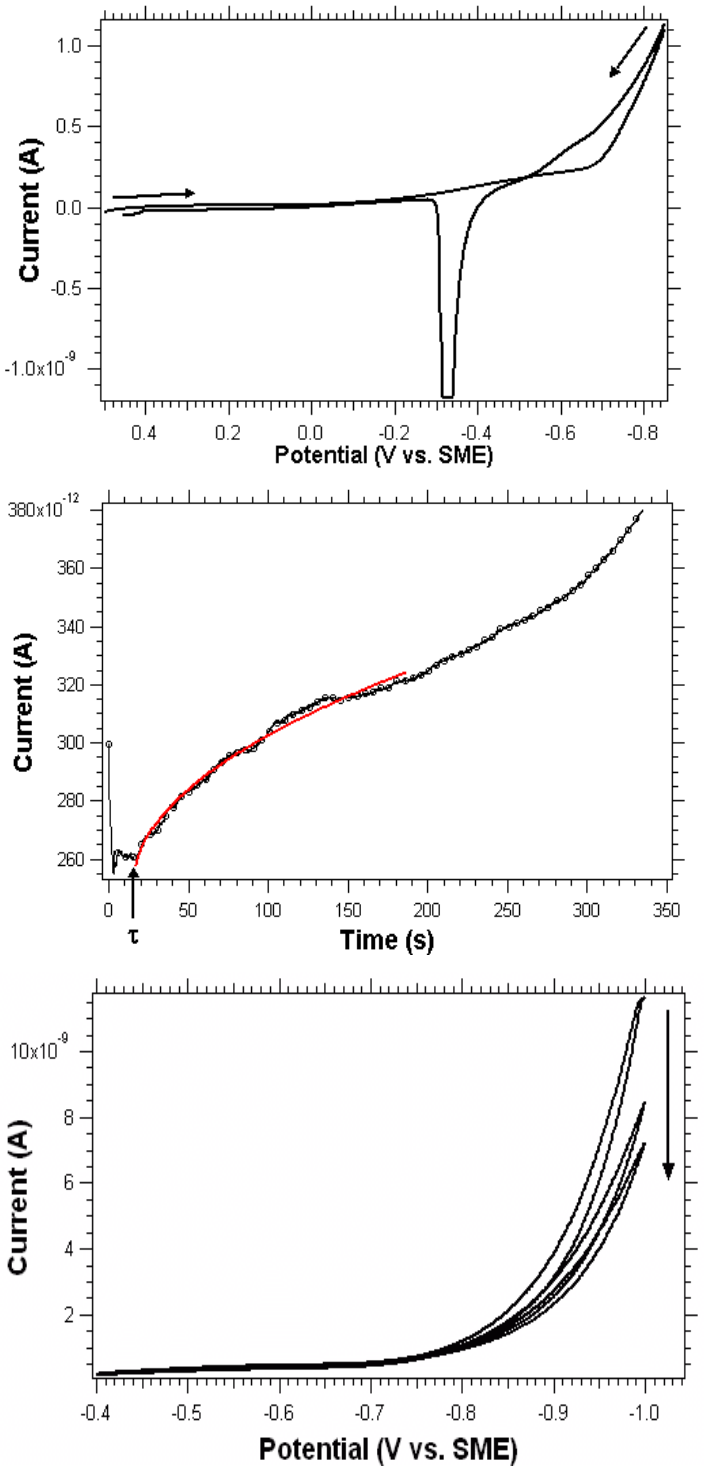

Figure 5.14: Hg electrodeposition on SECPM PtIr tips. (a) Cyclic voltammogram at 50 mV/s in 10 µM $HgNO_3$ with 0.1 M KNO_3 and 0.5 %(v) HNO_3. Arrows indicate initial scan polarity. (b) Subsequent chronoamperometry curve of Hg deposition on Pt stepped from -0.4 V to -0.6 V vs. SME. The current follows the expected $t^{1/2}$ dependence (red curve) after a lag time of 17 s. (c) Cyclic voltammetry experiment in 1 M H2SO4 to characterize newly formed PtIr-Hg tips. The hydrogen reduction wave is shifted to more negative values. The arrow indicates the evolution of the hydrogen wave over the 3 subsequent scans as Hg coverage of the Pt electrode is improved.

In Figure 5.14b, the current follows the predicted $t^{1/2}$ dependence over 300 s (red line fit) after the initial charging current and a lag time t = 17.4 s due to the delayed formation of the first stable nuclei. Then, a linear time-dependent regime is reached. This can be explained by depletion of Hg^+ from the $HgNO_3$ solution. Indeed, the steady-state current at a UME with the hemispherical approximation during a step voltammetry with quasi-irreversible or irreversible electron-transfer kinetics is given by[9]:

$$i = \frac{2pFD_{Hg^+}C^*k}{1+k\left(1+x^2q\right)}r \qquad (23)$$

r is the radius of the electrode. D_{Hg+} and D_{Hg} are the diffusion coefficients of Hg^+ and Hg respectively. Obviously, since Hg is deposited on the solid Pt surface in the case studied here, $D_{Hg} << D_{Hg+}$ and consequently: $x = \left(\frac{D_{Hg^+}}{D_{Hg}}\right)^{1/2} >> 1$. But, on the other hand, this is compensated by $q = \exp\left(h\frac{F}{RT}\left(E - E_0^{'}\right)\right) << 1$, since we operate at a large overpotential of the formal electrode potential $E_0^{'}$. One can now simplify the expression of the current:

$$i = \frac{2pFD_{Hg^+}C^*k}{1+k}r \qquad (24)$$

where $k = \frac{k_f}{D_{Hg^+}}r$ if k_f is the heterogeneous rate constant of the reduction reaction $Hg^+ + e^- +$ Pt → PtHg.

- Initially, at t ≈ t, r << 1 and k_f << 1, consequently k << 1 and, with the help of Equation (22):

$$i \approx 2pFD_{Hg^+}C^*kr = 2pFk_fC^*r^2 \propto t \qquad (24.1)$$

- For, $3t$ < t < 350 s, the apparent radius r and the electron-transfer rate constant k_f have reached a value for which k >> 1 and, with the help of Equation (22):

$$i \approx 2pFD_{Hg^+}C^*r \propto t^{1/2} \quad (24.2)$$

- For t > 350 s, the system gets depleted in Hg^+ near the electrode (10 µM initially) and k_f decreases rapidly. As the electrode is very small, Hg^+ depletion will have a heavy effect on the rate constant. Moreover, the diffusion is now limited so that D_{Hg+} is significantly lowered and r is now larger. In the end, this results in k << 1 and, with the help of Equation (22):

$$i \approx 2pFD_{Hg^+}C^*kr = 2pFk_fC^*r^2 \propto t \quad (24.3)$$

However, despite all the reasons mentioned above, k is still larger than in the first situation (t ≈ 0). This is justified by a larger slope for the current-time curve than in the first linear ($\alpha\, t$) regime as shown in Figure 5.14b.

In Figure 5.14c, the obtained Hg-PtIr electrode is checked with a voltammogram taken in 1 M sulfuric acid at 50 $mV.s^{-1}$ scanning 3 cycles negatively from -0.4 V vs. SME (negative of the Hg stripping potential) to the onset of hydrogen evolution. The arrow indicates the decrease in the hydrogen reduction current after each cycle. It corresponds to a shift of the onset of hydrogen reduction to even more negative potentials as the Pt/Hg interface evolves under the perturbation generated by H_2 bubbles until Hg coverage is optimized.

Additionally, PtIr-Hg tips for SECPM were checked by Linear Sweep Voltammetry (LSV) at 5 mV/s in 1 mM ferrocenemethanol with 0.1 M KCl between -0.05 V and 0.4 V vs. Ag/AgCl QRE. A resulting normalized voltammogram in ferrocenemethanol initially and after 400 s deposition in 100 µM $HgNO_3$ with 0.1 M KNO_3 and 0.5 %(v) HNO_3 is shown in Figure 5.15. The steady-state diffusion limited current increases by 30 % upon Hg deposition. According to Equation (22), this means an increase of 30 % in the apparent radius assuming a hemispherical geometry although some of the current increase is also due to a

geometry closer to the hemispherical approximation after formation of a stable mercury drop on the exposed platinum area.

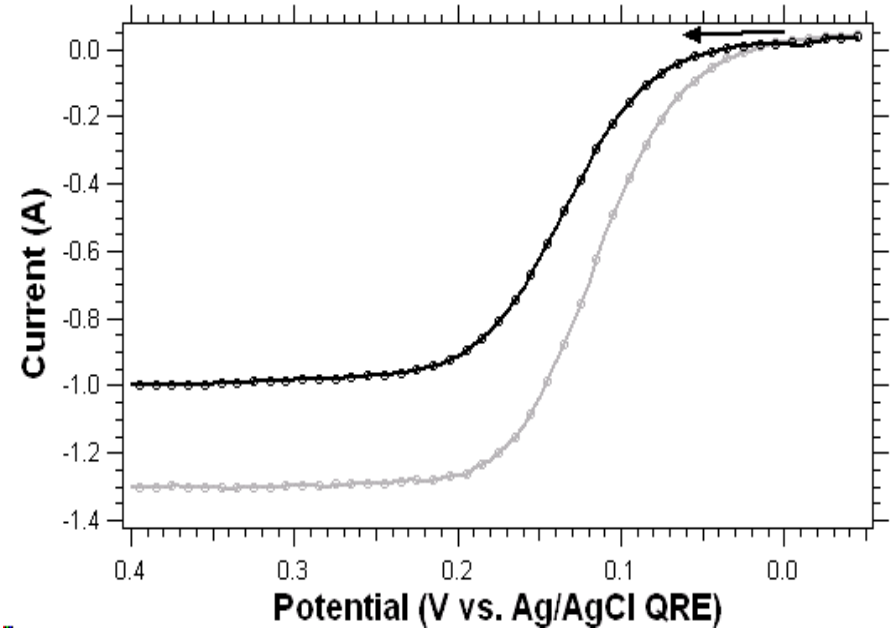

Figure 5.15: Linear Sweep Volatammetry in 1 mM Ferrocenemethanol with 0.1 M KCl supporting electrolyte of a PtIr tip before (black trace) and after deposition of a stable Hg drop from a 100 µM $HgNO_3$ solution with 0.1 M KNO_3 and 0.5 %(v) HNO_3 (grey trace). The current and therefore the apparent radius of an assumed hemispherical electrode increase by 30 %. The arrow indicates the initial scan polarization (scan rate: 5 mV/s). Potentials are measured with respect to the a Ag/AgCl QRE.

The rate constant for the formation of a single mercury nucleus is the inverse of the mean value of the lag time preceding the appearance of the first stable nucleation site as determined by the onset in the current[71]. Although a real statistical treatment is needed, a lag time of 20 s correspond to previously published results for these large overpotentials.

3.4 SECPM approach curves with PtIr-Hg tips

PtIr-Hg SECPM tips were prepared according tot the procedure exposed above directly in the SECPM setup by connecting a CH Instruments 900b electrochemical analyzer to the electrode connections and disconnecting the SECPM potentiostat module. They were immediately used to record approach curves over the Pt foil surface in a 10 µM KF solution carefully degassed with pure argon for 15-20 minutes prior to use. Additionally, a strong

stream of argon was kept flowing through the aluminium faraday cage all along the series of approach curves o keep oxygen out of the Teflon cell as best as possible. Approach curves were made for several values of the Pt foils surface potential. All potentials (tip and surface (WE)) were measured with respect to an Ag/AgCl QRE that was calibrated against a standard saturated KCl silver/silver chloride reference electrode (SSCE) with a 1.064 mM ferrocenemethanol in 0.1 M KCl. The shift of the half-wave potential of the sigmoidal steady-state current of ferrocenemethanol oxidation was -180 mV when switching from the SSCE to the Ag/AgCl QRE. Potential scales are summarized in Figure 5.16 for quick reference when needed.

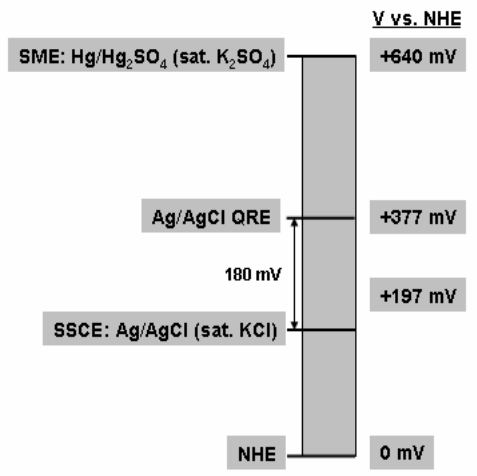

Figure 5.16: quick reference chart for reference electrodes potentials[72] used.

A voltammogram in 0.5 M H_2SO_4 was taken before and after approach curves in SECPM to check for the presence of Hg on the Pt tip and to make sure the Hg drop was not lost during an approach curve. Two potentials were tested: positive and negative with respect to the Ag/AgCl QRE.

3.4.1 Initial tip potential in dilute KF far away from the surface

Just after flushing the $HgNO_3$ and adding the degassed KF solution, the tip potential is equal to about +100 mV or -100 mV vs. Ag/AgCl QRE (-150 mV to -350 mV vs. SME) and drifts only about 5 mV per 100 seconds as the argon stream is flowing through the aluminium

faraday cage. This range of potentials values corresponds to open circuit potentials pinned in the double layer region of the voltammogram in sulfuric acid (Figure 5.14c). The initial open circuit potential value far away from the surface suggests sensitivity to dissolved oxygen has been reduced; less faradaic process from dissolved oxygen reduction occur at the tip in bulk 10 µM KF.

3.4.2 Surface held at a potential positive of the Ag/AgCl QRE

The Pt foil surface is approached in two steps. Initially, as the tip sits about 500 µm away from the surface, the system approaches the surface with a stepper motor and piezoelectric tube combination at an apparent speed of 500 nm ("sew tip"). It is stopped at about 150 mV away from the applied surface potential by choosing an appropriate potential setpoint value to avoid contact between the tip and the surface that might alter the Hg deposit and expose platinum. Then, the setpoint value is slowly increased up to 50 mV within the applied potential surface and the system is switched into the Potential-Separation plot mode where the surface can be approached with the piezoelectric elements only at slow speeds (40 nm/s typically).

Approach curves on Pt foil held at +400 mV vs. Ag/AgCl QRE will be shown and commented with the help of the Gouy-Chapman-Stern theory exposed earlier. Figure 5.17 shows a reproducible stable potential profile on Pt foil held at +400 mV. In this case the initial open-circuit tip potential far away from the surface was -10 mV vs. Ag/AgCl QRE but jumps to about +80 mV in Figure 5.17 100 nm away from the surface. Such a sudden increase in the open-circuit potential reveals a strong modification of the tip apex upon mechanical contact with the surface and/or faradaic processes from electrons leaving the surface. This is seen in Figure 5.17 as the potential profile is far off from the predicted profile obtained from the Gouy-Chapman-Stern model (red curve). The obtained potential profile suggests strong faradaic processes occurring at the mercury tip as it approaches the surface. Indeed, mercury gets oxidized around 400 mV vs. Ag/AgCl QRE (+140 mV vs. SME). Thus, when the Hg-covered platinum approaches the surface on the very first cycle, electrons transfer from the surface to oxidize Hg and strip it from the PtIr tip, which modifies its open-circuit potential far away from the surface for the subsequent second approach/retract cycle.

This result was observed with a similarly prepared PtIr tip but without electrodeposition of Hg. Since formation of surface platinum oxides starts at +400 mV vs. Ag/AgCl QRE as well, the potential profile was also far off from the predicted shape in case of only non-faradaic processes. In this case, the required stability of the probe is not met and does not allow proper measurements of diffuse double layers, but it can be a method to investigate local charge transfer processes in for example corrosion experiments.

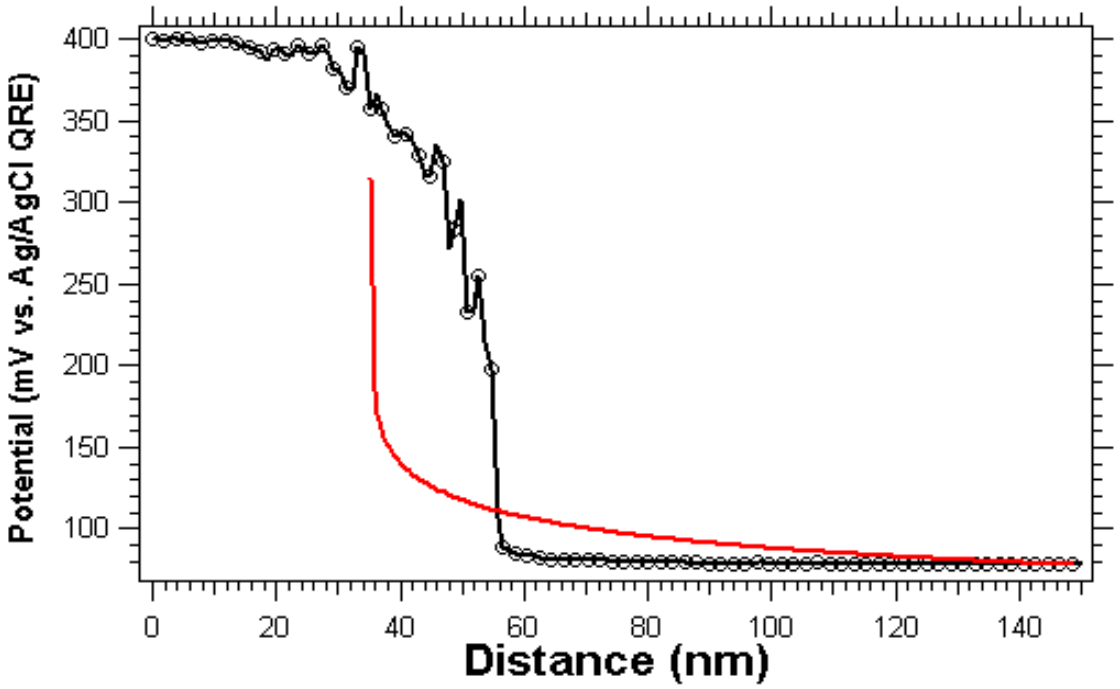

Figure 5.17: typical potential profile obtained when approaching a Pt foil surface held at +400 mV in a degassed 10 µM KF solution at 40 nm/s. Potentials are measured with respect to an Ag/AgCl QRE. The obtained profile strongly differs from the expected Gouy-Chapman-Stern model (solid curve) since the mercury tip undergoes perturbative faradaic process as it approaches the Pt surface. The system cannot be used to study surfaces at potentials positive of that of the QRE.

In addition, the voltammogram taken in 1 M sulfuric acid at the end of the series of SECPM curves shows the onset potential of hydrogen reduction had shifted from about -1.3 V vs. SME right after Hg deposition to -0.5 V vs. SME. This shows that most of the mercury had stripped from the PtIr apex during the series of experiments. This validates the hypothesis of faradaic processes occurring at this surface potential once the tip gets close enough to the surface.

3.4.3 Surface held at a potential negative of the Ag/AgCl QRE

The same Pt foil surface, held at -200 mV vs. Ag/AgCl QRE this time, is approached with the same procedure by a freshly prepared PtIr-Hg tip initially showing the expected shift of the onset potential of hydrogen reduction in 1 M H_2SO_4.

Figure 5.18 shows a reproducible stable potential profile obtained in a degassed 10 µM KF solution at 100 nm/s. The initial open-circuit tip potential far away from the surface right after Hg electrodeposition is -10 mV and is not significantly modified even after a large number of approach/retract cycles as can be seen in Figure 5.18 (-18 mV 500 nm away from the surface). This shows that no major modification of the tip is made as it gets within a few nanometers of the charged surface. However, the obtained potential profile still exhibits some discrepancy with the expected Gouy-Chapman-Stern model (red curve). At -200 mV vs. Ag/AgCl QRE (-463 mV vs. SME), proton reduction to H_2 occurs at the Pt surface (current – 100 nA for a 0.13 cm^2 area) at a very slow rate. But nanometer-sized bubbles of H_2 generated at the Pt surface may perturb the structure of the diffuse double layer and therefore the potential profiles measured by the PtIr-Hg probe. This is a very complex situation that will not be developed here.

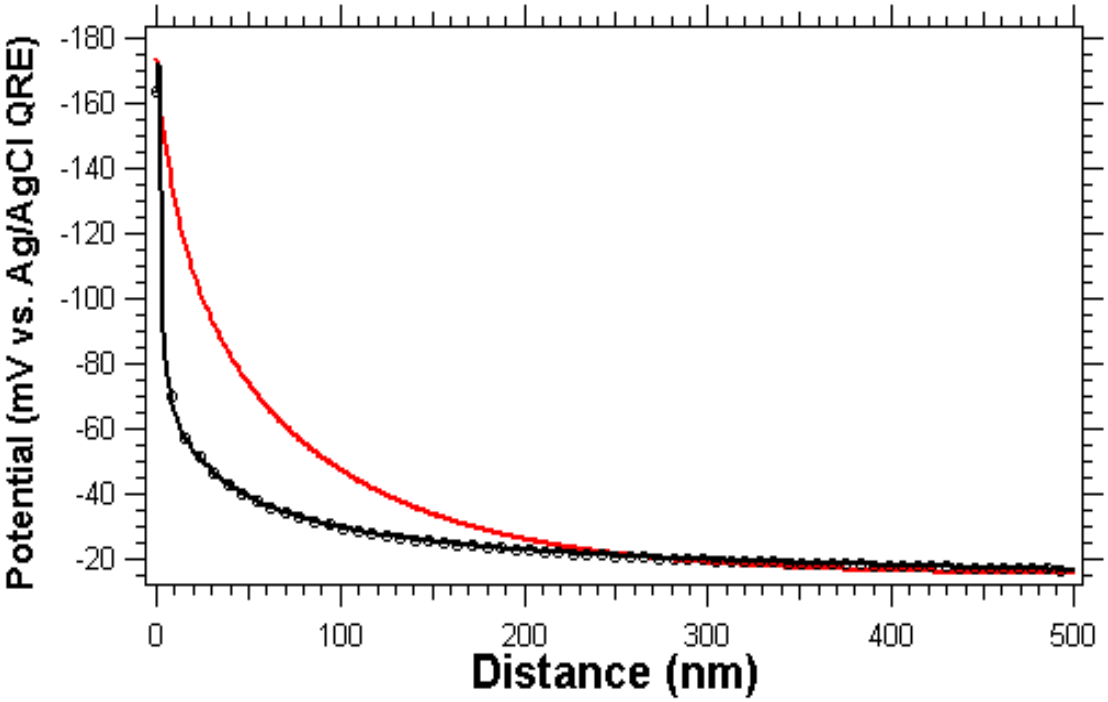

Figure 5.18: typical potential profile obtained when approaching a Pt foil surface held at -200 mV in a degassed 10 µM KF solution at 100 nm/s. Potentials are measured with respect to an Ag/AgCl QRE. The obtained profile still slightly differs from the expected Gouy-Chapman-Stern model (solid curve) since nanometer-sized H_2 generated at the surface at this potential can perturb the structure of the probed diffuse double layer.

After the series of SECPM experiments, the tip voltammogram in a 1 M sulfuric acid was recorded to check for the presence of the Hg deposit. The onset of hydrogen reduction appeared at a potential of -1.1 V vs. SME whereas it appeared at -1.3 V vs. SME after Hg electrodeposition and prior to use in SECPM approach curves. This validates the results presented since Hg was present throughout the experiments.

3.4.3 Tip response times and double layer relaxation

Results presented earlier show that electrodeposition of Hg on PtIr tips with small exposed areas can drastically decrease the sensitivity of the system to dissolved oxygen or protons from the unbuffered electrolyte, which is a prerequisite to measure non-faradaic double layer potential distributions.

However, many questions remain as to the response times of such tip compared to the undocumented characteristic relaxation times of diffuse double layers. Indeed, Figure 5.19 shows an intriguing observation. It shows, potential profiles obtained during the very first approach/retract cycle and the two subsequent ones as well as the expected GCS profile (red curve). These curves are recorded at a relatively slow speed of 100 nm/s over a Pt surface held at -200 mV vs. Ag/AgCl QRE. They reveal instabilities especially in the value of the open-circuit tip potential far away from the surface.

If the tip does not perturb the double layer and if the small tip double layer can react fast enough to changes in its ionic environments as it is brought from a bulk position in the dilute KF solution to the proximity of the surface where a strong excess of K^+ ions is maintained by the applied electrode potential, the open-circuit tip potential far away from the surface should not change within the time-course of an approach/retract cycle.

This observation raises fundamental questions on relaxation times of double layers at the ionic environment changes around the probe. One needs to understand how and how fast the metallic electrode will react to changes in the ionic environment as it I brought from a bulk situation to a surface situation where an excess of on ion species is present.

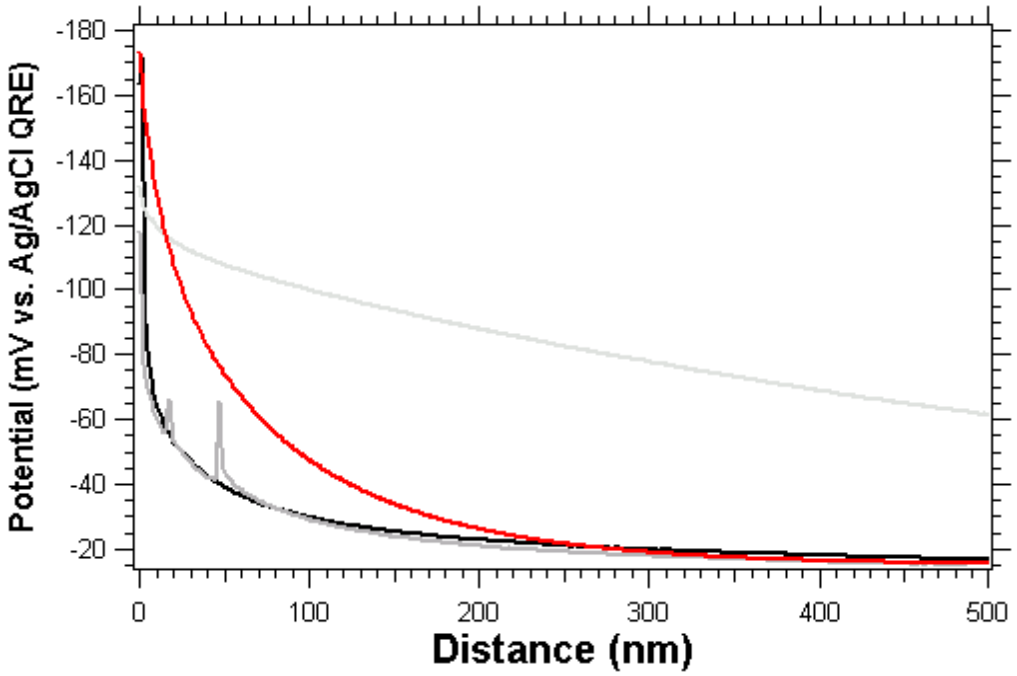

Figure 5.19: instabilities occurring in the very first (black), second (dark grey) and third (light grey) subsequent approach/retract cycles taken in 10 µM KF at 100 nm/s as the PtIr-Hg tip approaches the Pt surface held at -200 mV vs. Ag/AgCl QRE. The red curve is the expected potential profile from the GCS theory.

The only theoretical treatment available on double layer relaxation times is attributed to Feldberg in 1970[73] from simulations on data from Anson et al[74]. However, its treatment is made from coulostatic charge injection in a metallic electrode initially at its point of zero charge (pzc) in a model 10^{-4} M I-I electrolyte. Our situation is quite different since the probe operates at its open-circuit potential. Feldberg distinguishes two steps in the double layer relaxation: an initial fast charge neutralization as the electrode is stepped away from its pzc followed by, only once the first step is over and the transient electric field is nulled, a slower relaxation process scaling with $1/t^{2/3}$. If his formalism is adapted to the present situation in SECPM and if all approximations made are respected – especially those on small transferred charges –, the typical relaxation times in 10 µM KF are 20-40 µs. This is respected in the approach curves presented since, at 100 mn/s for instance, there is an approximately 10 ms interval between each of the 512 points over the typical 500-nm range. Nevertheless, Feldberg's conditions are quite different from the case here of, not a coulostatic charge injection, but more likely an electronic reorganization of energy levels of the metallic electrode upon changes in the ionic environment. One experimental parameter systematically

recorded after a series of approach/retract curves can provide elements of information. It is shown in Figure 5.20.

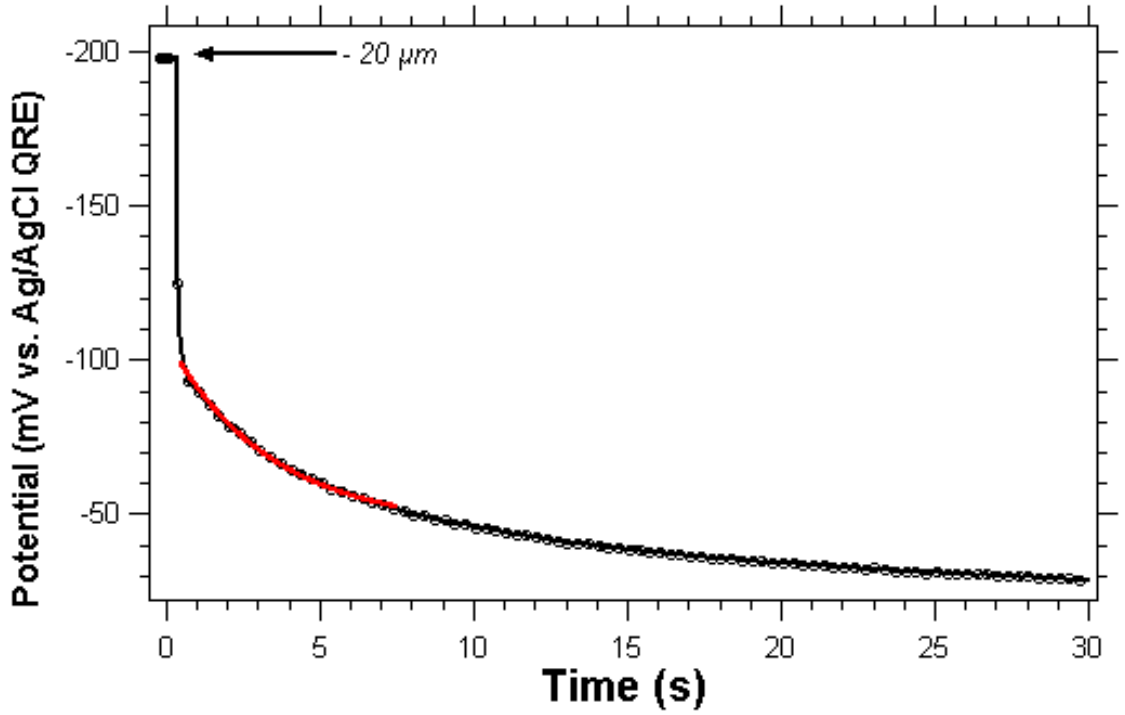

Figure 5.20: evolution of the tip potential (measured vs. Ag/AgCl QRE) as the tip is quickly withdrawn 20 µm away from the surface at -200 mV by the stepper motor. The solid line is a fit to an exponential decay with a time constant of 3.35 s after the initial much quicker step below the time resolution of the instrument. The tip potential slowly goes back to its bulk value around -10 mV vs. Ag/AgCl QRE.

Figure 5.20 shows the evolution of the tip potential as it is withdrawn 20 µm away from the charged Pt surface by the stepper motor. In this experiment, the PtIr-Hg tip is quickly moved from a region where it is surrounded by a large excess of K^+ due to the Pt surface maintained at -200 mV to the bulk of the 10 µM KF solution where electroneutrality of the solution is observed. This experiment corresponds to the relaxation of the tip double layer after a change in its ionic environment. The tip will slowly recover its initial open-circuit potential value far away from the surface before approaching the charged surface, i.e. about -10 mV vs. Ag/AgCl. Tips that showed recovery profiles that were slower than the one shown in Figure 5.20 were systematically discarded since their response time was judged to be too slow.

One can make a rough approximation to be tested. Moving the tip from near the surface to the bulk is equivalent to applying a potential step to an RC-circuit composed of the solution resistance in series with the differential double layer capacitance of the tip. The resistivity of 10 µM KF is 0.78 MO.cm. Over 20 µm, the solution resistance R_S is about 1.56 kΩ. The charge transferred through an RC circuit upon a potential step q is given by:

$$q = EC_d\left(1-\exp\left(-\frac{t}{t}\right)\right) \qquad (25)$$

With the time constant defined by: $t = 1/R_S C_d$. A fit of the data of Figure 5.20 to an Equation proportional to Equation (25) (red curve) gives t = 3.35 s. This with an expected solution resistance of 1.56 kΩ over the 20 µm traveled would give a value of C_d = 191 µF. This value is quite unlikely for double layer capacitances especially if the electrode area is small. This shows that more reflection on the relaxation of double layers is needed.

4 Conclusions and future perspectives

4.1 Conclusions on double layer measurements

We have developed a procedure to make reproducible tips with a small exposed metallic area and developed electrodeposition of Hg to minimize the sensitivity of these tips to traces of dissolved oxygen and protons present in unbuffered solutions. The Gouy-Chapman-Stern formalism fits quite well on the different conductive surfaces tested ad results obtained on non-conductive materials like silica or mica are encouraging but require many improvements of the commercial SECPM setup that we agreed to test here.

Once these improvements are made, the objective of approaching any charged surface by sensing diffuse double layers will be possible and will allow moving on to imaging and mapping potential profiles of biological materials deposited or immobilized on non-conductive surfaces with a nanometric resolution *in situ*, i.e. in their native active buffers and possibly even measure enzymatic activities.

4.2 Suggested improvements of SECPM

4.2.1 Probes

First, one can move to an insulating coating that exhibits less leakage than low-density polyethylene used here. Apiezon wax is already widely used in EC-STM experiments but was discarded here because of a low adherence with PtIr surfaces. This could be improved for instance by chemical treatment of the surface to render it more hydrophobic by forming self-assembled monolayers (SAM) of long-chain alkanethiols before coating with the wax and locally etching the apex. Since Apiezon wax is made of high molecular mass carbon residues of oil distillation, a hydrophobic interaction is thought to be more efficient.

Another promising insulating method is electrophoretic paint. This technique consists of electrochemically destabilizing a colloidal solution of polymethymethyacrylate by pH changes during bulk electrolysis to precipitate the polymer coating onto the tip surface and shrink it by heating. This technique has been used in scanning electrochemical microscopy (SECM) experiments for several years since its introduction in 1999[75].

Even smaller tips could be built by using focused-ion beam (FIB) techniques couple to scanning electron microscopy (SEM) to open the tip apex very locally by ion milling through an insulating coating. This will avoid the tip apex exposure sequence in EC-STM that has been shown to still contain a large uncontrolled mechanical part that may lead to bigger apex sizes than it is really possible in a totally controlled environment.

4.2.2 Electronics

One slight modification of the measuring setup has already been proposed, namely measuring the tip potential with respect to a stable reference electrode instead of the surface to be less sensitive to modification by adsorption of dissolved molecules. However, the reference electrode mainly used here is only a quasi-reference electrode that can lose ideal nonpolarizability in certain environments. This choice was guided by the restricted space available in the SECPM cell. Therefore, a better reference electrode could be used along with a Luggin-Haber capillary to allow more precise and more stable potential measurements.

Another problem encountered with the commercial setup is an efficient degassing of the cell containing the electrolyte. A way to circumvent this difficulty would be to immerse the cell in the electrolyte and bubble oxygen continuously far away enough from the surface to prevent perturbations. In this case the piezoelectric elements needed to scan and approach the surface could be positioned on top of the isolated cell.

Finally, as the attempts on muscovite mica showed earlier show, a much higher sensitivity in the picoampere (or better) regime is needed. This means modifying upgrading the STM pre-amplifier. Such an upgrade will inevitably enhance the sensitivity to noise which will have to be fixed as well by either analog or digital signal filtering for instance.

4.2.3 User-interface

A last improvement of the actual setup resides in the improvement interface to perform efficient simple electrochemical experiments like potential steps and sweeps, chronoamperometry or ultimately AC techniques. If this system is meant to compete with commercially available electrochemical instruments (BAS, EGG, CH Instruments…), an improvement in data acquisition and treatment during electrochemical experiments is expected.

More generally, more flexibility during, for example, the coarse approach of the surface by the stepper motor essentially would be appreciated. Many attempts on mica are believed to have failed because the approach speed during the coarse approach sequence was too high and the system could not prevent tip crashing.

References

[1] Binnig G., Rohrer H., Gerber Ch., and Weibel E. (1982), *Phys. Rev. Lett.*, **49**, 57-61
[2] for an early review: Hansma P.K., Ellings V.B., Marti O., and Brake C. E. (1988), *Science*, **242,** 209-215
[3] Travaglini G., Amrein M., Michel B., and Gross H. in *Scanning Tunneling Microscopy and Related Methods*, Behm R., Garcia N., and Rohrer H. Eds, 335, Kluwer, Dordrecht, 1990
[4] Friis E.B., Andersen J.E.T., Madsen L.L., Moller P., Nichols R.J., Olesen K.G., and Ulstrup J. (1998), *Electrochimica Acta,* **43(19-20)**, 2889-2897
[5] Bard A.J., Fan F.-R.F., Kwak J., and Lev O. (1989), *Anal. Chem.*, **61**, 132-138
[6] Bard A.J., and Mirkin M.V., *Scanning Electrochemical Microscopy*, Marcel Dekker, New York, 2001
[7] Li C.Z., Russel B., Maringer B., and Kjoller S. (2003), *Veeco Instruments, Inc.*, US Patent pending
[8] Li C., and Lesko S., *Forum de Microscopies à Champ Proche*, March 2003, Montpellier, France, poster
[9] Bard A.J., and Faulkner L.R., *Electrochemical Methods: Fundamentals and Applications*, 2nd Ed., John Wiley & Sons, New York (2002)
[10] Delahay P., *Double Layer and Electrode Kinetics*, John Wiley & Sons, New York, 1965
[11] Grahame D.C. (1953), *J. Chem. Phys.*, **21**, 1054-1060
[12] Macdonald J.R., and Barlow C.A. (1962), *J. Chem. Phys.*, **36**, 3062-3080
[13] Stillinger S.H., and Kirkwood J.G. (1960), *J. Chem. Phys.*,**33**, 1282-1290
[14] Anson F.C (1975), *Acc. Chem. Res.*, **8**, 400-407
[15] Grahame D.C., and Soderberg B.A. (1954), *J. Chem. Phys.*, **22**, 449-460
[16] Devanathan M.A.V., and Canagaratana S.G. (1963), *Electrochim. Acta.*, **8**, 77-85
[17] FETFE™ (Ace Glass, Inc.) is a fluoroelastomer with tetrafluoroethylene additives to improve chemical resistance in many concentrated mineral acid or base solutions, in ammonia, in alcohols, in aliphatic or chlorinated hydrocarbons, as well as in aromatics. It also performs over a wide temperature range.
[18] Hafner J.H., Cheung C.L., Woodley A.T., and Lieber C.M. (2001), *Prog. Biophys. Mol. Biol.*, **77**, 73-110
[19] Dietzel D., Faucher M., Iaia A., Aimé J.P., Marsaudon S., Bonnot A.M., Bouchiat V., and Couturier G. (2005), *Nanotechnology*, **16**, S73-S78
[20] Fotino M. (1993), *Rev. Sci. Instr.*, **64**, 159-167
[21] Melmed A.J. (1991), *J. Vac. Sci. Technol. B*, **9(2)**, 601-608
[22] Jambunathan K., and Hillier A.C. (2002), *J. Electroanal. Chem.*, **524-525**, 144-156
[23] Zalfaghari A., Chayer M., and Jerkiewicz G. (1997), *J. Electrochem. Soc.*, **144(9)**, 3034-3041
[24] Dean J.A., *Lange's Handbook of Chemistry*, Ch. 8, 997, McGraw-Hill, New York, 15th Ed., 1999
[25] A stable value of the cell current is believed to flow from proton reduction (pH around 6 in a deionized water solution left at ambient air for an hour) and dissolved oxygen reduction. Equilibration is quite slow due the large solution resistance.
[26] Heben M.J., Penner R.M., Lewis N.S., Dovek, M.M., and Quate C.F. (1989), *Appl. Phys. Lett.*, **54(15)**, 1421-1423
[27] According to the manufacturer's specifications for this particular instrument setup, the STM pre-amplifier has a maximum tunneling current sensitivity of 50 pA in this EC-STM setup.
[28] Hugelmann M., and Schindler W. (2003), *Surf. Sci.*, **541**, L643-648.
[29] Landau L.D., and Lifshitz E.M., *Course of Theoretical Physics VIII: Electrodynamics of Continuous Media*, Ch. 11, 39, Pergamon Press, London, 1960
[30] O'Dwyer J.J., *The Theory of Dielectric Breakdown of Solids*, Ch. I & IV, Oxford University Press, London, 1964
[31] Goodfellow Corporation, Devon, PA – online sources
[32] Conway B.E., and Tilak B.V. (2002), *Electrochim. Acta*, **47**, 3571-3594
[33] Vetter K.J., *Electrochemical Kinetics*, Academic Press, New York, 1967
[34] Pharr C.M., and Griffiths P.R. (1997), *Anal. Chem.*, **69**, 4673-4679
[35] Although potassium ferricyanide (K_3FeCN_6) and potassium ferrocyanide solutions (K_4FeCN_6) are available for purchase, the lifetime of the ideal K_4FeCN_6 stoechiometry on a shelf is not long because it gets oxidized to a hexaferrocyanide complex with mixed Fe(II)/Fe(III) content and a more complex stoechiometry.
[36] Conyers J., and White H.S. (2000), *Anal. Chem.*, **72**, 4441-4446
[37] Von Stackelberg M., Pilgram M., and Toome V. (1953), *Z. Elektrochem.*, **57**, 342

[38] Baranski A.S. (1991), *J. Electroanal. Chem.*, **307**, 287
[39] In the Gemini system, the main control (EHT for Extra High Tension) is the overall voltage applied to the electrostatic lenses in the column that accelerate/decelerate the emitted electrons. The temperature of the Shottky thermal filed emission and the voltage to initiate and accelerate electron emission from the tungsten tip (extraction voltage) are fixed. The beam emission current can only be controlled by using apertures.
[40] Hurth C., and Saadaoui H., unpublished.
[41] 70/30 Piranha solution is a very reactive mixture of 70 %(v/v) concentrated sulfuric acid and 30 %(v/v) fresh hydrogen peroxide (30 %). It is very efficient to clean metal surfaces like platinum or gold because these metals catalytically transform H_2O_2 to O_2 and/or H_2O in acidic media and reduce H^+ to H_2. This process generates adsorption/desorption cycles on the metal surface that eventually cleans the surface. Some roughening through chemical etching is believed to occur though, if the metal piece is left in the solution for too long.
[42] Verwey E.J.W., and Overbeek J.Th.G., *Theory of the Stability of Lyophoic Colloids*, Elsevier, Amsterdam, 1948
[43] Woo D.-H., Yoo J.-S., Park S.-M., Jeon I.C., and Kang H. (2004), *Bull. Korean Chem. Soc.*, **25(4)**, 577-580
[44] Israelachvili J.N., and Adams G.E. (1978), *J. Chem. Soc.Faraday Trans. I*, **74**, 975
[45] (a) Hillier A.C., Kim S., and Bard A.J. (1996), *J. Phys. Chem. B*, **100**, 18808-18817
(b) Hu K., Chai Z., Whitesell J.K., and Bard A.J. (1999), *Langmuir*, **15(9)**, 3343-3347
[46] Woo D.-H., Kang H., and Park S.-M. (2003), *Anal. Chem.*, **75(23)**, 6732-6736
[47] Anselmetti D., Bartoff A., Güntherodt H.-J., Gerber Ch., Michel B., and Rohrer H. (1994), *J. Vac. Sci. Technol. B*, **12(3)**, 1677-1680
[48] Nishikawa H., Shiba H., and Iri T. (1995), *Jap. J. Appl. Phys.*, **34(2A)**, 578-582
[49] Watson G, Dinite B., Blach J.A., and Myhra S. (2002), *J. Phys. D*, **35(16)**, 2066-2074
[50] Fomenko V., Hurth C., Ye T., and Borguet E. (2002), *J. Appl. Phys.*, **91(7)**, 4394-4398
[51] Binnig G., Rohrer H., Gerber Ch., and Weibel E. (1983), *Phys. Rev. Lett.*, **50(2)**, 120-125
[52] Sze S.M., *Physics of Semiconductor Devices*, Wiley, New York, 1981
[53] Israelachvili J.N., *Intermolecular and Surface Forces*, 2nd Edition, Academic Press, London, 1992
[54] Pashley R.M. (1980), *J. Coll. Interface Sci.*, **80(1)**, 153-162
[55] Gaines G.L.Jr. (1957), *J. Phys. Chem.*, **61**, 1408-1413
[56] Israelachvili J.N., and Adams G.E. (1978), *J. Chem. Soc. Faraday Trans. I*, **74**, 975-1001
[57] Mokma D.L., Syers J.K., and Jackson M.L. (1970), *Soil Sci. Soc. Amer. Proc.*, **34**, 146-153
[58] Pashley R.M. (1981), *J. Coll. Interface Sci.*, **83(2)**, 531-546
[59] Forouzan F., and Bard A.J. (1997), *J. Phys. Chem. B*, **101(50)**, 10876-10879
[60] Hugelmann P., and Schindler W. (2005), *J. Phys. Chem. B*¸**109**, 6262-6267
[61] Adzic R., in *Electrocatalysis*, Lipkowski J., and Ross P.N., Eds, Ch. 5, 197-215, Wiley-VCH, New York (1998)
[62] Clavilier J., Rodes A., El Achi K., and Zamakhchari M.A. (1991), *J. Chim .Phys.*, **88(7/8)**, 1291-1337
[63] Lingane J.J., *Electroanalytical Chemistry*, Ch. XI, 240, John Wiley & Sons, New York (1958)
[64] Lide D.R., *CRC Handbook of Physics and Chemistry*, 79th Ed., CRC Press, Boca Raton (1999)
[65] Böttger W., *Elektroanalyse*, Tl. II, 122, Akad. Verlag., Leipzig, 1936 in 63.
[66] Selzer Y., Tryan I., and Mandler D. (1999), *J. Phys. Chem. B*, **103(9)**, 1509-1517
[67] Vydra F., Stullk K., and Julakova E., *Electrochemical Stripping Analysis*, Wiley, New York (1976)
[68] Gunawardena G, Hills G.J., and Sharifker B. (1981), *J. Electroanal. Chem.*, **130**, 99-112
[69] Wehmeyer K.R., and Wightman R.M. (1985), *Anal. Chem.*, **57(9)**, 1989-1993
[70] Gunawardena G., Hills G.J., and Montenegro I. (1978), *Electrochim. Acta*, **23**, 693-697
[71] Hills G., Pour A.K., and Scharifker B. (1983), *Electrohim. Acta*, **28(7)**¸ 891-898
[72] Ives D.J.G., and Janz G.J., *Reference Electrodes*, Academic Press, New York, 1961
[73] Feldberg S.W. (1970), *J. Phys. Chem.*, **74(1)**, 87-90
[74] Anson F.C., Martin R.F., and Yarnitzky C. (1969), *J. Phys. Chem.*, **73(6)**, 1835-1842
[75] Slevin C.J., Gray N.J., Macpherson J.V., Webb M.A., and Unwin P.R. (1999), *Electrochem. Comm.*, **1**, 282-288

Conclusion

1. Chapter Highlights

Chapter 1 positions the work presented in this dissertation within the general framework of Scanning Probe Microscopy (SPM) techniques. It underlines elements already established by 20 years of heavy use of these techniques in a variety of domains. Moreover, it presents a short introductory reflection on what information the present work plans to draw from the studied active enzymes systems.

Chapter 2 exposes a systematic hydrodynamic thermal noise study of available commercial cantilevers to characterize the oscillation of such cantilevers in a more viscous liquid media like water. This work emphasis on the problem of the hydrodynamic force which is, for certain cantilevers, so large compared to the biological forces one wishes to measure that a screening effect will occur. This chapter gives a general view of the problems caused by the liquid media itself that arise when dynamic AFM is performed *in situ*. However, to relevantly study biological systems, this step forward cannot be avoided since previous studies performed in ambient air or even in vacuum may yield partially significant structural information[1], but, if one wishes to measure enzymatic activities by AFM, *in situ* AFM operation is unavoidable.

Chapter 3 is an application of the study presented in Chapter 2. The system chosen is a well-known phosphotransferase enzyme from *Saccharomyces cerevisiae*, i.e. 3-phosphoglycerate kinase (PGK), because many detailed biochemical or physical studies as well as an efficient overproduction protocol are available. Initial *in situ* imaging in the static mode (Contact Mode) insists on the need to switch to dynamic AFM to successfully image biological enzymes while preserving their structure and therefore their full activity; minimize the lateral shear force induced by the tip on soft biological samples like a small aggregate of enzyme molecules. Chapter 3 also copes with one essential question when working with immobilized surface-bound enzymes, i.e. assesses the residual enzymatic activity and compares it to values obtained from the free enzyme in solution under similar conditions. A reflection on the model used to treat the data from activity measurements on surface-bound enzymes is used.

Chapter 4 uses a second important technique that rejuvenated electrochemistry in the late 1980's, namely Scanning Electrochemical Microscopy (SECM). The system chosen is another

well-known redox active enzyme: Glucose Oxidase. SECM is an interesting technique because it allows measuring heterogeneous rate constants and the theory from digital simulations is available to analyze data obtained on insulators, conductors or even mixed surfaces. However, this work also presents an attempt to study the effect of an externally applied DC electric field by SECM. From the existing literature, it is concluded that two types of effects are expected; faradaic and non-faradaic. The strategy used to study this DC field dependence may be the reason for the lack of these experiments and is analyzed in details to draw important conclusions on the general use of Self-Assembled Monolayers (SAM) on thin film gold surfaces to covalently bind enzymes to a surface and study their activity. Subsequent work on SECM study of the catalytic decomposition of hydrogen peroxide by an enzyme (catalase), and platinum nanoparticles is presented since it helps preparing possible surface generation/tip collection SECM experiments to study the activity of Glucose Oxidase by collecting the released hydrogen peroxide at a Au(Hg) amalgam tip. This might be a better strategy to study the dependence of the activity on an external DC electric field.

Finally, Chapter 5 introduces Scanning Electrochemical Potential Microscopy (SECPM), and analyzes its limitations to study biological samples like active enzymes bound to a solid surface. This chapter essentially develops the fabrication and analysis of the best suitable tips for SECPM; efficient non-leaking insulation, the smallest possible exposed metallic area of known simple geometry (disc, cones or hemisphere) and the use of Hg deposition to decrease the influence of faradaic processes from dissolved oxygen and protons. Then, the chapter presents a Gouy-Chapman-Stern based study of potential profiles obtained by SECPM on several surfaces and the final attempt to switch to charged insulating surfaces of particular interest like mica.

2. The benefits of interdisciplinary work to study complex system

Active enzymes are complex systems especially if single-molecule resolution is sought. Therefore, in order to obtain a battery of physical and chemical elements at the single-molecule or better level a variety of local probe techniques should be employed.

Indeed, dynamic AFM may be the optimal choice to get relevant mechanical information on a soft system because of the non linear effects it thrives on. But it has limited chemical sensitivity

if the tip is not very carefully chemically treated and if an exhausting statistical treatment of a large surface area is not systematically performed. SECM can provide a better analysis in terms of chemical specificity of the sample response but is, however, limited to redox active systems. In principle, complex indirect measurements are possible on non-redox systems if a redox species appears at some point in the reaction sequences.

Finally, SECM appears to be the ultimate tool to study faradaic processes from redox active enzymes. Its main disadvantages are the limited resolution due to the difficulty of preparing electrode tips smaller and less fragile than say a 100 nm radius discs and the quite high noise level of the setup compared to that of the AFM/STM setups. These elements are incompatible with, for instance, mapping the surface potential of a single enzyme molecule with and without enzymatic activity to notice possible structural or physical changes. These types of experiments require focusing on non-faradaic issues. STM or, more precisely, its equivalent in a liquid environment, EC-STM, and its newer potential-focused version, SECPM, can provide the resolution needed. Again, new appropriate efficient probes are needed. SECPM may sound promising but, as Chapter 5 shows, many improvements are expected.

3. Suggested improvements for more results on active enzymes using local probe methods

3.1 Probe

Both in dynamic AFM and in SECM or SECPM, Chapters 2 and Chapter 5 respectively insist on the need of probes of smaller dimensions and better-defined geometries. In dynamic AFM, decreasing the size of the probes can drastically reduce the hydrodynamic screening of specific biological forces. In SECPM, smaller exposed areas will even further minimize the influence of faradaic processes from dissolved oxygen and protons. One possibility to improve the size and the geometry of SECPM probes would be to use the available battery of Focused-Ion Beam (FIB) techniques to literally carve a metallic electrode surrounded by an insulating glass sheath of glass or other inert polymers like Teflon or polyethylene combined with Electron Microscopy (EM) techniques to follow these processes *in situ*.

3.2 Time-resolution

Historically, biochemistry really started to have an impact when the time-resolution of the equipment used in enzymology allowed observation of the information-rich transient signals of the monitored biological activity. For instance, the introduction of stopped-flow fluorescence or absorbance measurements gave access to the transient regimes of enzymatic activities measured by these techniques.

In the case of dynamic AFM, work can be done at several levels to build a high-speed AFM successive high resolution images of much higher scan speeds can be recorded to follow structural changes accompanying certain biological activities[2]. This requires new smaller cantilevers with resonant frequencies in the MHz range as well as high-speed piezoelectric scanners and faster detection devices. Another axis of research is that of Micro-Electro-Mechanical Systems (MEMS) sensors that provided specific surface information with a high precision level[3].

3.3 In situ combination of several local probe techniques

The simultaneous acquisition of decoupled information on a system is also an important axis of development of research on biological systems by the means of local probe techniques. This can be done by coupling the main SPM techniques like AFM, STM and SECM or even coupling these techniques with other techniques not based on local probes.

For instance, dynamic AFM and SECM have been successfully coupled in the past[4] to image enzymatic activity of glucose oxidase. AFM, STM or SECM can also be coupled to other techniques like fluorescence[5] to locate a particular single molecule and then image it. To study other materials, not necessarily of biological origin, local temperature measurements can be made with AFM-based instruments with the advantage of sub-surface sensitivity[6].

---

[1]Bousset L., Thompson N.H., Radford S.E., and Melki R. (2002), *EMBO J.***, 21(12)**, 2903-2911
[2] Ando T., Kodera N ;, Takai E., Maruyama D., Saito K., and Toda A. (2001), *Proc. Nat. Acad. Sci. USA*, **98(22)**, 12468-12472
[3] Maboudian R., and Carraro C. (2004), *Ann. Rev. Chem. Phys.*, **55**, 35-54
[4] Kueng A., Kranz C., Lugstein A., Bertagnolli E., and Mizaikoff B. (2003), *Angew. Chem. Intl. Ed.*, **42(28)**, 3237-3240
[5] Yang T.J., Lessard G.A., and Quake S.R. (2000), *Appl. Phys. Lett.*, **76(3)**, 378-380
[6] Majumdar A. (1999), *Ann. Rev. Mat. Res.*, **29**, 505-585

References

CHAPTER 1

[1] Atkins P., and de Paula J., *Physical Chemistry*, 6th Ed., Oxford University Press, Oxford, 2002
[2] Garcia R., and Perez R. (2002), *Surf. Sci. Reports*, **47**, 197-301
[3] San Paulo A., and Ricardo G. (2001), *Phys. Rev. B*, **64**, 1934-38
[4] Dürig U. (2000), *Appl. Phys. Lett.*, **76**, 1203-1206
[5] Nony L., Boisgard R., and Aimé J.P. (1999), *J. Chem. Phys.*, **111(4)**, 1615-1627
[6] Cleveland J.P., Anczykowski B., Schmid A.E., and Elings V.B. (1998), *Appl. Phys. Lett.*, **72**, 2613-2615
[7] Nony L., Boisgard R., and Aimé J.P. (2001), *Biomacromolecules*, **2**, 227-235
[8] Branden C.I., and Tooze J., *Introduction to Protein Structure*, 2nd Ed., Garland Publishing, New York, 1999
[9] Engel A., and Müller D.J. (2000), *Nature Struct. Biol.*, **7(9)**, 715-718
[10] Rief M., Gautel M., Oesterhelt F., Fernandez J.M., and Gaub H.E. (1997), *Science*, **276**, 1109-112
[11] Vinckier A., Gervasoni P., Zaugg F., Ziegler U., Lindner P., Groscurth P., Plückthun A., and Semenza G. (1998), *Biophys. J.*, **74**, 3256-3263
[12] Wang T., Arakawa H., and Ikai A. (2001), *Biochem. Biophys. Res. Comm.*, **285**, 9-14
[13] Fotiadis D., Müller D.J., Tsiotis G., Hasler L., Tittmann P., Mini T., Jenö P, Gross H., and Engel A. (1998), *J. Mol. Bio.*, **283**, 83-94
[14] Stamouli A., Kafi S., Klein D.C.G., Oosterkamp T.H., Frenken J.W.M., Cogdell R.J., and Aartsma T.J. (2003), *Biophys. J.*, **84**, 2483-2491
[15] Paige M.F., Rainey J.K., and Goh M.C. (1998), *Biophys. J.*, **74**, 3211-3216
[16] Fisher T.E., Oberhauser A.F., Carrion-Vazquez M., Marszalek P.E., and Fernandez J.M. (1999), *Trends in Biochemical Sciences*, **24**, 379-384
[17] Müller DJ., Fotiadis D., and Engel A. (1998), *FEBS Lett.*, **430**, 105-111
[18] Oesterhelt F., Oesterhelt D., Pfeiffer M., Engel A., Gaub H.E., and Müller D.J. (2000), *Science*, **288**, 143-146
[19] Viani M.B., Pietrasanta L.I., Thompson J.B., Chand A., Gebeshuber I.B., Kindt J.H., Richter M., Hansma H.G, and Hansma P.K. (2000), *Nature Struct. Biol.*, **7(8)**, 644-647
[20] Yuan C., Chen A., Kolb P., and Moy V.T. (2000), *Biochemistry*, **39**, 10219-10223
[21] Jackson J.D., *Classical Electrodynamics*, 3rd Ed., John Wiley & Sons, New York, 1999
[22] Mas M.T., Resplandor Z.E., and Riggs A.D. (1987) , *Biochemistry*, **26(17)**, 5369-5377
[23] Lide D.R., *CRC Handbook of Physics and Chemistry*, 79th Ed., CRC Press, Boca Raton (1999)
[24] Kosevich A.M., Lifshitz E.M., Landau L.D., and Pitaevskii L.P., *Course of Theoretical Physics VII: Theory of Elasticity*, Pergamon Press, London, 1960
[25] Fleischmann M., Pons S., Rolison D.R., and Schmidt P., *Ultramicroelectrodes*, Datatech Systems, Inc. Publications, Morganton, 1987
[26] Amemiya S., and Bard A.J. (2000), *Anal. Chem.*, **72**, 4940-4948

[27] Horrocks B.R., Mirkin M.V., Pierce D.T., Bard A.J., Nagy G., and Toth K. (1993), *Anal. Chem.*, **65**, 1213-1224
[28] Carano M., Holt K.B., and Bard A.J. (2003), *Anal. Chem.*¸ **75**, 5071-5079
[29] Bard A.J., and Mirkin M.V., *Scanning Electrochemical Microscopy*, Marcel Dekker, New York, 2001
[30] Bard A.J., Fan F.R.F, Kwak J., and Lev O. (1989), *Anal. Chem.*, **61(2)**, 132-138
[31] Pierce D.T., Unwin P.R., and Bard A.J. (1992), *Anal. Chem.*, **64(17)**, 1795-1804
[32] Pierce D.T., and Bard A.J. (1993), *Anal. Chem.*, **65(24)**, 3598-3604
[33] Shiku H., Takeda T., Yamada H., Matsue T., and Uchida I. (1995), *Anal. Chem.*, **67(2)**, 312-317
[34] Shiku H., Matsue T., and Uchida I. (1996), *Anal .Chem.*, **68(7)**, 1276-1278
[35] Zaumseil J., Wittstock G., Bahrs S., and Steinrücke P. (2000), *Fresenius J. Anal. Chem.*, **367**, 352-357
[36] Zhao C., Sinha J.K., Wijayawardhana C.A., and Wittstock G. (2004), *J. Electroanal. Chem.*, **561**, 83-91
[37] Binnig G., Rohrer H., Gerber Ch., and Weibel E. (1982), *Phys. Rev. Lett.*¸**49(1)**, 57-61
[38] Cohen-Tannoudji C. Diu B., and Laloe F., *Quantum Mechanics*, Hermann, Paris, 1977
[39] Sarid D., *Scanning Force Microscopy*, Ch. 4, 55-64, Oxford University Press, Oxford, 1991

CHAPTER 2

[1] Walter D.A., Cleveland J.P., Thompson N.H., Hansma P.K., Wendman M.A., Gurley G., and Elings V.B. (1996), *Rev. Sci. Intr.* , **67**, 3583-3590
[2] Schäffer T.E., and Hansma P.K. (1998), *J. Appl. Phys.*, **84(9)**, 4661-4666
[3] Viani M.B., Schäffer T.E., Chand A., Rief M., Gaub H.E., and Hansma P.K. (1999), *J. Appl. Phys.*, **86(4)**, 2258-2262
[4] Tuck E.O. (1969), *J. Eng. Math.*, **3**, 29-44
[5] Sader J.E. (1998), *J. Appl. Phys.*, **84(1)**, 64-76
[6] Kirstein S., Mertesdorf M., and Schönhoff M. (1998), *J. Appl. Phys.*, **84(4)**, 1782-1790
[7] Hosaka K., Itao K., and Kuroda S. (1995), *Sensors and Actuators*, **49**, 87-95
[8] Kanwal R.P. (1955), *Z. Angew. Math. Mech.*, **35**, 17-28
[9] Elmer F.J., and Dreier M. (1997), *J. Appl. Phys.*, **81(12)**, 7709-7714
[10] Berker R., *Encyclopedia of Physics*, VII/2, Flügge, 1963
[11] Rosenhead F., *Laminary boundary layers*, Oxford University Press, Oxford, 1963
[12] Batchelor G.K., *Fluid Dynamics*, Cambridge University Press, Cambridge, 1974
[13] Landau L.D., and Lifshitz E.M., *Course of Theoretical Physics VI : Fluid Mechanics*, Pergamon Press, London, 1960
[14] Butt H.J., and Jaschke M. (1995), *Nanotechnology*, **6**, 1-7
[15] Rabe U., Janser K., and Arnold W. (1996), *Rev. Sci. Instrum.*, **67(9)**, 3281-3293
[16] Oesterhelt F., Oesterhelt D., Pfeiffer M., Engel A., Gaub H.E., and Müller D.J. (2000), *Science*, **288(7)**, 143-146
[17] Fisher T.E., Oberhauser A.F., Carrion-Vazquez M., Marszalek P.E., and Fernandez J.M. (1999), *Trends Biochem. Sciences*, **24**, 379-384

[18] Wang T., Arakawa H., and Ikai A. (2001), *Biophys. Biochem. Res. Comm.*, **285(1)**, 9-14
[19] Viani M.B., Schäffer T.E., Paloczi G.T., Pietrasanta L.I., Smith B.L., Thomson J.B., Richter M., Rief M. Gaub H.E., Plaxco K.W., Cleland A.N., Hansma H.G., and Hansma P.K. (1999), *Rev. Sci. Instr.*, **70(11)**, 4300-4303
[20] Vinogradova O.I. (1995), *Langmuir*, **11(6)**, 2213-2220
[21] Voet D., and Voet J.G., *Biochemistry*, John Wiley & Sons, New York, 1995
[22] O'Reilly J.P., Butts C.P., l'Anson I.A., and Shaw A.M. (2005), *J. Am. Chem. Soc.*, **127**, 1632-1633
[23] Shriver-Lake L., *Silane-modifed surfaces for biomaterial immobilization*, in *Immobilized Biomolecules in Analysis: a Practical Approach*¸Cass T., and Ligler F.S., Oxford University Press, London, 1998
[24] Noy A., Vezenov D.V., and Liber C.M. (1997), *Ann. Rev. Mater. Sci.*, **27**, 381-421
[25] Zsila F., Bikadi Z., Keresztes Z., Deli J., and Simonyi M. (2001), *J. Phys. Chem. B*, **105(39)**, 9413-9421
[26] Tipple C.A., Lavrik N.V., Culha M., Headrick J., Datskos P., and Sepaniak M.J. (2002), *Anal. Chem.*, **74(13)**, 3118-3126
[27] Maali A., Hurth C., Cohen-Bouhacina T., Couturier G., and Aimé J.-P., *Appl. Phys. Lett.*, submitted
[28] Rodriguez T.R., and Garcia R. (2003), *Appl. Phys. Lett.*, **82(26)**, 4821-4823
[29] Humphris A.D.L., Tamayo J., and Miles M.J. (2000), *Langmuir*, **16(21)**, 7891-7894

CHAPTER 3

[1] Bucher J.L., *The Metrology Handbook*, ASQ Quality Press, Milwaukee, 2004
[2] Mas M.T., Resplandor Z.E., and Riggs A.D. (1987), *Biochemistry*, **26(17)**, 5369-5377
[3] McPhillips T.M., Hsu B.T., Sherman M.A., Mas M.T., and Rees D.C. (1996) , *Biochemistry*, **35(13)**, 5369-5377
[4] Conway N.M.J., Ilie A., Robertson J., Milne W.I., and Tagliaferro A. (1998), *Appl. Phys. Lett.*, **73(17)**, 2456-2458
[5] Hahn J.R., and Kang H. (1999), *Phys. Rev. B*, **60(8)**, 6007-6017
[6] Nony L., Boisgard R., and Aimé J.P. (2001), *Biomacromolécules*, **2**, 827-835
[7] Auerbach G., Huber R., Grättinger M., Zaiss K., Schuring H., Jaenicke R., and Jacob U. (1997), *Structure*, **5**, 1475-1483
[8] Bernstein B.E., Michels P.A.M., and Hol W.G.J. (1997), *Nature*, **375**, 275-278
[9] Betton J.M., Desmadril M., Mitraki A., and Yon J.M. (1985), *Biochemistry*, **24**, 4570-4577
[10] Schmidt P.P., Travers F., and Barman T. (1995), *Biochemistry*, **34**, 824-832
[11] Souza J.M., and Radi R. (1998), *Arch. Biochem. Biophys.*, **360**, 187-194
[12] Boschi-Muller S., and Branlant G. (1999), *Arch. Biochem. Biophys.*, **363**, 259-266
[13] Daubenberger C.A., Pötl-Frank F., Jiang G., Lipp J., Certa U., and Pluschke G. (2000), *Gene*, **246**, 255-264
[14] Bücher T. (1955), *Methods Enzymol.*, **I**, 415-422
[15] Voet D., and Voet J.G., *Biochemistry*, J. Wiley & Sons, New York, 1995

[16] Minard P., Desmadril M., Ballery N., Perahia D., Mouawad L., Hall L., and Yon J.M. (1989), *Eur. J. Biochem.*, **185**, 419-423
[17] Molnar M., and Vas M. (1993), *Biochem. J.*, **295**, 595-599
[18] Collinet B., Hervé M., Pecorari F., Minard P., Elder O., and Desmadril M. (2000), *J. Biol. Chem.*, **275(23)**, 17428-17433
[19] Yang J., Mou J., and Shao Z. (1994), *FEBS Letters*, **338**, 89-92
[20] Fritz M., Radmacher M., Cleveland J.P., Allersma M.W., Stewart R.J., Gieselmann R., Janmey P., Schmidt C.F., and Hansma P.K. (1995), *Langmuir*, **11**, 3529-3535
[21] Bergkvist M., Carlsson J., Karlsson T., and Oscarsson S. (1998), *J. Colloid Interface Sci.*, **206**, 475-481
[22] You H.X, and Lowe C.R. (1996), *J. Colloid Interface Sci.*, **182**, 586-601
[23] Shiraishi F. (1995), *J. Ferm. Bioeng.*, **79(4)**, 373-377
[24] Kato M. (1995), *J. theor. Biol.*, **177**, 299-304
[25] Bard A.J., and Faulkner L.R., *Electrochemical Methods: Fundamentals and Applications*, 2nd Edition, John Wiley & Sons, New York, 2002
[26] Israelachvili J.N., *Intermolecular and Surface Forces*, 2nd Edition, Academic Press, London, 1992
[27] Michaelis L., and Menten M. (1913), *Biochem. Z.*, **49**, 333-369
[28] Dubourg F., Aimé J.P., Couturier G., and Salardenne J. (2003), *Europhys. Lett.*, **62(5)**, 671-676
[29] Plueddemann E.P., *Silane Coupling Agents*, 2nd Edition, Plenum Press, New York, 1991

CHAPTER 4

[2] McNaught A.D., and Wilkinson A., *IUPAC Compendium of Chemical Technology*, 2nd Edition, Blackwell Science, Cambridge, 1997
[3] Wienkamp R., and Steckhan E. (1982), *Angew. Chem. Intl. Ed.*, **21(10)**, 782-783
[4] Weaver R.F., *Molecular Biology*, McGraw-Hill, New York, 1999
[5] Purich D., Enzyme Kinetics and Mechanism Part A: Initial Rate and Inhibitor Methods in *Methods in Enzymology*, **63**, Academic Press, Orlando, 1979
[6] Kajiya Y., Sugai H., Iwakura C., and Yoneyama H. (1991), *Anal. Chem.*, **63(1)**, 49-54
[7] Yon-Hin B.F.Y., Smolander M., Crompton T., and Lowe C.R. (1993), *Anal. Chem.*, **65(15)**, 2067-2071
[8] Klibanov A.M. (2001), *Nature*, **409**, 241-246
[9] Radzicka A., and Wolfenden R.A. (1995), *Science*, **267**, 90-93
[10] Voet D., and Voet J.G., *Biochemistry*, John Wiley & Sons, New York, 1995
[11] Ravindra R., and Winter R. (2003), *ChemPhysChem*, **4(4)**, 359-365
[12] Black W.Z., and Hartley J.G., *Thermodynamics*, 3rd Edition, Harper Collins, New York, 1996
[13] Auerback G., Huber R., Grättinger M., Zaiss K., Jaenicke R., and Jacob U. (1997), *Structure*, **5**, 1475-1483
[14] Dossi G., Celentano F., Gianazza E., and Righetti P.G. (1983), *J. Biochem. Biophys. Methods*, **7**, 123-142
[15] Honig B., and Nicholls A. (1995), *Science*, **268**, 1144-1149
[16] Simonson T. (2001), *Curr. Opinion Struct. Biol.*, **11**, 243-252

[17] Van Belle D., Couplet I., Prevost M., and Wodak S.J. (1987), *J. Mol. Bio.*, **198**, 721-735
[18] Aqvist J., Luecke H., Quiocho F.A., and Warshel A. (1991), *Proc. Natl. Acad. Sci.*, **88**, 2026-2031
[19] Gunner M.R., Saleh M.A., Cross E., Ud-Doula A., and Wise M. (2000), *Biophys. J.*, **78**, 1126-1144
[20] Park E.S., Andrews S.S., Hu. R.B., and Boxer S.G. (1999), *J. Phys. Chem. B*, **103**, 9813-9817
[21] Park E.S., and Boxer S.B. (2002), *J. Phys. Chem. B*, **106**, 5800-5806
[22] Park E.S., Thomas M.R., and Boxer S.G. (2000), *J. Am. Chem. Soc.*, **122**, 12297-12303
[23] Kolodner P., Lukashev E.P., Ching Y., and Rousseau D.L. (1996), *Proc. Natl. Acad. Sci.*, **93**, 11618-11621
[24] Kolodner P., Lukashev E.P., and Ching Y. (2000), *Bioelectrochemistry*, **51**, 67-73
[25] Lanyi J. K. (1993), *Biochim. Biophys. Acta*, **1183,** 241–261
[26] Rousso I., Friedman N., Sheves M., and Ottolenghi M. (1995), *Biochemistry*, **34,** 12059–12065
[27] Tittor J., Schweiger U., Oesterhelt D., and Bamberg E. (1994), *Biophys. J.*, **67**, 1682-1690
[28] Horrocks B.R., and Mirkin M.V. (1998), *J. Chem. Soc. Faraday Trans.*, **94**, 1115-1118
[29] Hirst J., Sucheta A., Ackrell A.C., and Armstrong F.A. (1996), *J. Am. Chem. Soc.*, **118**, 5031-5038
[30] Santhanam K.S.V., Jespersen N., and Bard A.J. (1977), *J. Am. Chem. Soc.*, **99**, 274-276
[31] Egodage K.L., de Silva B.S., and Wilson G.S. (1997), *J. Am. Chem. Soc.*, **119**, 5295-5301
[32] Pearson M.A., Michel L.O., Hausinger R.P., and Karplus P.A. (1997), *Biochemistry*, **36**, 8164-8172
[33] Jabri E., and Karplus P.A. (1996), *Biochemistry*, **35**, 10616-10626
[34] Benini S., Rypniewski W.R., Wilson K.S., Miletti S., Ciurli S., and Mangani S. (1999), *Structure*, **7**, 205-216
[35] Ha N.C., Oh S.T., Sung J.Y., Cha K.A., Lee M.H., and Oh B.H. (2001), *Nature Struct. Biol.*, **8**, 505-509
[36] Rivat C., Fontaine M., Ropartz C., and Caullet C. (1973), *Eur. J. Immunol.*, **3**, 537-442
[37] Cass A.E., Davis G., Francis G.D., Hill H.A., Aston W.J., Higgins I.J., Plotkin E.V., Scott L.D.L., and Turner A.P.F. (1984), *Anal. Chem.*, **56(4)**, 667-671
[38] Hecht H.J., Kalisz H.M., Hendle J., Schmid R.D., and Schonburg D.J. (1993), *J. Mol. Bio*, **229**, 153-163
[39] Bourdillon C., Demaille C., Moiroux J., and Savéant J.M. (1993), *J. Am. Chem. Soc.*, **115(1)**, 2-10
[40] Badia A., Carlini R., Fernandez A., Battaglini F., Mikkelsen S.R., and English A.M. (1993), *J. Am. Chem. Soc.*, **115(16)**, 7053-7060
[41] Heller A. (1990), *Acc. Chem. Res.*, **23**, 128-138
[42] Bard A.J., and Mirkin M.V., *Scanning Electrochemical Microscopy*, Marcel Dekker, New York, 2001
[43] Pierce D.T., Unwin P.R., and Bard A.J. (1992), *Anal. Chem.*, **64(17)**, 1795-1804
[44] Pierce D.T., Unwin P.R., and Bard A.J. (1993), *Anal. Chem.*, **65(24)**, 3598-3604
[45] Wittstock G., and Schuhmann W. (1997), *Anal. Chem.*, **69(24)**, 5059-5066
[46] Frederick K.R., Tung J., Emerick R.S., Masiarz F.R., Chamberlain S.H., Vasavada A., Rosenberg S., Chakraborty S., Schopter L.M., and Massey V. (1990), *J. Biol. Chem.*, **7(5)**, 3793-3802
[47] Kelley R.L., and Reddy C.A. (1986), *J. Bacteriol.*, **166**, 269-274
[48] Sundberg R.J., and Carey F.A., *Advanced Organic Chemistry – Part B: Reaction and Synthesis*, 4th Edition, Plenum Press, New York, 2001

[49] Ulman A. (1996), *Chem. Rev.*, **96(4)**, 1533-1554
[50] Tzanov T., Costa S.A., Gübitz G.M., and Cavaco-Paulo A. (2002), *J. Biotechnol.*, **93**, 87-94
[52] Shriver-Lake L.C. in *Immobilized Biomolecules in Analysis: a Practical Approach*, Cass T., and Ligler F.S., Eds., Ch. 1, Oxford Univeristy Press, Oxford, 1999
[53] Jonas U., del Campo A., Krüger C., Glasser G., and Boos D. (2002), *Proc. Nat. Acad. Sci.*, **99(8)**, 5034-5039
[54] Thompson R.O., Mandoke C.S., and Womack J.P. (1985), *Anal. Letters*, **18(B1)**, 93-107
[55] Collinson M., Bowden E.F ., and Tarlov M.J. (1992), *Langmuir*, **8(5)**, 1247-1250
[56] Tedder J.M., Nechvatal A., and Murray A.W., *Basic organic chemistry*, John Wiley & Sons, London, Ch. 6, 1972
[57] Sehgal D., and Vijay I.K. (1994), *Anal. Biochem.*, **218**, 87-91
[59] Weibel M.K., and Bright H.J. (1971), *J. Biol. Chem.*, **246(9)**,
[60] Amphlett J.L., and Denuault G. (1998), *J. Phys. Chem B*, **102(49)**, 9946-9951
[61] Bright H.J., and Appleby M. (1969), *J. Biol. Chem.*, **244(18)**, 3625-3634
[62] Wohlfahrt G., Witt S., Hendle J., Schomburg D., Kalisz H.M., and Hecht H.J. (1999), *Acta Crystallogr. D*, **55**, 969-977
[63] Aoki K., and Kakiuchi T. (1999), *J. Electroanal. Chem.*, **478**, 101-107
[64] Molinero V., and Calvo E.J. (1998), *J. Electroanal. Chem.*, **445(1-2)**, 17-25
[65] Komura T., Yamaguchi T., Shimatani H., and Okushio R. (2004), *Electrochimica Acta*, **49(4)**, 597-606
[66] Macdonald J.R., and Kenan W.R., *Impedance Spectroscopy: Emphasizing Solid Materials and Systems*, John Wiley & Sons, New York, 1987
[67] Janek R.P., Fawcett W.R., and Ulman A. (1997), *J. Phys. Chem. B*, **101(42)**, 8550-8558
[68] Rohwerder M., de Weldige K., and Stratmann M. (1998), *J. Solid State Electrochem.*, **2**, 88-93
[69] Amatore C., Savéant J.M., and Tessier D. (1983), *J. Electroanal. Chem.*, **147**, 39-51
[70] Liedberg B., and Cooper J.M. in *Immobilized Biomolecules in Analysis: a Practical Approach*, Cass T., and Ligler F.S., Eds., Ch. 4, Oxford Univeristy Press, Oxford, 1999
[71] Zubovich I.A. (1955), *Zhur. Fiz. Khim*, **29**, 917-924
[72] McKee D.W. (1969), *J. Catalysis*, **14**, 355-362
[73] Pirault-Roy L., Kappenstein C., Guerin M., Eloirdi R., and Pillet N. (2003), *J. Propulsion Power*, **18**, 1235-1243
[74] Ariafard A., Aghabozorg H.R., and Salehirad F. (2003), *Catalysis Commun.*, **4**, 561-573
[75] Falcón H., Carbonio R.E., and Fierro J.L.G. (2001), *J. Catalysis*, **203**, 264-173
[76] Lysova A.A., Kuz'min A.O., and Parmon V.N. (2003), *Kinetics Catalysis*, **44**, 86-97
[77] Vago E.R., and Calvo E.J. (1995), *J. Electroanal. Chem.*, **388**, 161-172
[78] Labadi I., Szilagyi I., Jakab N.I., Hernadi K., and Palinko I. (2003), *Mat. Science*, **21**, 235-241
[79] Tarasevich M.R., and Zakharkin G.I. (1977), *Reaction Kinetics Catalysis Letters*, **6**, 77-81
[80] Çetinus S.A., and Öztop H.N. (2003), *Enzyme Microbial Technol,*. **32**, 889-896
[81] (a) Tarhan L. (1991), *Appl. Biochem. Biotechnol,*. **31**, 109-116 (b) Tarhan L., and Uslan H. (1990), *Process Biochem.*, **14**, 140-144
[82] Costa S.A., Tzanov T., Para A., Gudelj M., Gübitz G.M., and Cavaca-Paulo A. (2001), *Enzyme Microbial Technol.* **28**, 815-825
[83] Costa S.A., Tzanov T., Carneiro F., Gübitz, G.M., and Cavaca-Paulo A. (2002), *Biotechnol. Letters*, **24**, 173-183
[84] Akertek E.,and Tarhan L. (1995), *Appl. Biochem. Biotechnol,*. **50**, 291-298
[85] Adzic R. in *Electrocatalysis*, Lipkowski J., and Ross P. N., Eds., Ch. 5, Wiley-VCH, New York, 1998

[86] Mueller S., Rieder H.D., and Stremmel W. (1997), *Anal. Biochem.* **245**, 55-61
[87] Vetter T.A., and Philip Colombo D. Jr. (2003), *J. Chem. Ed.*, **80**, 788-796
[88] Wittstock G. (2001), *Fresenius J. Anal. Chem.*, **370**, 303-315
[89] Serebrennikova I., Lee,S., and White H.S. (2002), *Faraday Discuss.*, **121**, 199-212
[90] Selzer Y., Turyan I., and Mandler, D. (1999), *J. Phys. Chem. B,* **103**, 1509-1517
[91] Fernandez J.L., Hurth C., and Bard A.J. (2005), *J. Phys. Chem. B,* **109(19)**, 9532-9539
[92] Sarathy K.V., Raina G., Yadav R.T., Kulkarni G.U., and Rao C.N.R. (1997), *J. Phys. Chem. B,* **101,** 9876-9880
[93] Nony L., Boisgard R., and Aimé J.-P. (1999), *J. Chem. Phys.*, **111**, 1615-1627
[94] Ciani I., Burt D.P., Daniele S, and Unwin P.R. (2004), *J. Phys. Chem. B,* **108**, 3801-3809
[95] Mauzeroll J., Hueske E.A., and Bard A.J. (2003), *Anal. Chem.*, **75**, 3880-3889
[96] Selzer Y., and Mandler D. (2000), *Anal. Chem.*, **72**, 2383-2395
[97] Damjanovic A., Genshaw M.A., and Bockris J.O'M. (1967), *J. Electroanal. Chem.*, **15**, 173-188
[98] Taylor R.J., and Humffray A.A. (1975), *J. Electroanal. Chem.*, **64**,85-97
[99] Wightman R.M., and Wipf D.O. in *Electroanalytical Chemistry*, Bard A.J., Ed., Vol. 15, Marcel Dekker, New York, 1989
[100] Lawson D.R., Whiteley L.D., Martin C.R., Szentirmay M.N., and Song J.I. (1988), *J. Electrochem. Soc.*, **135**, 2247-2256
[101] McPherson A., and Rich A. (1973), *Arch. Biochem. Biophys.*, **157**, 23-31
[102] Protein Data Bank code 4BLC. Ko T.P., Jay D., Malkin A., and McPherson A. (1999), *Acta Crystallographica D*, **55**, 1383-1395
[103] Liu Z., Ling X.Y., Lee J.Y., Su X., and Gan L.M. (2003), *J. Mater. Chem.*, **13**, 3049-3055
[104] Furlong D.N., Launikonis A., and Sasse W.H.F. (1984), *J. Chem. Soc. Faraday Trans. I,* **80**, 571-591
[105] Macpherson J.V., Slevin C.J., and Unwin P.R. (1996), *J. Chem. Soc. Faraday Trans.*, **92**, 3799-3809
[106] Bard A.J., Mirkin M.V., Unwin P.R., and Wipf D.O. (1992), *J. Phys. Chem.*, **96(6)**, 1861-1875
[107] Boisgard R., Aimé J.P., and Couturier G. (2002), *Appl. Surf. Sci.*, **188**, 363-371
[108] Gammaitoni L., Hänggi P., Jung P., and Marchesoni F. (1998), *Rev. Mod. Phys.*, **70(1)**, 223-287

CHAPTER 5

[1] Binnig G., Rohrer H., Gerber Ch., and Weibel E. (1982), *Phys. Rev. Lett.*, **49**, 57-61
[2] for an early review: Hansma P.K., Ellings V.B., Marti O., and Brake C. E. (1988), *Science*, **242,** 209-215
[3] Travaglini G., Amrein M., Michel B., and Gross H. in *Scanning Tunneling Microscopy and Related Methods*, Behm R., Garcia N., and Rohrer H. Eds, 335, Kluwer, Dordrecht, 1990
[4] Friis E.B., Andersen J.E.T., Madsen L.L., Moller P., Nichols R.J., Olesen K.G., and Ulstrup J. (1998), *Electrochimica Acta,* **43(19-20)**, 2889-2897
[5] Bard A.J., Fan F.-R.F., Kwak J., and Lev O. (1989), *Anal. Chem.*, **61**, 132-138

[6] Bard A.J., and Mirkin M.V., *Scanning Electrochemical Microscopy*, Marcel Dekker, New York, 2001
[7] Li C.Z., Russel B., Maringer B., and Kjoller S. (2003), *Veeco Instruments, Inc.*, US Patent pending
[8] Li C., and Lesko S., *Forum de Microscopies à Champ Proche*, March 2003, Montpellier, France, poster
[9] Bard A.J., and Faulkner L.R., *Electrochemical Methods: Fundamentals and Applications*, 2nd Ed., John Wiley & Sons, New York (2002)
[10] Delahay P., *Double Layer and Electrode Kinetics*, John Wiley & Sons, New York, 1965
[11] Grahame D.C. (1953), *J. Chem. Phys.*, **21**, 1054-1060
[12] Macdonald J.R., and Barlow C.A. (1962), *J. Chem. Phys.*, **36**, 3062-3080
[13] Stillinger S.H., and Kirkwood J.G. (1960), *J. Chem. Phys.*, **33**, 1282-1290
[14] Anson F.C (1975), *Acc. Chem. Res.*, **8**, 400-407
[15] Grahame D.C., and Soderberg B.A. (1954), *J. Chem. Phys.*, **22**, 449-460
[16] Devanathan M.A.V., and Canagaratana S.G. (1963), *Electrochim. Acta.*, **8**, 77-85
[18] Hafner J.H., Cheung C.L., Woodley A.T., and Lieber C.M. (2001), *Prog. Biophys. Mol. Biol.*, **77**, 73-110
[19] Dietzel D., Faucher M., Iaia A., Aimé J.P., Marsaudon S., Bonnot A.M., Bouchiat V., and Couturier G. (2005), *Nanotechnology*, **16**, S73-S78
[20] Fotino M. (1993), *Rev. Sci. Instr.*, **64**, 159-167
[21] Melmed A.J. (1991), *J. Vac. Sci. Technol. B*, **9(2)**, 601-608
[22] Jambunathan K., and Hillier A.C. (2002), *J. Electroanal. Chem.*, **524-525**, 144-156
[23] Zalfaghari A., Chayer M., and Jerkiewicz G. (1997), *J. Electrochem. Soc.*, **144(9)**, 3034-3041
[24] Dean J.A., *Lange's Handbook of Chemistry*, Ch. 8, 997, McGraw-Hill, New York, 15th Ed., 1999
[26] Heben M.J., Penner R.M., Lewis N.S., Dovek, M.M., and Quate C.F. (1989), *Appl. Phys. Lett.*, **54(15)**, 1421-1423
[28] Hugelmann M., and Schindler W. (2003), *Surf. Sci.*, **541**, L643-648.
[29] Landau L.D., and Lifshitz E.M., *Course of Theoretical Physics VIII: Electrodynamics of Continuous Media*, Ch. 11, 39, Pergamon Press, London, 1960
[30] O'Dwyer J.J., *The Theory of Dielectric Breakdown of Solids*, Ch. I & IV, Oxford University Press, London, 1964
[32] Conway B.E., and Tilak B.V. (2002), *Electrochim. Acta*, **47**, 3571-3594
[33] Vetter K.J., *Electrochemical Kinetics*, Academic Press, New York, 1967
[34] Pharr C.M., and Griffiths P.R. (1997), *Anal. Chem.*, **69**, 4673-4679
[36] Conyers J., and White H.S. (2000), *Anal. Chem.*, **72**, 4441-4446
[37] Von Stackelberg M., Pilgram M., and Toome V. (1953), *Z. Elektrochem.*, **57**, 342
[38] Baranski A.S. (1991), *J. Electroanal. Chem.*, **307**, 287
[42] Verwey E.J.W., and Overbeek J.Th.G., *Theory of the Stability of Lyophoic Colloids*, Elsevier, Amsterdam, 1948
[43] Woo D.-H., Yoo J.-S., Park S.-M., Jeon I.C., and Kang H. (2004), *Bull. Korean Chem. Soc.*, **25(4)**, 577-580
[44] Israelachvili J.N., and Adams G.E. (1978), *J. Chem. Soc.Faraday Trans. I*, **74**, 975
[45] (a) Hillier A.C., Kim S., and Bard A.J. (1996), *J. Phys. Chem. B*, **100**, 18808-18817
(b) Hu K., Chai Z., Whitesell J.K., and Bard A.J. (1999), *Langmuir*, **15(9)**, 3343-3347
[46] Woo D.-H., Kang H., and Park S.-M. (2003), *Anal. Chem.*, **75(23)**, 6732-6736

[47] Anselmetti D., Bartoff A., Güntherodt H.-J., Gerber Ch., Michel B., and Rohrer H. (1994), *J. Vac. Sci. Technol. B*, **12(3)**, 1677-1680
[48] Nishikawa H., Shiba H., and Iri T. (1995), *Jap. J. Appl. Phys.*, **34(2A)**, 578-582
[49] Watson G, Dinite B., Blach J.A., and Myhra S. (2002), *J. Phys. D*, **35(16)**, 2066-2074
[50] Fomenko V., Hurth C., Ye T., and Borguet E. (2002), *J. Appl. Phys.*, **91(7)**, 4394-4398
[51] Binnig G., Rohrer H., Gerber Ch., and Weibel E. (1983), *Phys. Rev. Lett.*, **50(2)**, 120-125
[52] Sze S.M., *Physics of Semiconductor Devices*, Wiley, New York, 1981
[53] Israelachvili J.N., *Intermolecular and Surface Forces*, 2nd Edition, Academic Press, London, 1992
[54] Pashley R.M. (1980), *J. Coll. Interface Sci.*, **80(1)**, 153-162
[55] Gaines G.L.Jr. (1957), *J. Phys. Chem.*, **61**, 1408-1413
[56] Israelachvili J.N., and Adams G.E. (1978), *J. Chem. Soc. Faraday Trans. I*, **74**, 975-1001
[57] Mokma D.L., Syers J.K., and Jackson M.L. (1970), *Soil Sci. Soc. Amer. Proc.*, **34**, 146-153
[58] Pashley R.M. (1981), *J. Coll. Interface Sci.*, **83(2)**, 531-546
[59] Forouzan F., and Bard A.J. (1997), *J. Phys. Chem. B*, **101(50)**, 10876-10879
[60] Hugelmann P., and Schindler W. (2005), *J. Phys. Chem. B*¸**109**, 6262-6267
[61] Adzic R., in *Electrocatalysis*, Lipkowski J., and Ross P.N., Eds, Ch. 5, 197-215, Wiley-VCH, New York (1998)
[62] Clavilier J., Rodes A., El Achi K., and Zamakhchari M.A. (1991), *J. Chim .Phys.*, **88(7/8)**, 1291-1337
[63] Lingane J.J., *Electroanalytical Chemistry*, Ch. XI, 240, John Wiley & Sons, New York (1958)
[64] Lide D.R., *CRC Handbook of Physics and Chemistry*, 79th Ed., CRC Press, Boca Raton (1999)
[65] Böttger W., *Elektroanalyse*, Tl. II, 122, Akad. Verlag., Leipzig, 1936 in 63
[66] Selzer Y., Tryan I., and Mandler D. (1999), *J. Phys. Chem. B*, **103(9)**, 1509-1517
[67] Vydra F., Stullk K., and Julakova E., *Electrochemical Stripping Analysis*, Wiley, New York (1976)
[68] Gunawardena G, Hills G.J., and Sharifker B. (1981), *J. Electroanal. Chem.*, **130**, 99-112
[69] Wehmeyer K.R., and Wightman R.M. (1985), *Anal. Chem.*, **57(9)**, 1989-1993
[70] Gunawardena G., Hills G.J., and Montenegro I. (1978), *Electrochim. Acta*, **23**, 693-697
[71] Hills G., Pour A.K., and Scharifker B. (1983), *Electrohim. Acta*, **28(7)**¸ 891-898
[72] Ives D.J.G., and Janz G.J., *Reference Electrodes*, Academic Press, New York, 1961
[73] Feldberg S.W. (1970), *J. Phys. Chem.*, **74(1)**, 87-90
[74] Anson F.C., Martin R.F., and Yarnitzky C. (1969), *J. Phys. Chem.*, **73(6)**, 1835-1842
[75] Slevin C.J., Gray N.J., Macpherson J.V., Webb M.A., and Unwin P.R. (1999), *Electrochem. Comm.*, **1**, 282-288

CONCLUSION

[1] Bousset L., Thompson N.H., Radford S.E., and Melki R. (2002), *EMBO J.***, 21(12)**, 2903-2911
[2] Ando T., Kodera N ;, Takai E., Maruyama D., Saito K., and Toda A. (2001), *Proc. Nat. Acad. Sci. USA*, **98(22)**, 12468-12472
[3] Maboudian R., and Carraro C. (2004), *Ann. Rev. Chem. Phys.*, **55**, 35-54

[4] Kueng A., Kranz C., Lugstein A., Bertagnolli E., and Mizaikoff B. (2003), *Angew. Chem. Intl. Ed.*, **42(28)**, 3237-3240
[5] Yang T.J., Lessard G.A., and Quake S.R. (2000), *Appl. Phys. Lett.*, **76(3)**, 378-380
[6] Majumdar A. (1999), *Ann. Rev. Mat. Res.*, **29**, 505-585

Vita

Cedric Michael Hurth was born on June 8th 1977 in Strasbourg, France.

He received his early education at the Collège des Roseaux in Illkirch, France and attended High School at the Lycée Kléber in Strasbourg France where he obtained a Baccalaureate in Sciences in June 1995. He then attended Preparatory School still at the Lycée Kléber to enter the Ecole Normale Supérieure de Cachan in Cachan, France in September 1998 with a final ranking of 121st out of more than 8,000 candidates to obtain a Masters Degree in Science (MSc.) in July 2001. Simultaneously, he completed his undergraduate studies at the Université Paris XI in Orsay, France from which he received his Bachelor of Sciences (BSc) in July 2000 including a 3-month stay at the University of Pittsburgh for a Summer Research Experience.

In September 2001, he entered an unprecedented graduate exchange program between the University of Texas at Austin in the United Sates of America and Université Bordeaux 1 in France for which he received a grant from both the French Minsitry of Research and the Centre National de la Recherche Scientifique (CNRS). He worked mainly in Pr. Allen J. Bard's group in Austin and with Dr. Jean-Pierre Aimé in Bordeaux.

His main research interests include surface chemistry as well as scanning probe microscopies with local probe methods applied to enzyme studies.

Permanent Address: Cedric Michael Hurth, 17 rue des Roseaux, 67400 Illkirch, France

This dissertation was typed by the author.